N° d'ordre NNT : xxx

THÈSE DE DOCTORAT DE L'UNIVERSITÉ DE LYON
opérée au sein de
l'INSA Lyon

École Doctorale EDA160
École Doctorale Électronique, Électrotechnique et Automatique

Spécialité de doctorat : Département Sciences pour l'ingénieur
Discipline : Génie électrique

Soutenue publiquement/à huis clos le 06/12/2018, par :
Denis Bujoreanu

Échographie compressée: une nouvelle stratégie d'acquisition et de formation pour une imagerie ultra rapide

---

Devant le jury composé de :

Nom Prénom, grade/qualité, établissement/entreprise	Président(e)
Basarab Adrian, Maître de conférences HDR, Université Paul Sabatier de Toulouse	Rapporteur
Luo Jianwen, Maître de conférences HDR, Université Tsinghua	Rapporteur
Thiran Jean-Philippe, Professeur, Ecole Fédérale Polytechnique de Lausanne	Rapporteur
Bridal Lori, Directrice de recherche CNRS, Sorbonne Université	Examinatrice
Friboulet Denis, Professeur, INSA Lyon	Directeur de thèse
Nicolas Barbara, Chargée de recherche HDR CNRS, INSA Lyon	Co-directrice de thèse
Liebgott Hervé, Professeur, Université Claude Bernard Lyon 1	Co-encadrant

Département FEDORA – INSA Lyon - Ecoles Doctorales – Quinquennal 2016-2020

SIGLE	ECOLE DOCTORALE	NOM ET COORDONNEES DU RESPONSABLE
CHIMIE	**CHIMIE DE LYON** **http://www.edchimie-lyon.fr** Sec. : Renée EL MELHEM Bât. Blaise PASCAL, 3e étage **secretariat@edchimie-lyon.fr** INSA : R. GOURDON	M. Stéphane DANIELE Institut de recherches sur la catalyse et l'environnement de Lyon IRCELYON-UMR 5256 Équipe CDFA 2 Avenue Albert EINSTEIN 69 626 Villeurbanne CEDEX **directeur@edchimie-lyon.fr**
E.E.A.	**ÉLECTRONIQUE, ÉLECTROTECHNIQUE, AUTOMATIQUE** **http://edeea.ec-lyon.fr** Sec. : M.C. HAVGOUDOUKIAN **ecole-doctorale.eea@ec-lyon.fr**	M. Gérard SCORLETTI École Centrale de Lyon 36 Avenue Guy DE COLLONGUE 69 134 Écully Tél : 04.72.18.60.97 Fax 04.78.43.37.17 **gerard.scorletti@ec-lyon.fr**
E2M2	**ÉVOLUTION, ÉCOSYSTÈME, MICROBIOLOGIE, MODÉLISATION** **http://e2m2.universite-lyon.fr** Sec. : Sylvie ROBERJOT Bât. Atrium, UCB Lyon 1 Tél : 04.72.44.83.62 INSA : H. CHARLES **secretariat.e2m2@univ-lyon1.fr**	M. Philippe NORMAND UMR 5557 Lab. d'Ecologie Microbienne Université Claude Bernard Lyon 1 Bâtiment Mendel 43, boulevard du 11 Novembre 1918 69 622 Villeurbanne CEDEX **philippe.normand@univ-lyon1.fr**
EDISS	**INTERDISCIPLINAIRE SCIENCES-SANTÉ** **http://www.ediss-lyon.fr** Sec. : Sylvie ROBERJOT Bât. Atrium, UCB Lyon 1 Tél : 04.72.44.83.62 INSA : M. LAGARDE **secretariat.ediss@univ-lyon1.fr**	Mme Emmanuelle CANET-SOULAS INSERM U1060, CarMeN lab, Univ. Lyon 1 Bâtiment IMBL 11 Avenue Jean CAPELLE INSA de Lyon 69 621 Villeurbanne Tél : 04.72.68.49.09 Fax : 04.72.68.49.16 **emmanuelle.canet@univ-lyon1.fr**
INFOMATHS	**INFORMATIQUE ET MATHÉMATIQUES** **http://edinfomaths.universite-lyon.fr** Sec. : Renée EL MELHEM Bât. Blaise PASCAL, 3e étage Tél : 04.72.43.80.46 Fax : 04.72.43.16.87 **infomaths@univ-lyon1.fr**	M. Luca ZAMBONI Bât. Braconnier 43 Boulevard du 11 novembre 1918 69 622 Villeurbanne CEDEX Tél : 04.26.23.45.52 **zamboni@maths.univ-lyon1.fr**
Matériaux	**MATÉRIAUX DE LYON** **http://ed34.universite-lyon.fr** Sec. : Marion COMBE Tél : 04.72.43.71.70 Fax : 04.72.43.87.12 Bât. Direction **ed.materiaux@insa-lyon.fr**	M. Jean-Yves BUFFIÈRE INSA de Lyon MATEIS - Bât. Saint-Exupéry 7 Avenue Jean CAPELLE 69 621 Villeurbanne CEDEX Tél : 04.72.43.71.70 Fax : 04.72.43.85.28 **jean-yves.buffiere@insa-lyon.fr**
MEGA	**MÉCANIQUE, ÉNERGÉTIQUE, GÉNIE CIVIL, ACOUSTIQUE** **http://edmega.universite-lyon.fr** Sec. : Marion COMBE Tél : 04.72.43.71.70 Fax : 04.72.43.87.12 Bât. Direction **mega@insa-lyon.fr**	M. Jocelyn BONJOUR INSA de Lyon Laboratoire CETHIL Bâtiment Sadi-Carnot 9, rue de la Physique 69 621 Villeurbanne CEDEX **jocelyn.bonjour@insa-lyon.fr**
ScSo	**ScSo*** **http://ed483.univ-lyon2.fr** Sec. : Viviane POLSINELLI Brigitte DUBOIS INSA : J.Y. TOUSSAINT Tél : 04.78.69.72.76 **viviane.polsinelli@univ-lyon2.fr**	M. Christian MONTES Université Lyon 2 86 Rue Pasteur 69 365 Lyon CEDEX 07 **christian.montes@univ-lyon2.fr**

*ScSo : Histoire, Géographie, Aménagement, Urbanisme, Archéologie, Science politique, Sociologie, Anthropologie

INSTITUT NATIONAL DES SCIENCES APPLIQUÉES LYON

DEPARTEMENT FEDORA
FORMATION PAR LA RECHERCHE
ET ÉTUDES DOCTORALES
Bâtiment INSA direction

Année Universitaire 2017-2018

ECOLES DOCTORALES – DISCIPLINES
A REMPLIR LORS DE VOTRE INSCRIPTION

Doctorant :
Nom : _____ Prénom : _____ **Signature :**

Directeur de thèse :
Nom : _____ Prénom : _____ **Signature :**

UNE SEULE DISCIPLINE POSSIBLE, à choisir parmi la liste suivante :

ECOLES DOCTORALES n° code national	DISCIPLINES	Cocher la case correspondante
ED CHIMIE DE LYON **(Chimie, Procédés, Environnement)** **EDA206**	Chimie Procédés Environnement	☐ ☐ ☐
HISTOIRE, GEOGRAPHIE, AMENAGEMENT, URBANISME, ARCHEOLOGIE, SCIENCE POLITIQUE, SOCIOLOGIE, ANTHROPOLOGIE **(ScSo)** **EDA483**	Géographie – Aménagement - Urbanisme	☐
ELECTRONIQUE, ELECTROTECHNIQUE, AUTOMATIQUE **(E.E.A.)** **EDA160**	Automatique Génie Electrique Electronique, micro et nanoélectronique, optique et laser Ingénierie pour le vivant Traitement du Signal et de l'Image	☐ ☐ ☐ ☐ ☐
EVOLUTION, ECOSYSTEMES, MICROBIOLOGIE, MODELISATION **(E2M2)** **EDA 341**	Paléoenvironnements et évolution Micro-organismes, interactions, infections Biologie Evolutive, Biologie des Populations, écophysiologie Biomath-Bioinfo-Génomique évolutive Ecologie des communautés, fonctionnement des écosystèmes, écotoxicologie	☐ ☐ ☐ ☐ ☐
INFORMATIQUE ET MATHEMATIQUES DE LYON **(InfoMaths)** **EDA 512**	Informatique Informatique et applications Mathématiques et applications Génie Industriel	☐ ☐ ☐ ☐
INTERDISCIPLINAIRE SCIENCES-SANTE **(EDISS)** **EDA205**	Biochimie Physiologie Ingénierie biomédicale	☐ ☐ ☐
ED MATERIAUX DE LYON **EDA 034**	Matériaux	☐
MEGA DE LYON **(MECANIQUE, ENERGETIQUE, GENIE CIVIL, ACOUSTIQUE)** **(MEGA)** **EDA162**	Mécanique des Fluides Génie Mécanique Biomécanique Thermique Energétique Génie Civil Acoustique	☐ ☐ ☐ ☐ ☐ ☐

Pour le Directeur de l'INSA Lyon
Et par délégation

Florence POPOWYCZ
Directrice du Département FEDORA
Formation par la Recherche Et des Etudes Doctorales

Cette liste est mise à jour annuellement par le Département FEDORA en collaboration avec les Ecoles Doctorales.

I do not know what I may appear to the world,
but to myself I seem to have been only like a boy
playing on the seashore, and diverting myself in
now and then finding a smoother pebble or a
prettier shell than ordinary, whilst the great ocean
of truth lay all undiscovered before me.
— Isaac Newton

To my family…

Acknowledgements

Before detailing the work of my Ph.D, I would like to express my sincere gratitude to the people without whom all of this would not be possible. First, to my supervisors Denis Friboulet, Hervé Liebgott and Barba Nicolas, whose merit in this work is as great as mine. To my Ph.D colleagues Yanis and Emilia for the fruitful collaborations that helped me greatly in my quest for the ultrasound imaging understanding. And of-course to Kenny, for being an all-around nice guy.

I would like to thank the scientists from the LTS5 Laboratory at the EPFL: Adrien Besson, Dimitris Perdios, Marcel Adriti and Jean-Philippe Thiran. It is beyond the reasonable doubt that the exchanges between our teams helped me to explore the inverse problem framework in the context of ultrasound imaging. I want also to acknowledge the useful exchange of ideas with our INSA de Lyon colleagues from the CITI Lab: Claire Goursaud, Leonardo Cardoso and Jean-Marie Gorce.

Special thanks to David Rousseau who was the person who welcomed me at CREATIS for my master thesis and then greatly motivated me to candidate for this Ph.D.

Contents

Manuscript in English Part I

1 Introduction

1.1 Context

It is beyond doubt that the relative low cost of ultrasound scanners, the quick procedure and the ability to image soft biological tissues helped ultrasound imaging to become one of the most common medical diagnostic tool. Moreover, since the acoustic waves used for imaging are not very energetic, they do not have a biological effect on the insonified tissue, thus in a wide spectrum of applications such as cardiology, angiology, obstetrics, musculoskeletal and others, echography is considered as a key examination tool. Unfortunately, ultrasound still has some drawbacks when compared to other medical imaging techniques (such as X-ray tomography and Magnetic Resonance Imaging) mainly in terms of the provided image quality and details. Nonetheless, its ability to provide images in real time allows to survey tissue motion, to perform such imaging modalities as pulsed / continuous wave Doppler and even to follow the movement of ultrasound shear waves. However, in the quest for an improved performance of these techniques, a better ultrasound image quality is required, which can be achieved easily at the expense of the frame acquisition rate. This deep rooted trade-off between the provided image quality and the acquisition time, is perhaps one of the most challenging in today's ultrasound research and its overcoming could lead to diagnostic improvements in the already existing ultrasound applications [Hansen et al., 2014] and even pave the way towards novel uses of echography [Tanter and Fink, 2014].

More specifically, this work comes to extend the concept of ultrasound plane wave insonifications. Plane wave imaging represents an ultrafast acquisition technique that relies on broad beam emissions / receptions in order to reconstruct full images of the medium at once. However, the lack of emission beam focusing considerably impairs the provided image quality with regard to classical focused ultrasound. Coherent sommation of images reconstructed after the emission / reception of mutually tilted plane waves can be employed in order to boost the image quality, however this improvement comes again at the expense of the acquisition rate.

1.2 Objective

This study addresses the previously stated trade-off between the image quality and the frame acquisition time. Through a mix of such concepts as plane wave imaging, multiple-input / multiple-output systems and inverse problems, this study aims at acquiring ultrasound images of the insonified tissue simultaneously, thus providing an increased frame rate while not degrading the image quality.

1.3 Manuscript layout

This manuscript is divided into four Chapters:

- **Introduction** – in this very Chapter the brief summary of ultrasound imaging advantages and applications is given. The problem this work addresses is stated and the thesis objectives are formulated. A succinct summary of this manuscript is also provided.
- **Principles of acoustics and ultrasound imaging** – here the theoretical background for the acoustic wave propagation is fixed. Furthermore, based on this formulation, the conventional ultrasound acquisition schemes are reviewed and the usual metrics that quantify the image quality are introduced. Here also are summarized the already existing approaches meant to overcome the trade-off between image quality and frame acquisition rate.
- **Temporal encoding for increasing the frame acquisition rate** – this Chapter presents the first contribution of this work. Firstly, it details the theoretical background of an ultrasound imaging approach based on a reduced model of the propagation of temporally encoded ultrasound waves inside soft tissues. Then, simulation and in-vitro results are shown and discussed, the advantages / limitations of the method being underlined.
- **An Advanced Model for Coded UltraSound imaging (AMCUS)** – the performance of an imaging approach based on an advanced direct model of ultrasound wave propagation is presented in this Chapter. First, the general direct model is built. Then, the advanced model is combined with the concept of temporal encoding of ultrasound waves and its adaptation to a specific ultrafast acquisition scheme is shown. Furthermore an inverse problem approach is proposed in order to reconstruct the image of the insonified medium. The performance of both direct model and reconstruction method is assessed through numerical simulations.

2 Principles of acoustics and ultrasound imaging

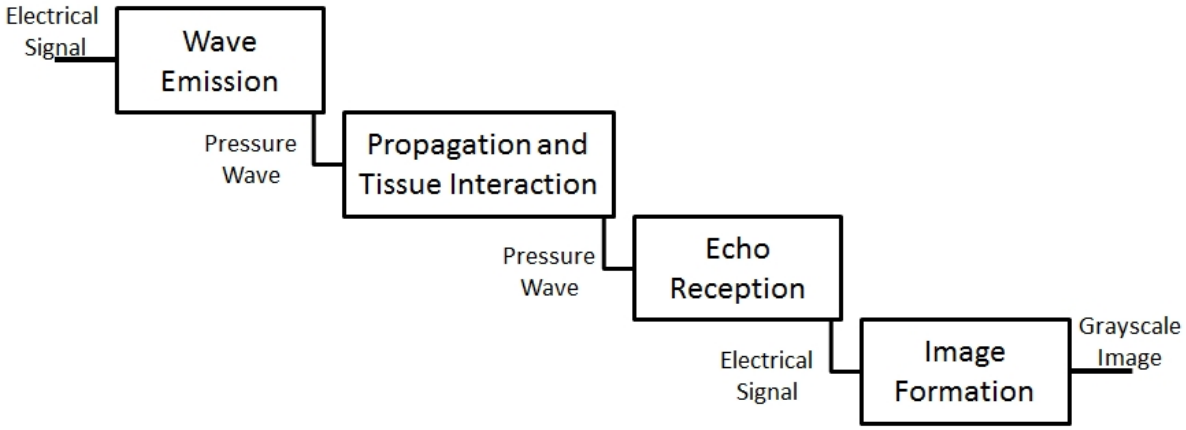

Figure 2.1: The conventional pipeline for ultrasound image formation

The process of conventional ultrasound imaging is presented in Fig.2.1.Here, this complete pipeline is addressed and each block is detailed in order to better understand the background of this work. The purpose being to present a general framework that allows describing all the existing ultrasound acquisition schemes: focused / plane / diverging waves. Relying on this framework, the already existing modifications for each of the blocks in Fig.2.1, aiming to overcome the provided image quality / frame acquisition rate trade-off, are presented. In addition to its purpose of succinctly modeling all the existing acquisition schemes, the framework developed here will also allow to better understand the contributions presented in the next Chapters.

2.1 Principle of ultrasound wave propagation

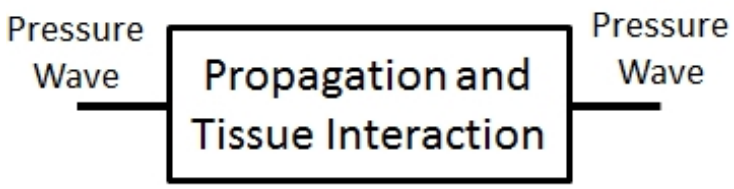

Figure 2.2: The ultrasound's pipeline block detailed in Section 8.1

The ultrasound propagation phenomenon represents the main building block (see Fig.2.2) on which

relies all the existing ultrasound imaging techniques and the methods developed in this thesis are no exceptions. In this Section, the principle of this phenomenon is explained and the basis for the understanding of both existing and proposed ultrasound imaging methods is set.

As previously stated, echography employs low energetic acoustic waves to insonify what is supposed to be a soft biological tissue at rest [Jensen, 1991, Schmerr Jr, 2014]. In these conditions, one can make the assumption that, before the wave generation, the insonified medium at each point (defined by the position vector $\vec{r} = (x_r, y_r, z_r)$) has a mean pressure P_0 and a density $\rho_0(\vec{r})$ [Jensen, 1991, Jensen, 1999]. While the medium can be inhomogeneous, meaning that $\rho_0(\vec{r})$ could vary, for soft tissues at rest the pressure will be supposed to be constant. In these conditions, the small perturbation generated by the acoustic wave, generates slight ripples $p_1(\vec{r}, t)$ and $\rho_1(\vec{r}, t)$ inside the pressure and density fields respectively. Thus, for a point $\vec{r}$, the new pressure and density can be written as [Jensen, 1991, Morse et al., 1969]:

$$\begin{matrix} P(\vec{r}, t) = P_0 + p_1(\vec{r}, t) \\ \rho(\vec{r}, t) = \rho_0(\vec{r}) + \rho_1(\vec{r}, t) \end{matrix} \text{ with } \begin{cases} p_1(\vec{r}, t) << P_0 \\ \rho_1(\vec{r}, t) << \rho_0(\vec{r}) \end{cases} \tag{2.1}$$

2.1.1 Linear wave equation

Relying on the conservation laws of mass and momentum, as demonstrated in Appendix A, it can be shown that there is a close relation between the spatial-temporal evolution of the pressure and density fields. This relation can be written as follows:

$$\nabla^2 p_1(\vec{r}, t) - \frac{1}{c_m^2} \frac{\partial^2 p_1(\vec{r}, t)}{\partial t^2} = -\frac{2\Delta c_0(\vec{r})}{c_m^3} \cdot \frac{\partial^2 p_1(\vec{r}, t)}{\partial t^2} + \frac{1}{\rho_m} \nabla \big[\Delta \rho_0(\vec{r})\big] \cdot \nabla p_1(\vec{r}, t) \tag{2.2}$$

where c_m is the propagation speed of sound inside soft tissues at rest. ρ_m is the density of the soft tissue at rest. $\Delta\rho_0(\vec{r})$ and $\Delta c_0(\vec{r})$ are the local variations of the density and of the propagation speed of sound respectively. As one can see, in (2.2), the left side of the equation represents the pressure evolution as a function of time and space while the right side represents the wave behavior when it encounters tissue inhomogeneities that appear as speed and density variations $\Delta c_0(\vec{r})$ and $\Delta\rho_0(\vec{r})$ respectively. This relation is called the equation of acoustic wave propagation inside inhomogeneous media. For a perfectly homogeneous medium, equation (2.2) becomes:

$$\nabla^2 p_1(\vec{r}, t) - \frac{1}{c_m^2} \frac{\partial^2 p_1(\vec{r}, t)}{\partial t^2} = 0 \tag{2.3}$$

2.1.2 Pressure Wave Scattering

In the previous Section, two equations that model the acoustic wave propagation inside inhomogeneous (2.2) and homogeneous (2.3) soft tissues, were deduced. Here, the effect of scattering is presented and the echoes pressure, in a given point of the medium, is calculated.

As shown in (2.2), if there is a variation in the medium density field, a pressure wave scattering is generated. This phenomenon can be seen as a generation of a new pressure field $p_s(\vec{r}_1, t_{\vec{r}_1})$ at the point $\vec{r}_1$. In these conditions, the total pressure disturbance $p_1(\vec{r}_1, t_{\vec{r}_1})$, at any point $\vec{r}_1$ inside the medium, can be seen as a superposition of an incident pressure field $p_i(\vec{r}_1, t_{\vec{r}_1})$ (related to the incident acoustic wave) and a scattered pressure field $p_s(\vec{r}_1, t_{\vec{r}_1})$(related to the echoes):

$$p_1(\vec{r}_1, t_{\vec{r}_1}) = p_i(\vec{r}_1, t_{\vec{r}_1}) + p_s(\vec{r}_1, t_{\vec{r}_1}) \tag{2.4}$$

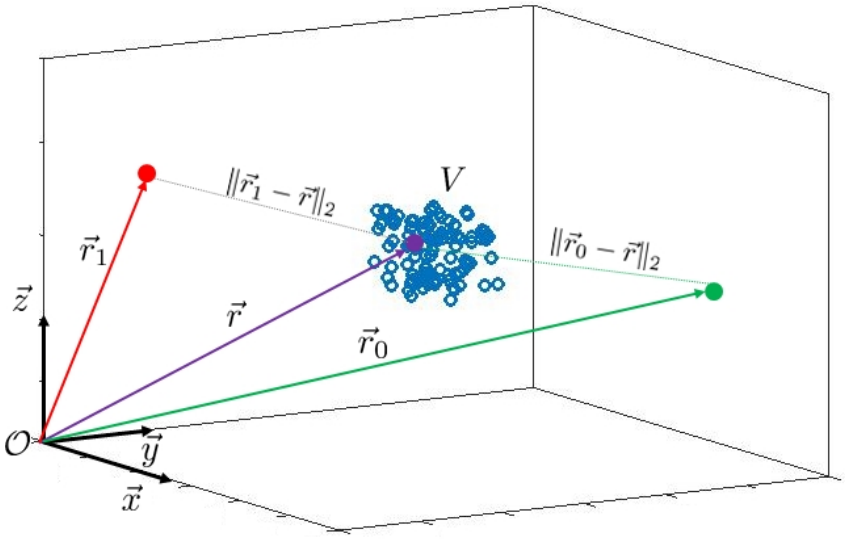

Figure 2.3: Schematic representation of a medium and its associated coordinate system. The medium is homogeneous except in the volume V where it contains some density inhomogeneities (blue). The point of calculation of the scattered pressure is $\vec{r}_1$. The generation point of the wave inside the medium is $\vec{r}_0$. The acoustic wave is emitted at $\vec{r}_0$, it scatters in V and is received at $\vec{r}_1$.

Thus, in order to solve (2.2), one needs to first estimate the values of the pressure fields $p_i(\vec{r}_1, t_{\vec{r}_1})$ and $p_s(\vec{r}_1, t_{\vec{r}_1})$. Consider the following relation, equivalent to (2.2):

$$\begin{aligned} &\mathscr{L}\, p_1(\vec{r}, t) = \mathscr{F}\, p_1(\vec{r}, t) \\ \text{with: } &\begin{cases} \mathscr{L} = \nabla^2 - \frac{1}{c_m^2} \cdot \frac{\partial^2}{\partial t^2} \\ \mathscr{F} = -\frac{2\Delta c_0(\vec{r})}{c_m^3} \cdot \frac{\partial^2}{\partial t^2} + \frac{1}{\rho_m} \nabla\big[\Delta\rho_0(\vec{r})\big] \cdot \nabla \end{cases} \end{aligned} \tag{2.5}$$

In (2.5), the differential operator $\mathscr{L}$ represents the space / time evolution of the pressure field and $\mathscr{F}$, as stated in the previous section, represents the behavior of the wave when it encounters a density inhomogeneity and it will be called scattering operator. Thus, it can be deduced that around any scatterer placed at the position $\vec{r}$, the total pressure $p_1(\vec{r}, t)$ can be seen as a superposition of two pressure fields: incident ($p_i(\vec{r}, t)$) and scattered ($p_s(\vec{r}, t)$). The idea here is to first solve the following equation:

$$\begin{aligned} \mathscr{L}\mathscr{G}_p(\vec{r}_1, t_{\vec{r}_1} | \vec{r}, t) = \delta(x_{\vec{r}_1} - x_r)\delta(y_{\vec{r}_1} - y_r)\delta(z_{\vec{r}_1} - z_r)\delta(t_{\vec{r}_1} - t) \Longleftrightarrow \\ \mathscr{L}\mathscr{G}_p(\vec{r}_1, t_{\vec{r}_1} | \vec{r}, t) = \delta(\vec{r}_1 - \vec{r})\delta(t_{\vec{r}_1} - t) \end{aligned} \tag{2.6}$$

The term $\mathscr{L}\mathscr{G}(\vec{r}_1, t_{\vec{r}_1} | \vec{r}, t)$ in equation (2.6) models the propagation of an acoustic wave to the point $\vec{r}_1$ (at time $t_{\vec{r}_1}$) generated at time $t_{\vec{r}}$ by a punctual source placed at the medium point $\vec{r}$. The solution of this equation is the Green function [Jensen, 1991, Morse et al., 1969]:

$$\mathscr{G}_p(\vec{r}_1, t_{\vec{r}_1} | \vec{r}, t) = \frac{1}{4\pi \|\vec{r}_1 - \vec{r}\|_2} \delta\Big(t - t_{\vec{r}} - \frac{\|\vec{r}_1 - \vec{r}\|_2}{c_m}\Big) \tag{2.7}$$

Now, consider the case displayed in Fig.2.3, where an acoustic wave travels in free field conditions until it reaches the inhomogeneities inside the volume V where it scatters. $\mathscr{G}_p(\vec{r}_1, t_{\vec{r}_1} | \vec{r}, t)$ represents the effect of the propagation (to a point $\vec{r}_1$) on a short impulsion generated by a point $\vec{r} \in V$. This effect can be split in two parts, the first one ($1/(4\pi\|\vec{r}_1 - \vec{r}\|_2)$) models the impulsion amplitude loss due to propagation and the second one ($t_{\vec{r}} + \|\vec{r}_1 - \vec{r}\|_2 / c_m$) represents the time delay needed for propagation.

Since V contains an indefinite amount of scatterers each one of them behaving as set in (2.6), and since each scatterer scatters the pressure field $p_1(\vec{r},t)$ as set by $\mathscr{F}$, (2.6) can be rewritten as:

$$\int_V \int_t \left[\delta(\vec{r}_1 - \vec{r})\delta(t_{\vec{r}_1} - t)\mathscr{F}(\vec{r},t) \right] \mathrm{d}t\,\mathrm{d}^3\vec{r} = \int_V \int_t \left[\mathscr{L}\mathscr{G}_p(\vec{r}_1, t_{\vec{r}_1}|\vec{r},t)\mathscr{F}\,p_1(\vec{r},t) \right] \mathrm{d}t\,\mathrm{d}^3\vec{r} \tag{2.8}$$

Since $\mathscr{L}$ is a linear operator, (2.8) can be reformulated as follows:

$$\mathscr{F}\,p_1(\vec{r}_1, t_{\vec{r}_1}) = \mathscr{L}\left[\int_V \int_t \mathscr{G}_p(\vec{r}_1, t_{\vec{r}_1}|\vec{r},t)\mathscr{F}\,p_1(\vec{r},t)\,\mathrm{d}t\,\mathrm{d}^3\vec{r} \right] \tag{2.9}$$

Now combining the result of (2.9) with (2.5) one can obtain:

$$\begin{gathered}
\mathscr{L}\,p_s(\vec{r}_1, t_{\vec{r}_1}) = \mathscr{L}\left[\int_V \int_t \mathscr{G}_p(\vec{r}_1, t_{\vec{r}_1}|\vec{r},t)\mathscr{F}\,p_1(\vec{r},t)\,\mathrm{d}t\,\mathrm{d}^3\vec{r} \right] \Longleftrightarrow \\
p_s(\vec{r}_1, t_{\vec{r}_1}) = \int_V \int_t \mathscr{G}_p(\vec{r}_1, t_{\vec{r}_1}|\vec{r},t)\mathscr{F}\,p_1(\vec{r},t)\,\mathrm{d}t\,\mathrm{d}^3\vec{r} \Longleftrightarrow \\
p_s(\vec{r}_1, t_{\vec{r}_1}) = \int_V \int_t \mathscr{G}_p(\vec{r}_1, t_{\vec{r}_1}|\vec{r},t)\left[-\frac{2\Delta c_0(\vec{r})}{c_m^3} \cdot \frac{\partial^2 p_1(\vec{r},t)}{\partial t^2} + \frac{1}{\rho_m}\nabla\big[\Delta\rho_0(\vec{r})\big] \cdot \nabla p_1(\vec{r},t) \right] \mathrm{d}t\,\mathrm{d}^3\vec{r}
\end{gathered} \tag{2.10}$$

As it can be intuitively deduced, the integral over the volume V and over the time t, in (2.10), allows considering all the scatterings the acoustic wave $p_1(\vec{r},t)$ undergoes (in V). At this point, given (2.4), the integral (2.10) cannot be found, since each scattering of the incident wave can generate more scatterings and so on. Thus, an approximation needs to made, that will allow solving (2.10). First, consider the linear operator $\mathbb{G}_i$, defined for an arbitrary pressure field $p(\vec{r},t)$ as follows:

$$\mathbb{G}_i\mathscr{F}\,p(\vec{r},t) = \int_V \int_t \mathscr{G}_p(\vec{r}_1, t_{\vec{r}_1}|\vec{r},t)\mathscr{F}\,p(\vec{r},t)\,\mathrm{d}t\,\mathrm{d}^3\vec{r} \tag{2.11}$$

Using (2.11), one can deduce that the first scattering through the volume V of the incident field $p_i(\vec{r},t)$ will generate a field:

$$p_{s_1}(\vec{r}_1, t_{\vec{r}_1}) = \mathbb{G}_i\mathscr{F}\,p_i(\vec{r},t) = \int_V \int_t \mathscr{G}_p(\vec{r}_1, t_{\vec{r}_1}|\vec{r},t)\mathscr{F}\,p_i(\vec{r},t)\,\mathrm{d}t\,\mathrm{d}^3\vec{r} \tag{2.12}$$

Since after the first scattering the pressure $p_1(\vec{r},t)$ becomes equal to $p_i(\vec{r},t) + p_{s_1}(\vec{r},t)$ the second scattering of the wave will generate a pressure wave:

$$p_{s_2}(\vec{r}_1, t_{\vec{r}_1}) = \mathbb{G}_i\mathscr{F}\,p_1(\vec{r},t) = \mathbb{G}_i\mathscr{F}\Big(p_i(\vec{r},t) + p_{s_1}(\vec{r},t)\Big) \underset{\text{Using (2.12)}}{=} \mathbb{G}_i\mathscr{F}\,p_i(\vec{r},t) + (\mathbb{G}_i\mathscr{F})^2 p_i(\vec{r},t) \tag{2.13}$$

From (2.12) and (2.13) it can be deduced that:

$$p_s(\vec{r}_1, t_{\vec{r}_1}) = \mathbb{G}_i\mathscr{F}\,p_i(\vec{r},t) + (\mathbb{G}_i\mathscr{F})^2 p_i(\vec{r},t) + (\mathbb{G}_i\mathscr{F})^3 p_i(\vec{r},t) + \cdots \tag{2.14}$$

(2.14) represents the Born-Neumann expansion of the scattered field. The terms $(\mathbb{G}_i\mathscr{F})^N p_i(\vec{r},t)$ represent N^{th} order scatterings and will be considered weak ($(\mathbb{G}_i\mathscr{F})^N p_i(\vec{r},t) << \mathbb{G}_i\mathscr{F}\,p_i(\vec{r},t)$, $\forall N \geq 2$) for the rest of this work. This assumption, called first order Born approximation, gives [Jensen, 1991,

Jensen, 1999, Morse et al., 1969]:

$$p_s(\vec{r}_1, t_{\vec{r}_1}) \approx \mathbb{G}_i \mathscr{F}\, p_i(\vec{r}, t) \Longleftrightarrow$$
$$p_s(\vec{r}_1, t_{\vec{r}_1}) = \int_V \int_t \mathscr{G}_p(\vec{r}_1, t_{\vec{r}_1} | \vec{r}, t) \left[-\frac{2\Delta c_0(\vec{r})}{c_m^3} \cdot \frac{\partial^2 p_i(\vec{r}, t)}{\partial t^2} + \frac{1}{\rho_m} \nabla\left[\Delta\rho_0(\vec{r})\right] \cdot \nabla p_i(\vec{r}, t) \right] \mathrm{d}t\, \mathrm{d}^3\vec{r} \tag{2.15}$$

The relation (2.15) allows computing the pressure of the echoes generated in the volume V, when

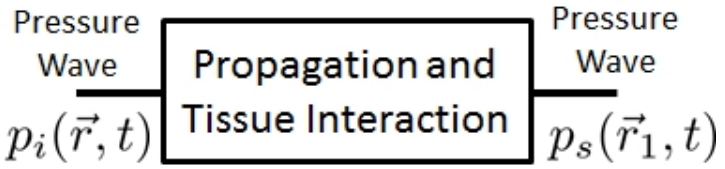

Figure 2.4: The "Wave propagation" block with the corresponding input and output described in Subsections 2.1.1-2.1.2

V is insonified with an incident pressure field $p_i(\vec{r}, t)$. At this point, the block "Wave propagation" (Fig.2.2) is complete, and its new representation is shown in Fig.2.4. Thus, this Section presented a complete description of the physical phenomenon of acoustic wave propagation inside homogeneous / inhomogeneous soft tissues.

2.1.3 Two planar transducers

Here, the two highlighted blocks ("Wave emission" and "Echo reception") in Fig.2.5, will be described. The main goal being to find out how the incident acoustic wave $p_i(\vec{r}, t)$ is generated and what is the electrical signature of the backscattered pressure wave $p_s(\vec{r}_1, t)$. The case of two planar piezoelectric transducers submersed in an inhomogeneous media (Fig.2.6) will be analyzed.

As seen in (2.15), for the case displayed in Fig.2.3, the scattered wave generated in the volume V

Figure 2.5: The two blocks of the ultrasound imaging pipeline studied in Subsection 2.1.3

depends on the incident pressure $p_1(\vec{r}, t)$ (generated by the a punctual source placed at $\vec{r}_0$). In the case of Fig.2.6, the source (resp. receiver) is a planar surface of area S_e (resp. S_r). Suppose that the medium surrounding the transducers is homogeneous (pressure P_0 and density ρ_m) and that during vibration, both surfaces remain parallel to their initial position. In such conditions, one can deduce that the vibrating velocities $\mathcal{V}_{S_e}(t)$ (resp. $\mathcal{V}_{S_r}(t)$) do not change as a function of the position on the S_e (resp. S_r) surfaces. Furthermore, since the medium is homogeneous between the surface S_e and the volume V, the emitted acoustic wave propagates in free-field conditions between S_e and V and verifies (2.3). Now in order to solve (2.3) in the case of a planar transducer, in [Tupholme, 1969, Stepanishen, 1971] was proposed to use the velocity potential $\psi(\vec{r}, t)$ of the acoustic wave inside the volume V. In homogeneous medium $\psi(\vec{r}, t)$ satisfies the following relation:

$$\nabla^2\psi(\vec{r}, t) - \frac{1}{c_m^2} \frac{\partial^2\psi(\vec{r}, t)}{\partial t^2} = 0 \tag{2.16}$$

Following the same reasoning as in (2.5)–(2.7) it can be deduced that the Green function that satisfies (2.16) is:

$$\mathscr{G}_\psi(\vec{r},t|\vec{r}_0+\vec{r}_{S_e},t_{\vec{r}_0})=\frac{1}{2\pi\|\vec{r}-\vec{r}_0-\vec{r}_{S_e}\|_2}\delta\Big(t-t_{\vec{r}_0}-\frac{\|\vec{r}-\vec{r}_0-\vec{r}_{S_e}\|_2}{c_m}\Big) \tag{2.17}$$

where $\vec{r}_0$ (resp. $\vec{r}_1$) are the closest points on the surface S_e (resp. S_r) to the coordinate system origin $\mathscr{O}$. The position vector $\vec{r}_{S_e}$ (resp. $\vec{r}_{S_r}$) is chosen in such way that any point described by $\vec{r}_0+\vec{r}_{S_e}$ (resp. $\vec{r}_1+\vec{r}_{S_r}$) belongs to the surface S_e (resp. S_r). The general solution of (2.16) (obtained using a similar reasoning as in (2.8)–(2.10)) is then:

$$\psi(\vec{r},\vec{r}_0,t)=\int_S\int_t \mathscr{V}_{S_e}(t)\mathscr{G}_\psi(\vec{r},t|\vec{r}_0+\vec{r}_{S_e},t_{\vec{r}_0})\,\mathrm{d}t_{\vec{r}_0}\,\mathrm{d}^2\vec{r}_{S_e} \tag{2.18}$$

where $\psi(\vec{r},\vec{r}_0,t)$ can be interpreted as the value of the velocity potential at the point $\vec{r}$, generated by the vibration of the surface S_e at the position $\vec{r}_0$. The continuous sum over all the points on the vibrating surface S_e in (2.18) represents the Huygens principle. In other words $\psi(\vec{r},\vec{r}_0,t)$ can be seen as a superposition of an infinite amounts of spherical waves generated by an infinite amount of points on the surface S_e. Since in (2.18) $\mathscr{V}_{S_e}(t)$ is constant for all $\vec{r}_{S_e}$, (2.18) can be rewritten as:

$$\begin{gathered}
\psi(\vec{r},\vec{r}_0,t)=\int_t \mathscr{V}_{S_e}(t)\left[\int_S \mathscr{G}_\psi(\vec{r},t|\vec{r}_0+\vec{r}_{S_e},t_{\vec{r}_0})\,\mathrm{d}^2\vec{r}_{S_e}\right]\mathrm{d}t_{\vec{r}_0}\iff\\
\psi(\vec{r},\vec{r}_0,t)=\int_t \mathscr{V}_{S_e}(t)\,g_{S_e}(\vec{r},t-t_{\vec{r}_0})\,\mathrm{d}t_{\vec{r}_0}\\
\text{with: } g_{S_e}(\vec{r},t-t_{\vec{r}_0})=\int_S \mathscr{G}_\psi(\vec{r},t|\vec{r}_0+\vec{r}_{S_e},t_{\vec{r}_0})\,\mathrm{d}^2\vec{r}_{S_e}\iff\\
g_{S_e}(\vec{r},t-t_{\vec{r}_0})=\int_S \frac{1}{2\pi\|\vec{r}-\vec{r}_0-\vec{r}_{S_e}\|_2}\delta\Big(t-t_{\vec{r}_0}-\frac{\|\vec{r}-\vec{r}_0-\vec{r}_{S_e}\|_2}{c_m}\Big)\,\mathrm{d}^2\vec{r}_{S_e}
\end{gathered} \tag{2.19}$$

At this point, one can see that in (2.19) the term $g_{S_e}(\vec{r},t-t_{\vec{r}_0})$ does not depend on the physical properties of the medium and takes into account only the geometry of the emitting source (S_e) and the point where the velocity potential is calculated ($\vec{r}$). Thus $g_{S_e}(\vec{r},t-t_{\vec{r}_0})$ is called the spatial impulse response of the source S_e in emission [Jensen, 1991, Jensen, 1999, Jensen and Svendsen, 1992]. One can observe in (2.19) that the velocity potential expression can be further simplified as follows:

$$\begin{gathered}
\psi(\vec{r},\vec{r}_0,t)=\int_t \mathscr{V}_{S_e}(t)\,g_{S_e}(\vec{r},t-t_{\vec{r}_0})\,\mathrm{d}t_{\vec{r}_0}\\
\psi(\vec{r},\vec{r}_0,t)=\mathscr{V}_{S_e}(t)*_t g_{S_e}(\vec{r},t)
\end{gathered} \tag{2.20}$$

where $*_t$ represents the temporal convolution between two signals. From $\psi(\vec{r},\vec{r}_0,t)$, the incident pressure field in the point $\vec{r}$ can be deduced as follows [Jensen, 1991, Stepanishen, 1971, Jensen and Svendsen, 1992]:

$$p_i(\vec{r},t)=\rho_m\frac{\partial\psi(\vec{r},\vec{r}_0,t)}{\partial t}\underset{\text{Using 2.20}}{=}\rho_m\frac{\partial\mathscr{V}_{S_e}(t)}{\partial t}*_t g_{S_e}(\vec{r},t) \tag{2.21}$$

Equations (2.15) and (2.21) represent the scattered pressure field measured at any point of the medium $\vec{r}_1$ and the incident pressure field at any point of the medium $\vec{r}$ respectively.

Let us define the total force $\mathscr{U}_{S_r}(t_{\vec{r}_1})$ exerted by the acoustic wave on the surface S_r. At this point,

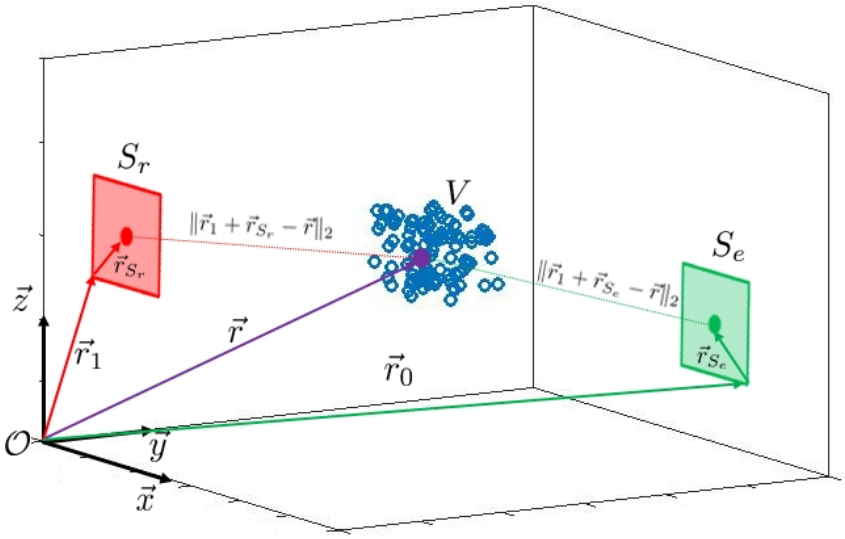

Figure 2.6: Schematic representation of a homogeneous medium that contains a volume V with density inhomogeneities. Two vibrating transducers are submerged into the medium. S_e is the planar surface that generates a pressure wave inside the medium. Thus the acoustic wave propagates in free field conditions under it reaches V where it scatters and then is received by S_r.

one can choose $\vec{r} \in V$ and $\vec{r}_1 \in S_r$, implying that by using (2.15), $\mathcal{U}_{S_r}(t_{\vec{r}_1})$ becomes:

$$\begin{aligned} \mathcal{U}_{S_r}(t_{\vec{r}_1}) &= \int_{S_r} p_s(\vec{r}_1 + \vec{r}_{S_r}, t)\, \mathrm{d}^2\vec{r}_{S_r} \Longleftrightarrow \\ \mathcal{U}_{S_r}(t_{\vec{r}_1}) &= \int_{S_r}\int_{V}\int_{t} \mathcal{G}_p(\vec{r}_1 + \vec{r}_{S_r}, t_{\vec{r}_1}|\vec{r}, t)\mathcal{F}\,p_i(\vec{r}, t)\, \mathrm{d}t\, \mathrm{d}^3\vec{r}\, \mathrm{d}^2\vec{r}_{S_r} \end{aligned} \tag{2.22}$$

Since the scattering at the point $\vec{r}$ (represented by the term $\mathcal{F}\,p_i(\vec{r}, t)$) does not depend on the surface S_r, by rearranging the terms in (2.22), one can obtain the following relation:

$$\begin{aligned} \mathcal{U}_{S_r}(t_{\vec{r}_1}) &= \int_{V}\int_{t} \left[\mathcal{F}\,p_i(\vec{r}, t) \int_{S_r} \mathcal{G}_p(\vec{r}_1 + \vec{r}_{S_r}, t_{\vec{r}_1}|\vec{r}, t)\, \mathrm{d}^2\vec{r}_{S_r} \right] \mathrm{d}t\, \mathrm{d}^3\vec{r} \Longleftrightarrow \\ \mathcal{U}_{S_r}(t_{\vec{r}_1}) &= \tfrac{1}{2}\int_{V}\int_{t} \left[\mathcal{F}\,p_i(\vec{r}, t)\, g_{S_r}(\vec{r}, t_{\vec{r}_1} - t) \right] \mathrm{d}t\, \mathrm{d}^3\vec{r} \\ \text{with: } g_{S_r}(\vec{r}, t_{\vec{r}_1} - t) &= \int_{S} \mathcal{G}_p(\vec{r}_1 + \vec{r}_{S_r}, t_{\vec{r}_1}|\vec{r}, t)\, \mathrm{d}^2\vec{r}_{S_r} \Longleftrightarrow \\ g_{S_r}(\vec{r}, t_{\vec{r}_1} - t) &= \int_{S} \frac{1}{2\pi\|\vec{r} - \vec{r}_1 - \vec{r}_{S_r}\|_2} \delta\Big(t_{\vec{r}_1} - t - \frac{\|\vec{r} - \vec{r}_1 - \vec{r}_{S_e}\|_2}{c_m}\Big)\, \mathrm{d}^2\vec{r}_{S_e} \end{aligned} \tag{2.23}$$

In (2.23), the signal $g_{S_r}(\vec{r}, t)$ represents the spatial impulse response of the vibrating transducer S_r at the medium point $\vec{r}$ [Jensen, 1991, Jensen, 1999, Jensen and Svendsen, 1992]. By employing this term in the expression of $\mathcal{U}_{S_r}(t_{\vec{r}_1})$ in (2.23), one can obtain:

$$\mathcal{U}_{S_r}(t_{\vec{r}_1}) = \frac{1}{2}\int_{V} \mathcal{F}\,p_i(\vec{r}, t) *_t g_{S_r}(\vec{r}, t_{\vec{r}_1})\, \mathrm{d}^3\vec{r} \tag{2.24}$$

(2.24) is the expression of the total force exerted on the receiving transducer and represents the sum over all the volume V of each scatterer's reflection convolved with the spatial impulse response of the transducer.

Using (2.21) and (2.24), the total force expression becomes:

$$\begin{gathered}\mathscr{U}_{S_r}(t) = \tfrac{1}{2}\int_V \mathscr{F}\left[\rho_m \frac{\partial \mathscr{V}_{S_e}(t)}{\partial t} *_t g_{S_e}(\vec{r},t)\right] *_t g_{S_r}(\vec{r},t)\,\mathrm{d}^3\vec{r} \underset{\mathscr{F},*_t-\text{linear}}{\Longleftrightarrow} \\ \mathscr{U}_{S_r}(t) = \tfrac{\rho_m}{2}\frac{\partial \mathscr{V}_{S_e}(t)}{\partial t} *_t \int_V \left[-\frac{2\Delta c_0(\vec{r})}{c_m^3}\cdot\frac{\partial^2 g_{er}(\vec{r},t)}{\partial t^2} + \frac{1}{\rho_m}\nabla\big[\Delta\rho_0(\vec{r})\big]\cdot\nabla g_{er}(\vec{r},t)\right]\mathrm{d}^3\vec{r} \\ \text{with: } g_{er}(\vec{r},t) = g_{S_e}(\vec{r},t) *_t g_{S_r}(\vec{r},t)\end{gathered} \tag{2.25}$$

where $g_{er}(\vec{r},t)$ is spatial impulse response of the point $\vec{r}$ when the transducer S_e emits and S_r receives.

Under the condition that the spatial impulse response $g_{er}(\vec{r},t)$ is slowly varying over the small volume V, (2.25) can be rewritten as [Jensen, 1991, Jensen, 1999, Jensen and Svendsen, 1992]:

$$\mathscr{U}_{S_r}(t) = \frac{\rho_m}{2}\frac{\partial \mathscr{V}_{S_e}(t)}{\partial t} *_t \int_V \left[-\frac{2\Delta c_0(\vec{r})}{c_m^3}\cdot\frac{\partial^2 g_{er}(\vec{r},t)}{\partial t^2} + \frac{1}{\rho_m}\Delta\rho_0(\vec{r})\cdot\nabla^2 g_{er}(\vec{r},t)\right]\mathrm{d}^3\vec{r} \tag{2.26}$$

Moreover, since the spatial impulse response $g_{er}(\vec{r},t)$ is a function of distance (between transducers and the scatterer) which is related to time by the the propagation speed of sound c_m the following relation holds [Jensen, 1991, Jensen, 1999]:

$$\nabla^2 g_{er}(\vec{r},t) = \frac{1}{c_m^2}\frac{\partial^2 g_{er}(\vec{r},t)}{\partial t^2} \tag{2.27}$$

Combining (2.27) and (2.26) yields:

$$\begin{gathered}\mathscr{U}_{S_r}(t) = \tfrac{\rho_m}{2}\frac{\partial \mathscr{V}_{S_e}(t)}{\partial t} *_t \int_V \left[-\frac{2\Delta c_0(\vec{r})}{c_m^3} + \frac{\Delta\rho_0(\vec{r})}{c_m^2\rho_m}\right]\frac{\partial^2 g_{er}(\vec{r},t)}{\partial t^2}\,\mathrm{d}^3\vec{r} \Longleftrightarrow \\ \mathscr{U}_{S_r}(t) = \tfrac{\rho_m}{2c_m^2}\frac{\partial \mathscr{V}_{S_e}(t)}{\partial t} *_t \int_V \left[-\frac{2\Delta c_0(\vec{r})}{c_m} + \frac{\Delta\rho_0(\vec{r})}{\rho_m}\right]\frac{\partial^2 g_{er}(\vec{r},t)}{\partial t^2}\,\mathrm{d}^3\vec{r}\end{gathered} \tag{2.28}$$

It can be seen that, relying on the behavior of the convolution product with respect to differentiation, (2.28) can be written as follows:

$$\mathscr{U}_{S_r}(t) = \tfrac{\rho_m}{2c_m^2}\frac{\partial^3 \mathscr{V}_{S_e}(t)}{\partial t^3} *_t \int_V \left[-\frac{2\Delta c_0(\vec{r})}{c_m} + \frac{\Delta\rho_0(\vec{r})}{\rho_m}\right] g_{er}(\vec{r},t)\,\mathrm{d}^3\vec{r} \tag{2.29}$$

Finally, the expression of the total force applied by the acoustic wave on the transducer's surface S_r (2.29) can be used in order to obtain the electrical signal generated by this transducer [Jensen, 1999, Stepanishen, 1971]:

$$\begin{gathered}y_{S_r}(t) = h_{S_r}(t) *_t \mathscr{U}_{S_r}(t) = \tfrac{\rho_m}{2c_m^2} h_{S_r}(t) *_t \frac{\partial^3 \mathscr{V}_{S_e}(t)}{\partial t^3} *_t \int_V \left[-\frac{2\Delta c_0(\vec{r})}{c_m} + \frac{\Delta\rho_0(\vec{r})}{\rho_m}\right] g_{er}(\vec{r},t)\,\mathrm{d}^3\vec{r} \Longleftrightarrow \\ y_{S_r}(t) = h_{S_r}(t) *_t \mathscr{U}_{S_r}(t) = h_{S_r}(t) *_t a(t) *_t h_{S_e}(t) *_t \int_V \left[-\frac{2\Delta c_0(\vec{r})}{c_m} + \frac{\Delta\rho_0(\vec{r})}{\rho_m}\right] g_{er}(\vec{r},t)\,\mathrm{d}^3\vec{r}\end{gathered} \tag{2.30}$$

where $a(t)$ represents the electrical excitation of the emitting transducer (S_e). In (2.30), $h_{S_e}(t)$ and $h_{S_r}(t)$ are the acousto-electrical impulse responses of the emitting and receiving transducers respectively. The term $-2\Delta c_0(\vec{r})/c_m + \Delta\rho_0(\vec{r})/\rho_m$ depends only on the inhomogeneities inside the medium density field, it represents the scattering strength of of the medium point $\vec{r}$ inside the volume V.

2.1.4 Summary

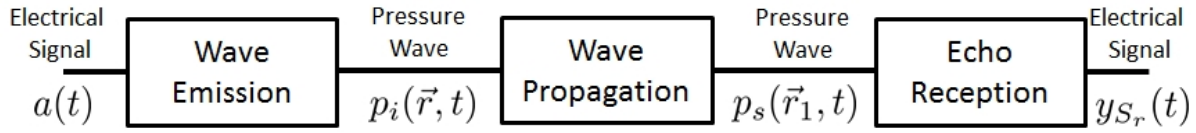

Figure 2.7: Result of Subsection 8.1 study. The output electrical signal $y_{S_r}(t)$ is modeled as a function of the transducer's geometry, medium inhomogeneities and the input electrical signal $a(t)$

In this Section, the pipeline displayed in Fig.2.7 was detailed. A complete theoretical study of the acoustic wave propagation phenomenon allowed to link the electrical signal received by a piezoelectric transducer to the source excitation signal. The employed formalization allowed to take into account the following physical properties:

- excitation signal of the source transducer
- acousto-electrical impulse response of the source and receiver transducers
- inhomogeneities in the medium density and in the propagation speed of sound
- spatial impulse response of the source and receiver transducers.

The following hypotheses had to be made in order to obtain the final relation:

- before insonification, the medium is completely still, implying a constant pressure field and a density field with small inhomogeneities
- the disturbances inside the pressure and density fields induced by the acoustic wave propagation are very small compared to the mean values of these fields
- first order Born approximation which imposes only single scatterings of the incident pressure wave
- spatial impulse responses of the transducers are slowly varying over small volumes inside the media.

2.2 Ultrasound imaging

Here, the process of conventional ultrasound imaging is detailed. First, the different parts that are involved in the process of ultrasound imaging are presented, then the relation between the pipeline displayed in Fig.2.7 and the image reconstruction is showed. Furthermore, the metrics that allow to quantify the performance of the imaging approach is detailed. Thus, when finally the different ultrasound methods are presented, they are compared in terms of the provided values of the performance metrics.

2.2.1 General background

As shown in Fig.2.8, the process of conventional ultrasound imaging involves four parts:

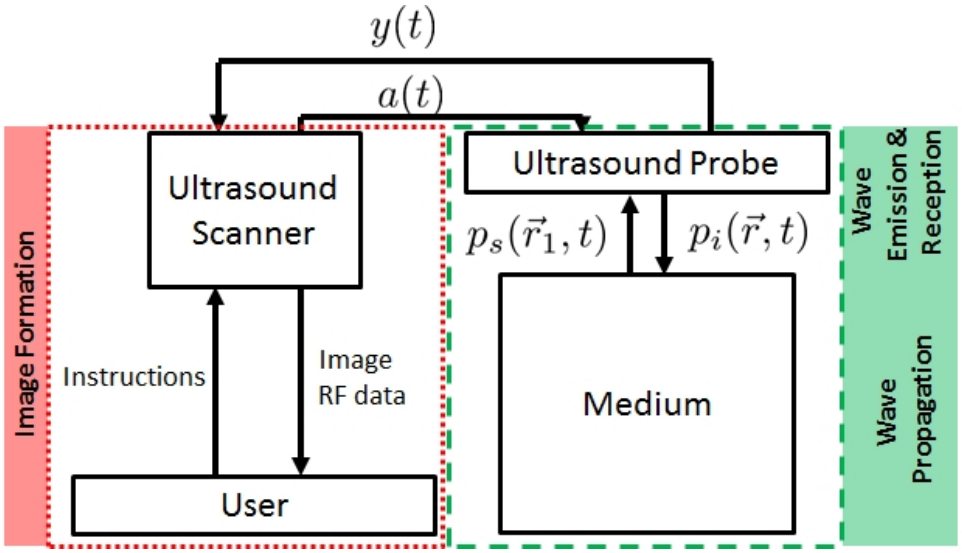

Figure 2.8: Schematic representation of the different parts involved in the process of ultrasound imaging and the corresponding tasks that each part accomplishes. Relying on the user instructions, the ultrasound scanner generates a set of excitation signals $a(t)$ which are transformed in acoustic waves $p_i(\vec{r}, t)$ by the probe. This wave propagates inside the medium and the scattered echoes $p_s(\vec{r}_1, t)$ are received by the ultrasound probe, which transforms them in electrical signals $y(t)$. The Radio Frequency (RF) data $y(t)$ is used by the scanner in order to reconstruct the ultrasound image.

- The User – is the person in charge of the ultrasound acquisition. Normally the user sets a certain number of parameters (that will be further described in this chapter) such as: emission beamforming type, shape of the excitation signals, imaging depth, pulse repetition frequency, number of acquired frames etc. This parameters define the type of ultrasound acquisition and have a primordial impact on the provided image quality. Ultrasound images (for clinical and research scanners) are returned to the user. Research ultrasound scanners also have the option to return to the user Radio Frequency (RF) data (raw data used to reconstruct the images). RF data can be further post-processed using specific algorithms depending on the application.

- The Ultrasound Scanner – has the function to process the parameters set by the user and to consequently drive the electro-acoustic transducers of the ultrasound probe. Thus, the scanner sends electrical signals to the probe during the "Wave Emission" phase and receives electrical signatures of the backscattered echoes, during the "Echo Reception" phase. For conventional imaging approaches, the scanner can be set software / hardware wise in order to reconstruct ultrasound images (for clinical and research scanners), however the option that allows the user to benefit of the raw acquisition data is only available for research ultrasound scanners.

- The Ultrasound Probe – is responsible for the direct and reverse conversion of the electrical energy into mechanical energy during the "Wave Emission" and "Echo reception" phases respectively. This function is realized mostly thanks to a certain number of electro-acoustic elements (Fig.2.9) located on the ultrasound probe head.

- The Medium – represents the ultrasound imaging's object of study. This is the support for the "Wave Propagation" and its density inhomogeneities generate echoes that are further reconstructed into an ultrasound image.

Before going more into the detail of imaging approaches it will be appropriate first to talk about how the pipeline displayed in Fig.2.7 is employed in the process of ultrasound image formation. As shown in Fig.2.9, a conventional linear array probe consists of several identical (of the same surface

$S = S_r = S_e$ and same acousto electrical impulse response in emission and reception $h(t)$), equally spaced elements (N_{el}) that are arranged in a line. During the phase of "Wave Emission" each element j of the probe is excited by the ultrasound scanner using an electrical signal $a_j(t)$. Then, during the phase of "Echo Reception" the same probe receives the backscattered echoes, thus, each element i of the probe records an electrical signal $y_i(t)$. The relation between the received signal $y_i(t)$ and the emitted signal $a_j(t)$, is modeled by the pipeline showed in Fig.2.7 and the phenomenon of N_{el} simultaneous emission of acoustic waves is modeled by assuming that the following phenomena are linear: wave emission by the transducer elements, wave propagation inside the imaged medium and echo reception by the transducer elements. By adapting the spatial impulse responses $g_{S_e}(\vec{r},t)$ (2.19) and $g_{S_r}(\vec{r},t)$ (2.23) to a pair (j,i) of probe elements one can obtain the following expressions:

$$g_{S_e}(\vec{r},t) = \delta(t-t_j) *_t g_j(\vec{r},t)$$

$$g_{S_r}(\vec{r},t) = \delta(t-t_i) *_t g_i(\vec{r},t)$$

$$\text{with:} \begin{cases} g_j(\vec{r},t) = \displaystyle\int_S \frac{1}{2\pi\|\vec{r}-\vec{r}_j-\vec{r}_S\|_2}\delta\Big(t-\frac{\|\vec{r}-\vec{r}_j-\vec{r}_S\|_2}{c_m}\Big)\mathrm{d}^2\vec{r}_S \\ g_i(\vec{r},t) = \displaystyle\int_S \frac{1}{2\pi\|\vec{r}-\vec{r}_i-\vec{r}_S\|_2}\delta\Big(t-\frac{\|\vec{r}-\vec{r}_i-\vec{r}_S\|_2}{c_m}\Big)\mathrm{d}^2\vec{r}_S \end{cases} \tag{2.31}$$

where t_j and t_i are the delays at emission and reception respectively. The relation (2.31) is introduced here purely for the modeling purpose. It allows separating the spatial impulse responses $g_j(\vec{r},t)$ and $g_i(\vec{r},t)$ of the transducer j and i respectively (that depend only on the geometry of the transducer elements and on the point $\vec{r}$) from the time delay t_j and t_i. At this point another important assumption, on which ultrasound imaging relies, needs to be reminded: the acoustic wave scattering happens in the transducer element's far field [Thomenius, 1996, Lockwood et al., 1998]. Under such conditions, using (2.19), (2.23) and (2.25) the spatial impulse responses $g_j(t)$, $g_i(t)$ and $g_{ji}(t)$ can be approximated as follows:

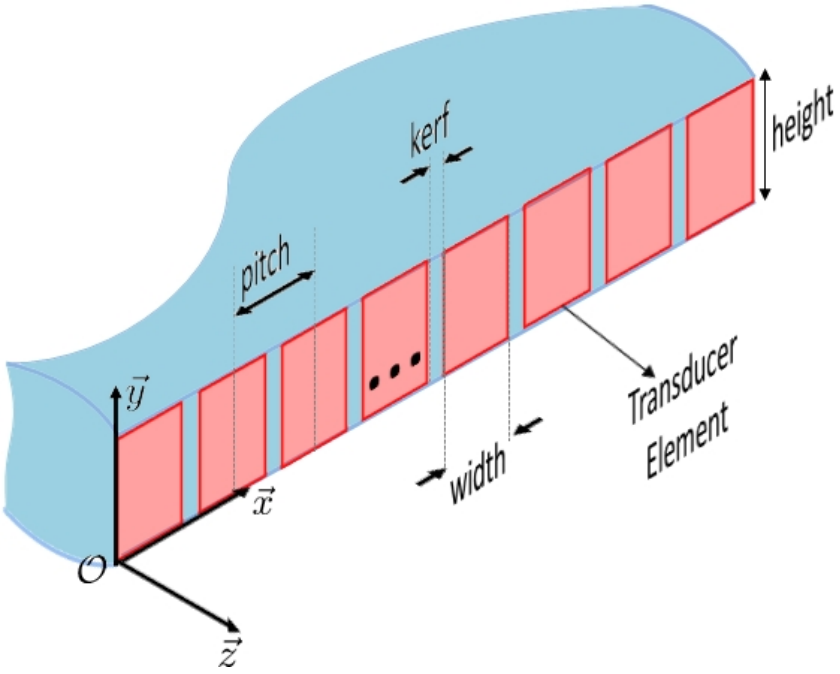

Figure 2.9: Schematic representation of The Ultrasound Probe's head. Each element of the probe (red) represents a transducer that is able to convert electrical energy in mechanical energy (vibrations). The architecture presented here is typical for a linear probe.

$$\begin{cases} g_j(\vec{r},t) = \int\limits_S \dfrac{1}{2\pi\|\vec{r}-\vec{r}_j-\vec{r}_S\|_2}\delta\Big(t-\dfrac{\|\vec{r}-\vec{r}_j-\vec{r}_S\|_2}{c_m}\Big)\,\mathrm{d}^2\vec{r}_S \approx \dfrac{S\delta\Big(t-\frac{\|\vec{r}-\vec{r}_j\|_2}{c_m}\Big)}{2\pi\|\vec{r}-\vec{r}_j\|_2} \\ g_i(\vec{r},t) = \int\limits_S \dfrac{1}{2\pi\|\vec{r}-\vec{r}_i-\vec{r}_S\|_2}\delta\Big(t-\dfrac{\|\vec{r}-\vec{r}_i-\vec{r}_S\|_2}{c_m}\Big)\,\mathrm{d}^2\vec{r}_S \approx \dfrac{S\delta\Big(t-\frac{\|\vec{r}-\vec{r}_i\|_2}{c_m}\Big)}{2\pi\|\vec{r}-\vec{r}_i\|_2} \\ g_{ji}(\vec{r},t) = g_j(\vec{r},t) *_t g_i(\vec{r},t) = \dfrac{S^2\delta\Big(t-\frac{\|\vec{r}-\vec{r}_j\|_2+\|\vec{r}-\vec{r}_i\|_2}{c_m}\Big)}{4\pi^2\|\vec{r}-\vec{r}_j\|_2\|\vec{r}-\vec{r}_i\|_2} \end{cases} \tag{2.32}$$

While, as it will be shown further in this Section, the emission delays depend on the acquistion scheme, the reception delays are conventionally set to 0 ($t_i = 0$). Using (2.32), the total electrical signal received by the i^{th} element of the probe when all elements emitted can be written as:

$$y_i(t) = w_i \sum_{j=1}^{N_{el}} w_j y_{ji}(t) + b_i(t) \tag{2.33}$$

In (2.33), the terms w_j and w_i are weighting coefficients applied on the emitted and received electrical signals respectively in order to alter the pressure field inside the imaged medium [Capon, 1969, Holfort et al., 2009, Tong et al., 2014]. This terms vary spatially as a function of the emitting / receiving element and are usually chosen between the following windows: boxcar, Hanning, Tuckey .

$$\begin{gathered} y_i(t) \underset{\text{Using (2.30)}}{=} w_i \sum_{j=1}^{N_{el}} \Big[w_j h(t) *_t a_j(t) *_t h(t) *_t \int\limits_V \gamma(\vec{r}) g_{ji}(\vec{r},t)\,\mathrm{d}^2\vec{r}\,\Big] + b_i(t) \\ \text{where: } y_{ji}(t) = h(t) *_t a(t) *_t h(t) *_t \int\limits_V \gamma(\vec{r}) g_{ji}(\vec{r},t)\,\mathrm{d}^2\vec{r} \end{gathered} \tag{2.34}$$

Depending on the emission scheme, the excitation signals $a_j(t)$ are delayed in such way so a tilted / focused /diverging ultrasound wave is emitted inside te medium, thus the signals $a_j(t)$ already contain the emission delays t_j. In (2.33), $b_i(t)$ represents an additive acquisition noise. The Tissue Reflectivity Function (TRF) $\gamma(\vec{r})$ used in order to define the received signals in (2.33) represents the scatterer strength at each position $\vec{r}$ of the medium. By comparing (2.33) to (2.30) it can be seen that:

$$\gamma(\vec{r}) = -\frac{2\Delta c_0(\vec{r})}{c_m} + \frac{\Delta\rho_0(\vec{r})}{\rho_m} \tag{2.35}$$

Given the spatial distribution of the probe elements, that, as it will be shown further in this Section, allow a beam steering only in a plane Π (where each point $\vec{r}$ has a constant $y = 0$ coordinate), the recorded signals $y_i(t)$ are the electrical signature of the backscattered echoes from the plane Π of the imaged medium.

Image reconstruction

While in the literature there exist a large number of image reconstruction methods that operate either in the time / space domain [Wright, 1985, Shoup and Hart, 1988, Montaldo et al., 2009, David et al., 2015] or temporal / spatial frequencies [Nagai, 1985, Mayer et al., 1990, Lu, 1997, Garcia et al., 2013], the conventional algorithm relies on the coherent summation of the backscattered echoes and is called Delay

And Sum (DAS). The DAS estimation of the TRF is obtained using the following relation:

$$\begin{gathered}\hat{\gamma}_{DAS}(\vec{r}) = \sum_{i=1}^{N_{el}} y_i(\tau_i(\vec{r})) \\ \text{with: } \tau_i(\vec{r}) = \frac{1}{c_m} \min_{j\in[1..N_{el}]} \Big[c_m t_j + \|\vec{r} - \vec{r}_j\|_2 \Big] + \frac{1}{c_m} \|\vec{r} - \vec{r}_i\|_2\end{gathered} \tag{2.36}$$

where $\tau_i(\vec{r})$ represents the time of flight needed for the wave to propagate between the emission / scattering in the medium point $\vec{r}$ / reception at the i^{th} element of the probe. As it can be seen, for any emission scheme, this delay can be approximated by the sum of two terms. The rightmost term ($\|\vec{r} - \vec{r}_i\|_2 / c_m$), is the backwards propagation delay and represents the time needed for an echo, generated in the point $\vec{r}$, to reach the receiver element i. The left term ($\min_{j\in[1..N_{el}]} \big[c_m t_j + \|\vec{r} - \vec{r}_j\|_2 \big] / c_m$), represents the time needed for the point $\vec{r}$ to be reached by any spherical wave emitted by an element j. In the literature, this is presented under different forms (depending on the emission scheme) the main idea being to calculate the time needed for the total wavefront generated by the probe emission to reach the point $\vec{r}$ [Montaldo et al., 2009]. However, as it will be further shown in this Section, since the emission delays t_j are generated in such way so the desired wavefront is created in emission, the "min" function in the calculation of the forward propagation delay in (2.36) is not needed anymore (because $c_m t_j + \|\vec{r} - \vec{r}_j\|_2$ becomes constant for all j). Clearly, this relation performs the best in the near field (as compared to the full expressions): indeed, since DAS makes the assumption that the wave is already in the far field, the classical delays are slightly drifted.

In order to understand how the estimation of the TRF (2.36) can be deduced from the expression of the received signals (2.33), one needs first to consider the approximations on which DAS relies [Thomenius, 1996, David et al., 2015]:

- H1 – the acquisition noise $b_i(t)$ is ignored
- H2 – short, Dirac like acousto electrical impulse response of the probe elements: $h(t) = \delta(t)$
- H3 – short, Dirac like excitation signals: $a_j(t) = \delta(t)$
- H4 – the weighting terms w_j and w_i are considered constant
- H5 – the amplitude loss term[1] $1/(4\pi^2 \|\vec{r} - \vec{r}_j\|_2 \|\vec{r} - \vec{r}_i\|_2)$ is ingored and set to 1
- H6 – the forward propagation time of the total pressure field (between each element and the point $\vec{r}$) is equal to the fastest time of flight needed for one spherical acoustic wave emitted by an element of the probe to reach $\vec{r}$.

In the previously stated conditions, using (2.32), (2.33) can be reduced to:

$$\begin{gathered}y_i(t) \underset{H1-4}{\approx} \sum_{j=1}^{N_{el}} \int_V \gamma(\vec{r}) g_{ji}(\vec{r}, t)\, \mathrm{d}^2\vec{r} \underset{H5}{\approx} \sum_{j=1}^{N_{el}} \int_V \gamma(\vec{r}) \delta\Big(t - t_j - \frac{\|\vec{r} - \vec{r}_j\|_2 + \|\vec{r} - \vec{r}_i\|_2}{c_m}\Big)\, \mathrm{d}^2\vec{r} \Longleftrightarrow \\ y_i(t) \underset{H6}{\approx} \int_V \gamma(\vec{r}) \delta\big(t - \tau_i(\vec{r})\big)\, \mathrm{d}^2\vec{r} \\ \text{with: } \tau_i(\vec{r}) \underset{H6}{\approx} \min_{j\in[1..N_{el}]} \left(t_j + \frac{\|\vec{r} - \vec{r}_j\|_2}{c_m} \right) + \frac{\|\vec{r} - \vec{r}_i\|_2}{c_m}\end{gathered} \tag{2.37}$$

In (2.37), the expression for the time of flight $\tau_i(\vec{r})$ is obtained using the sixth hypothesis of the DAS algorithm and, in other words, represents the sum between the delay needed for the fastest spheric

[1] This term sometimes is compensated either by the ultrasound scanner in reception or by the user in post processing using the so called "Time Gain Compensation"

Figure 2.10: The ultrasound image formation block and its corresponding inputs and outputs. The RF data represents all the N_{el} recorded signals $y_i(t)$

wave (emitted by the element of the probe) to reach the point $\vec{r}$ and the backward propagation time from $\vec{r}$ to the i^{th} receiver position ($\vec{r}_i$). Now, in (2.37) can be observed that:

$$y_i(\tau_i(\vec{r})) = \int_{V^i} \gamma(\vec{r})\, \mathrm{d}^2\vec{r}' \tag{2.38}$$

where V^i represents all the points $\vec{r}^i$ for which the time of flight equals $\tau_i(\vec{r})$. If in V^i there was only one point $\vec{r}^i$ that satisfied $\tau_i(\vec{r}^i) = \tau_i(\vec{r})$, then the solution of (2.38) would be trivial ($\gamma_{DAS}(\vec{r}) = y_i(\tau_i(\vec{r}))$), however DAS offers the same solution for the case where there are multiple points in V^i. At the base of this approximation is the fact that, since for different elements i the points $\vec{r}^i$ in V^i change all except the one that satisfies $\tau_i(\vec{r}^i) = \tau_i(\vec{r})$, $\forall i \in [1..N_{el}]$, the amplitude of this echo will constructively interfere through the summation of all the corresponding echoes $y_i(\tau_i(\vec{r}))$. Thus, from (2.38), (2.36) can be deduced. Finally, on the obtained 2D image $\hat{\gamma}_{DAS}(\vec{r})$, envelope extraction and log-compression are performed in order to obtain a gray-scale image with intensity values that can vary between $-\infty$ and 0. The final gray-scale image is also often called B-mode images and when displayed, usually, a limited intensity dynamic scale is used (e. g. between $-60dB$ and $0dB$ or between $-50dB$ and $0dB$). At this point, the last block of the ultrasound imaging process has been detailed (Fig.2.10). In Fig.2.11 are represented the typical B-mode images that one can obtain through ultrasound acquisitions.

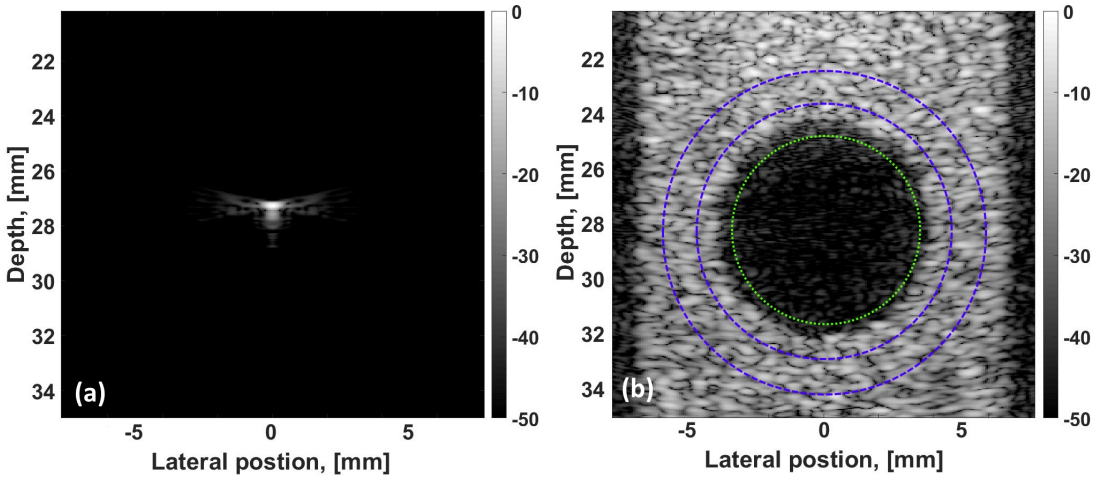

Figure 2.11: Typical B-mode images of a resolution (a) and of an anechoic cyst (b) phantom respectively. The dotted green line represents the zone where the image SNR is measured and the background zone for the CNR computation. The zone between the two dashed blue lines represents the region of interest for the CNR calculation.

Image quality quantifiers

The image in Fig.2.11(a) is obtained by imaging a very anechoic medium that contains only a point scatterer at the position $\vec{r} = (0, 0, 27.5)\ mm$. Such images are usually acquired in order to assess the Point Spread Function (PSF) of the imaging approach [Van Wijk and Thijssen, 2002]. As one can observe in Fig.2.11(a), the point reconstructed at the position $\vec{r}$ is blurry and has some artifacts that extend in all directions what now became more of a spot than a point. The effect of blurring and widening of the imaged point represents the imaging method PSF. In order to assess the quality of the PSF, usually its axial and lateral profiles are analyzed (Fig.2.12). Conventionally, the quality of the PSF is quantified by its full width at half maximum ($-6dB$ on a log-scale) of its axial and lateral profiles. These measures are also an indicator of the imaging method *axial* and *lateral resolution*. In fact, axial and lateral resolution are defined as the ability of the system to discern two scatterrers in the parallel / perpendicular direction of the ultrasound beam used for imaging. Thus, thiner axial / lateral profiles of the PSF imply a better image axial / lateral resolution. Using the profiles displayed in Fig.2.12, one can measure a 250 μm axial resolution and a 500 μm lateral resolution of the image showed in Fig.2.11(a).

The image displayed in Fig.2.11(b) is typical for ultrasound acquisitions on mediums that have high scatterer density. In this case, the imaged medium has 100 scatt./mm^2, and contains an anechoic cyst of radius 4 mm centered at the position $\vec{r}_c = (0, 0, 28.25)\ mm$. It can be observed that the image contains a granular texture in the regions where the scatters are located. This effect is obtained in the image due to the fact that the PSF of the closely placed scatterers interfere, thus creating larger clusters that are called speckle. The size of this speckle depends indeed, on the scatterer density inside

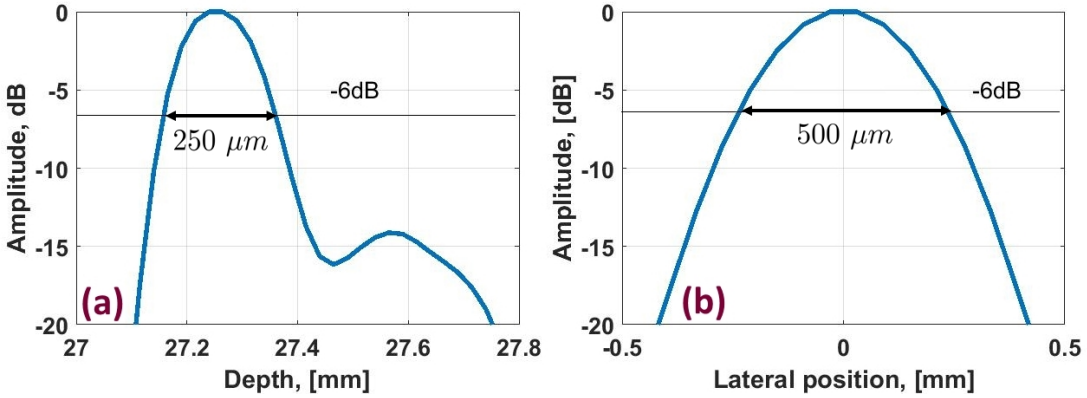

Figure 2.12: Axial (a) and Lateral (b) profiles of the PSF represented in Fig.2.11

the medium but also on the capacity of the imaging approach to separate closely placed scatterers. While, as previously explained, the speckle size depends on the axial and lateral resolutions that the ultrasound approach is able to provide, two different measures are used in order to quantify it. These metrics are called *Axial* and *Lateral Auto-Correlation Lengths* ($Ax.AC_x$ and $Lat.AC_z$ respectively) and are defined as follows [Benane et al., 2018]:

$$\begin{aligned} Ax.AC_x[z] &= \sum_{{}_d z=-\infty}^{+\infty} \hat{\gamma}[x, {}_d z]\hat{\gamma}[x, z + {}_d z] \\ Lat.AC_z[x] &= \sum_{{}_d x=-\infty}^{+\infty} \hat{\gamma}[{}_d x, z]\hat{\gamma}[x + {}_d x, z] \end{aligned} \tag{2.39}$$

In (2.39), both measures are performed on the TRF estimation $\hat{\gamma}$ before envelope extraction and log-compression (in other words $Ax.AC_x$ and $Lat.AC_z$ are not computed on the B-mode images showed in Fig.2.11). Wider $Ax.AC_x$ and $Lat.AC_z$ main lobes implies that the speckle is larger in the axial and lateral direction respectively [Rouyer et al., 2015, Benane et al., 2018].

Another metric that will be used in order to quantify the speckle in the estimated TRF images $\hat{\gamma}$ is

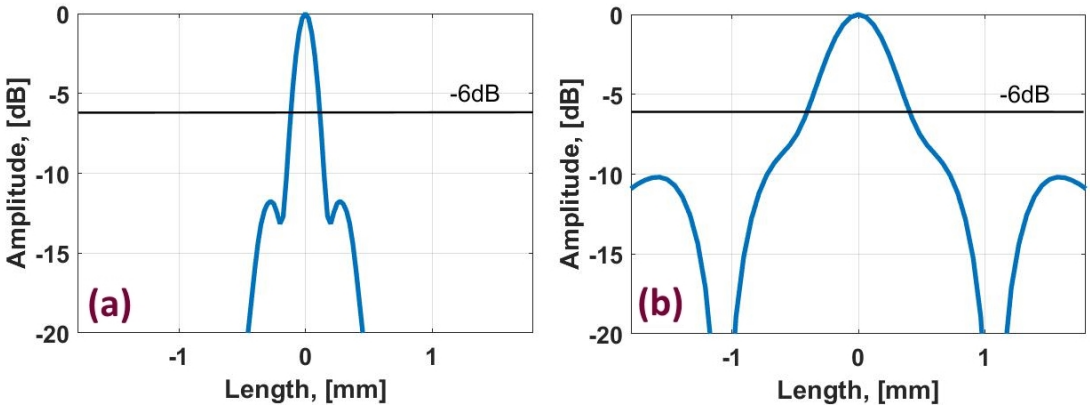

Figure 2.13: Plots of the axial (a) and lateral (b) autocorrelations computed on the image displayed in Fig.2.11(b). $Ax.AC_x$ was performed on the axial line $x = -5\ mm = const.$. $Lat.AC_z$ was performed on lateral line $z = 34\ mm = const.$. These plots are showed on a logarithmic scale, obtained by extracting the envelope and then log-compressing the $Ax.AC_x$ and $Lat.AC_z$ results obtained using (2.39).

the Speckle Consistency (SC). SC measures the similarity of the reference speckle (inside γ) and the estimated speckle (inside $\hat{\gamma}$) and is defined as:

$$SC[q,n] = \sum_{l=-L/2}^{L/2} \sum_{s=-L/2}^{L/2} \boldsymbol{p}_{\gamma}[l,s]\hat{\gamma}[q+l,n+s] \tag{2.40}$$

where $\boldsymbol{p}_{\gamma}$ is a patch of size $L \times L$ extracted from the speckle image γ. The shape of the main lobe of SC is directly related to the speckle consistency between $\boldsymbol{p}_{\gamma}$ and $\hat{\gamma}$: thinner lobes correspond to a more similar speckle while wider lobes imply that the discrepancy between the speckle of γ and $\hat{\gamma}$ is more substantial.

As it can be seen in Fig.2.11(b), even if the cyst is completely anechoic some signal is nevertheless present in the reconstructed B-mode image. Precursors of these artifacts are already visible in the PSF image (Fig.2.11(a)), where the scatterer PSF is already spatially distorted. However, these artifacts can appear also due to the acquisition noise, multiple reflections, under-performance of the beamforming algorithm, etc. This reconstruction noise can be measured using the image *Signal to Noise Ratio* (SNR) [Wagner, 1983, Thijssen, 2003], which for a region of interest, quantifies the quantity of noise using the following relation:

$$SNR = 10log_{10}\left(\frac{|\mu_{back}|}{\sigma_{back}}\right) \tag{2.41}$$

In (2.41), μ_{back} and σ_{back} stand for the mean and standard deviation of the pixel values in a background region of a B-mode image. For an ultrasound image, a background zone is called a region which does not contain scatterers, thus, ideally this zone will be of a very low gray shade when displayed. In Fig.2.11(b), an example of a background region for the calculation of the SNR is highlighted with a dotted green line. Since as seen in Fig.2.11(b) the background zone has a mean value very close to -60 dB with some noise defined by its standard deviation, it is clear, that using (2.41), the SNR of such zone will be very high. Ideally, when no noise is present in this zone, the SNR can reach $+\infty$.

Another metric used to quantify the visual discrepancy between two regions of the estimated TRF image (that have different mean reflectivity scattering coefficients) is the *Contrast to Noise Ratio* (CNR) [Stetson et al., 1997, Thijssen, 2003]. The CNR is defined as follows:

$$CNR = 20log_{10}\left(\frac{|\mu_{ROI} - \mu_{back}|}{\sqrt{\frac{\sigma^2_{ROI}+\sigma^2_{back}}{2}}}\right) \tag{2.42}$$

where, as for SNR calculation, the background zone usually represents a part of the image with lower intensity (the surface surrounded by the dotted green line in Fig.2.11(b)) and the Region Of Interest (ROI) represents a part of the image with higher intensity (the surface between the two dashed blue lines in Fig.2.11(b)). As one can see in (2.42), the CNR is very low for two zones (*back* and *ROI*) that have very similar mean values of pixels. This value becomes even smaller, if the variance of each of these zones increases. Ideally, in an ultrasound B-mode image where *back* and *ROI* are two homogeneous hypo-echogenic and hyper-echogenic zones respectively, the CNR would be positive and very high.

Finally, the last two omnipresent metrics that allow to evaluate an imaging method, less from the point of view of the image quality and more through the scope of the acquisition scheme performance, are: the *echo Signal to Noise Ratio* ($eSNR$) and the *Frame Acquisition Rate* (FAR). The $eSNR$ represents the ratio between the power of the backscattered echoes and the power of the acquisition noise and, using (2.33), can be defined as [Oelze, 2007, Liu and Insana, 2005]:

$$eSNR = 10log_{10}\left(\frac{E\left\{|w_i \sum_{j=1}^{N_{el}} w_j y_{ji}(t)|^2\right\}}{E\left\{|b_i(t)|^2\right\}}\right) \tag{2.43}$$

One can see in (2.43), that for very low amplitudes of noise (when compared to the amplitude of the echoes), the $eSNR$ can reach very high values, on the other hand, for equal and higher amplitudes of noise (with respect to echoes), the $eSNR$ can be null and even negative. Since as it will be shown later in this Section, various emission schemes can generate echoes with different energies, the $eSNR$ is directly related to the acquisition scheme and does not depend on the reconstruction algorithm.

The FAR (Frame Acquisition Rate) represents the number of full ultrasound images that an imaging scheme can provide per unit of time [Tanter and Fink, 2014, Montaldo et al., 2009, Jespersen et al., 1998]. Since different imaging methods use various amounts of RF data for the image reconstruction, the formula for the calculation of this metric is different from one method to another. However, since usually for the ultrafast techniques the amount of RF data is so high that is not possible to do the reconstruction at the same rate as the acquisition data is provided, the FAR does not take into account the reconstruction time.

2.2.2 Acquisition Methods

In this Section are shown the principles of the most used imaging methods in present day ultrasound. For each method, its relation with the "Ultrasound imaging pipeline" (Fig.2.1), described in Section 8.1 and 2.2.1, will be detailed. Furthermore, by presenting the evolution of the image quality quantifying metrics, defined in Section 2.2.1, the advantages of each technique are underlined. Through the evolution of the FAR the notions of "fast" and "ultrafast" acquisition schemes are introduced. Finally, a general comparison between the image qualities provided by the "slow" and "ultrafast" methods is presented and the inherent trade-off between good FAR and better CNR, SNR, image resolution is highlighted. The study will be carried on a medium that presents one scatterer at the position $\vec{r} = (-0.02, 0, 0.06)m$ using an ultrasound probe with $N_{el} = 256$ elements with a pitch of 300 mm centered at $\nu_0 = 2.5\ MHz$.

Focused Ultrasound Imaging (FUI)

FUI is a ultrasound acquisition method vastly used in the medical scanners [Briguet et al., 2014]. As it names suggests, it relies on emission of focused ultrasound beams inside the imaged medium [Drukarev et al., 1993]. Consider a linear probe with N_{el} elements and a pitch $\wp$ (Fig.2.14). In order to do FUI using this probe, first, a set of medium points $\vec{r}_{f_k} | \ k \in [1..N_l]$ where ultrasound beams will be focused, needs to be fixed. Then, in order to focus all the N_{el} emitted spherical waves (by each element

of the probe) at the medium point $\vec{r}_{f_k}$, one needs to compensate the difference of travel time between all the element positions ($\vec{r}_j$) and the focal point $\vec{r}_{f_k}$.

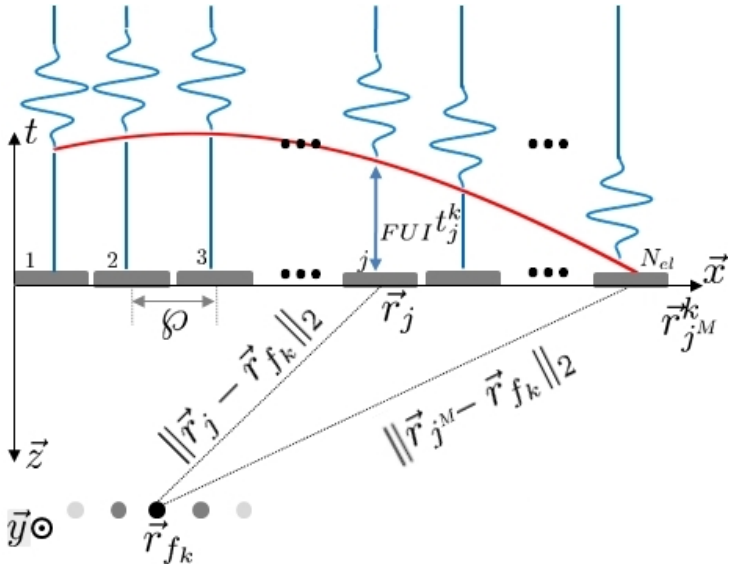

Figure 2.14: Ultrasound probe excited with sinusoid signals $a(t)$, delayed at the j^{th} element with a duration $_{FUI}t_j^k$ in order to emit a focused beam at the position $\vec{r}_{f_k}$ ($z_{f_k} > 0$). The red line represents the evolution of $_{FUI}t_j^k$ as a function of j.

This can be done by, first, finding the element j^M for which this distance is maximal (in Fig.2.14, $j^M = N_{el}$) and then for each probe element by adding an emission delay $_{FUI}t_j^k$ that accounts for the distance difference between $\vec{r}^{\,k}_{j^M}$ to $\vec{r}_{f_k}$ and $\vec{r}_j$ to $\vec{r}_{f_k}$. Thus the delays $_{FUI}t_j^k$ can be computed using the following relation:

$$_{FUI}t_j^k = \frac{\|\vec{r}^{\,k}_{j^M} - \vec{r}_{f_k}\|_2 - \|\vec{r}_j - \vec{r}_{f_k}\|_2}{c_m} \tag{2.44}$$

In (2.44), it can be seen that for the element j^M the emission delay is null and, for closer to the focal point elements, this delay increases. An example of delay law $_{FUI}t_j^k$ is shown in Fig.2.14 (red line).

Assuming that the general waveform of the excitation signal is $a(t)$, one can deduce the electrical excitation for each of the element j as follows:

$$_{FUI}a_j^k(t) = a(t - {}_{FUI}t_j^k) = a(t) *_t \delta(t - {}_{FUI}t_j^k) \tag{2.45}$$

The normalized root mean square of the pressure field $p_i(\vec{r},t)$ inside the medium, following the emission of a focused wave is shown in Fig.2.15(a). Here it can be seen that the pressure amplitude is maximal at the focal point $\vec{r}_{f_k}$ which proves the correct beam focusing. After the emission step, the signals $_{FUI}y_i^k(t)$ (that can be modeled using (2.33)) are received (Fig.2.15(b)):

$$_{FUI}y_i^k(t) = w_i *_t h(t) *_t a(t) *_t h(t) *_t \sum_{j=1}^{N_{el}} \left[w_j \delta(t - {}_{FUI}t_j^k) *_t \int_V \gamma(\vec{r}) g_{ji}(\vec{r},t)\, \mathrm{d}^2\vec{r} \right] + b_i(t) \tag{2.46}$$

Usually, since almost all the energy of the emitted wave was focused on only a medium line that contains $\vec{r}_{f_k}$, from the RF data $_{FUI}y_i^k(t) |\ i \in [1..N_{el}]$ only the same line $_{FUI}\hat{\gamma}_{\vec{r}_{f_k}}$ (Fig.2.15(c)) will be reconstructed using DAS (2.36). Finally, in order to obtain a full B-mode image (Fig.2.15(d)), the process of emission / reception / beamforming will be repeated N_l times for each focal point $\vec{r}_{f_k}$. As it can be seen in Fig.2.15(d), the medium TRF is well reconstructed, the PSF being very small (good

axial and lateral resolutions). Furthermore, it can be seen that no important artifacts are generated by the reconstructing method. This implies that the SNR and the CNR provided by FUI are also high. Concerning the $eSNR$, the value of this metric is also high, since in the focal region the amplitude of the pressure field is the highest (Fig.2.15(a)).This method's FAR can be computed using the following relation:

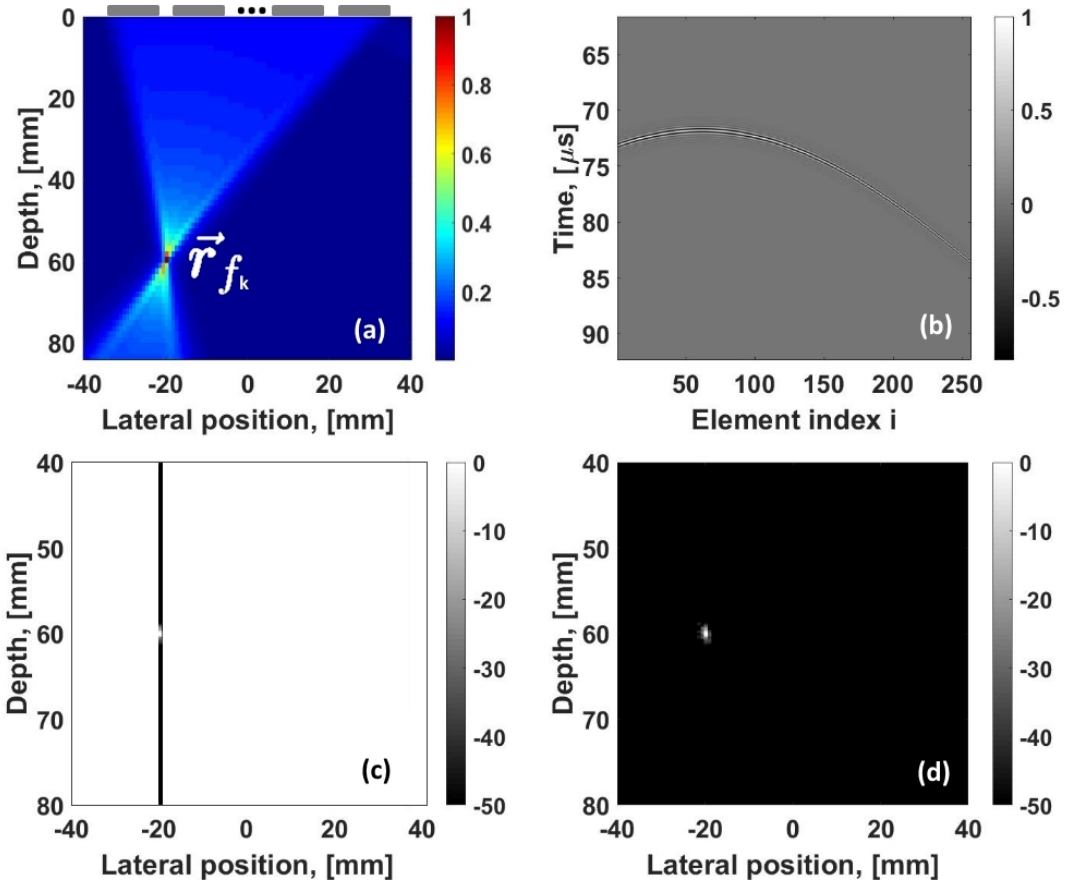

Figure 2.15: Principle of FUI: (a) - Normalized Root Mean Square (RMS) of the pressure field $p_i(\vec{r},t)$ inside the medium (maximal value of $RMS(p_i(\vec{r},t))$ is 180.34 Pa), (b) - Received RF signals ${}_{FUI}y_i^k(t)$ after one emission of a focused beam, (c) - A B-mode image line reconstructed from the RF data shown in (b), (d) - A full B-mode image reconstructed after N_l repetitions of the steps (a) to (c)

$$ {}_{FUI}FAR = \frac{1}{N_l(t_a + t_{rec} + t_{SW}) + \sum_{k=1}^{N_l} {}^M\vec{r}_j^k / c_m} \underset{t_a, t_{SW}, {}^m\vec{r}_j / c_m << t_{rec}}{\approx} \frac{1}{N_l t_{rec}} \tag{2.47} $$

where t_a is the duration of the waveform $a(t)$, t_{rec} is twice the duration (forward and backward propagation) needed for an acoustic wave to propagate between the probe and the deepest point that one wants to reconstruct. In (2.47), the duration t_{SW} is related only to the ultrasound scanner and represents the time required by the hardware to switch between the emission and reception modes. Since, usually t_{rec} is much higher than the emission delays, the duration of the excitation waveform and the switch time, it can be deduced that ${}_{FUI}FAR$ is inversely proportional to $N_l t_{rec}$. This implies that, for the same imaging depth, if one wants to increase the number of focusing lines, the FAR will decrease.

Multi Line Transmit (MLT)

MLT relies heavily on the principle of FUI. It consists in simultaneous emission of N_{MLT} beams focused in N_{MLT} points $\vec{r}_{f_k}$ [Tong et al., 2014, Drukarev et al., 1993, Mallart and Fink, 1992, Badescu et al., 2017]. Using the principle of linear propagation of acoustic waves it can be deduced that, in the case of MLT, the excitation signals for the j^{th} element of the transducer are the linear superposition of the N_{MLT} excitation signals for each of the beam k. Thus one obtains:

$$ {}_{MLT}a_j(t) = \sum_{k=1}^{N_{MLT}} {}_{FUI}a_j^k(t) = \sum_{k=1}^{N_{MLT}} a(t - {}_{FUI}t_j^k) = a(t) *_t \sum_{k=1}^{N_{MLT}} \delta(t - {}_{FUI}t_j^k) \tag{2.48} $$

where the delays ${}_{FUI}t_j^k$ for each of the beam k are computed using (2.44).

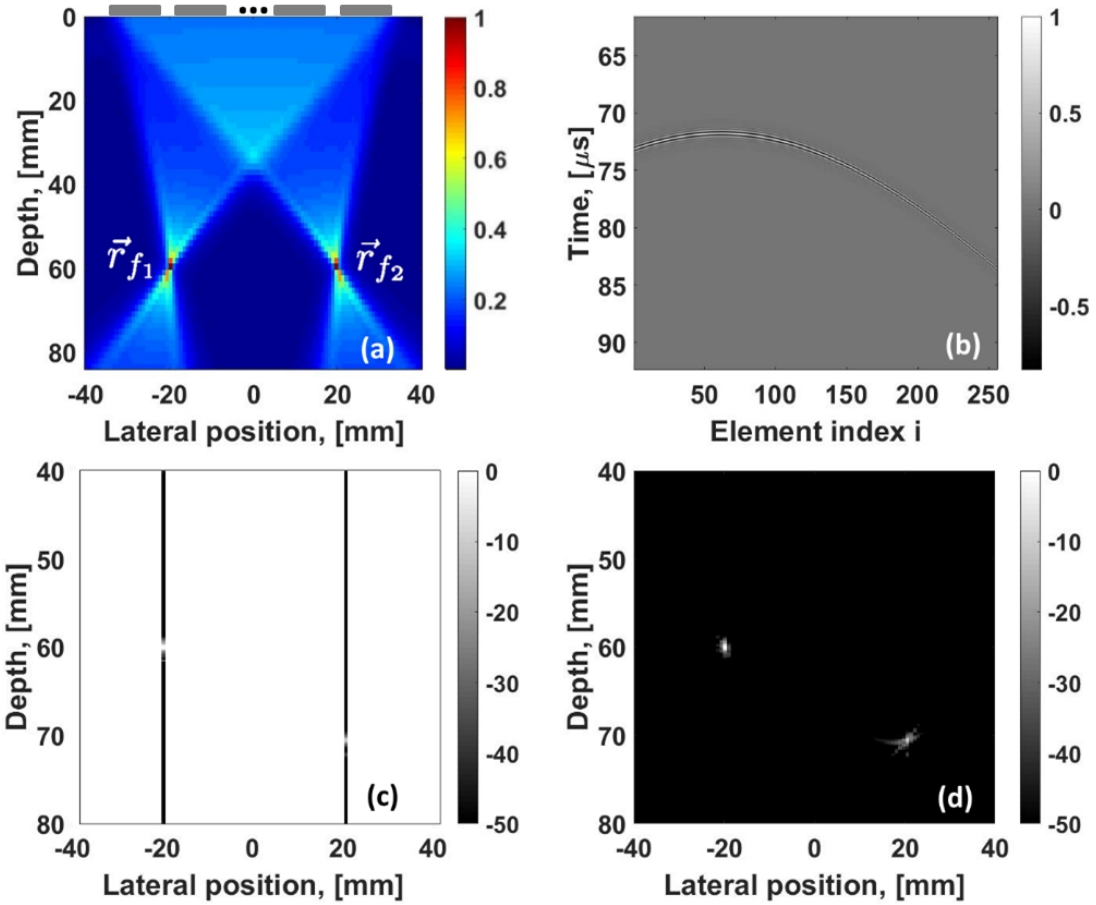

Figure 2.16: Principle of MLT, $N_{MLT} = 2$: (a) - Normalized root mean square of the pressure field $p_i(\vec{r}, t)$ inside the medium (maximal value of $RMS(p_i(\vec{r}, t))$ is 180.32 Pa), (b) - Received RF signals ${}_{MLT}y_i(t)$ after one emission of a focused beam, (c) - A B-mode image line reconstructed from the RF data shown in (b), (d) - A full B-mode image reconstructed after N_l / N_{MLT} repetitions of the steps (a) to (c)

In Fig.2.16(a), is presented the normalized root mean square of the pressure field $p_i(\vec{r}, t)$ in the case where only two focused beams are emitted simultaneously inside the medium. As it can be seen, $p_i(\vec{r}, t)$ reaches the highest amplitudes in the focal points $\vec{r}_{f_1}$ and $\vec{r}_{f_2}$, however when compared to the FUI beam, it can be seen that in the region near the ultrasound probe the pressure field amplitudes are higher. Combining (2.33) with (2.48) it can be deduced that:

$$
\begin{aligned}
{}_{MLT}y_i(t) = w_i \sum_{j=1}^{N_{el}} \left[w_j h(t) *_t {}_{MLT}a_j(t) *_t h(t) *_t \int_V \gamma(\vec{r}) g_{ji}(\vec{r},t)\, \mathrm{d}^2\vec{r} \right] + b_i(t) \Longleftrightarrow \\
{}_{MLT}y_i(t) = {}_{FUI}y_i^k(t) + \sum_{q=1,q\neq k}^{N_{MLT}} {}_{FUI}y_i^q(t) + b_i(t)
\end{aligned}
\tag{2.49}
$$

From the RF data ${}_{MLT}y_i(t)$, after each emission / reception event, N_{MLT} lines ${}_{MLT}\hat{\gamma}_{\vec{r}_{f_k}}$ can be reconstructed using DAS (2.36). However as one can see, between the RF data used for the calculation of ${}_{MLT}\hat{\gamma}_{\vec{r}_{f_k}}$ (${}_{FUI}y_i^k(t)$ in 2.46) and the RF data of ${}_{MLT}\hat{\gamma}_{\vec{r}_{f_k}}$ (${}_{MLT}y_i(t)$ in 2.49) there is a difference of:

$$
\zeta_i^k(t) = {}_{MLT}y_i^k(t) - {}_{FUI}y_i^k(t) = \sum_{q=1,q\neq k}^{N_{MLT}} {}_{FUI}y_i^q(t)
\tag{2.50}
$$

For the reconstruction of each image line k, this signal $\zeta_i^k(t)$ represents the echoes generated by the rest of $N_{MLT}-1$ focused beams emitted simultaneously with k. Conventionally the noise induced by these echoes is called crosstalk [Tong et al., 2014, Denarie et al., 2013]. In Fig.2.16(b) are shown the echoes generated by the pressure field showed in Fig.2.16(a). As it can be seen, for each element j, the signals ${}_{MLT}y_i(t)$ are very close to ${}_{FUI}y_i(t)$ (Fig.2.16(b)). This result is expected since, as the scatterer is placed at the position $\vec{r}_s = \vec{r}_{f_1}$ and the second beam is focused in $\vec{r}_{f_2} \neq \vec{r}_{f_1}$, the additional pressure generated by the second beam in the point $\vec{r}_s$ is very low when compared to the pressure generated by the first beam. However, after the reconstruction of the two B-mode image lines (Fig.2.16(c)), it can be seen that on the line corresponding to the second beam an artifact appears which is the result of crosstalk. In MLT, a full B-mode image (Fig.2.16(d)) is reconstructed after N_l/N_{MLT} emission / reception / reconstruction events. As it can be seen in Fig.2.16(d), the final image has two spots (for $N_{MLT}=2$), one that corresponds to a real scatterer PSF, and another that is the result of crosstalk. The shape, axial and lateral resolutions of the real PSF are identical to the ones provided by the FUI. However, the crosstalk artifacts generate a reduction of the $eSNR$, SNR and CNR. Relying on the same approximations used for (2.47), the FAR of MLT can be computed as follows:

$$
{}_{MLT}FAR = \frac{1}{\frac{N_l}{N_{MLT}}(t_a + t_{rec} + t_{SW}) + \sum_{k=1}^{N_l/N_{MLT}} {}^{M}\vec{r}_j^k / c_m} \approx \frac{N_{MLT}}{N_l t_{rec}}
\tag{2.51}
$$

(2.51) shows that the MLT allows increasing the frame acquisition rate by an factor of N_{MLT} however, as previously detailed, this achievement comes at the expense of image quality.

Plane Wave Imaging (PWI)

As FUI and MLT, PWI also relies on the linear superposition of the spherical waves (generated by each element j of the probe). In this case however, the spherical waves are generated in such way so the wavefront that propagates inside the medium is a plane [Sandrin et al., 1999, Tanter et al., 2002, Sandrin et al., 2002] (dashed red line in Fig.2.17). Consider the linear probe shown in Fig.2.17. In order to emit a plane wave k tilted in the direction ${}_{PWI}\theta^k$, one needs first to calculate the excitation delays ${}_{PWI}t_j^k$ using the following relation:

$$
{}_{PWI}t_j^k = (j-1)\wp \frac{\tan({}_{PWI}\theta^k)}{c_m}
\tag{2.52}
$$

Using (2.52), the PWI excitation signals for each element j of probe can be written as:

$$
{}_{PWI}a_j^k(t) = a(t) *_t \delta(t - {}_{PWI}t_j^k) = a(t - {}_{PWI}t_j^k)
\tag{2.53}
$$

where $a(t)$ is the excitation signal waveform.

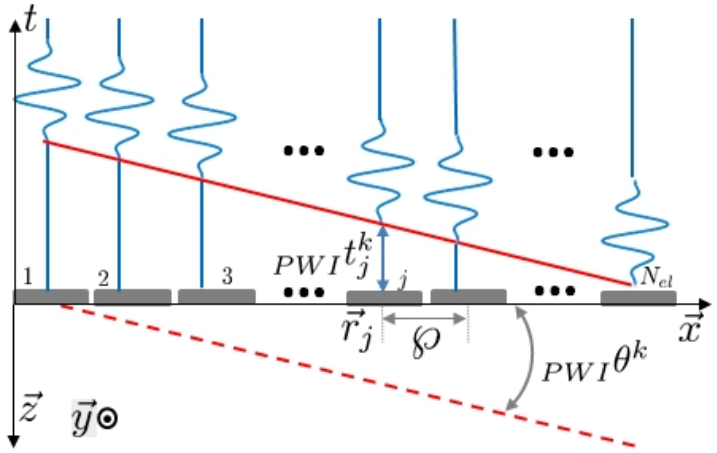

Figure 2.17: Ultrasound probe excited with sinusoid signals $a(t)$, delayed at the j^{th} element with a duration $_{PWI}t_j^k$ in order to emit plane wave in the direction $_{PWI}\theta^k$. The solid red line represents the evolution of $_{PWI}t_j^k$ as a function of j and the dashed red line represents the emitted waveform.

The normalized root mean square of the pressure field $p_1(\vec{r},t)$, generated after the emission of a plane wave in the direction $_{PWI}\theta^k = -15°$, is shown in Fig.2.18(a). Here, one can observe that following the plane wave insonification, a wide region of the medium (that depends only on the plane wave tilt), receives the same amount of energy. To be noted, that even though in Fig.2.18(a), Fig.2.16(a) and Fig.2.15(a) all three pressure fields seem to reach same amplitudes due to normalization, this is not the case for the absolute values of the pressure field. Indeed for FUI and MLT the pressure fields in the focal points are comparable, however, due to the lack of emission focusing in PWI, the PWI pressure field is far less energetic (a ratio of 8 between the pressure field amplitudes implies that, in the focal point, the FUI pressure field is 64 times more energetic than the PWI one). The backscattered echoes received at each element i of the probe can be written as:

$$\begin{aligned} &_{PWI}y_i^k(t) = w_i *_t h(t) *_t a(t) *_t h(t) *_t \\ &\sum_{j=1}^{N_{el}} \left[w_j \delta(t - {}_{PWI}t_j^k) *_t \int_V \gamma(\vec{r}) g_{ji}(\vec{r},t)\, \mathrm{d}^2\vec{r} \right] + b_i(t) \end{aligned} \tag{2.54}$$

Fig.2.18(b) shows the received signals after the one plane wave emission ($_{PWI}\theta^k = -15°$). Since, as it can be seen in Fig.2.18(a), all the medium is insonified by the plane wavefront, the RF data $_{PWI}y_i^k(t)|\ k \in [1..N_{el}]$ contains echoes from all the scatterers inside the medium (in the limit of the recorded range of-course). This means that a full B-mode $_{PWI}\hat{\gamma}^k$ image of the medium can be reconstructed using DAS (2.36). In Fig.2.18(c), the image reconstructed from the RF data (Fig.2.18(b)) is shown. As one can observe, the scatterer PSF is reconstructed at the correct position $\vec{r}_s$, however, while its axial resolution is comparable with the one provided by FUI and MLT, its lateral resolution is degraded. Furthermore, it can be seen that the PSF contains pronounced artifacts which are typical for PWI and represent the limitation of DAS related to the algorithm assumptions seen in Section 2.2.1. A PSF with such artifacts implies that the SNR and the CNR of the provided B-mode image are low, and is this case, lower than for FUI. The lack of emission focusing, which generates a pressure field of lowered amplitude (when compared to the one generated by FUI), generates echoes of lower amplitude. In these conditions, using (2.43), it is immediate to conclude that the $eSNR$ of the PWI RF data is lower than the one provided by FUI.

In order to increase the quality of the PWI images, spatial compounded is usually employed

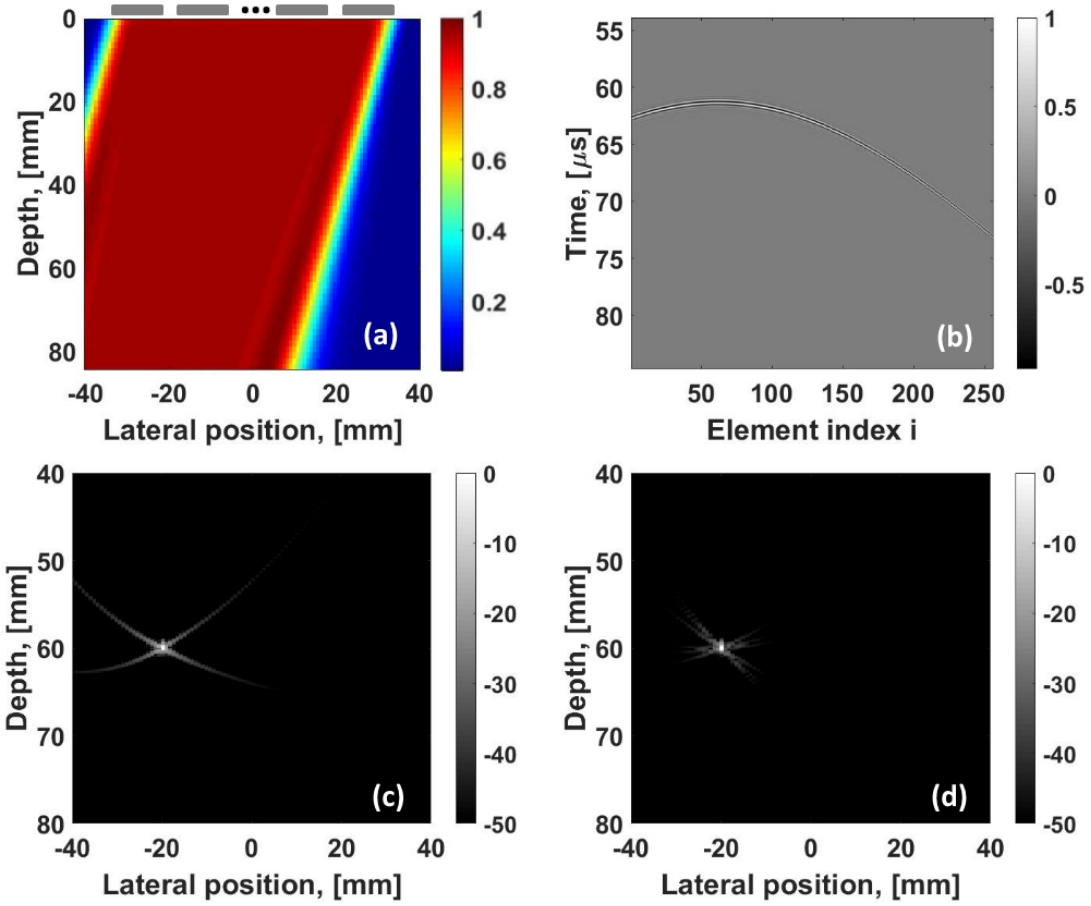

Figure 2.18: Principle of PWI: (a) - Normalized root mean square of the pressure field $p_i(\vec{r},t)$ inside the medium when the emitted plane wave is tilted by $-15°$ (maximal value of $RMS(p_i(\vec{r},t))$ is 22.44 Pa), (b) - Received RF signals ${}_{PWI}y_i(t)$ after one plane wave emission, (c) - A full B-mode image reconstructed from the RF data shown in (b), (d) - A full B-mode image reconstructed after $N_{pwi} = 4$ repetitions of the steps (a) to (c): ${}_{PWI}\theta^k \in \{-15°, -7.5°, 7.5°, 15°\}$

[Montaldo et al., 2009, Tanter et al., 2002]. It consists in emitting successively N_{pwi} plane waves tilted in slightly different directions. Relying on the principle of linear ultrasound (emission / propagation / reception), successive transmission of rigorously tilted plane waves can be seen as a emission beam focusing, not by delaying the transducer excitations during the same firing, but by doing so across successive firings. After each emission / reception event, a low quality image is beamformed. Finally, once all the N_{pwi} low quality images are reconstructed they are coherently added in order to obtain an improved image:

$$ {}_{PWI}\hat{\gamma} = \sum_{k=1}^{N_{pwi}} {}_{PWI}\hat{\gamma}^k \tag{2.55} $$

Fig.2.18(d) shows the result of compounding with $N_{pwi} = 4$ plane waves. By comparing ${}_{PWI}\hat{\gamma}^k$ (Fig.2.18(c)) with ${}_{PWI}\hat{\gamma}$ (Fig.2.18(d)), one can observe that the spatial compounding improves the image quality, by mostly reducing the artifacts. The lateral resolution is also improved. This yields significantly better image SNR and CNR. The PWI's FAR can be computed as follows:

$$ {}_{PWI}FAR = \frac{1}{N_{pwi}(t_a + t_{rec} + t_{SW}) + \sum_{k=1}^{N_{pwi}} \max_{j\in[1..N_{el}]} {}_{PWI}t_j^k} \approx \frac{1}{N_{pwi}\, t_{rec}} \tag{2.56} $$

In order to achieve, the same image quality as provided by FUI, PWI requires a compounding of a high number of plane waves ($N_{pwi} \approx N_l$ [Montaldo et al., 2009]). In such conditions, from (2.47) and (2.56), it can be seen that ${}_{PWI}FAR \approx {}_{FUI}FAR$. This implies that PWI does not allow to increase the frame rate without losing image quality when compared to FUI. Nonetheless, in [Toulemonde et al., 2015], it was shown that starting with $N_{pwi} \approx 11$ the image quality of the provided images improves very little. Thus, it can be concluded that accepting a slight loss in image quality, plane wave imaging can provide a FAR boost by a factor 10.

Diverging Wave and Synthetic Transmit Aperture imaging (DWI)

DWI and STA are two imaging methods that employ diverging wave insonifications of the medium in order to reconstruct full B-mode images. Even though in the literature there exist a large number of DWI [Hasegawa and Kanai, 2011, Papadacci et al., 2014, Zhang et al., 2016, Porée et al., 2016] and STA [Jensen et al., 2006, Tasinkevych et al., 2012, Tasinkevych et al., 2013, Karaman et al., 1998] variations, the process used to generate a full B-mode image can be generalized as follows. Suppose the ultrasound probe shown in Fig.2.19. In order to transmit a diverging wave using this probe, one should consider a punctual virtual source located at the point $\vec{r}_{v_k} \mid z_{v_k} < 0$. Depending on the region of interest in the medium, which imposes a certain angular aperture ${}_{DWI}\theta^k$, n elements of the probe are excited with the same excitation $a(t)$ delayed depending on the position of each active element. n can be defined as follows:

$$n = \frac{2|z_{v_k}|\tan({}_{DWI}\theta^k)}{\wp} \tag{2.57}$$

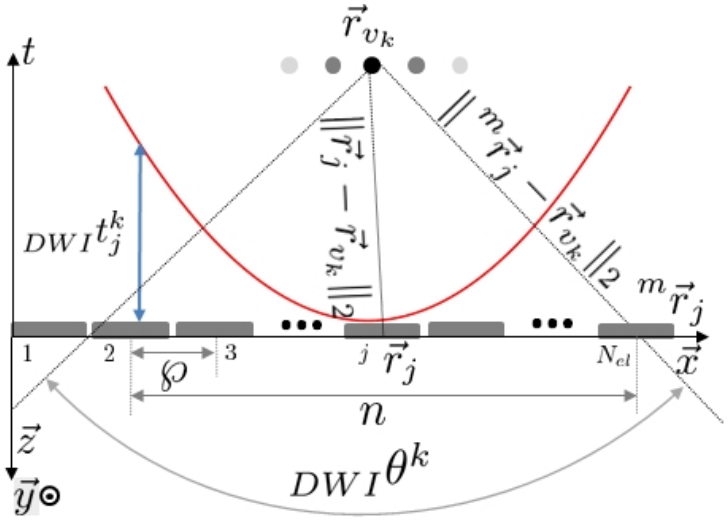

Figure 2.19: Sketch of an ultrasound probe that emits a diverging wave. In red are represented the ${}_{DWI}t_j^k$ delays used in order to generate a virtual source at the position $\vec{r}_{v_k} \mid z_{v_k} < 0$. The generated angular aperture is ${}_{DWI}\theta^k$

Using (2.57), the emission delays can be computed as follows:

$${}_{DWI}t_j^k = \frac{\left|\|\vec{r}_j - \vec{r}_{v_k}\|_2 - \|{}^m\vec{r} - \vec{r}_{v_k}\|_2\right|}{c_m} \tag{2.58}$$

where ${}^m\vec{r}$ represents the position of the most distant active element from the focal point $\vec{r}_{v_k}$. Using

(2.58), the excitation signal for each active element j of the probe can be deduced:

$$_{DWI}a_j^k = a(t) *_t \delta(t - {}_{DWI}t_j^k) = a(t - {}_{DWI}t_j^k) \tag{2.59}$$

The normalized root mean square of the pressure field $p_i(\vec{r},t)$, generated by the emission of $_{DWI}a_j^k$ is shown in Fig.2.20(a). As expected, one can observe that the lines of constant pressure are concentric circle arcs, which in the context of 2D waves, represent diverging wave wavefronts. Furthermore, one can observe that the pressure amplitude decreases with the distance. This is the result of the geometrical spreading term seen in the Green function in (2.7), which implies that the total energy of the wave is dispersed over the surface of the wavefront.

From the expression of the excitation signals (2.59), using (2.33), the received RF data can be modeled as follows:

$$_{DWI}y_i^k(t) = w_i *_t h(t) *_t a(t) *_t h(t) *_t \sum_{j=1}^{n} \left[w_j \delta(t - {}_{DWI}t_j^k) *_t \int_V \gamma(\vec{r}) g_{ji}(\vec{r},t)\, \mathrm{d}^2\vec{r} \right] + b_i(t) \tag{2.60}$$

This RF data can be further processed using DAS algorithm (2.36) in order to obtain a B-mode image $_{DWI}\hat{\gamma}^k$. In Fig.2.20(b) are displayed the received signals after the scattering of the pressure field shown in Fig.2.20(a). The result of DAS applied on this data is displayed in Fig.2.20(c). As one can observe, similar to PWI, DWI allows reconstructing the PSF in the correct position however the image contains artifacts, which again, are linked to the approximations on which DAS relies (Section 2.2.1). While the axial resolution is still comparable with the ones provided by FUI and PWI, the lateral resolution is degraded when compared to the one of FUI. Furthermore, as for PWI, the reconstruction artifacts, decrease considerably the SNR and CNR provided by DWI. In order to improve the image quality, spatial compounding is also implemented in DWI [Papadacci et al., 2014, Zhang et al., 2016], N_{dwi} virtual sources being distributed at a constant depth z_{v_k} between two lateral position x_{v_m} and x_{v_M}. After each N_{dwi} successive firings by the virtual sources, N_{dwi} low quality images $_{DWI}\hat{\gamma}^k$ are reconstructed. Finally, the improved image is obtained by:

$$_{DWI}\hat{\gamma} = \sum_{k=1}^{N_{dwi}} {}_{DWI}\hat{\gamma}^k \tag{2.61}$$

The result of compounding with $N_{dwi} = 4$ diverging wave images is shown in Fig.2.20(d). Here it can be seen that, when compared to the image without compounding (Fig.2.20(c)), this image provides a better overall image quality. Moreover, comparing the obtained PSF with the one provided by PWI (Fig.2.18(d)), it can be seen that DWI and PWI provide similar results. The advantage, however, that DWI has on PWI is that, since the emitted pressure wave is divergent, with depth, the insonified volume of the medium increases. This means that the received signals will contain echoes from larger regions in the medium and thus the reconstructed image will have larger field of view. Concerning the DWI's FAR, this parameter can be computed as follows:

$$_{DWI}FAR = \frac{1}{N_{dwi}(t_a + t_{rec} + t_{SW}) + \sum_{k=1}^{N_{pwi}} \max_{j\in[1..N_{el}]} {}_{DWI}t_j^k} \approx \frac{1}{N_{dwi}\, t_{rec}} \tag{2.62}$$

As one can observe in (2.62), similar to PWI, DWI provides close to FUI image qualities when N_{dwi} is high. However, for high number of diverging waves used for compounding, the frame rate of the final image decreases, which again shows the inherent trade-off between the FAR and good image quality.

Depending on the application, different DWI approaches exist. However, all of these imaging methods can be seen as a variation of the approach presented previously. Thus, by fixing the number of active elements at $n = N_{el}$ and by moving the virtual source position along different patterns (circles,

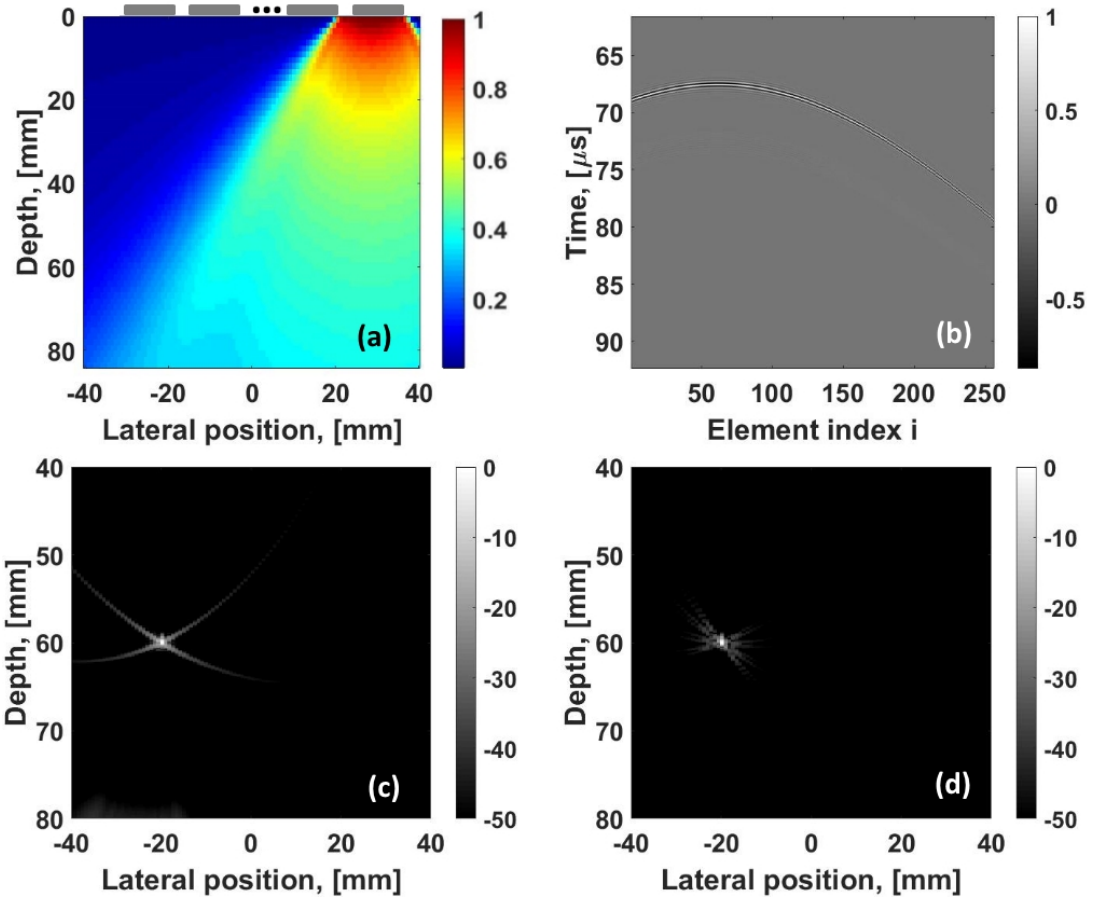

Figure 2.20: Principle of DWI: (a) - Normalized root mean square of the pressure field $p_i(\vec{r},t)$ inside the medium when the position of the virtual source is $\vec{r}_{v_k} = (50.76, 0, 10)\ mm$ (maximal value of $RMS(p_i(\vec{r},t))$ is 12.01 Pa), (b) - Received RF signals ${}_{DWI}y_i^k(t)$ after one diverging wave emission, (c) - A full B-mode image reconstructed from the RF data shown in (b), (d) - A full B-mode image reconstructed after $N_{dwi} = 4$ repetitions of the steps (a) to (c): $x_{v_k} \in \{15.4, 30.7, 46.1, 57.6\}\ mm$

ellipses), the generated pressure field $p_i(\vec{r},t)$ can be varied in order to insonify the medium in different ways (Fig. 2.21(a-d)). The classical variation of Synthetic Transmit Aperture (STA) imaging can be also seen as a variation of the emission scheme described previously in this Subsection. Classical STA consists in successive emissions, with a single element, of diverging waves inside the medium [Jensen et al., 2006]. After each emission / reception event a low quality image is reconstructed and finally these images are compounded. Thus, one can observe that, by forcing in (2.57) $n = 1$, and by following exactly the rest of the reasoning, the presented DWI approach becomes similar to classical STA. Finally, variations of STA that are exactly the same as the presented DWI approach exist [Karaman et al., 1998].

Summary on the imaging methods

In Fig.2.22 a diagram that sums up the performance of the different imaging methods presented in this Section is shown. As one can observe here, the best image quality is achieved by the conventional (focused) acquisition scheme. It can be also observed that the imaging methods that provide a faster acquisition rate, imply a decrease of the provided image quality.

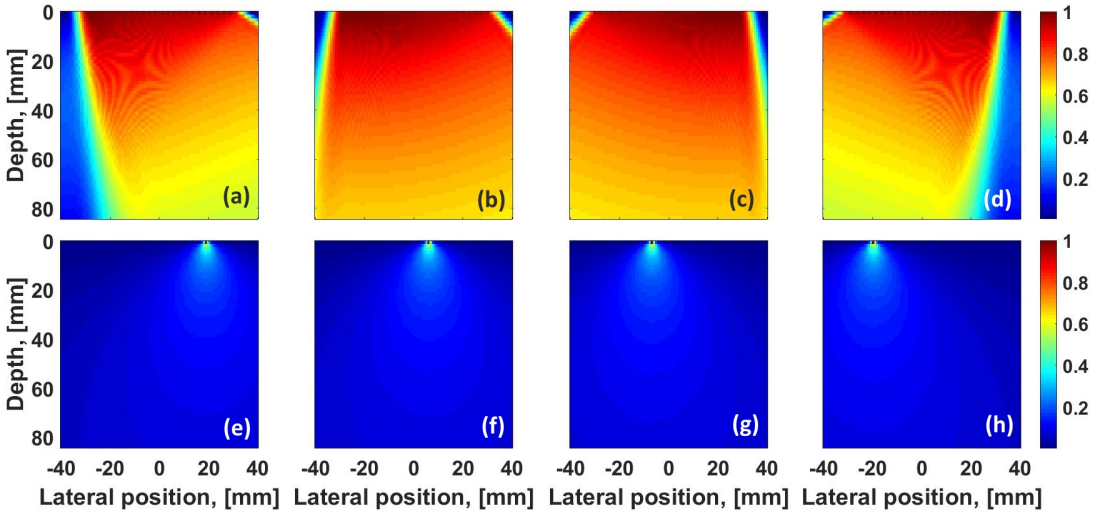

Figure 2.21: (a-d) - Root mean square of the pressure field $p_i(\vec{r},t)$ in the case where the virtual sources are displaced on an ellipse, (e-h) - Classical STA emission scheme (here only four emissions are shown)

Method / Metric	FUI	MLT	PWI	DWI
FAR	⊖	⊕	⊕	⊕
Ax. res.	⊕	⊕	⊕	⊕
Lat. res.	⊕	⊖	⊖	⊖
Ax. cor.	⊕	⊕	⊕	⊕
Lat. cor.	⊕	⊖	⊖	⊖
SNR	⊕	⊖	⊖	⊖
CNR	⊕	⊖	⊖	⊖
eSNR	⊕	⊖	⊖	⊖

Figure 2.22: Evolution of the image quality metric for the different imaging approaches presented in Section 2.2.2

2.3 Temporal encoding for increasing the echo signal to noise ratio

2.3.1 Generalities

So far, the evolution of the image quality in terms of resolution, CNR, SNR, $eSNR$ as a function of FAR was presented. However, for a given acquisition method, the attainable performance can be also altered by the noise inside the RF data. The aim of this Section is to briefly present the impact of the noise on the image quality and most importantly to show how temporal encoding of the excitation signals allows overcoming its unwanted effects.

As shown in (2.33), the received RF data can be modeled as a linear superposition between the backscattered echoes and a noise. During an acquisition, this noise can be of an electronic origin (thermal, analog to digital conversion noise, etc.) and of acoustic origin (generated by the effects that do not satisfy the imaging hypothesis seen in Section 2.1.4). Usually, in ultrasound it is assumed that the acoustic noise is predominant over the electronic one and that it has a normal distribution of amplitudes and is thus considered as an Additive White Gaussian Noise. In such conditions, the noise

$b_i(t)$ will populate the entire bandwidth of the ultrasound probe (since, during the reception, the noise outside the bandwidth of the acousto-electrical impulse response of the probe $h(t)$ is attenuated). In

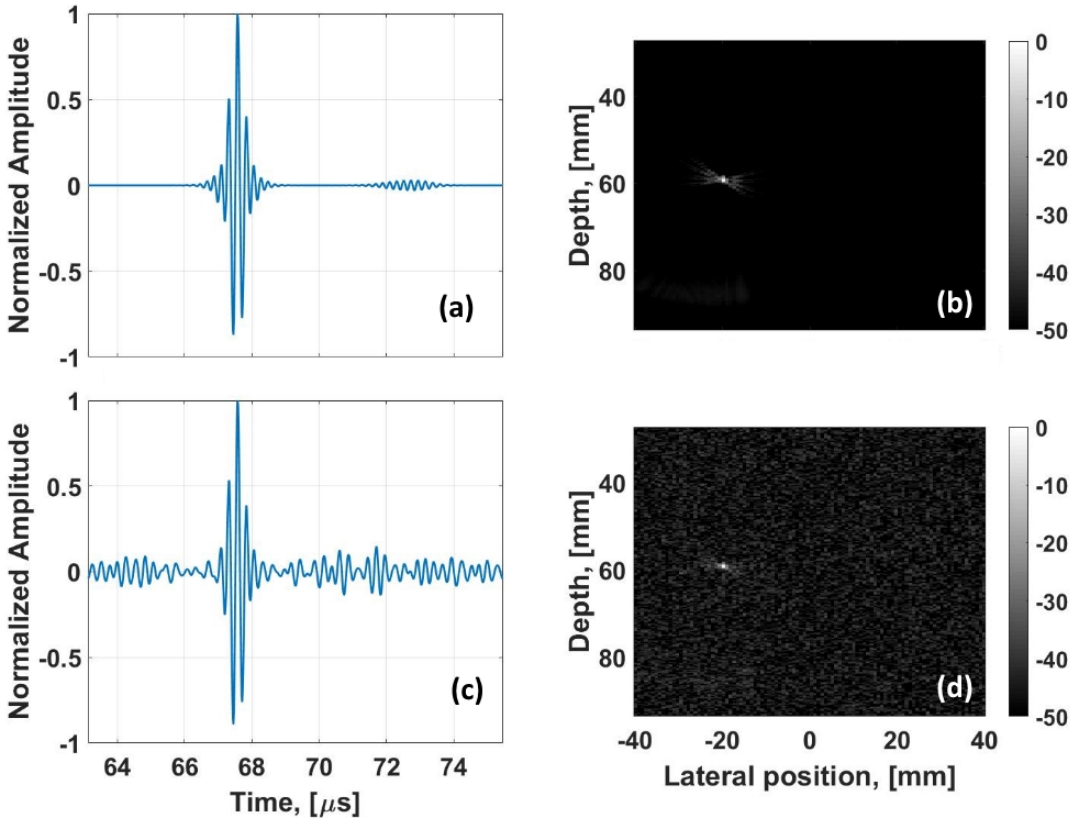

Figure 2.23: Impact of the $eSNR$ on the B-mode image (obtained using FUI method): (a) - RF data without noise, (b) - reconstructed image from RF data without noise, (c) - RF data with 15 dB noise, (d) - reconstructed image from noisy RF data

Fig.2.23(a) is shown a typical echo received by an element of the probe ($i = 64$ of the RF data showed in Fig.2.20). Using (2.43), it can be deduced that the $eSNR$ of this signal is infinity (since no noise is added). By adding to this signal a white Gaussian noise with an $eSNR$ of 15 dB the signal displayed in Fig.2.23(c) is obtained. Now, as it can be seen on the images reconstructed from the RF data with an $eSNR = \infty$ (Fig.2.23(b)) and from the RF data with an $eSNR = 15$ dB (Fig.2.23(d)), the acquisition noise impacts directly the image quality. While the provided spatial resolution of the PSF remains the same, the RF data with lower $eSNR$ value generates more background noise in the reconstructed image. Thus, using (2.41) and (2.42), it can be deduced that SNR and the CNR of the provided B-mode images will be decreased.

In order to understand how the $eSNR$ can be increased, one needs to consider a simple case where the imaged medium contains a single scatterer (Fig.2.23). In such case, using (2.32), (2.33) and (2.43), it can be deduced that:

$$eSNR = 10\log_{10}\left(\frac{\mathbb{E}\left\{|w_i \sum_{j=1}^{N_{el}} w_j y_{ji}(t)|^2\right\}}{\mathbb{E}\left\{|b_i(t)|^2\right\}}\right) = 10\log_{10}\left(\frac{1}{\sigma_i^2}\mathbb{E}\left\{|w_i \sum_{j=1}^{N_{el}} w_j y_{ji}(t)|^2\right\}\right) =$$

$$10\log_{10}\left(\frac{1}{\sigma_i^2}\mathbb{E}\left\{\left|w_i \sum_{j=1}^{N_{el}} w_j \gamma(\vec{r}) a(t) *_t \delta(t - {}_{DWI}t_j^k) *_t h(t) *_t h(t) *_t \frac{S^2\delta\left(t - \frac{\|\vec{r}-\vec{r}_j\|_2 + \|\vec{r}-\vec{r}_i\|_2}{cm}\right)}{4\pi^2\|\vec{r}-\vec{r}_j\|_2\|\vec{r}-\vec{r}_i\|_2}\right|^2\right\}\right) \tag{2.63}$$

where σ_i^2 represents acquisition noise variance and $\mathbb{E}\{.\}$ represents the expected value. (2.63) can be reduced (in the temporal frequency domain ν) as follows:

$$\begin{aligned} eSNR = 10\log_{10}\left(\frac{1}{\sigma_i^2}\mathbb{E}\left\{\left|A(\nu)H(\nu)H(\nu)\sum_{j=1}^{N_{el}}\frac{S^2\gamma^2(\vec{r})w_i w_j}{4\pi^2\|\vec{r}-\vec{r}_j\|_2\|\vec{r}-\vec{r}_i\|_2}\right|^2\right\}\right) \leq \\ 10\log_{10}\left(\frac{1}{\sigma_i^2}\mathbb{E}\left\{\left|A(\nu)H(\nu)H(\nu)\right|^2\right\}\right) + 10\log_{10}\left(\mathbb{E}\left\{\left|\sum_{j=1}^{N_{el}}\frac{S^2\gamma^2(\vec{r})w_i w_j}{4\pi^2\|\vec{r}-\vec{r}_j\|_2\|\vec{r}-\vec{r}_i\|_2}\right|^2\right\}\right) \end{aligned} \tag{2.64}$$

where $A(\nu)$ and $H(\nu)$ represent the Fourier transforms of $a(t)$ and $h(t)$ respectively. In (2.64), it can

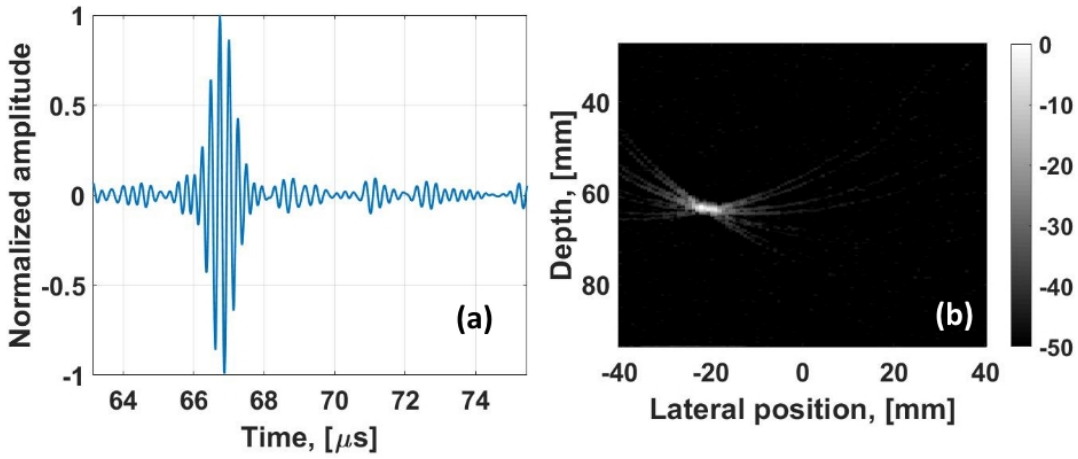

Figure 2.24: Impact of the excitation signal duration on the B-mode image quality: (a) - Noisy RF data, the excitation signal is twice as long as in the one used in Fig.2.23, (b) - reconstructed B-mode image from the RF data showed in (a)

be seen that the $eSNR$ can be split in two terms. The first term depends on the energy of the emitted signal ($a(t)$), on the acousto-electrical impulse response of the probe ($h(t)$) and on the variance of the noise. This represents the maximal ratio between the power of an echo and the noise power. The second term depends on the scattering coefficient at the point $\vec{r}$ and on the propagation distance ($\|\vec{r}-\vec{r}_j\|_2$ and $\|\vec{r}-\vec{r}_i\|_2$). Since for deeper scatterers $\vec{r}$ the propagation distance increases, the value of the second term decreases, which implies that the value of the $eSNR$ drops, resulting in a worse image quality. In absence of frequency dependent tissue attenuation effect, this represents the main cause of the image quality degradation with depth.

Since in (2.64), all the parameters are fixed (for a given configuration of: probe, medium, noise) except the excitation waveform, the only option that allows increasing the $eSNR$ is boosting the energy of the signal $a(t)$. Theoretically, here one can proceed in two ways: by increasing the maximal amplitude at the output of the source that drives the probe elements or by increasing the duration of the signals $a(t)$. Increasing the source voltage, however, can generate negative biological effects in the imaged medium, thus, usually the second option to boost the $eSNR$ is employed [Oelze, 2007, Zachary et al., 2001, Hamilton et al., 1998]. In Fig.2.24(a) is shown an echo that is received in the case where the medium is insonified with a waveform twice as long as the one used for Fig.2.23. For the same noise (as used in Fig.2.23(c) and (d)), the obtained $eSNR$ is 18.42 dB (coherent with the fact that the energy of the excitation signal was doubled). As one can observe on the reconstructed image (Fig.2.24(b)), the background noise is significantly reduced when compared to Fig. 2.23(d), however the PSF's spatial resolution is diminished. Thus, a need for specific excitation signals $a(t)$, that in the same time, carry a large amount of energy and provide a good image resolution emerges.

A naive, direct solution to this challenge is not physically feasible, since it would consist in using a Dirac as excitation signal. A realistic, feasible solution consist in using a particular class of signals that, despite their long duration, can be filtered in order to compress their energy in a short time span.

Suppose now that $^\circ a(t)$ is such a signal. In Fig.2.25 is showed how the "Image formation" block can be

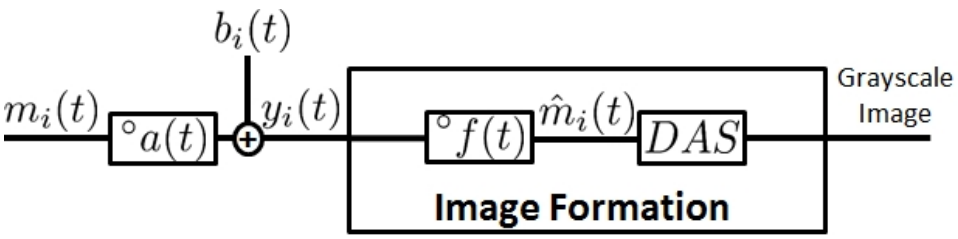

Figure 2.25: Schematic representation of the "Image reconstruction" block of the ultrasound imaging process employing $eSNR$ boosting excitation signals $^\circ a(t)$

modified in order to compress the energy of the excitation signal. Basically, the only difference between the classical "Image formation" block and the one presented in Fig.2.25 is that, here, an additional filtering step $^\circ f(t)$ has been added. Classically, this filters depend only on the excitation signals $^\circ a(t)$ and can be computed as follows. In Section 2.2.1, it has been shown that for any acquisition scheme that uses the excitation signals $^\circ a(t)$, the received RF data can be written as:

$$\begin{gathered} y_i(t) \underset{\text{Using 2.33}}{=} {}^\circ a(t) *_t m_i(t) + b_i(t) \\ \text{with: } m_i(t) = w_i \sum_{j=1}^{N_{el}} w_j \delta(t - t_j) *_t h(t) *_t h(t) *_t \int_V \gamma(\vec{r}) g_{ji}(\vec{r}, t)\, \mathrm{d}^2\vec{r} \end{gathered} \tag{2.65}$$

In (2.65), the signals $m_i(t)$ represent the backscattered echoes that one would obtain if the excitation signal was a short impulsion $\delta(t)$. As it can be seen from Fig.2.25, the input data for the DAS algorithm is not the RF data $y_i(t)$ (as for classical approaches) but the signals $\hat{m}_i(t)$ that can be seen as estimations of $m_i(t)$:

$$\hat{m}_i(t) = {}^\circ f(t) *_t y_i(t) \Longleftrightarrow \hat{M}_i(\nu) = {}^\circ F(\nu) Y_i(\nu) = {}^\circ F(\nu)\, {}^\circ A(\nu) M_i(\nu) + {}^\circ F(\nu) B_i(\nu) \tag{2.66}$$

where the capital letterers represent the Fourier Transforms (FT) of the corresponding temporal signals (e. g. for an arbitrary signal $s(t)$ its Fourier transform is defined as $S(\nu) = \mathrm{FT}(s(t))$). Thus, from (2.66), one can deduce that if the $^\circ f(t)$ filters give an exact estimation of $m_i(t)$, the spatial resolution of the image is optimal (since the emitted signal is very short), however, the new noise term $^\circ F(\nu) B_i(\nu)$ can pollute this result. In order to find the optimal filters $^\circ f(t)$ one needs to consider the following minimization problem:

$$^\circ F(\nu) = \underset{^\circ F(\nu)}{\operatorname{argmin}}\, \mathbb{E}\left\{ |M_i(\nu) - \hat{M}_i(\nu)|^2 \right\} \tag{2.67}$$

Using (2.66), the expected value in (2.67) can be written as follows:

$$\mathbb{E}\left\{ |M_i(\nu) - \hat{M}_i(\nu)|^2 \right\} = \left[1 - {}^\circ F(\nu)\, {}^\circ A(\nu)\right] \left[1 - {}^\circ F(\nu)\, {}^\circ A(\nu)\right]^* \mathbb{E}\{|M_i(\nu)|^2\} + {}^\circ F(\nu)\, {}^\circ F^*(\nu) \mathbb{E}\{|B_i(\nu)|^2\} \tag{2.68}$$

where $F^*(\nu)$ represents the complex conjugate of the signal $F(\nu)$. At this point, by computing the derivative of (2.68) with respect to $^\circ F(\nu)$, one can find the critical point of $\mathbb{E}\left\{ |M_i(\nu) - \hat{M}_i(\nu)|^2 \right\}$ and thus

the solution to (2.67):

$$\frac{\mathrm{d}\mathbb{E}\left\{|M_i(\nu)-\hat{M}_i(\nu)|^2\right\}}{\mathrm{d}\,{}^{\circ}F(\nu)} = {}^{\circ}F^*(\nu)\mathbb{E}\{|B_i(\nu)|^2\} - {}^{\circ}A(\nu)\left[1-{}^{\circ}F(\nu)\,{}^{\circ}A(\nu)\right]^*\mathbb{E}\{|M_i(\nu)|^2\} \underset{\text{critical point}}{=} 0 \Rightarrow$$

$${}^{\circ}F(\nu) = \frac{{}^{\circ}A^*(\nu)}{{}^{\circ}A(\nu)\,{}^{\circ}A^*(\nu)+\frac{\mathbb{E}\left\{|B_i(\nu)|^2\right\}}{\mathbb{E}\left\{|M_i(\nu)|^2\right\}}} = \frac{{}^{\circ}A^*(\nu)}{|{}^{\circ}A(\nu)|^2+\frac{1}{eSNR_{M_i}(\nu)}} = \begin{cases} \frac{1}{{}^{\circ}A(\nu)}, & 1/eSNR_{M_i}(\nu) << |{}^{\circ}A(\nu)|^2 \\ {}^{\circ}A^*(\nu), & \text{otherwise} \end{cases} \tag{2.69}$$

where $eSNR_{M_i}(\nu)$ represents the echo signal to noise ratio (for each frequency band ν) of the case where an impulsion was used as excitation signal (with the condition that the noise has the same variance as in the acquisition with the excitation ${}^{\circ}a(t)$). Now, as one can see in (2.69), if the acquisition noise is very low ($1/eSNR_{M_i}(\nu) << |{}^{\circ}A(\nu)|^2$), ${}^{\circ}F(\nu)$ becomes an inverse filter, meaning that the provided resolution is optimal. However, if the noise increases, ${}^{\circ}F(\nu)$ becomes more of a matched filter. This family of filters is called Wiener filters [Wiener et al., 1949].

Indeed, in the case where no noise is present (or very low amount), the inverse filter would provide an optimal spatial resolution and no background noise (generated by $B_i(\nu)$), since the estimation $\hat{M}_i(\nu)$ corresponds perfectly to $M_i(\nu)$. In such cases, any excitation signal would be applicable for acquisition. However, in all the other cases, where ${}^{\circ}F(\nu)$ is intermediate between an inverse and a matched filter, signals that have a "good" autocorrelation product (defined as: ${}^{\circ}a(t) *_t {}^{\circ}a(-t)$) are suitable. By "good", in this application is implied that the power spectral density (defined as ${}^{\circ}A(\nu)\,{}^{\circ}A^*(\nu) = \mathrm{FT}\{{}^{\circ}a(t) *_t {}^{\circ}a(-t)\}$) is constant, which implies that the autocorrelation product generates a very thin main lobe and that the secondary lobes are low with respect to the main lobe. Long before their ultrasound application, in RADAR and telecommunication systems such signals were already implemented in order to achieve the same final objectives [Nathanson et al., 1991, Skolnik, 1962, Siebert, 1988, Prasad and Ojanpera, 1998]. These signals can be split in two main groups depending on their generation scheme: Binary Phase Shift Keyed (BPSK) signals and Linear Frequency Modulated (LFM) signals (also called chirps). The principles of each of these two groups and their variations will be presented in the following two sections.

2.3.2 BPSK modulated sequences

Consider a binary sequence (or code) s of length n_s, defined as follows:

$$s = s_0, s_1, s_2, \cdots, s_j, \cdots, s_{n-1} |\ s_j \in \{-1,1\}\ \forall\, j \in [0..n-1] \tag{2.70}$$

Suppose now that this sequence possesses a "good" autocorrelation product (as previously explained: narrow main lobe and low side lobe levels), in order to employ such sequence in an ultrasound acquisition scheme, one needs to shift its frequency content in the bandwidth of the ultrasound probe (given by $h(t)$). The process of frequency shifting of a baseband signal (s) to a frequency band adapted for the propagation is called modulation. For the sake of convenience, in this work the modulation of the sequence s will be defined as:

$$\begin{aligned} a^s(t) = \sum_{j=1}^{n_s}\left[s_j\delta(t-jm_mT_0) *_t \left(\cos\left(\frac{2\pi t}{T_0}\right)\mathrm{rect}\left(\frac{t}{m_mT_0}\right)\right)\right] = \\ \left(\cos\left(\frac{2\pi t}{T_0}\right)\mathrm{rect}\left(\frac{t}{m_mT_0}\right)\right) *_t \sum_{j=1}^{n_s} s_j\delta(t-jm_mT_0) \end{aligned} \tag{2.71}$$

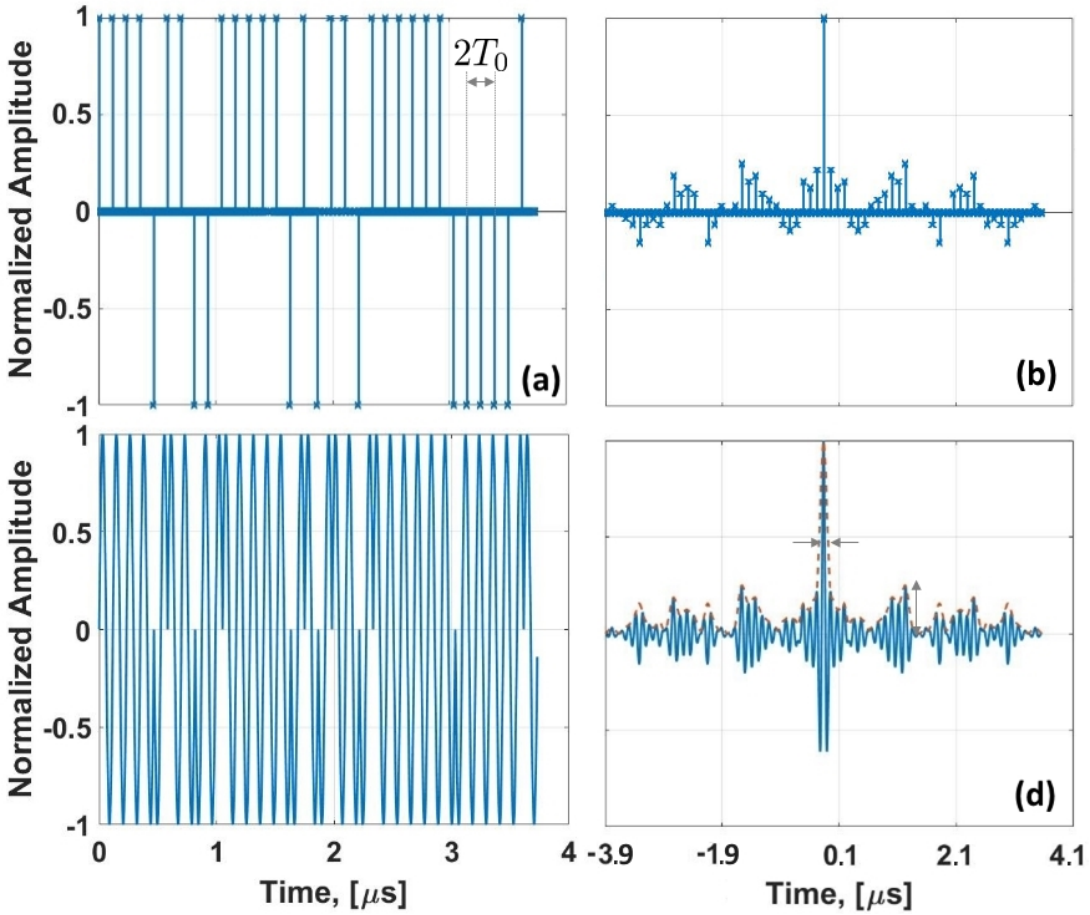

Figure 2.26: Schematic representation of the BPSK modulated sequence generation ($n_s = 32$): (a) - binary sequence s, every bit being spaced by an interval T_0 ($m_m = 1$), (b) - autocorrelation of the sequence s which already contains the temporal spacing between bits, (c) - modulated sequence ($s_m(t)$) with $\nu_0 = 8.5\ MHz$ and $m_m = 1$ (in solid blue), (d) - autocorrelation product of $s_m(t)$ (in solid blue). The dashed red line represents the envelope of the corresponding signal. The two horizontal arrows in (d) represent the width of the main autocorrelation lobe and the vertical arrow measures the maximal side lobe level.

where $T_0 = 1/\nu_0$ is the period corresponding to the central frequency component ν_0 in the bandwidth of the probe and m_m is a modulation parameter that sets the emission rate of the s_j symbols. As one can see in (2.71), the modulation can be split in two parts. The first part ($\delta(t - j m_m T_0)$) consists in separating the elements of the sequence s by a duration $m_m T_0$ (Fig.2.26(a)). The second part ($s_j \cos\left(\frac{2\pi t}{T_0}\right) \text{rect}\left(\frac{t}{m_m T_0}\right)$) consists in emitting during $m_m T_0$ a sinusoidal signal centered at the frequency ν_0. Since the emitted signal for each duration $m_m T_0$ is weighted by an element of the sequence s_j, this means that the emission rate of the s is $1/(m_m T_0)$ and that the modulated signal $a^s(t)$ (Fig.2.26(b)) is a sinusoidal signal that changes its amplitude between $+1$ and -1. Since this amplitude oscillations can be seen as a phase shift between 0 and π finally one can see (2.71) as a phase shifting process on a carrier sinusoidal signal centered at ν_0. Thus, (2.71) can be also called the Binary Phase Shift Keying (BPSK) of the sequence s. At this point, one can compute the autocorrelation product of $a^s(t)$

as follows:

$$\begin{aligned} a^s(t) *_t a^s(-t) \underset{\text{Using (2.71)}}{=} & \left[\left(\sum_{j=1}^{n_s} s_j \delta(t - j m_m T_0) \right) *_t \left(\sum_{j=1}^{n_s} s_j \delta(-t + j m_m T_0) \right) \right] *_t \\ & \left[\left(\cos\left(\frac{2\pi t}{T_0}\right) \text{rect}\left(\frac{t}{m_m T_0}\right) \right) *_t \left(\cos\left(\frac{-2\pi t}{T_0}\right) \text{rect}\left(\frac{-t}{m_m T_0}\right) \right) \right] = \text{FT}^{-1} \left\{ A^s(\nu) \left(A^s(\nu)\right)^* \right\} \end{aligned} \tag{2.72}$$

In (2.72), one can observe that the autocorrelation product of the BPSK modulated signal $a^s(t)$ can be seen as a convolution between two terms. The first term (Fig.2.26(b)), depends only on s_j elements, and represents the autocorrelation product of the binary sequence s. This term intrinsic to s and it sets mostly the ratio between the amplitude of the main and side lobes. The second term (Fig.2.26(d)), depends on the carrier signal, and is the main factor that impacts both the resolution of the main lobe and the side lobe level. The evolution of the autocorrelation product (2.72) as a function of the carrier signal will be addressed more in details in Appendix D.

In order to fully benefit from the autocorrelation properties of the codes s, sometimes the classical acquisition schemes need to be modified. Thus, depending on the impact on the emission schemes, the BPSK signals can be split in the following groups: standalone codes and joint operating codes.

Standalone Codes

The following codes belong to the standalone family: m-sequences, Gold, Kasami (small and large sets) [Miwa et al., 1981, Shen and Ebbini, 1996]. Their implementation is very straightforward:

1. the sequence s is generated
2. s is BPSK modulated
3. every emitting element of the transducer is excited using $s_m(t)$ delayed depending on the acquisition scheme
4. in reception all the RF signals are filtered using the filters derived in (2.69)
5. on the filtered data the classical image reconstruction algorithm is applied

The advantage of such binary codes is their implementation simplicity (when compared to other codes presented in this section), since, as their name implies, only one code is needed to improve the $eSNR$. However, their drawback consists in the fact that the ratio between the main and side lobe amplitudes decreases with the length n_s of the sequence, in some application, pushes towards the use of joint codes, that are described in the next section.

Joint codes

As the name implies, in order to fully benefit from the properties of this class of sequences, one needs to employ two ore more codes for one wavefront. An example of such codes are the Golay and Hadamard families. Their implementation in an acquisition scheme is a bit more complicated than for standalone codes and can be summarized as follows.

– For the Golay family [Chiao and Thomas, 2000, Trots, 2015]:

G1 generation of N_G complementary codes s^k. The complementarity property implying that [Tseng and Liu, 1972]:

$$\sum_{k=1}^{N_G} s^k \circ s^k = 2 n_s \delta \tag{2.73}$$

where $\circ$ represent the correlation product, n_s is the length of the s^k sequences and δ is the Dirac delta function.

G2 BPSK modulation of the code s^1

G3 emission of the sequence $s^1_m(t)$ with all the elements of the probe

G4 filtering of the backscattered echoes using the filters derived in (2.69)

G5 repeat the steps G2 to G4 for all the N_G codes

G6 add all the filtered data (obtained at the step G3) for each element in reception in order to benefit from the complementarity property (2.73)

G7 apply the classical image reconstruction algorithm on the data obtained in G6

– For the Hadamard family [Tiran et al., 2015, Chiao et al., 1997, Mosca et al., 2008]:

HM1 generation of N_{HM} codes s^k

HM2 for a wavefront j, generate the excitation signal by BPSK modulating s^k_j

HM3 emit simultaneously n_s wavefronts

HM4 receive the backscattered data $y^k_i(t)$ (for each element i of the probe)

HM5 repeat N_{HM} times the steps HM2 to HM4

HM6 reconstruct the data corresponding to each wavefront j using the following relation:

$$y^j_i(t) = \sum_{k=1}^{N_{HM}} s^k_j y^k_i(t) \tag{2.74}$$

This represents the compression of the Hadamard codes, which, as one can observe, does not use the filters derived in (2.69).

HM7 reconstruct, from the RF data $y^j_i(t)$, an image (or an image line, in the case of focused emissions) for all the N_{HM} wavefronts

Despite their convoluted implementation, the advantage of the Golay and Hadamard codes, over the standalone families, is that they generate zero side lobes during the compression.

2.3.3 Frequency Modulated (FM) signals

Another way of generating $a(t)$ excitation signals with "good" autocorrelation product is by generating long temporal signals that span a certain frequency band [Miwa et al., 1981, O'Donnell, 1992, Haider et al., 1998, Misaridis and Jensen, 1999]. Suppose that the bandwidth of the employed ultrasound probe allows emitting signals of a bandwidth $B_{FM} = \nu_H - \nu_L$ centered around the frequency ν_0. Then, in order to generate a signal that sweeps B_{FM} in the time duration T_{FM} (Fig.2.27(a)), one can create a sinusoidal function with an instantaneous frequency $\nu(t)$ that evolves between ν_L and ν_H following different laws (Fig.2.27(a)). Thus, one can write an FM modulated signal (chirp) as follows:

$$a^{FM}(t) = A \cdot \cos\big(2\pi\nu(t)\,t\big)\,\mathrm{rect}\Big(\frac{t - T_{FM}/2}{T_{FM}}\Big) \tag{2.75}$$

In (2.75), A stands for the amplitude of the chirp, and the rectangular function is added to limit the signal duration to T_{FM}. Now, as previously stated, the evolution of the frequency as function of time can be different, the classical ones being the linear, quadratic and logarithmic ones:

$$\nu(t) = \begin{cases} \nu_L + \frac{\nu_H - \nu_L}{T_{FM}}\,t, \text{ linear} \\ \nu_L + \frac{\nu_H - \nu_L}{T_{FM}}\,t^2, \text{ quadratic} \\ \nu_L \Big(\frac{\nu_H}{\nu_L}\Big)^{\frac{t}{T_{FM}}} \text{ logarithmic} \end{cases} \tag{2.76}$$

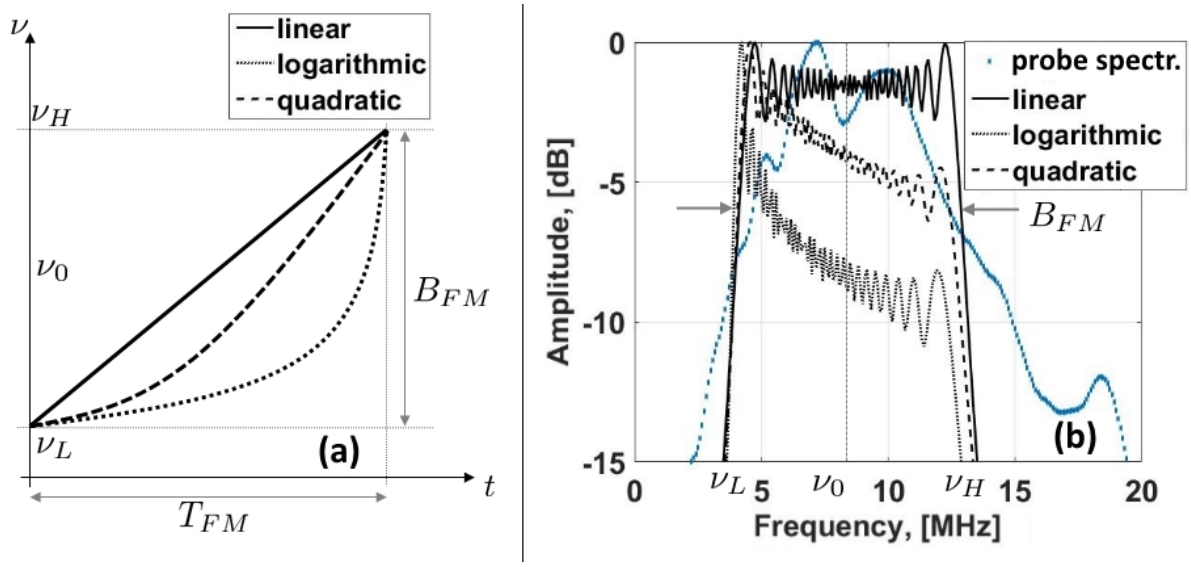

Figure 2.27: (a) - Evolution, as a function of time, of a frequency modulated signal. Three types of dependencies are depicted: linear (solid line), quadratic (dashed line) and logarithmic (dotted line). (b) - Corresponding normalized spectra of the signals showed in (a). In blue is represented an ultrasound probe spectrum for which these signals were generated: $\nu_0 = 8.5$ MHz, $B_{FM} = 9$ MHz, $T_{FM} = 12$ μs

However, as it can be seen in Fig.2.27(b), the nonlinear evolution of the frequency makes the chirp to carry more energy at lower frequencies (closer to ν_H). In the context of a band-limited probe (as the one showed in Fig.2.27(b)), the fact that the signal energy is not distributed symmetrically around ν_0 will result in a reduction of the chirp energy during the emission and reception. In the case of linear modulation of the chirp, as it can be seen in Fig.2.27(b), the signal energy is uniformly distributed around ν_0 which results in less energy loss during the emission and reception (using the employed probe). Since FM signals are used in ultrasound with the main objective to increase the $eSNR$, reducing the energy of the signal in emission and reception can be a serious drawback. Thus, in ultrasound mainly linear modulated chirps (Fig.2.28(a)) are used. At this point, using (2.75), (2.76) and the filter

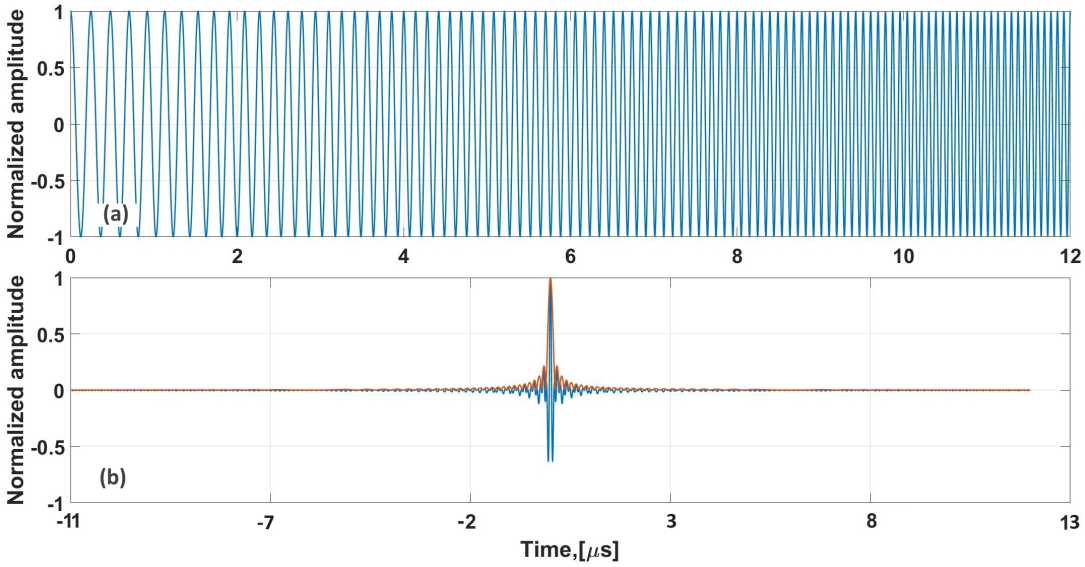

Figure 2.28: (a) - Linear frequency modulated chirp with $\nu_0 = 8.5$ MHz, $B_{FM} = 9$ MHz, $T_{FM} = 12$ μs, (b) - In solid blue is represented the autocorrelation product of the signal showed in (a), in solid red is shown the envelope of the autocorrelation product

derived in (2.69) one can write the expression of the autocorrelation product of the linear chirp as follows [Lashkari et al., 2016, Cook, 2012]:

$$a^{FM}(t) *_t a^{FM}(-t) = \mathrm{FT}^{-1}\left\{A^{FM}(\nu)\left(A^{FM}(\nu)\right)^*\right\} \approx$$
$$A \cdot \frac{sin\left(\frac{\mu T_{FM} t}{2}\right)}{\mu t} \cdot \cos(2\pi\nu_0 t) \cdot \mathrm{rect}\left(\frac{t}{2T_{FM}}\right) \approx \frac{AT_{FM}}{2}\,\mathrm{sinc}\left(\frac{\mu T_{FM} t}{2}\right) \cdot \cos(2\pi\nu_0 t) \cdot \mathrm{rect}\left(\frac{t}{2T_{FM}}\right) \tag{2.77}$$

where $\mu = B_{FM}/T_{FM}$ and $\mathrm{sinc}(x)$ represents the sine cardinal function of x. An example of an autocorrelation product of a linear chirp signal is shown in Fig.2.28(b). Between the relation (2.77) and the Fig.2.28(b), one can observe that the result of the linear chirp autocorrelation is a signal centered at the frequency ν_0 that has an instantaneous amplitude which follows the evolution of a sinc function. Thus, this sinc function will also set the amplitude of the main lobe which will be achieved for a zero lag ($\mathrm{sinc}(t=0)=1$). In such case, the maximum of the autocorrelation function of a linear chirp is $AT_{FM}/2$.

The implementation of such excitation signal in an ultrasound acquisition scheme is as straightforward as the method presented for the standalone codes (Section 2.3.2), however the advantage of chirps over the BPSK modulated sequences is that, for the same duration and bandwidth of the excitation signals, the chirps generate lower compression side-lobes.

2.4 Temporal encoding for increasing the frame acquisition rate

As shown in the previous section, the first methods based on the amplitude / frequency modulated signals had the only objective to increase the received signals $eSNR$. However, inspired by the Frequency and Coded Division Multiple Access (FDMA and CDMA) approaches vastly used in telecommunication systems [Prasad and Ojanpera, 1998, Black and Black, 1994, Jonassen et al., 2008], coded excitations begun to be employed in the mid-2000s with the goal to increase the FAR of the existing ultrasound acquisition schemes. Simply put, in telecommunication systems, FDMA and CDMA allow multiple pairs of users to communicate over a shared resource (usually channel) without interference and information loss. As their name implies, this is achieved either by splitting the total bandwidth of the channel in sub-bandwidths (each pair communicating through its sub-channel) or by attributing to each pair a specific spreading code used in emission and reception (the code of each pair being orthogonal to the others, the interference between pairs is reduced). By drawing the parallel between the ultrasound and telecommunication systems, it can be thus concluded that similar approaches can be applied to ultrasound in order to increase the FAR. Suppose the following equivalences between telecommunication systems $\Longleftrightarrow$ ultrasound imaging system: channel $\Longleftrightarrow$ imaged medium, message $\Longleftrightarrow$ excitation signal, user pair (or user antenna pair) $\Longleftrightarrow$ ultrasound probe in emission and ultrasound probe in reception. In these conditions, the process of ultrasound imaging (which, as it was shown in Section 2.2, tries to reconstruct the medium's TRF) can be seen as an equivalent of the channel estimation methods widely used in telecommunications [Coleri et al., 2002, Zhao and Huang, 1997, Torlak and Xu, 1997, Kang et al., 2003]. Thus, relying on this core principle, in [Gran and Jensen, 2008, Gran and Jensen, 2004, Gran et al., 2004, Kotowick et al., 2013] an ultrasound acquisition scheme was developed, that employs simultaneous emission of coded acoustic waves in order to increase the frame rate of classical STA.

As it was shown in Section 2.2.2, classical STA employs successive firings of diverging waves in order to obtain a final improved image by spatial compounding. Compared to the conventional approach, the coded STA method employs simultaneous emission of N_{dwi} diverging ultrasound waves, each of it carrying a BPSK signal $a^k(t)$ (Fig.2.29(a)). Using (2.60), it can be deduced that the total received signal

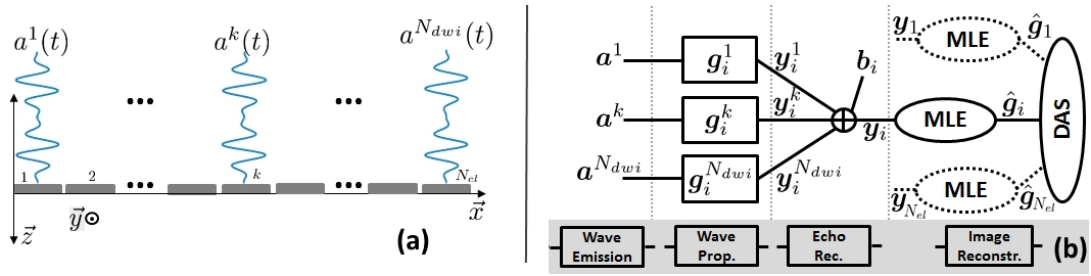

Figure 2.29: (a) - Schematic representation of the coded STA emission event, (b) - Block diagram of the coded STA imaging approach. MLE and DAS stand for Maximum Likelihood Estimator and Delay And Sum respectively.

at the element i of the probe can be written as:

$$\begin{aligned} y_i(t) &= \sum_{k=1}^{N_{dwi}} {}_{DWI}y_i^k(t) + b_i(t) = \sum_{k=1}^{N_{dwi}} a^k(t) *_t g_i^k(t) + b_i(t) \\ \text{with: } g_i^k(t) &= w_i w_k h(t) *_t h(t) *_t \int_V \gamma(\vec{r}) g_{ki}(\vec{r},t)\,\mathrm{d}^2\vec{r} \end{aligned} \tag{2.78}$$

In (2.78), it can be seen that the signal $g_i^k(t)$ depends only on the emission element k, the medium TRF $\gamma(\vec{r})$ and the reception element i. Thus, $g_i^k(t)$ can be seen as the impulse response of the medium when k emits and i receives. Reconstructing these signals using DAS would yield a good image resolution, since they correspond to the RF data that one would receive if a short impulsion was used as excitation. In order to find an estimation $\hat{g}_i^k(t)$ of the signals $g_i^k(t)$, first, one needs to write (2.78) in its discrete time form [Gran and Jensen, 2008, Gran and Jensen, 2004, Gran et al., 2004]:

$$\boldsymbol{y}_i = \sum_{k=1}^{N_{dwi}} \boldsymbol{a}^k *_t \boldsymbol{g}_i^k + \boldsymbol{b}_i = \begin{bmatrix} \boldsymbol{A}^1 & \boldsymbol{A}^2 & \cdots & \boldsymbol{A}^{N_{dwi}} \end{bmatrix} \cdot \begin{bmatrix} \boldsymbol{g}_i^1 \\ \boldsymbol{g}_i^2 \\ \vdots \\ \boldsymbol{g}_i^{N_{dwi}} \end{bmatrix} + \boldsymbol{b}_i \tag{2.79}$$

where the boldface symbols represent the sampled versions of the corresponding continuous time signals. In (2.79), $\boldsymbol{A}^k$ are convolution matrices built from the corresponding $\boldsymbol{a}^k$ signals. A more detailed description of steps needed to obtain (2.79) will be presented in Chapter 3. At this point, as shown in Fig.2.29(b), another step is required before doing the DAS reconstruction. This step is called Maximum Likelihood Estimator and allows computing all the signals $\hat{g}_i^k(t)$ from (2.79), relying on the fact that the noise $\boldsymbol{b}_i$ is white Gaussian. Thus, one obtains:

$$\begin{aligned} \hat{\boldsymbol{g}}_i &= \left(\boldsymbol{A}^T \cdot \boldsymbol{A}\right)^{-1} \cdot \boldsymbol{A}^T \cdot \boldsymbol{y}_i \\ \text{with: } \hat{\boldsymbol{g}}_i &= \begin{bmatrix} \hat{\boldsymbol{g}}_i^1 \\ \hat{\boldsymbol{g}}_i^2 \\ \vdots \\ \hat{\boldsymbol{g}}_i^{N_{dwi}} \end{bmatrix} \text{ and } \boldsymbol{A} = \begin{bmatrix} \boldsymbol{A}^1 & \boldsymbol{A}^2 & \cdots & \boldsymbol{A}^{N_{dwi}} \end{bmatrix} \end{aligned} \tag{2.80}$$

where $\boldsymbol{A}^T$ represents the transpose of the matrix $\boldsymbol{A}$ and $\left(\boldsymbol{A}^T \cdot \boldsymbol{A}\right)^{-1} \cdot \boldsymbol{A}^T$ represents its pseudo-inverse.

Fig.2.30(a) shows the B-mode image obtained using coded STA in the Field II simulation environment [Jensen and Svendsen, 1992, Jensen, 1996]. It can be seen, that when compared to classical STA (Fig.2.30(b)), no difference between the two obtained B-mode images can be assessed. This results

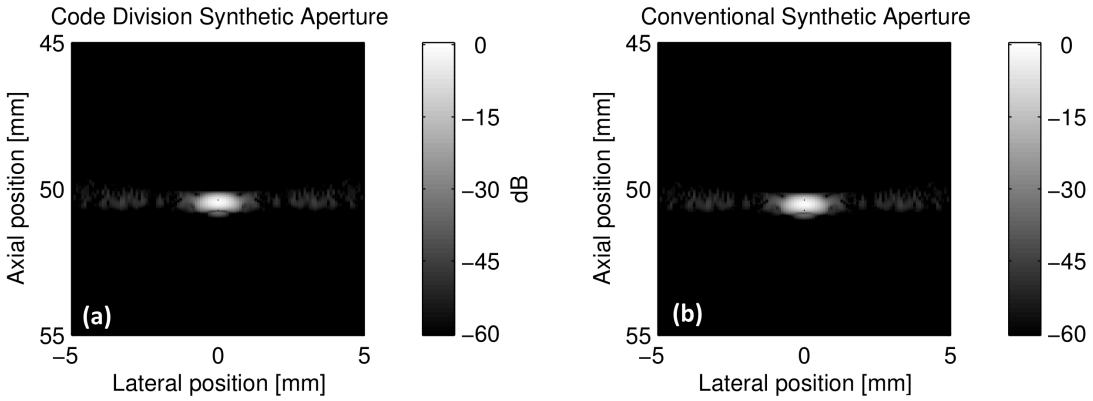

Figure 2.30: B-mode images obtained using: (a) - Coded STA, (b) - Classical STA (with a Dirac delta function as excitation signal). This is a faithful reproduction of the Fig.4 published in [Gran et al., 2004]

from the fact, that as previously explained, coded STA allows estimating the RF data that one would obtain if Dirac impulsions were used as excitation in conventional STA. Finally, as N_{dwi} diverging waves are emitted simultaneously and their echoes are separated in reception using MLE, this means that theoretically, coded STA increases the FAR by a factor of N_{dwi} (when compared to conventional STA). However, as shown in this Chapter, the $eSNR$ of the STA techniques (DWI) is the lowest compared with other imaging approaches (e. g. focused and plane wave ultrasound). Is this very method stable to such high amount of noises? Can this method be applied on other types of acquisition schemes other than STA? What are the hypothesis that need to be made in order for this method to work well? How to chose the excitation signals? Can it be implemented on a ultrasound scanner? At this point, in order to answer all these questions, a more in-depth study of the method needs to be made.

Summary

In this Chapter, the principle of acoustic wave propagation was detailed. The hypothesis on which conventional ultrasound imaging methods rely were presented, and the corresponding models were built for each one of the conventional acquisition schemes. Furthermore, the evolution of the provided image quality as a function of the acquisition time was depicted and the deep-rooted trade-off between image quality and frame rate was underlined. The different types of excitation signals coupled with the corresponding filtering techniques and provided advantages was shown. Their impact on the ultrasound image quality was discussed. Finally, it was shown how these specific excitation signals can be used in an imaging approach that theoretically can provide a boost in frame acquisition rate. This state of the art method relies on simultaneous STA emissions and echo separation using inverse problem approaches. However, despite its theoretical appeal, this method was not completely validated and a more detailed study needs to be made in order to perceive its limits. This will be done in the next Chapter, by addressing its compatibility with a plane wave acquisition scheme. The choice of the PWI over the FUI as an acquisition scheme comes from the fact that for each firing, PWI provides full images of the medium which compounded give a comparable to FUI image quality while using less firings (Subsection 2.2.2).

3 Simultaneous Coded Ultrasound Imaging: Estimation of the Pulse-Echo Impulse Response of the Tissue

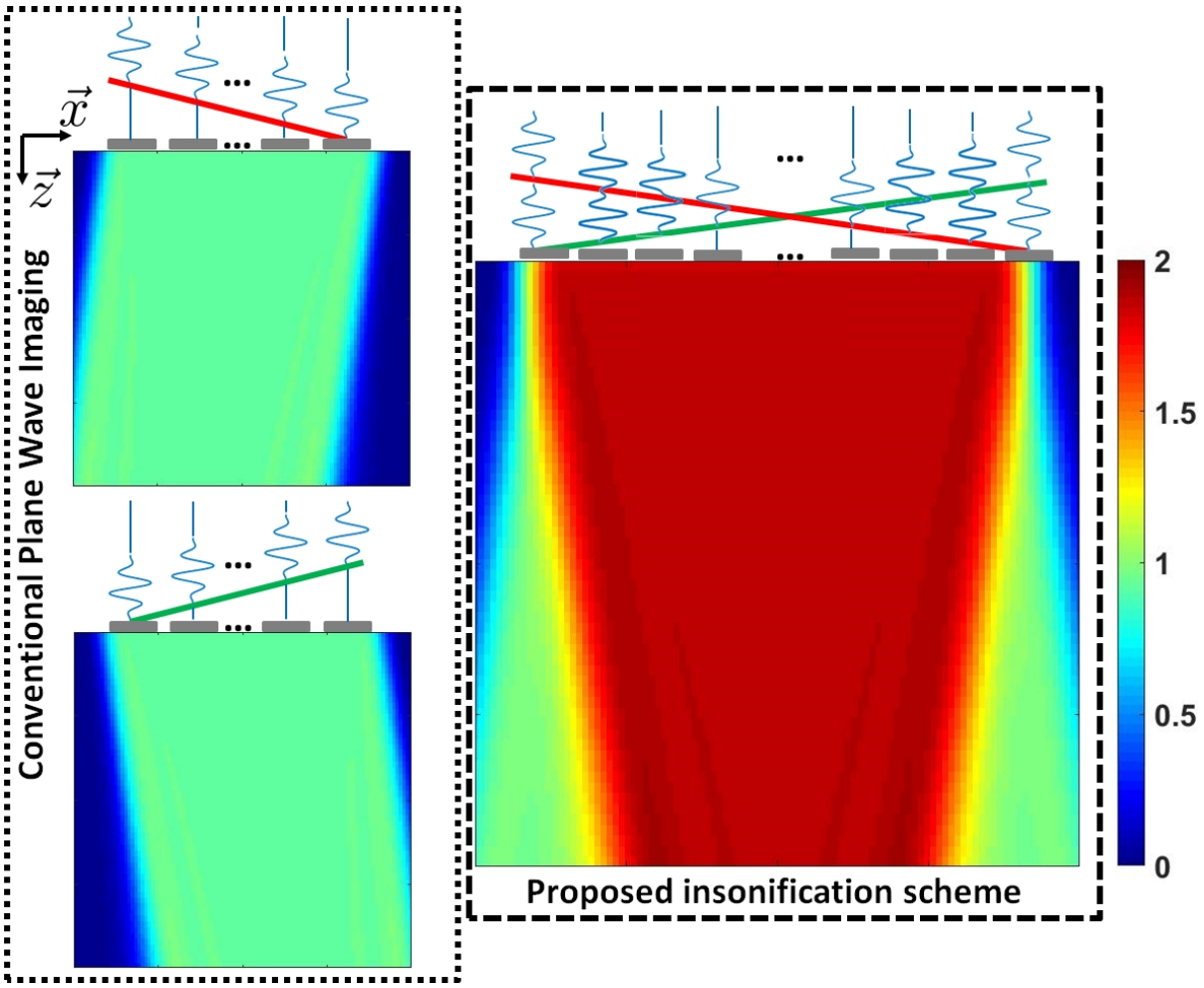

Figure 3.1: Representation of the proposed emission scheme. Whereas for conventional plane wave imaging (dotted canvas), each plane wave (corresponding to the red and green emission delay laws) is emitted successively, the solution proposed here (dashed canvas) consists in simultaneous emission of the plane waves. The colormap represents the root mean square of the pressure fields generated by the different emissions.

In this Chapter, a method that has the potential to increase the frame acquisition rate of the conventional plane wave imaging approach is detailed. The synopsis of the proposed solution is shown in

Fig.3.1. As it can be observed, whereas in conventional plane wave imaging (dotted canvas), each plane wave (corresponding to the red and green emission delay laws) is emitted successively, the solution proposed here (dashed canvas) employs simultaneous emission of the plane waves. This means that each scatterer of the medium is insonified at the same time by two wavefronts (red and green), implying that it generates a backscattered wave that is a mix of echoes the same scatterer would generate if each plane wave was emitted successively. The inherent problem, of separating the mix of echoes inside the received data in order to discriminate the contribution of each plane wave, is addressed. First, the direct model that allows writing the received backscattered echoes as a function of the emitted signals and the pulse echo impulse responses of the medium to each plane wave is built. Second, relying on the built direct model, a method that allows estimating the pulse echo impulse responses of the medium from the received data is proposed. The impact of the different modeling parameters on the estimation is also studied. Two hypothesis are stated:

H3.1 The "Blind" and "Perturbation" zones[1] are completely anechoic

H3.2 No acquisition noise is superposed to the RF data.

The performance of the method when these hypothesis are verified and violated is addressed. Furthermore, simulation and in vitro acquisition results are shown and discussed. Finally, the advantages and the drawbacks of the proposed method are underlined.

To be noted that in this Chapter the only emission type studied is "plane wave" thus the equations derived in Section 2.2.2 will be developed however, for simplicity sake, the PWI prescript notation is dropped.

This work is an extension of the idea presented in [Pages et al., 2015], and was published in [Bujoreanu et al., 2017b, Bujoreanu et al., 2017a, Bujoreanu et al., 2017c].

3.1 One plane wave insonification

Before going into the details of the direct model for simultaneous emission of plane waves (dashed canvas in Fig. 3.1), let us first built the direct model for one plane wave emission. Consider the transmission scheme presented in Fig. 3.2(a). As it was shown in Section 2.2.2 (relation (2.53)), in order to emit a plane wave in the direction k, the excitation signals at each element j of the probe need to be generated as follows:

$$\begin{gathered} a_j^k(t) = a^k(t) *_t \delta\left(t - t_j^k\right) = a_j^k\left(t - t_j^k\right) \\ \text{with: } t_j^k = (j-1)\wp\frac{\tan(\theta^k)}{c_m} \end{gathered} \tag{3.1}$$

Resuming the calculations shown in Section 2.2.2, the received echoes at each element i (noiseless acquisition) of the probe can be written as:

$$\begin{gathered} y_i^k(t) = a^k(t) *_t g_i^k(t) \\ \text{with: } g_i^k(t) = w_i h(t) *_t h(t) *_t \sum_{j=1}^{N_{el}} \left[w_j \delta(t - t_j^k) *_t \int_V \gamma(\vec{r}) g_{ji}(\vec{r}, t)\, \mathrm{d}^2\vec{r} \right] \end{gathered} \tag{3.2}$$

In (3.2), it can be seen that the signal $g_i^k(t)$ corresponds perfectly to the signal ${}_{PWI}y_i^k(t)$ (in (2.54), if the emitted signal was a short impulsion $a^k(t) = \delta(t)$). Thus $g_i^k(t)$ can be called the pulse echo

[1] The definition of this regions will be introduced later in this Chapter

impulse response of the medium, seen by the i^{th} element of the probe, when the k^{th} wave is emitted. In other words, $g_i^k(t)$ are the signals that probe elements i would receive if the k^{th} emitted plane wave carried a short impulsion. Since, as previously shown in Section 2.3, the beamforming of such signals will provide the best image quality, the main idea behind the proposed approach is to emit arbitrary waveforms $a^k(t)$ then, from the received signals $y_i^k(t)$ (3.2), to estimate $g_i^k(t)$ and beamform the B-mode image $\boldsymbol{\gamma}^k$ using DAS (2.36).

Upon reception, the received signals are sampled at a frequency ν_s, thus (3.2) can be written in its discrete time form as:

$$\boldsymbol{y}_i^k = \boldsymbol{a}^k *_t \boldsymbol{g}_i^k \tag{3.3}$$

Since the signal $\boldsymbol{y}_i^k$ is sampled at the frequency ν_s, it results that the vectors $\boldsymbol{a}^k$ (of length N_a) and $\boldsymbol{g}_i^k$

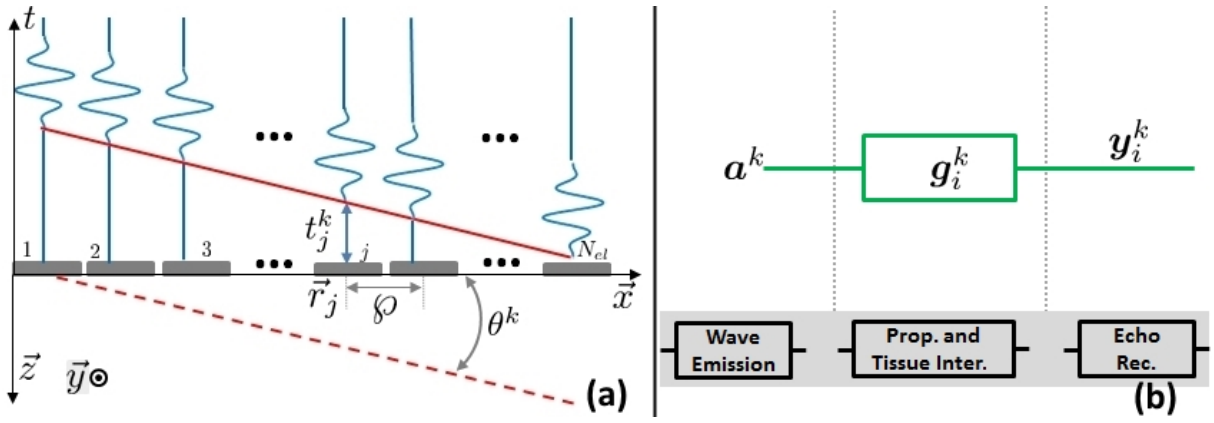

Figure 3.2: Principle of conventional plane wave imaging: (a) - Ultrasound probe excited with sinusoid signals $a^k(t)$, delayed at the j^{th} element with a duration t_j^k in order to emit a plane wave in the direction θ^k. The solid red line represents the evolution of t_j^k as a function of j and the dashed red line represents the emitted wavefront. (b) - The direct model built for a single plane insonification. It can be seen that the "Wave Emission" is modeled only by the excitation signal waveform $\boldsymbol{a}^k$. The "Propagation and Tissue Interaction" is modeled by the pulse echo impulse response of the medium to the plane wave k, seen by the element i of the probe $\boldsymbol{g}_i^k$. The signal recorded at the i^{th} element of the probe, in a noiseless acquisition case, $\boldsymbol{y}_i$ is modeled as the convolution between the excitation waveform $\boldsymbol{a}^k$ and the pulse echo impulse response $\boldsymbol{g}_i^k$ of the medium to the plane wave k.

are also discrete time equivalents of the corresponding signals $a(t)$ and $g_i^k(t)$ respectively. The one dimensional vector $\boldsymbol{y}_i^k$ (of length N_y) is obtained by starting sampling the signal $y_i^k(t)$ at a given time t_0. Thus the n^{th} sample of $y_i^k(t)$ can be expressed as follows: $\boldsymbol{y}_i^k[n] = y_i^k(t_0 + n/\nu_s)$. Suppose, for a moment, that the emitted signal and the acousto-electrical impulse response of the ultrasound probe are Dirac impulsions and that $w_j = w_i = 1$. Thus, from (3.3) and (2.32), one can deduce that:

$$\begin{cases} y_i^k(t_0) = \sum_{j=1}^{N_{el}} \left[\int_V \gamma(\vec{r}) \dfrac{S^2 \delta\left(t_0 - t_j^k - \frac{\|\vec{r}-\vec{r}_j\|_2 + \|\vec{r}-\vec{r}_i\|_2}{c_m}\right)}{4\pi^2 \|\vec{r}-\vec{r}_j\|_2 \|\vec{r}-\vec{r}_i\|_2} \mathrm{d}^2\vec{r} \right] \\ y_i^k(t_0 + \frac{N_y-1}{\nu_s}) = \sum_{j=1}^{N_{el}} \left[\int_V \gamma(\vec{r}) \dfrac{S^2 \delta\left(t_0 + \frac{N_y-1}{\nu_s} - t_j^k - \frac{\|\vec{r}-\vec{r}_j\|_2 + \|\vec{r}-\vec{r}_i\|_2}{c_m}\right)}{4\pi^2 \|\vec{r}-\vec{r}_j\|_2 \|\vec{r}-\vec{r}_i\|_2} \mathrm{d}^2\vec{r} \right] \end{cases} \iff \tag{3.4}$$

$$\begin{cases} t_0 = t_j^k + \frac{\|\vec{r}_0-\vec{r}_j\|_2 + \|\vec{r}_0-\vec{r}_i\|_2}{c_m} \\ t_0 + \frac{N_y-1}{\nu_s} = t_j^k + \frac{\|\vec{r}_{N_y}-\vec{r}_j\|_2 + \|\vec{r}_{N_y}-\vec{r}_i\|_2}{c_m} \end{cases} \iff \begin{cases} t_0 = t_j^k + \frac{\|\vec{r}_0-\vec{r}_j\|_2 + \|\vec{r}_0-\vec{r}_i\|_2}{c_m} \\ \frac{N_y-1}{\nu_s} = \frac{\|\vec{r}_{N_y}-\vec{r}_j\|_2 + \|\vec{r}_{N_y}-\vec{r}_i\|_2}{c_m} - \frac{\|\vec{r}_0-\vec{r}_j\|_2 + \|\vec{r}_0-\vec{r}_i\|_2}{c_m} \end{cases}$$

where $\vec{r}_0$ and $\vec{r}_{N_y}$ represent the positions of the scatterers that generate an echo which arrives at time t_0 and $t_0 + (N_y - 1)/v_s$ respectively. From (3.4) one can deduce two consequences. The first one, is related to the recording start time t_0 and implies that if one starts to record data at higher t_0, the first observed echoes would be generated at higher[2] distance from the probe element i. The second consequence of (3.4), this time related to the length N_y of the recorded signals $\boldsymbol{y}_i^k$, implies that longer are these signals, further from the probe element i are placed the scatterers whose echoes are recorded. In conclusion, it can be deduced that, by carefully tuning t_0 and N_y one can chose a certain field of view inside the imaged medium (ROI).

Fig. 3.3 shows a graphical representation of the convolution product (3.2). As one can observe in the left side of the figure, the fact that the recording of the backscattered echoes starts with the sample $n_0 = t_0/v_s$ implies that the echoes generated between the $\boldsymbol{g}_i^k$ samples $(n_0 - N_a)$ and $(n_0 - 1)$ are recorded partially (segments colored in red in Fig.3.3), and the echoes generated before the sample $(n_0 - N_a)$ are not even recorded (segments colored in violet in Fig.3.3). This effect in ultrasound is called "Blind zone" (echoes colored in red[3] in Fig. 3.3) and can have a negative effect on the method output. For instance, if $\boldsymbol{a}^k$ was a chirp or a BPSK modulated sequence, the output of the compression filter would not be optimal in this zone since the missing parts of the echoes does not allow to reach the maximum of the autocorrelation function. Furthermore, in Fig. 3.3 it can be seen that the echoes generated between the impulse response samples n_0 and $(n_f - N_a)$ (colored in green) fall entirely between the recorded samples (n_0 to n_f) of the RF data $\boldsymbol{y}_i^k$. This represents the "Full echo recording zone" (colored in green) and, as it can be seen in Fig. 3.3, as long as the recorded signal is longer than the excitation waveform $(N_y > N_a)$, at least one full echo will be completely recorded in this zone. Finally, towards the end of the RF data recording (from $(n_f - N_a)$ to n_f), the received echoes are again recorded partially generating what it will be called from now on the "Perturbation zone" (colored in blue). Similar to the "Blind zone", a potential pulse compression filter applied in such zone would not yield optimal results.

In Fig. 3.3 one can identify that the transformation matrix, that allows passing from the $\boldsymbol{g}_i^k$ to the $\boldsymbol{y}_i^k$ samples respectively, is a circulant matrix $\boldsymbol{A}^k$ generated using the excitation signal $\boldsymbol{a}^k$. As it can be seen in here, the number of lines of the matrix $\boldsymbol{A}^k$ is set by the number of recorded samples N_y. The number of its columns, however, is given by the amount of $\boldsymbol{g}_i^k$ samples that impact $\boldsymbol{y}_i^k$ between n_0 and n_f. In Fig. 3.3, it can be seen that the echoes that are recorded between the n_0 and n_f samples of the received signal, are generated between the $(n_0 - N_a)$ and n_f samples of the pulse echo impulse response. Thus, the total number of columns in the matrix A^k is $n_f - (n_0 - N_a) = n_0 + N_y - 1 - n_0 + N_a = N_y + N_a - 1$. Therefore $\boldsymbol{A}^k$ can be written as:

$$\boldsymbol{A}^k = \begin{bmatrix} \boldsymbol{a}^k[N_a-1] & \boldsymbol{a}^k[N_a-2] & \cdots & \boldsymbol{a}^k[0] & 0 & \cdots & 0 & 0 & \cdots & 0 \\ 0 & \boldsymbol{a}^k[N_a-1] & \cdots & \boldsymbol{a}^k[1] & \boldsymbol{a}^k[0] & \cdots & 0 & 0 & \cdots & 0 \\ \vdots & \vdots & \ddots & \vdots & \vdots & \ddots & \vdots & \vdots & \ddots & \vdots \\ 0 & 0 & \cdots & \boldsymbol{a}^k[N_a-1] & \boldsymbol{a}^k[N_a-2] & \ddots & \boldsymbol{a}^k[0] & 0 & \cdots & 0 \\ 0 & 0 & \cdots & 0 & \boldsymbol{a}^k[N_a-1] & \ddots & \boldsymbol{a}^k[1] & \boldsymbol{a}^k[0] & \cdots & 0 \\ \vdots & \vdots & \ddots & \vdots & \vdots & \ddots & \vdots & \vdots & \ddots & \vdots \\ 0 & 0 & \cdots & 0 & 0 & \ddots & \boldsymbol{a}^k[N_a-1] & \boldsymbol{a}^k[N_a-2] & \cdots & \boldsymbol{a}^k[0] \end{bmatrix} \tag{3.5}$$

What the previous reasoning shows, is that the N_y – long recorded signal $\boldsymbol{y}_i^k$ in (3.3) can be written as a product between a $N_y \times (N_y + N_a - 1)$ circulant matrix $\boldsymbol{A}^k$ and a $(N_y + N_a - 1)$ – long pulse echo

[2] In the context of Born approximation made in Section 2.1.2, the reverberation artifacts are ignored.

[3] The colors of the "Blind", "Full echo recording" and "Perturbation" zones (that represent groups of echoes recorded partially / completely) should not be confused with the colors of plane waves (that represent the processing pipe followed by a plane wave in the model) displayed in Fig. 3.2(b), Fig. 3.4(b) and Fig. 3.5

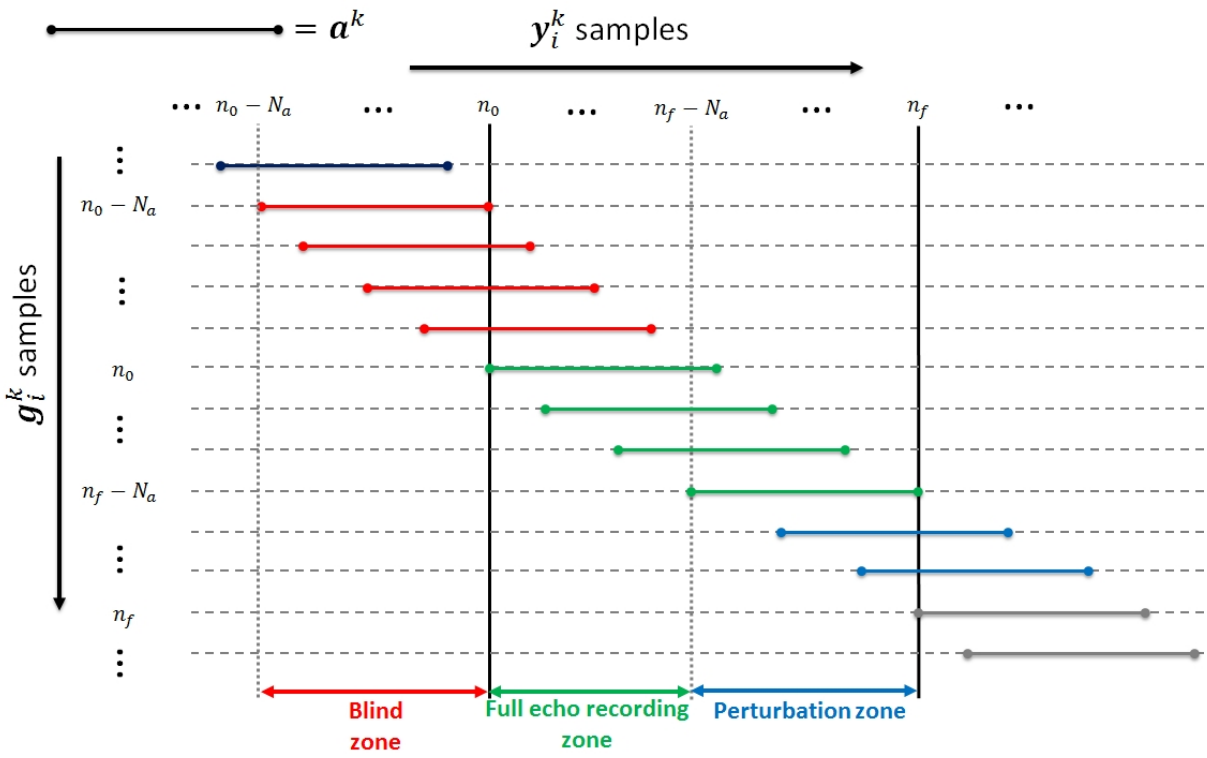

Figure 3.3: Schematic representation of the convolution product between the signal $\boldsymbol{a}^k$ and the vector $\boldsymbol{g}_i^k$. Vertically are aligned the samples of the pulse echo impulse response $\boldsymbol{g}_i^k$ and horizontally are aligned the samples of the received signal $\boldsymbol{y}_i^k$. $n_0 = t_0/\nu_s$ is the sample at which the received echoes $\boldsymbol{y}_i^k$ start to be recorded. $n_f = n_0 + N_y - 1$ is the last recorded sample of the signal $\boldsymbol{y}_i^k$. The multicolor line segments represent the echoes (of identical waveform as the excitation signal $\boldsymbol{a}^k$) generated at each sample of $\boldsymbol{g}_i^k$, the color showing the association of the echo to one of the three zones: "Blind" (red), "Full echo recording" (green) and "Perturbation" (blue).

impulse response $\boldsymbol{g}_i^k$:

$$\boldsymbol{y}_i^k = \boldsymbol{A}^k \cdot \boldsymbol{g}_i^k \tag{3.6}$$

3.2 Simultaneous plane wave insonification

From (3.6), one can deduce the signals $\mathbf{g}_i^k(t)$. However as shown in Section 2.2.2, beamforming the backscattered echoes from only one plane wave insonification is not sufficient in order to achieve good image quality. Successive emissions and then compounding seem at first a fitting solution. Nonetheless, as previously stated in Section 2.2.2, successive emissions reduce the method FAR. Therefore, a more efficient way of emitting the plane waves is required. Similar to modified STA, where distinct probe elements are emitting synchronously ultrasound waves (described in Section 2.4), the main idea of the proposed approach consists in the simultaneous emission of plane waves.

Suppose the ultrasound probe represented in Fig. 3.4(a). In the previous section it was shown that in order to emit a plane wave in the direction θ^k, each element j of the probe needs to emit an excitation signal $a^k(t)$ delayed with a lag t_j^k. Assuming that the superposition of multiple pressure fields (generated by each simultaneously emitted plane wave) does not violate the hypothesis made in (A.1) of Section 8.1 (the pressure and density field variations generated by the wave superposition are much smaller than the steady state values of these fields), it can be concluded that the excitation signal required in order to emit simultaneously N_{pwi} represents the linear superposition of each N_{pwi}

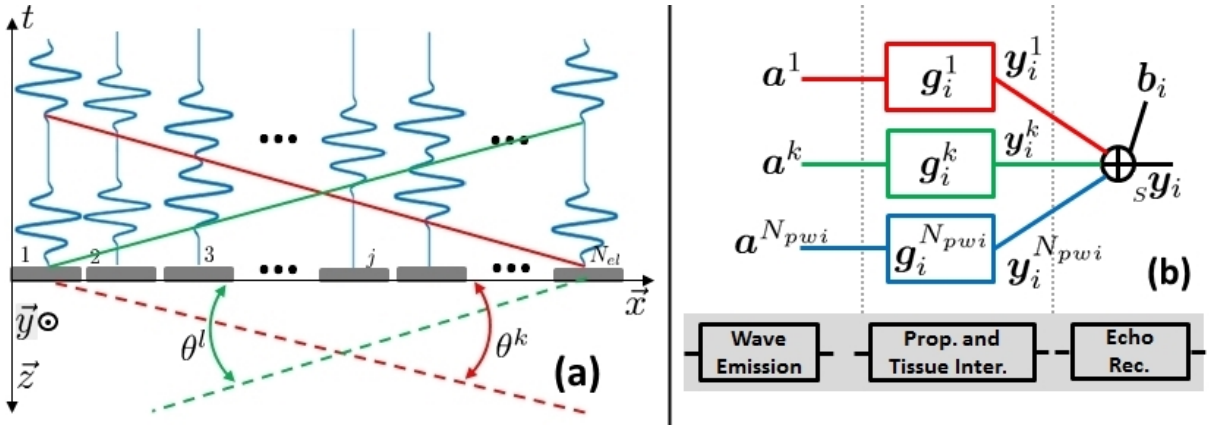

Figure 3.4: Principle of simultaneous emission of plane wave: (a) - The ultrasound probe is excited with a superposition of excitations signals that one would use in order to emit each plane wave successively. Here an example of simultaneous emission of two plane waves is displayed. The excitation delays that follow the solid red line produce a wavefront that propagates in the direction θ^k and the delays that follow the solid green line generate a wavefront that propagates in the direction θ^l. (b) - The direct model built for the simultaneous emission of N_{pwi} plane waves. It can be seen that for each plane wave k, the "Wave Emission" and "Propagation and Tissue Interaction" blocks are modeled identically as in Fig. 3.2(b). The simultaneous "feature" of the method appears in the modeling of the "Echo Reception" block. This layer represents the total received signal ${}_S\boldsymbol{y}_i$ as a linear superposition of the signals $\boldsymbol{y}_i^k$ that one would receive if each plane wave was emitted successively. $\boldsymbol{b}_i$ represents an additive acquisition noise. Here, each color (except black), highlights the pipeline followed by a specific plane wave: $k=1 \Longleftrightarrow$ red, $k \Longleftrightarrow$ green and $k=N_{pwi} \Longleftrightarrow$ blue.

excitation signals for each plane wave. Thus:

$$ {}_Sa_j(t) = \sum_{k=1}^{N_{pwi}} a_j^k(t) = \sum_{k=1}^{N_{pwi}} a^k(t-t_j^k) \tag{3.7} $$

The excitation signals, used in the case where only two plane waves are emitted simultaneously, are schematically represented in Fig. 3.4(a). At this point, by combining the definition of the excitation signals (3.7) with the general expression of the received echoes (2.33), one can deduce the relation that links the RF data (in the case of simultaneous coded emission) to the N_{pwi} excitation signals $a^k(t)$ and to the N_{pwi} pulse echo impulse responses of the medium $g_i^k(t)$:

$$ \begin{aligned} {}_Sy_i(t) &= w_i \sum_{j=1}^{N_{el}} \left[w_j h(t) *_t {}_Sa_j(t) *_t h(t) *_t \int_V \gamma(\vec{r}) g_{ji}(\vec{r},t)\, \mathrm{d}^2\vec{r} \right] + b_i(t) \underset{\text{Using (3.2)}}{\Longleftrightarrow} \\ {}_Sy_i(t) &= \sum_{k=1}^{N_{pwi}} a^k(t) *_t g_i^k(t) + b_i(t) = \sum_{k=1}^{N_{pwi}} y_i^k(t) + b_i(t) \end{aligned} \tag{3.8} $$

where $b_i(t)$ is the acquisition noise superposed to the echoes on the i^{th} element of the probe. It can be observed in (3.8) that the total received echoes ${}_Sy_i(t)$ are a superposition of the signals that one would receive if each plane wave was emitted successively. In its discrete time form, (3.8) becomes:

$$ {}_S\boldsymbol{y}_i = \sum_{k=1}^{N_{pwi}} \boldsymbol{y}_i^k + \boldsymbol{b}_i = \sum_{k=1}^{N_{pwi}} \boldsymbol{A}^k \cdot \boldsymbol{g}_i^k + \boldsymbol{b}_i \tag{3.9} $$

where $\boldsymbol{b}_i$ is the noise vector of length equal to the one of ${}_S\boldsymbol{y}_i$ (and thus of $\boldsymbol{y}_i^k$) which is N_y. A schematic representation of (3.9) is shown in Fig. 3.4(b). As it can be seen here, the simultaneous "feature" of

the emission is modeled in the "Echo Reception" block, which models the total received signal ${}_S\boldsymbol{y}_i$ as a linear superposition of the signals $\boldsymbol{y}_i^k$ (modeled in Fig. 3.2(b)) that one would receive if each plane wave was emitted successively. Relying on the properties of the matrix product, (3.9) can be written as follows:

$$
\begin{gathered}
{}_S\boldsymbol{y}_i = \boldsymbol{A}\cdot\boldsymbol{g}_i + \boldsymbol{b}_i \\
\text{with: } \boldsymbol{A} = \begin{bmatrix} \boldsymbol{A}^1 & \boldsymbol{A}^2 & \cdots & \boldsymbol{A}^{N_{pwi}} \end{bmatrix} \text{ and } \boldsymbol{g}_i = \begin{bmatrix} \boldsymbol{g}_i^1 \\ \boldsymbol{g}_i^2 \\ \vdots \\ \boldsymbol{g}_i^{N_{pwi}} \end{bmatrix}
\end{gathered}
\tag{3.10}
$$

In (3.10), the size of the $\boldsymbol{A}$ matrix and of the $\boldsymbol{g}_i$ vector can be derived from the sizes of $\boldsymbol{A}^k$ and $\boldsymbol{g}_i^k$ respectively. Thus, it can be deduced that the total matrix $\boldsymbol{A}$ of the direct model has N_y rows and $N_{pwi}(N_y+N_a-1)$ columns and that the vector $\boldsymbol{g}_i$ has $N_{pwi}(N_y+N_a-1)$ samples.

3.3 Statement of the inverse problem

In the previous section was built a direct model that links, in the case of the simultaneous plane wave emission, the received backscattered echoes to the emitted waveforms and to the impulse responses of the medium to each of the plane wave. The objective here is to present how to separate, using the generated direct model, the pulse-echo impulse response of the medium to each of the plane waves. Thus, in this very section is detailed the "Image Reconstruction" block displayed in Fig.3.5.

As it can be seen in Fig. 3.5, the "Image Reconstruction" block takes as inputs the recorded RF data that contains N_{el} vectors ${}_S\boldsymbol{y}_i$. We showed in Section 3.2 that (summarized in Fig. 3.4(b) and relation (3.10)), in the case of simultaneous emission of plane waves, the received echoes can be written as a linear superposition of the echoes that the probe would receive if each plane wave was emitted successively. In order to separate the contribution of each plane wave inside these signals (${}_S\boldsymbol{y}_i$), in the proposed method, the "Estimation" step ("Est." in Fig. 3.5) is implemented. After the separate estimation of N_{el} vectors $\hat{\boldsymbol{g}}_i$, the relation (3.10) can be used in order to find each pulse-echo impulse response of the medium. Thus, it can be seen that by splitting the N_{el} vectors $\hat{\boldsymbol{g}}_i$ in N_{el} sets of N_{pwi} vectors, each signal $\hat{\boldsymbol{g}}_i^k$ can be isolated. At this point the contribution of each plane wave k (represented by different colors in Fig. 3.5), at each element i of the probe, can be separated and used as an input for a DAS algorithm in order to find a low quality image of the TRF $\boldsymbol{\gamma}^k$. As seen in Section 2.2.2, the N_{pwi} images $\boldsymbol{\gamma}^k$ can be then coherently added in order to obtain an improved final image $\boldsymbol{\gamma}$.

3.3.1 The estimation layer

In the above detailed pipeline, one can observe that, once the N_{el} sets of N_{pwi} vectors $\hat{\boldsymbol{g}}_i^k$ are isolated, the proposed processing follows the same path as the classical plane wave imaging. Thus, the most important actor of the proposed "Image Reconstruction" block, is the "Estimation" layer. Consider now the relation (3.10). Here, one can see that, by applying a simple matrix multiplication to the left and right equation sides, the following relation can be deduced:

$$
\boldsymbol{A}^T\,{}_S\boldsymbol{y}_i = \boldsymbol{A}^T\cdot\boldsymbol{A}\cdot\boldsymbol{g}_i + \boldsymbol{A}^T\cdot\boldsymbol{b}_i \tag{3.11}
$$

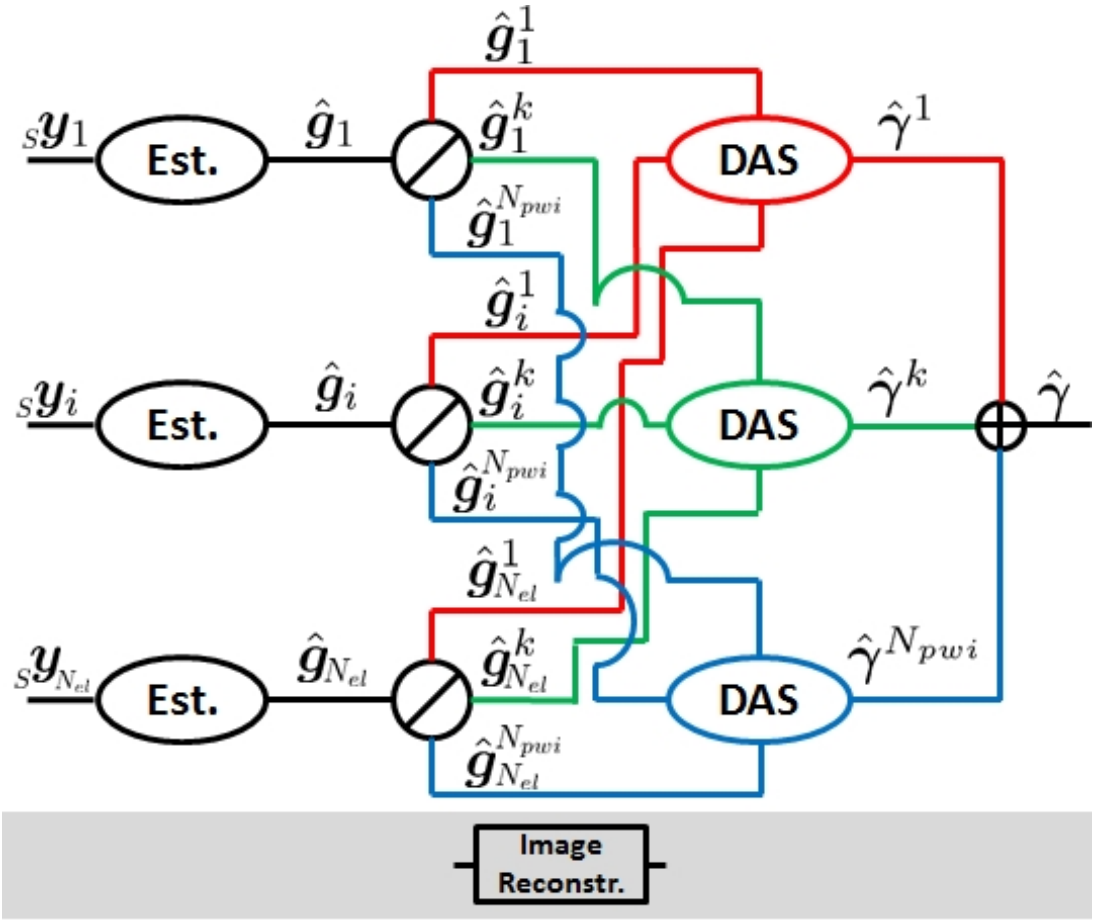

Figure 3.5: The "Image Reconstruction" block of the proposed imaging approach. Once the received RF data ${}_S\boldsymbol{y}_i$ is recorded (after simultaneous plane wave emission), the signal received by each element of the probe is passed through a step that allows separating the echoes for each plane wave ("Est."). After this estimation step, each of the N_{el} vectors $\boldsymbol{g}_i$ is split ($\oslash$) in N_{pwi} vectors $\boldsymbol{g}_i^k$ (represented in different colors) that represent the pulse echo impulse response of the medium to the plane wave k, seen by the element i of the probe. The N_{pwi} sets of N_{el} vectors $\boldsymbol{g}_i^k$ are passed through the DAS algorithm in order to reconstruct the corresponding low quality image $\boldsymbol{\gamma}^k$. Finally, the N_{pwi} images $\boldsymbol{\gamma}^k$ are coherently added and the final, improved image $\boldsymbol{\gamma}$ is obtained. Here, each color (except black), highlights the pipeline followed by a specific plane wave: $k=1 \Longleftrightarrow$ red, $k \Longleftrightarrow$ green and $k=N_{pwi} \Longleftrightarrow$ blue.

Finally, one can multiply again the right part of the relation and the left one, this time with the term $(\boldsymbol{A}^T \cdot \boldsymbol{A})^{-1}$:

$$\begin{gathered} \hat{\boldsymbol{g}}_i = (\boldsymbol{A}^T \cdot \boldsymbol{A})^{-1} \cdot \boldsymbol{A}^T \cdot \boldsymbol{A} \cdot \boldsymbol{g}_i + (\boldsymbol{A}^T \cdot \boldsymbol{A})^{-1} \cdot \boldsymbol{A}^T \cdot \boldsymbol{b}_i \\ \text{where: } \hat{\boldsymbol{g}}_i = (\boldsymbol{A}^T \cdot \boldsymbol{A})^{-1} \cdot \boldsymbol{A}^T \cdot {}_S\boldsymbol{y}_i \end{gathered} \tag{3.12}$$

The previous relation represents the conventional estimator used in order to minimize the least square error on the data term $\| {}_S\boldsymbol{y}_i - \boldsymbol{A} \cdot \boldsymbol{g}_i \|_2^2$ [Beck and Teboulle, 2009]. Here it can be seen that, if the inverse matrix $(\boldsymbol{A}^T \cdot \boldsymbol{A})^{-1}$ exists, then $(\boldsymbol{A}^T \cdot \boldsymbol{A})^{-1} \cdot \boldsymbol{A}^T \cdot \boldsymbol{A} = \boldsymbol{I}$ (where $\boldsymbol{I}$ is the identity matrix). Thereby, if the acquisition noise $\boldsymbol{b}_i$ is null, then the signal $\hat{\boldsymbol{g}}_i$ corresponds perfectly to $\boldsymbol{g}_i$. In all other cases, where $\boldsymbol{b}_i$ is not null, $\hat{\boldsymbol{g}}_i$ is degraded but, represents the best estimation of the $\boldsymbol{g}_i$ that minimizes the term $\| \hat{\boldsymbol{g}}_i - \boldsymbol{g}_i \|_2$ [Quarteroni et al., 2008]. Thus, for now on in this Chapter, $\hat{\boldsymbol{g}}_i$ will be referred to as the estimation of the vector $\boldsymbol{g}_i$, that contains N_{pwi} estimations $\hat{\boldsymbol{g}}_i^k$ of the corresponding vectors $\boldsymbol{g}_i^k$. As it can be deduced from (3.12), the process that allows to pass from the RF data ${}_S\boldsymbol{y}_i$ to the vectors $\hat{\boldsymbol{g}}_i$ is a matrix

multiplication with the term $(\boldsymbol{A}^T \cdot \boldsymbol{A})^{-1} \cdot \boldsymbol{A}^T$. Thus, this term, also called matrix $\boldsymbol{A}$ pseudo-inverse, represents the "Estimation" block: $Est. \equiv (\boldsymbol{A}^T \cdot \boldsymbol{A})^{-1} \cdot \boldsymbol{A}^T$.

In order to predict the behavior of the proposed estimator as a function of the different modeling parameters (e. g. excitation signals, recording time, acquisition noise etc), it would be more pertinent to analyze the direct kernel $\boldsymbol{A}$. In order to better understand the properties of this matrix, one can analyze its singular value decomposition, defined as follows:

$$\boldsymbol{A} = \boldsymbol{U} \cdot \boldsymbol{S} \cdot \boldsymbol{V}^T \tag{3.13}$$

where $\boldsymbol{U}$ and $\boldsymbol{V}$ are two orthonormal matrices of sizes $N_y \times N_y$ and $N_{pwi}(N_y+N_a-1) \times N_{pwi}(N_y+N_a-1)$ respectively. On the other hand, $\boldsymbol{S}$ is a diagonal matrix of size $N_y \times N_{pwi}(N_y+N_a-1)$ which contains as diagonal entries the singular values σ_i of $\boldsymbol{A}$. Thus the properties of the matrices $\boldsymbol{U}$, $\boldsymbol{V}$ and $\boldsymbol{S}$ can be written as:

$$\begin{gathered} \boldsymbol{U}_i \cdot \boldsymbol{U}_j = \begin{cases} 1, \text{ if } i = j \\ 0, \text{ if } i \neq j \end{cases} \quad \text{and } \boldsymbol{V}_i \cdot \boldsymbol{V}_j = \begin{cases} 1, \text{ if } i = j \\ 0, \text{ if } i \neq j \end{cases} \\ \boldsymbol{S} = \text{diag}\begin{bmatrix} \sigma_1 & \sigma_2 & \cdots & \sigma_{N_y} \end{bmatrix}, \text{ with: } \sigma_1 > \sigma_2 > \cdots > \sigma_{N_y} \end{gathered} \tag{3.14}$$

where $\boldsymbol{U}_i$, $\boldsymbol{V}_i$ represent the i^{th} columns of the matrices $\boldsymbol{U}$ and $\boldsymbol{V}$ respectively. There are exactly N_y singular values of $\boldsymbol{A}$ since this matrix has less rows than columns ($N_y < N_{pwi}(N_y + N_a - 1)$).

3.3.2 On the inverse problem condition number and the choice of the excitation signals

Assume now that one tries to solve (3.10) using (3.12). In (3.12) it can be seen that the estimation error made when computing $\hat{\boldsymbol{g}}_i$ depends on the term $(\boldsymbol{A}^T \cdot \boldsymbol{A})^{-1} \cdot \boldsymbol{A}^T \cdot \boldsymbol{b}_i$. In order to assess the impact of this very term on the solution $\hat{\boldsymbol{g}}_i$, one can study the properties of the matrix $(\boldsymbol{A}^T \cdot \boldsymbol{A})^{-1} \cdot \boldsymbol{A}^T$:

$$\begin{gathered} (\boldsymbol{A}^T \cdot \boldsymbol{A})^{-1} \cdot \boldsymbol{A}^T \underset{\text{Using 3.13, } \boldsymbol{U}^T \cdot \boldsymbol{U} = \boldsymbol{I}}{=} (\boldsymbol{V} \cdot \boldsymbol{S}^T \cdot \boldsymbol{S} \cdot \boldsymbol{V}^T)^{-1} \cdot \boldsymbol{V} \cdot \boldsymbol{S}^T \cdot \boldsymbol{U}^T \underset{\text{Using 3.14, } (\boldsymbol{V}^T)^{-1} = \boldsymbol{V} \text{ and } (\boldsymbol{V})^{-1} \cdot \boldsymbol{V} = \boldsymbol{I}}{\Longleftrightarrow} \\ (\boldsymbol{A}^T \cdot \boldsymbol{A})^{-1} \cdot \boldsymbol{A}^T = \boldsymbol{V} \cdot \boldsymbol{S}^{-1} \cdot \boldsymbol{U}^T \end{gathered} \tag{3.15}$$

where $\boldsymbol{I}$ is the identity matrix. From (3.12) and (3.15) it can be seen that even for a low noise $\boldsymbol{b}_i$, if the singular values σ_i are very low, their inversion (materialized in $\boldsymbol{S}^{-1} = \text{diag}\begin{bmatrix} \sigma_1^{-1} & \sigma_2^{-1} & \cdots & \sigma_{N_y}^{-1} \end{bmatrix}$) will amplify this noise thus impairing the estimation $\hat{\boldsymbol{g}}_i$. This effect can be quantified by the following relation [Quarteroni et al., 2008]:

$$\begin{gathered} \frac{1}{K(\boldsymbol{A})} \frac{\|\boldsymbol{b}_i\|_2}{\|_S \boldsymbol{y}_i\|_2} \leq \frac{\|\delta \hat{\boldsymbol{g}}_i\|_2}{\|\hat{\boldsymbol{g}}_i\|_2} \leq K(\boldsymbol{A}) \frac{\|\boldsymbol{b}_i\|_2}{\|_S \boldsymbol{y}_i\|_2} \\ \text{with: } K(\boldsymbol{A}) = \frac{\sigma_1}{\sigma_{N_y}} \end{gathered} \tag{3.16}$$

where $K(\boldsymbol{A})$ is called the condition number of the matrix $\boldsymbol{A}$. (3.16) shows that, if the condition number of the matrix $\boldsymbol{A}$ is very high then, even for small values of noise ($\|\boldsymbol{b}_i\|_2 << \|\boldsymbol{y}_i\|_2$), the variation ($\|\delta \hat{\boldsymbol{g}}_i\|_2$) on the estimated solution ($\hat{\boldsymbol{g}}_i$) can become very large. Thus, in order to stabilize the estimation with regards to noise, one needs to have a matrix $\boldsymbol{A}$ with a small condition number and, ideally, with $K(\boldsymbol{A}) = 1$. Assuming that $K(\boldsymbol{A}) = 1$ yields that $\sigma_i = 1$, $\forall i \in [1..N_y]$ and $\boldsymbol{U}, \boldsymbol{V} = \boldsymbol{I}$. In such hypothetical case, $\boldsymbol{A}^T \cdot \boldsymbol{A} = \boldsymbol{V} \cdot \boldsymbol{S}^T \cdot \boldsymbol{S} \cdot \boldsymbol{V}^T = \boldsymbol{S}^T \cdot \boldsymbol{S} = \boldsymbol{I}$. Given $\boldsymbol{A}$, constructed as shown in (3.10), the following equality

is obtained:

$$\boldsymbol{A}^T \cdot \boldsymbol{A} = \begin{bmatrix} (\boldsymbol{A}^1)^T \\ (\boldsymbol{A}^2)^T \\ \cdots \\ (\boldsymbol{A}^{N_{pwi}})^T \end{bmatrix} \cdot \begin{bmatrix} \boldsymbol{A}^1 & \boldsymbol{A}^2 & \cdots & \boldsymbol{A}^{N_{pwi}} \end{bmatrix} \Longleftrightarrow$$

$$\boldsymbol{A}^T \cdot \boldsymbol{A} = \begin{bmatrix} (\boldsymbol{A}^1)^T \boldsymbol{A}^1 & (\boldsymbol{A}^1)^T \boldsymbol{A}^2 & \cdots & (\boldsymbol{A}^1)^T \boldsymbol{A}^{N_{pwi}} \\ (\boldsymbol{A}^2)^T \boldsymbol{A}^1 & (\boldsymbol{A}^2)^T \boldsymbol{A}^2 & \cdots & (\boldsymbol{A}^2)^T \boldsymbol{A}^{N_{pwi}} \\ \vdots & \vdots & \ddots & \vdots \\ (\boldsymbol{A}^{N_{pwi}})^T \boldsymbol{A}^1 & (\boldsymbol{A}^{N_{pwi}})^T \boldsymbol{A}^2 & \cdots & (\boldsymbol{A}^{N_{pwi}})^T \boldsymbol{A}^{N_{pwi}} \end{bmatrix} = \begin{bmatrix} \boldsymbol{I} & \boldsymbol{0} & \cdots & \boldsymbol{0} \\ \boldsymbol{0} & \boldsymbol{I} & \cdots & \boldsymbol{0} \\ \vdots & \vdots & \ddots & \vdots \\ \boldsymbol{0} & \boldsymbol{0} & \cdots & \boldsymbol{I} \end{bmatrix} \tag{3.17}$$

where $\boldsymbol{0}$ represents the null matrix. (3.17) shows that, in order to have an ideal condition number of the direct model kernel $\boldsymbol{A}$, one needs to respect the following condition:

$$(\boldsymbol{A}^k)^T \cdot \boldsymbol{A}^q = \begin{cases} \boldsymbol{I}, \, k = q \\ \boldsymbol{0}, \, k \neq q \end{cases} \tag{3.18}$$

Combining the definition of the $\boldsymbol{A}$ matrix (3.5) with the relation (3.18), it can be deduced that:

$$\begin{cases} \begin{bmatrix} \boldsymbol{r}_{\boldsymbol{a}^k\boldsymbol{a}^k}[0] & \boldsymbol{r}_{\boldsymbol{a}^k\boldsymbol{a}^k}[1] & \cdots & \boldsymbol{r}_{\boldsymbol{a}^k\boldsymbol{a}^k}[N_y+N_a-1] \\ \boldsymbol{r}_{\boldsymbol{a}^k\boldsymbol{a}^k}[1] & \boldsymbol{r}_{\boldsymbol{a}^k\boldsymbol{a}^k}[0] & \cdots & \boldsymbol{r}_{\boldsymbol{a}^k\boldsymbol{a}^k}[N_y+N_a-2] \\ \vdots & \vdots & \ddots & \vdots \\ \boldsymbol{r}_{\boldsymbol{a}^k\boldsymbol{a}^k}[N_y+N_a-1] & \boldsymbol{r}_{\boldsymbol{a}^k\boldsymbol{a}^k}[N_y+N_a-2] & \cdots & \boldsymbol{r}_{\boldsymbol{a}^k\boldsymbol{a}^k}[0] \end{bmatrix} = \begin{bmatrix} 1 & 0 & \cdots & 0 \\ 0 & 1 & \cdots & 0 \\ \vdots & \vdots & \ddots & \vdots \\ 0 & 0 & \cdots & 1 \end{bmatrix} \\ \begin{bmatrix} \boldsymbol{r}_{\boldsymbol{a}^k\boldsymbol{a}^q}[0] & \boldsymbol{r}_{\boldsymbol{a}^k\boldsymbol{a}^q}[1] & \cdots & \boldsymbol{r}_{\boldsymbol{a}^k\boldsymbol{a}^q}[N_y+N_a-1] \\ \boldsymbol{r}_{\boldsymbol{a}^k\boldsymbol{a}^q}[1] & \boldsymbol{r}_{\boldsymbol{a}^k\boldsymbol{a}^q}[0] & \cdots & \boldsymbol{r}_{\boldsymbol{a}^k\boldsymbol{a}^q}[N_y+N_a-2] \\ \vdots & \vdots & \ddots & \vdots \\ \boldsymbol{r}_{\boldsymbol{a}^k\boldsymbol{a}^q}[N_y+N_a-1] & \boldsymbol{r}_{\boldsymbol{a}^k\boldsymbol{a}^q}[N_y+N_a-2] & \cdots & \boldsymbol{r}_{\boldsymbol{a}^q\boldsymbol{a}^k}[0] \end{bmatrix} = \begin{bmatrix} 0 & 0 & \cdots & 0 \\ 0 & 0 & \cdots & 0 \\ \vdots & \vdots & \ddots & \vdots \\ 0 & 0 & \cdots & 0 \end{bmatrix} \end{cases} \tag{3.19}$$

where $\boldsymbol{r}_{\boldsymbol{a}^k\boldsymbol{a}^q}$ represents the cross-correlation function between the signals $\boldsymbol{a}^k$ and $\boldsymbol{a}^q$ ($k \neq q$). In other words, (3.19) shows that, in order to have a kernel with low condition number, the cross-correlation between the N_{pwi} excitation signals must be very low ($\boldsymbol{r}_{\boldsymbol{a}^k\boldsymbol{a}^q}[n] \longrightarrow 0$, $\forall n \in \mathcal{N}$) and the auto-correlation of each excitation signal must contain a single non null value ($\boldsymbol{r}_{\boldsymbol{a}^k\boldsymbol{a}^k}[n] \longrightarrow 1$, for $n = 0$ and 0 otherwise). As shown in Section 2.3, the families of standalone BPSK modulated codes and FM signals (chirps) possess the previously listed properties. However, for this work, the family of BPSK modulated pseudo-orthogonal codes was picked. This choice was based purely on the fact that for the same duration and bandwidth, the number of orthogonal chirps (that provide the same resolution and compression lobes) is limited [Lashkari et al., 2016], whereas for pseudo-random sequences, this number grows exponentially with the length of the binary codes [Kettunen, 1997]. Thus, using the properties of the kernel $\boldsymbol{A}$, it was shown that the waveforms $a^k(t)$ that each plane wave k needs to carry must be BPSK modulated pseudo-random sequences. For the rest of this Chapter only such type of signals are studied.

3.3.3 On the inverse problem well-posedness and the size of the different vectors inside the model

Another impairing aspect of the direct model (3.10) is that the inverse problem is underdetermined, in other words, the system contains more unknowns ($\boldsymbol{g}_i$ samples) than equations ($_S\boldsymbol{y}_i$ samples).

This results in a flat matrix $\boldsymbol{A}$, that contains more columns ($N_{pwi}(N_y+N_a-1)$) than rows (N_y). The precursors of this effect are the $\boldsymbol{A}^k$ matrices, each of them being already flat (since $N_y < N_y+N_a-1$). In order to understand how the fact that $\boldsymbol{A}$ is flat affects the estimated solution, one needs first to define its null space: $\text{Null}(\boldsymbol{A}) = \{\boldsymbol{v} | \boldsymbol{A}\cdot\boldsymbol{v} = 0\}$. In other words, the null space of the matrix $\boldsymbol{A}$ represents the space generated by all the vectors whose product with the matrix $\boldsymbol{A}$ gives zero. From the singular value decomposition (3.14), it can be seen that:

$$\boldsymbol{V}^T\cdot\boldsymbol{V}_i = \begin{bmatrix} \boldsymbol{v}_1 \\ \vdots \\ \boldsymbol{v}_j \\ \vdots \\ \boldsymbol{v}_{N_{pwi}(N_y+N_a-1)} \end{bmatrix}, \text{with:} \boldsymbol{v}_j = \begin{cases} 1, & j = i \\ 0, & j \neq i \end{cases} \tag{3.20}$$

and that:

$$\boldsymbol{S}\cdot\begin{bmatrix} \boldsymbol{v}_1 \\ \vdots \\ \boldsymbol{v}_j \\ \boldsymbol{v}_{j+1} \\ \vdots \\ \boldsymbol{v}_{N_{pwi}(N_y+N_a-1)} \end{bmatrix} = \begin{bmatrix} \sigma_1\boldsymbol{v}_1 \\ \vdots \\ \sigma_{N_y}\boldsymbol{v}_{N_y} \\ 0 \\ \vdots \\ 0 \end{bmatrix} \tag{3.21}$$

Combining (3.20) and (3.21) it can be thus concluded that the null space of $\boldsymbol{A}$ is spanned by the columns $i \in [N_y+1..N_{pwi}(N_y+N_a-1)]$ of the matrix $\boldsymbol{V}$:

$$\text{Null}(\boldsymbol{A}) = \boldsymbol{V}_{N_y+1\longrightarrow N_{pwi}(N_y+N_a-1)} \tag{3.22}$$

Combining (3.22) with the expression of the direct model (3.10) it can be deduced that:

$$\begin{gathered} {}_S\boldsymbol{y}_i = \boldsymbol{A}\cdot\left(\boldsymbol{g}_i+\boldsymbol{\lambda}\cdot\text{Null}(\boldsymbol{A})\right)+\boldsymbol{b}_i \Longleftrightarrow {}_S\boldsymbol{y}_i = \boldsymbol{A}\cdot\boldsymbol{g}_i+\boldsymbol{A}\cdot\boldsymbol{\lambda}\cdot\text{Null}(\boldsymbol{A})+\boldsymbol{b}_i \underset{\text{Null}(\boldsymbol{A})=\boldsymbol{V}_{N_y+1\longrightarrow N_{pwi}(N_y+N_a-1)}}{\Longleftrightarrow} \\ {}_S\boldsymbol{y}_i = \boldsymbol{A}\cdot\boldsymbol{g}_i+\boldsymbol{b}_i \end{gathered} \tag{3.23}$$

with $\boldsymbol{\lambda} \in \mathscr{R}^{N_{pwi}(N_y+N_a-1)-N_y-1}$. Thus, using (3.23), one can conclude, that if the matrix $\boldsymbol{A}$ has a non null null-space, the system (3.10) has an infinite number of solutions (defined by $\boldsymbol{g}_i+\boldsymbol{\lambda}\cdot\text{Null}(\boldsymbol{A})$). From this reasoning, the next requirement follows: for a well conditioned system ($K(\boldsymbol{A})$ small), in order to have an unique solution $\hat{\boldsymbol{g}}_i$, one needs to have a well-determined kernel $\boldsymbol{A}$ ($\boldsymbol{A}$ is square).

Consider now that the medium inside the "Blind" and "Perturbation" zones is completely anechoic (hypothesis H3.1). In such conditions, regardless of the plane wave tilt θ^k, the pulse-echo impulse response $g_i^k(t)$ generated by the medium will always be null between the samples (n_0-N_a) to n_0 and between the samples n_f to (n_f+N_a). Suppose now that between the "Blind" and "Perturbation" zones the pulse echo impulse responses $\boldsymbol{g}_i^k$ have a length N_g. This means that for a given length N_a of the excitation signals $\boldsymbol{a}^k$, there is a length N_y of the recorded RF data ${}_S\boldsymbol{y}_i$ for which all the echoes generated between the samples n_0 and (n_0+N_g-1) of all $\boldsymbol{g}_i^k$ are completely recorded. This effect is represented in the correspondingly adapted schematic representation of the convolution showed in Fig.3.6. By comparing the Fig.3.3 and Fig.3.6 it can be seen that the transition from $\boldsymbol{g}_i^k$ and $\boldsymbol{y}_i^k$ is not the same after constraining the impulse responses. In other words, the kernel $\boldsymbol{A}^k$ evolved. As it can be

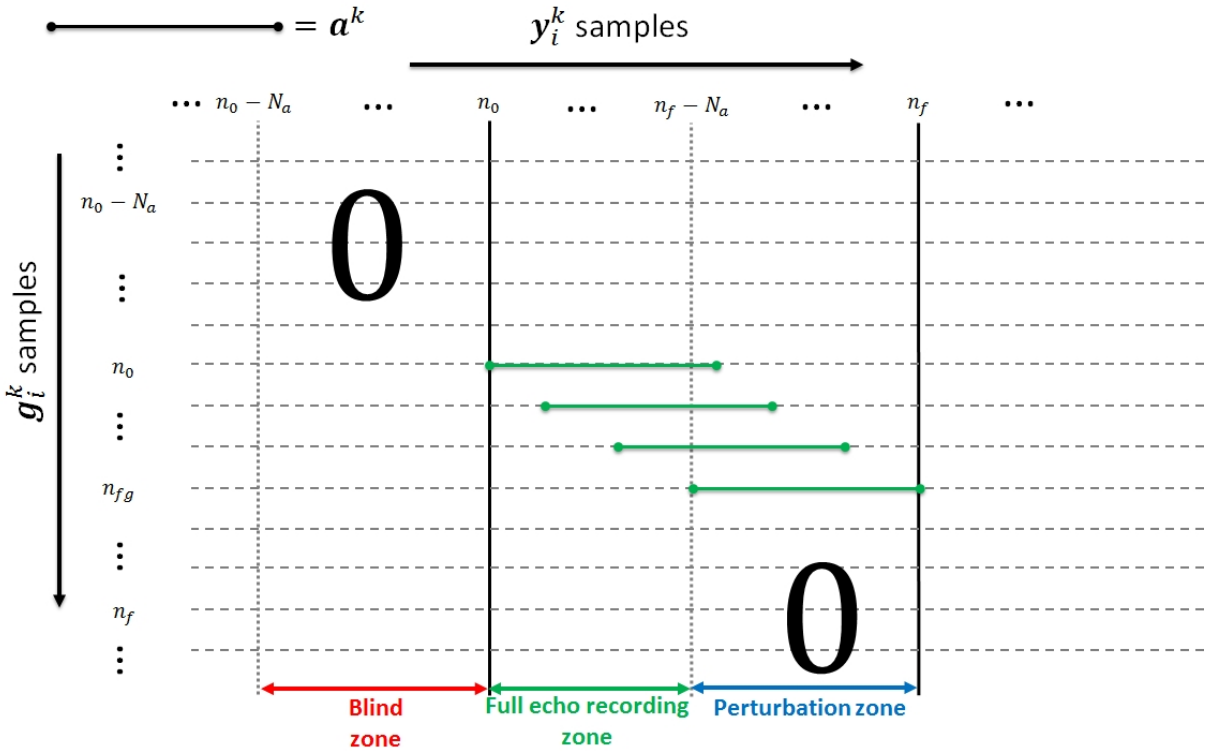

Figure 3.6: Schematic representation of the convolution product between the signal $\boldsymbol{a}^k$ and the vector $\boldsymbol{g}_i^k$ when the anechoic constraints have been applied on the "Blind" and "Perturbation" zones. Vertically are disposed the samples of the pulse echo impulse response $\boldsymbol{g}_i^k$ and horizontally are aligned the samples of the received signal $\boldsymbol{y}_i^k$. $n_0 = t_0/v_s$ is the sample at which the received echoes $\boldsymbol{y}_i^k$ start to be recorded. $n_f = n_0 + N_y - 1$ is the last recorded sample of the signal $\boldsymbol{y}_i^k$. $n_{fg} = n_0 + N_g - 1$ is the last non null sample of the impulse response $\boldsymbol{g}_i$, thus N_g is the length of the impulse response of the medium that needs to be estimated. The line segments represent the excitation signal $\boldsymbol{a}^k$.

seen in Fig.3.6, the new kernel can be written as follows:

$$\boldsymbol{A}^k = \begin{bmatrix} \boldsymbol{a}^k[0] & 0 & \cdots & 0 \\ \boldsymbol{a}^k[1] & \boldsymbol{a}^k[0] & \cdots & 0 \\ \vdots & \vdots & \ddots & \vdots \\ \boldsymbol{a}^k[N_a-1] & \boldsymbol{a}^k[N_a-2] & \cdots & \boldsymbol{a}^k[0] \\ 0 & \boldsymbol{a}^k[N_a-1] & \cdots & \boldsymbol{a}^k[1] \\ \vdots & \vdots & \ddots & \vdots \\ 0 & 0 & \cdots & \boldsymbol{a}^k[N_a-1] \end{bmatrix} \tag{3.24}$$

Thus, from Fig.3.6 it can be seen that the new matrix $\boldsymbol{A}^k$ has $N_y = n_f - n_0$ rows and $N_g = n_{fg} - n_0$ columns. This evolution of the matrix $\boldsymbol{A}^k$ generates also a change in the total kernel $\boldsymbol{A}$ which, in these conditions, becomes a matrix with N_y rows and $N_{pwi}N_g$ columns. Given the assumption that all the echoes generated between the samples n_0 and $(n_0 + N_g - 1)$ of $\boldsymbol{g}_i$ are completely recorded, it means that the length of the RF data must be $N_y \geq N_g + N_a - 1$ (property of the convolution product). Thus the size of the matrix $\boldsymbol{A}$ can be written as:

$$(N_g + N_a - 1) \times (N_{pwi}N_g) \tag{3.25}$$

As previously stated, in order to have an unique solution for the inverse problem, the kernel $\boldsymbol{A}$ needs to have at least the same amount of rows as columns. Since for a simultaneous emission of N_{pwi} plane

waves the parameter N_g is fixed by the imaged medium, the only parameter that can be adapted in the relation (3.25) in order to account for the longer / shorter impulses responses $\boldsymbol{g}_i^k$ is the length of the emitted signals. Thus, using (3.25) it can be deduced that:

$$(N_g + N_a - 1) \geq (N_{pwi} N_g) \Longleftrightarrow N_a \geq (N_{pwi} - 1) N_g + 1 \tag{3.26}$$

This means that the length of the emitted signals is directly proportional to the depth of the imaged medium which sets the length of the medium pulse echo impulse responses. The inherent consequence of this is that, for the same length N_g of the pulse echo impulse responses of the medium to the plane waves, if the number N_{pwi} of the simultaneous emitted plane waves increases, the length N_y of the recorded data should also increase.

3.4 Study of the inverse problem behavior with respect to acquisition noise

In Sections 3.3.2 and 3.3.3, the impact of the kernel $\boldsymbol{A}$ on the estimation of the medium pulse echo impulse responses $\boldsymbol{g}_i$ has been studied. It was shown that in order to have a good stability of the solution with respect to noise, it is necessary to have a total matrix $\boldsymbol{A}$ with a small condition number, which implies that the excitation signals for all the plane waves need to be mutually orthogonal. For this work they was chosen to be BPSK modulated pseudo-random sequences. Furthermore, it was shown that in order to have an unique solution for the inverse problem, the matrix $\boldsymbol{A}$ needs to be square. This introduces a strong constraint on the length of the excitation and recorded signals that implies that these vectors should be longer if the imaged medium is deeper or the number of simultaneously emitted plane wave increases.

Before advancing to the case of the noisy RF data, it would me more accurate first to study how the model behaves when no acquisition noise is present in the RF data (hypothesis H3.2). This case will allow to assess the influence of the null space of the direct model's kernel $\boldsymbol{A}$ on the estimated solution. In order to produce the RF data, the simulation program Field II [Jensen, 1996, Jensen and Svendsen, 1992] is used. A numerical model of the LA523E probe (Esaote, Florence, Italy) was created in order to emit / receive the ultrasound waves. Its properties are summarized in Table 3.1. Two types of mediums are imaged. The first phantom (Fig.3.7)(a), very sparse, contains only

Parameter	**Value**
No. active elements N_{el}	128
Element width w	215 μm
Kerf	30 μm
Pitch $\wp$	245 μm
Height h	6 mm
Central frequency ν_0	8.5 MHz
Aperture size $N_{el}\wp$	3.14 cm
Sampling frequency ν_s	50 MHz

Table 3.1: Specifications of the LA523E ultrasound probe

three scatterers and is used to understand the concept of pulse echo impulse response of the medium. The effect of the matrix $\boldsymbol{A}$ null space and of the acquisition noise can be also easy to assess on this kind of medium. The second phantom (Fig.3.7(b)) contains a very large number of scatterers and an anechoic cyst, and allows measuring the performance of the method in terms of contrast and signal to noise ratio. Suppose now a set of $N_{pwi} = 5$ plane waves with the following steering angles $\theta_k \in \{-7^\circ, -5^\circ, 0^\circ, 3.5^\circ, 7^\circ\}$. As shown in Fig.3.7, the ROI of the medium is located between the $z_{min} = 50$ mm and $z_{max} = 80$ mm of depth, which makes a depth differential of $\Delta z = 30$ mm. In these

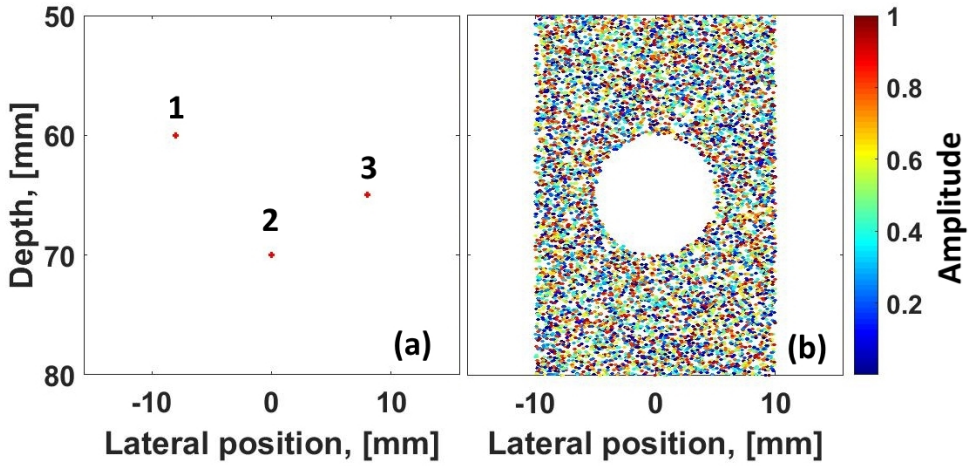

Figure 3.7: Tested mediums: (a) - Phantom containing three punctual scatterers with an amplitude 1, (b) - Phantom containing a completely anechoic cyst of diameter 1 cm, and a scatterer distribution of 94 scatterers per square millimeter. For the simulated acquisitions, the probe is positioned at depth $z = 0$ mm. It will be assumed that both mediums, outside the limits showed in these two figures, are completely anechoic.

conditions, one can deduce first, the starting recording sample n_0 and second, the maximal non null length N_g of the pulse echo impulse responses $\boldsymbol{g}_i^k$ using the following formulas:

$$\begin{cases} n_0 = \left\lceil \frac{2v_s z_{min}}{c_m} \right\rfloor \\ N_g = \left\lceil \frac{2v_s \sqrt{(N_{el}\wp)^2 + (\Delta z)^2}}{c_m} \right\rfloor \end{cases} \tag{3.27}$$

where $\lceil \, \rfloor$ represents the nearest integer function. In (3.27) N_g represents, the geometrical computation of the propagation delay (that appears in the impulse responses (2.32)) measured between the two most distant scatterers inside the medium (which correspond to the scatterers that would be located at the positions $\vec{r}_1 = (-15.7, 0, 50)$ mm and $\vec{r}_2 = (15.7, 0, 80)$ mm (in other words the opposite corners of the medium's ROI)). On the other hand, n_0 represents the geometrical computation of the delay needed for the fastest echo to reach back the most proximal receiving element of the probe. Applying the parameter values from Table 3.1 to (3.27), it can be deduced that in this case $n_0 = 3200$ and $N_g = 2800$. Inserting the values of N_g and N_{pwi} in (3.26) it can be deduced that $N_a = (5-1) \times 2800 + 1 = 11201$.

In Fig.3.8 are displayed the reference pulse echo impulse responses of the sparse medium (Fig.3.7(a)) to each of the five plane waves, seen by the $i = 64^{th}$ element of the probe. More specifically, in Fig.3.8(a) are shown all the samples of the vector $\boldsymbol{g}_{64}^3$. Using the n_0 and N_g values previously computed, the estimated part of this section will be the segment included between the samples n_0 and $(n_0 + N_g - 1)$. In Fig. 3.8(b)-(e) are shown the pulse echo impulse responses $\boldsymbol{g}_{64}^1$, $\boldsymbol{g}_{64}^2$, $\boldsymbol{g}_{64}^4$ and $\boldsymbol{g}_{64}^5$ respectively already cropped between the samples n_0 and $(n_0 + N_g - 1)$. The estimation $\hat{\boldsymbol{g}}_{64}^3$, obtained using Est. $\equiv (\boldsymbol{A}^T \cdot \boldsymbol{A})^{-1} \cdot \boldsymbol{A}^T$, of the impulse response $\boldsymbol{g}_{64}^3$ is shown in Fig.3.9. As one can see, on a noiseless acquisition data and in the conditions where the "Blind" and "Perturbation" zones are completely anechoic, the estimation error is null. The B-mode images of the sparse medium obtained after all the processing using the pipeline shown in Fig.3.4(b) and Fig. 3.5 (with Est. $\equiv (\boldsymbol{A}^T \cdot \boldsymbol{A})^{-1} \cdot \boldsymbol{A}^T$) are displayed in Fig.3.10. By comparing Fig.3.10(a) with (b) and Fig.3.10(c) with (d), one can deduce that there is no difference in terms of image quality between the images obtained using successive emission of plane waves (that carry short impulsions) and the ones provided by the proposed approach. Axial and lateral resolution for both methods are 140 / 390 μm respectively. Thereby, it can be concluded that the proposed method which employs simultaneous emission of plane waves, can achieve same

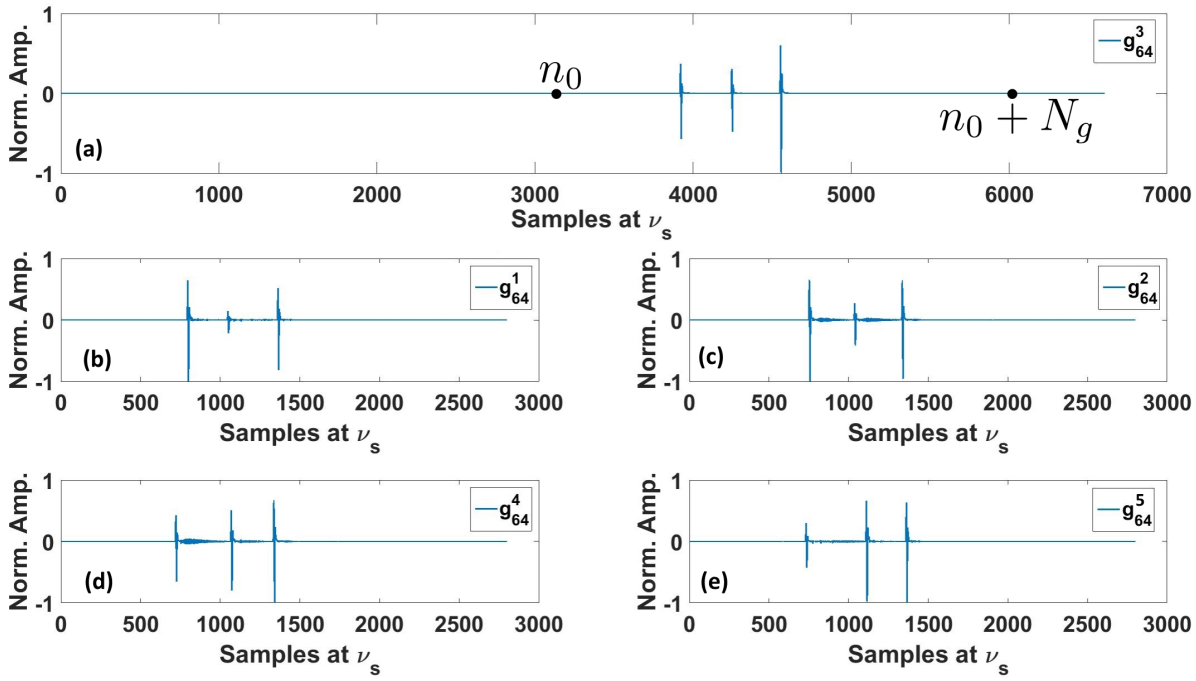

Figure 3.8: Reference pulse echo impulse responses $\boldsymbol{g}_i^k$ of the medium showed in Fig.3.7(a) for each plane wave k, seen by the $i = 64^{th}$ element of the probe: (a) - all the samples of the pulse echo impulse response $\boldsymbol{g}_{64}^3$, the estimated part will be situated between n_0 and $(n_0 + N_g - 1)$, (b) - $\boldsymbol{g}_{64}^1$ between n_0 and $(n_0 + N_g - 1)$, (c) - $\boldsymbol{g}_{64}^2$ between n_0 and $(n_0 + N_g - 1)$, (d) - $\boldsymbol{g}_{64}^4$ between n_0 and $(n_0 + N_g - 1)$, (e) - $\boldsymbol{g}_{64}^5$ between n_0 and $(n_0 + N_g - 1)$

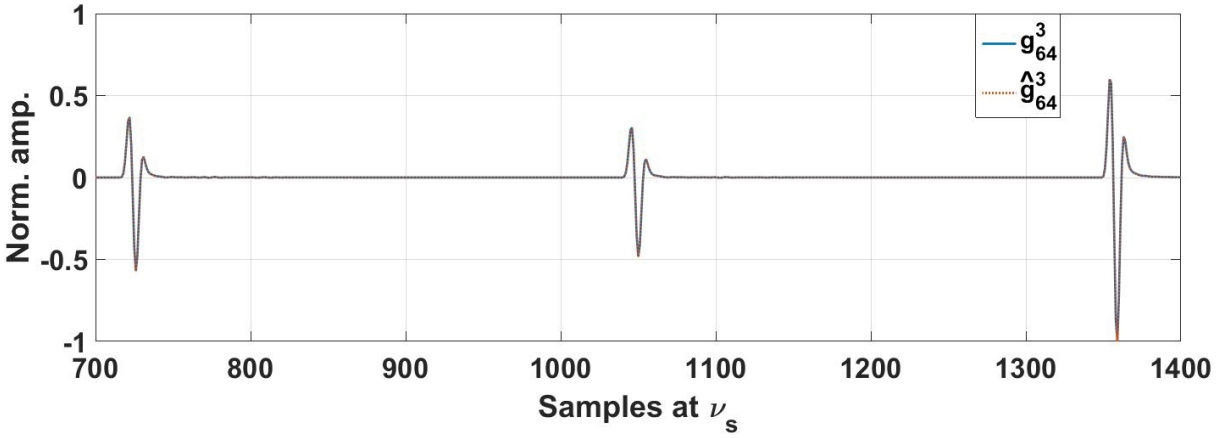

Figure 3.9: Comparison between the reference pulse echo impulse response $\boldsymbol{g}_{64}^3$ (solid blue line) and its estimation$\hat{\boldsymbol{g}}_{64}^3$ (dotted red line). In this particular case, the impulse response and its estimate overlap.

image qualities as the conventional plane wave coherent compounding (when short pulses are used as excitations).

Now that the noiseless case was studied and the best results achievable by the proposed method have been exposed, one can analyze the case where the RF data ${}_S\boldsymbol{y}_i$ contains some acquisition noise $\boldsymbol{b}_i$. As the relation (3.12) shows, the estimation $\hat{\boldsymbol{g}}_i^k$ (that can be split from the vector $\hat{\boldsymbol{g}}_i$, as shown in Fig.3.5) is related to the noise $\boldsymbol{b}_i$ through the pseudo-inverse $(\boldsymbol{A}^T \cdot \boldsymbol{A})^{-1} \cdot \boldsymbol{A}^T$. In Fig.3.11 are shown the results of inversion of a noisy ($eSNR = 30dB$) and noiseless RF data ${}_S\boldsymbol{y}_{64}$. As one can see, if no additional processing is applied to the pseudo-inverse, the estimation ${}_n\hat{\boldsymbol{g}}_{64}^1$ (obtained from the noisy RF data) is far from the reference $\hat{\boldsymbol{g}}_{64}^1$ (obtained from noiseless RF data). As previously stated in Section 3.3.2, this is the result of the acquisition noise amplification. In fact the condition number of the $\boldsymbol{A}$

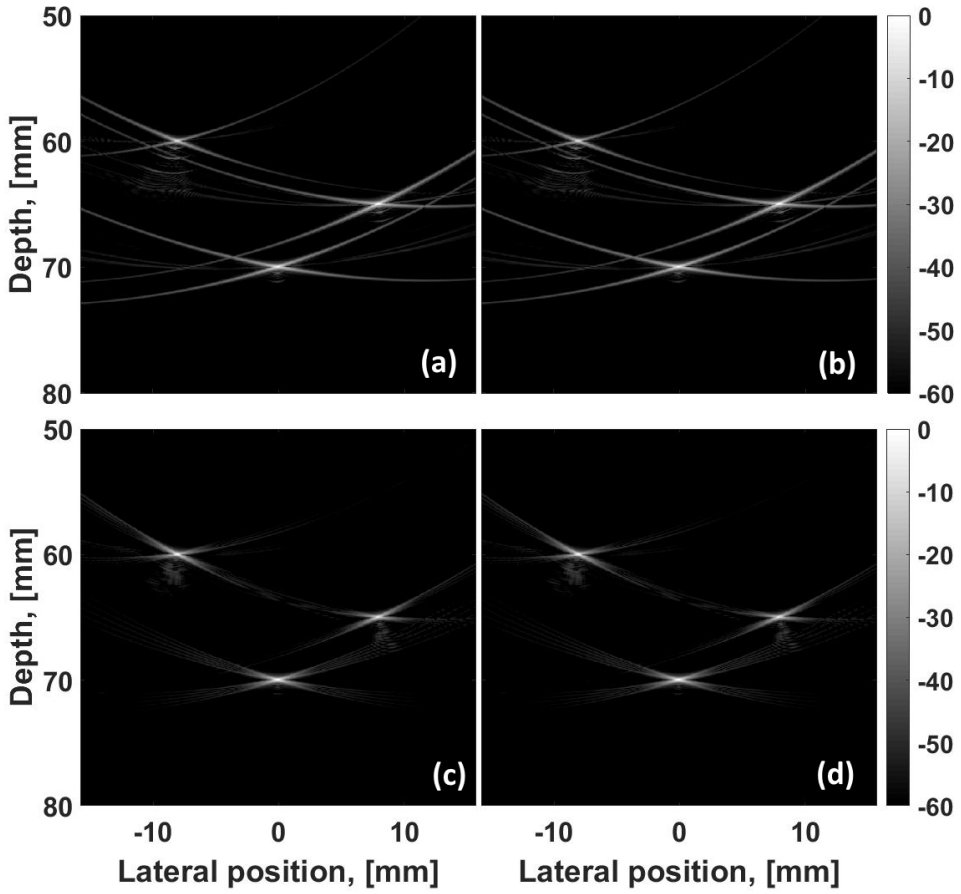

Figure 3.10: B-mode images of the sparse medium TRF: (a) - obtained after a single plane wave emission ($\theta^k = 0°$), (b) - obtained after simultaneous emission of $N_{pwi} = 5$ plane waves and reconstruction of only one low quality image ($\theta^k = 0°$), (c) - obtained after successive emission of N_{pwi} plane waves and coherent compounding of the low quality images, (d) - obtained after simultaneous emission of $N_{pwi} = 5$ plane waves and compounding of all the low quality images. Here Est. $\equiv (\boldsymbol{A}^T \cdot \boldsymbol{A})^{-1} \cdot \boldsymbol{A}^T$.

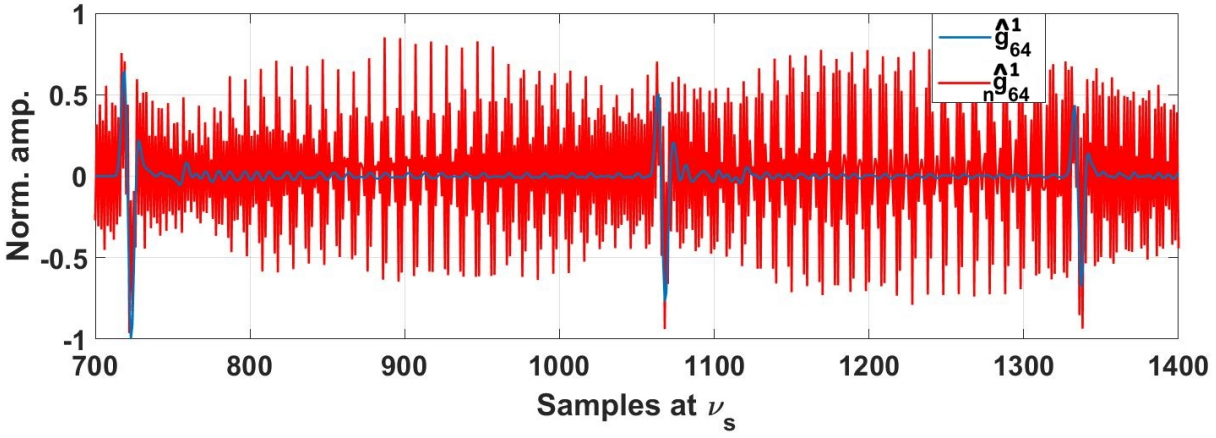

Figure 3.11: Comparison between the estimation $\hat{\boldsymbol{g}}^1_{64}$ (solid blue line) obtained from noiseless ${}_S\boldsymbol{y}_{64}$ data and the estimation ${}_n\hat{\boldsymbol{g}}^1_{64}$ (solid red line) obtained from noisy ($eSNR = 30dB$) ${}_S\boldsymbol{y}_{64}$ data.

matrix is $K(\boldsymbol{A}) = 140000 >> 1$ which means that the inverse problem is ill-conditioned. Using the definition (3.16) of $K(\boldsymbol{A})$, it can be deduced that by increasing the value of the smallest singular value σ_{N_y}, the condition number $K(\boldsymbol{A})$ will drop. This can be achieved by forcing in $\boldsymbol{S}^{-1}$ all the singular

values $\sigma_r^{-1} | r \in (r_0..N_y]$ to be equal to zero [Quarteroni et al., 2008]:

$$\boldsymbol{S}^{\dagger} = \text{diag}\begin{bmatrix}\sigma_1^{-1} & \sigma_2^{-1} & \cdots & \sigma_{r_0}^{-1} & 0 & \cdots & 0\end{bmatrix} \tag{3.28}$$

The process of singular value cancellation beyond an arbitrary value of r is called truncation of the singular values. Under such conditions, the condition number of the new problem becomes $K_{r_0}(\boldsymbol{A}) = \sigma_1/\sigma_{r_0}$ and the new pseudo inverse matrix can be written as:

$$\boldsymbol{A}^{\dagger} = \boldsymbol{V} \cdot \boldsymbol{S}^{\dagger} \cdot \boldsymbol{U}^T \tag{3.29}$$

Indeed, adjusting the condition number implies that the obtained solution, even in a noiseless acquisition will slightly deviate from the reference. This deviation can be computed as follows:

$${}_F\hat{\boldsymbol{g}}_i - {}_T\hat{\boldsymbol{g}}_i \underset{\text{Using 3.15 and 3.29}}{=} \boldsymbol{V} \cdot \boldsymbol{S}^{-1} \cdot \boldsymbol{U}^T \cdot {}_S\boldsymbol{y}_i - \boldsymbol{V} \cdot \boldsymbol{S}^{\dagger} \cdot \boldsymbol{U}^T \cdot {}_S\boldsymbol{y}_i = \boldsymbol{V} \cdot \left(\boldsymbol{S}^{-1} - \boldsymbol{S}^{\dagger}\right) \cdot \boldsymbol{U}^T \cdot {}_S\boldsymbol{y}_i \tag{3.30}$$

Where the estimations ${}_F\hat{\boldsymbol{g}}_i$ and ${}_T\hat{\boldsymbol{g}}_i$ are calculated without and with singular value truncation respectively. Consider a matrix $\boldsymbol{M}_d^r$ of the same size as $\boldsymbol{S}$ (as in the singular value decomposition (3.13) of $\boldsymbol{A}$) which contains only zero entries except for the position $[r,r]$ where the entry is one:

$$\boldsymbol{M}_d^r[j,i] = \begin{cases} 1,\ j = i = r \\ \\ 0, \text{otherwise} \end{cases} \tag{3.31}$$

By using $\boldsymbol{M}_d^r$ in (3.30), one can obtain the following relation:

$${}_F\hat{\boldsymbol{g}}_i - {}_T\hat{\boldsymbol{g}}_i = \sum_{r=r_0}^{N_y} \frac{1}{\sigma_r} \boldsymbol{V} \cdot (\boldsymbol{M}_d^r)^T \cdot \boldsymbol{U}^T \cdot {}_S\boldsymbol{y}_i \tag{3.32}$$

At this point, one can observe in (3.32) that the product $(\boldsymbol{M}_d^r)^T \cdot \boldsymbol{U}^T$ generates a matrix of size similar as $(\boldsymbol{M}_d^r)^T$ that contains only one non null row r which is equal to the r^{th} column of $\boldsymbol{U}$. Thus, the product $\boldsymbol{V} \cdot (\boldsymbol{M}_d^r)^T \cdot \boldsymbol{U}^T$ generates an orthonormal matrix $\boldsymbol{M}_o^r$ of size equal to the one of $(\boldsymbol{M}_d^r)^T$. (3.32) becomes:

$$\begin{gathered} {}_F\hat{\boldsymbol{g}}_i - {}_T\hat{\boldsymbol{g}}_i = \sum_{r=r_0}^{N_y} \frac{1}{\sigma_r} \boldsymbol{M}_o^r \cdot {}_S\boldsymbol{y}_i \iff \\ \| {}_F\hat{\boldsymbol{g}}_i - {}_T\hat{\boldsymbol{g}}_i \|_2 = \left\| \sum_{r=r_0}^{N_y} \frac{1}{\sigma_r} \boldsymbol{M}_o^r \cdot {}_S\boldsymbol{y}_i \right\|_2 \underset{\sigma_r>0,\ \forall r}{\leq} \sum_{r=r_0}^{N_y} \frac{1}{\sigma_r} \left\| \boldsymbol{M}_o^r \cdot {}_S\boldsymbol{y}_i \right\|_2 \underset{\|\boldsymbol{M}_d^r\|_2=1}{\leq} \sum_{r=r_0}^{N_y} \frac{1}{\sigma_r} \left\| {}_S\boldsymbol{y}_i \right\|_2 \end{gathered} \tag{3.33}$$

The previous relation demonstrates, that by adjusting the condition number of the inverse problem, a computation error which is inversely proportional to the value of the truncated singular value is induced. Moreover, it can be seen that since $1/\sigma_{r_1} < 1/\sigma_{r_2}$ if $r_1 > r_2$, the biggest error is made when the smaller singular values are truncated (which decreases the most the condition number) and after, the error increment decreases (since the values of σ_r become larger). In Fig.3.12 is represented the evolution of the estimations ${}_{eSNR=\infty}\hat{\boldsymbol{g}}_{64}^1$ (left column) and ${}_{eSNR=30dB}\hat{\boldsymbol{g}}_{64}^1$ (right column) as a function of the number of truncated singular values obtained from RF data with different levels of noise ($eSNR = \infty$ and $eSNR = 30dB$ respectively). As one can observe, if there is no acquisition noise (left column), the fact that one truncates more singular values increases the computation error. This behavior is coherent with (3.32). However, on the second column in Fig.3.12, it can be seen that in presence of noise (right column), the best solution is achieved for an optimal number of truncated singular values. In Fig.3.12 it can be seen, that while moving upwards, the best estimation (less noisy)

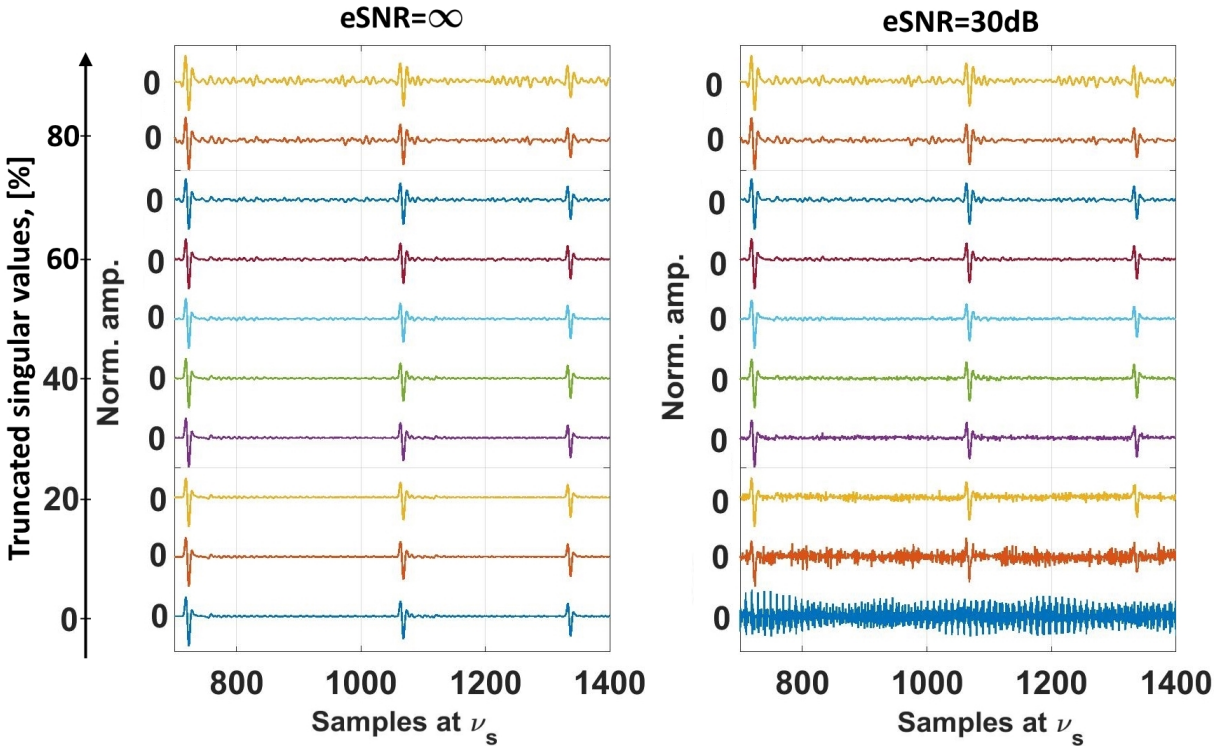

Figure 3.12: Evolution of ${}_{eSNR=\infty}\hat{\boldsymbol{g}}^1_{64}$ (left column) and ${}_{eSNR=30dB}\hat{\boldsymbol{g}}^1_{64}$ (right column) as a function of the number of the truncated singular values. Each horizontal line represents a pair of signals ${}_{eSNR=\infty}\hat{\boldsymbol{g}}^1_{64}$ and ${}_{eSNR=30dB}\hat{\boldsymbol{g}}^1_{64}$ estimated using the same Moore-Penrose pseudo-inverse. Starting from the bottom and going up, each step represents a truncation of 10% smallest singular values, the bottommost line representing the signals obtained without truncation. The RF data $eSNR$ for the first and second column is ∞ and $30dB$ respectively.

is achieved on the sixth line which corresponds to a truncation of 50% of singular values. This result is obtained due to the combination of the two following effects:

- while truncating between 0 and the optimal number (here 50%) of the singular values, the estimation error decreases since the solution becomes more stable to noise
- when the optimal truncation number is exceeded, the error increases, since the error made by truncation (first column in Fig.3.12) increases and thus prevails over the slightly (by now decreased condition number $K_{r_0}(\boldsymbol{A})$) amplified acquisition noise.

While on signals as the ones shown in Fig.3.12 (obtained by imaging very sparse media) it is easy to assess the estimation error and thus to conclude what is the "sweet spot" for truncation, on data obtained from acquisitions on more complex media (e. g. Fig.3.7(b)), this task becomes more challenging. In order to overcome this impediment, it is more appropriate to judge on the number of truncated singular values directly on a graph of an image quality evolution. As it can be seen in Fig.3.12, the temporal resolution of the backscattered echoes does not change thus, the spatial resolution of the image would not be a good indicator for the optimal truncation of the singular values. The convenient measure would be either the SNR or the CNR. In this work, the evolution of the CNR is analyzed. In Fig.3.13(a) is displayed the evolution of the reconstructed images from noiseless (top line) and noisy (bottom line, $eSNR = 30dB$) as a function of the number of truncated singular values. It can be observed that, in the case of noiseless acquisition (top line), the image quality degrades steadily with the number of truncated singular values, whereas in the case of noisy RF data (bottom line) the cyst quality presents an optimum value around column six (corresponding to 50% truncated

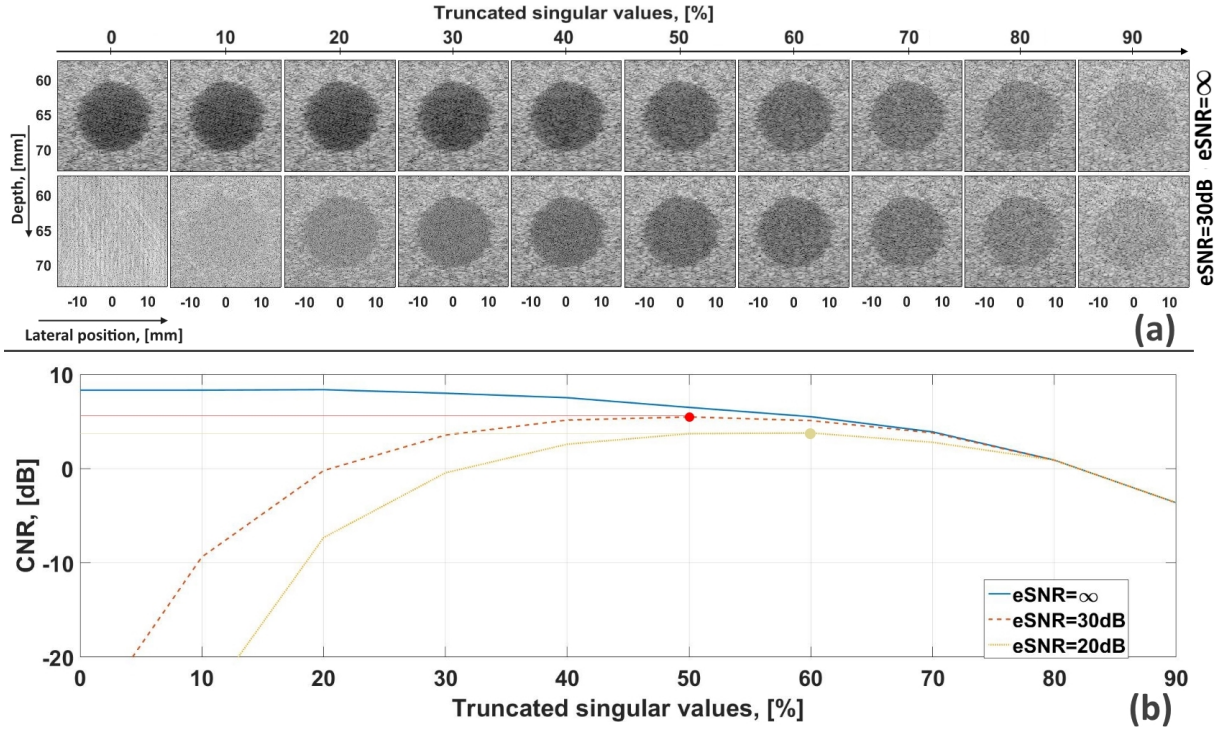

Figure 3.13: (a) - Evolution of the reconstructed images from noiseless (top line) and noisy (bottom line, $eSNR = 30dB$) RF data as a function of the number of truncated singular values (dynamic range is $60dB$). Starting with the first column, where 0% of the singular values are truncated, between two consecutive columns 10% more of the singular values are truncated. (b) - Evolution of the CNR (measured on the cysts in (a)) as a function of the number of truncated singular values. The solid blue line is obtained when noiseless RF data is used, the dashed red line is obtained when RF data with $eSNR = 30dB$ is used and finally the dotted green line is obtained when RF data with $eSNR = 20dB$ is used.

singular values) which is coherent with the results seen in Fig.3.12. The measured values of the CNR (Fig.3.13(b)) consolidate the visual assessments and present, for the noisy RF data, a concave curve where the optimal quality ($CNR = 5.74dB$) is obtained at 50% ($eSNR = 30dB$) truncated singular values. Moreover, it can be seen that if the $eSNR$ decreases, (corresponding to more acquisition noise) the optimal image quality decreases ($CNR = 3.77dB$) and is obtained when more singular values are truncated (60%). Thus it can be concluded, that regardless of the level of noise inside the RF data, there will be always an optimal value of the number of truncated singular values that will provide the best achievable image quality. However, the best achievable image quality will be different between two estimations from RF datasets with different noise levels (higher image quality obtained from less noisy RF data).

3.5 Study of the inverse problem behavior with respect to the increase in acquisition rate

In Section 3.4, was demonstrated that when the hypothesis H3.1 and H3.2 are verified, the image quality (in terms of spatial resolution and CNR) provided by the proposed approach (based on the simultaneous emission of plane waves) is exactly the same as the one provided by the conventional plane wave coherent compounding method (where the excitation signals are short impulsions). Thus, the only metric remaining that will allow to discriminate both methods, is the FAR. Thus, in this Section, the evolution of the image quality (provided by the proposed method) as a function of the

provided gain in FAR, will be studied.

First, consider the gain τ in acquisition time that the simultaneous emission of plane waves provides over the conventional, successive emission of plane waves. τ can be defined as follows:

$$\tau = \frac{{}_C t_{rec} - {}_S t_{rec}}{{}_C t_{rec}} \cdot 100\% \quad \text{with: } {}_C t_{rec} = N_{pwi}\, {}_{PWI} t_{rec} \tag{3.34}$$

where ${}_C t_{rec}$ is the total time needed to record all the echoes of the successively emitted plane waves and ${}_{PWI} t_{rec}$ is the time needed to record the echoes generated by one plane wave. ${}_S t_{rec}$ is the time needed to record the generated echoes when N_{pwi} plane waves are emitted simultaneously. Surely, for a fair comparison, in both successive and simultaneous emissions the image mediums must be of the same size which implies that for both methods N_g will be the same. At this point one can deduce that, if H3.1 is verified (which, as seen in Section 3.3.3, can be summarized by the following two relations: $N_y \geq N_g + N_a - 1$ and $N_a \geq (N_{pwi} - 1)N_g + 1)$, then $N_y = N_{pwi} N_g$ which implies that ${}_S t_{rec} = N_y / \nu_s = N_{pwi} N_g / \nu_s$. Since, for very short excitations in conventional plane wave insonification, the length of the recorded RF data after each emission can be approximated as N_g then ${}_C t_{rec} = N_{pwi}\, {}_{PWI} t_{rec} = N_{pwi} N_g / \nu_s$. In such conditions, using 3.34, it can be deduced that if H3.1 is verified then no FAR improvement is provided by the simultaneous emission approach.

As it can be observed in Fig. 3.6, a straightforward approach of increasing the frame acquisition rate of the proposed method, consists in reducing the length N_y of the recorded RF data ${}_S \boldsymbol{y}_i$. Indeed, it this figure, the decrease in N_y results in a decrease of the sample index n_f (since $n_f = n_0 + N_y - 1$). Nonetheless, while the new value of n_f is still higher than the old value of $(n_f - N_a)$, this means that the same number of samples in the impulse response of the medium $\boldsymbol{g}_i^k$ will generate echoes between the samples n_0 and the new value of n_f of the recorded signal ${}_S \boldsymbol{y}_i$. Thus, it can be concluded that using the proposed method, by violating the hypothesis H3.1 one can achieve higher FAR for the same number N_{pwi} of plane waves. Another approach for increasing the FAR would be to decrease the length N_a of the excitation signals for the same length N_g of the pulse echo impulse response of the medium (thus violating the inequality $N_a \geq (N_{pwi} - 1)N_g + 1)$. However, by employing either of this ways of increasing the FAR, either a "Perturbation" zone or both a "Blind" and a "Perturbation" zone will be created, which results in a underdetermined direct model (thus flat $\boldsymbol{A}$ matrix). The theoretical

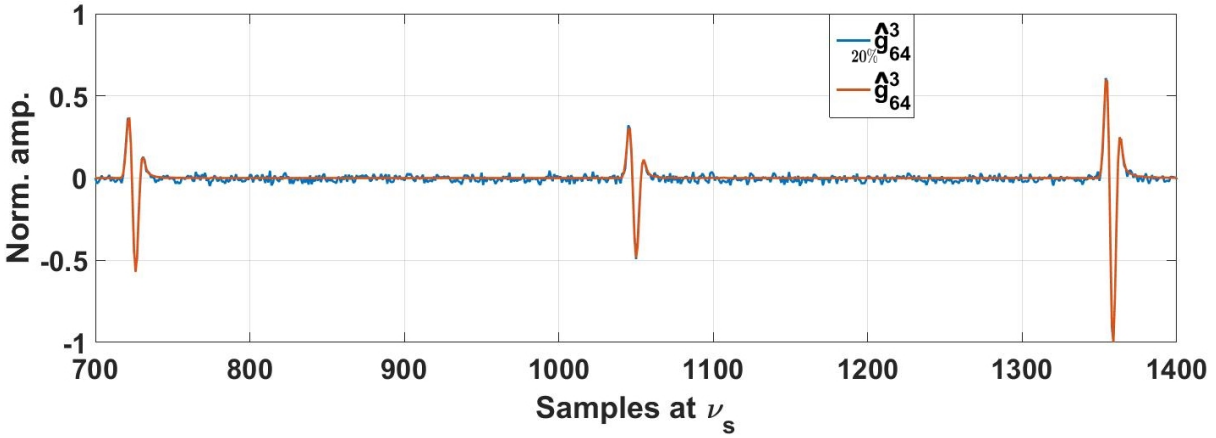

Figure 3.14: Comparison between the estimation $\hat{\boldsymbol{g}}^3_{64}$ (solid red line) obtained using a square $\boldsymbol{A}$ matrix and the estimation ${}_{\tau=20\%}\hat{\boldsymbol{g}}^3_{64}$ (solid red line) obtained using a flat (designed to obtain $\tau = 20\%$ time gain) $\boldsymbol{A}$ matrix.

background of the null space impact on the estimation $\hat{\boldsymbol{g}}_i^k$ was detailed in Subsection 3.3.3. In Fig.3.14 is shown an example of $\hat{\boldsymbol{g}}^3_{64}$ estimation when the $\boldsymbol{A}$ matrix is designed to obtain a time gain $\tau = 20\%$ (same excitation length used as for Fig.3.9, N_y reduced by 20%). As one can observe, when compared to the solution obtained used a square matrix $\boldsymbol{A}$, the novel estimation ${}_{\tau=20\%}\hat{\boldsymbol{g}}^3_{64}$ comes up as a noisy

version of the expected solution $\hat{\boldsymbol{g}}_{64}^{3}$. In Fig.3.16 are shown the B-mode images of the wire and cyst

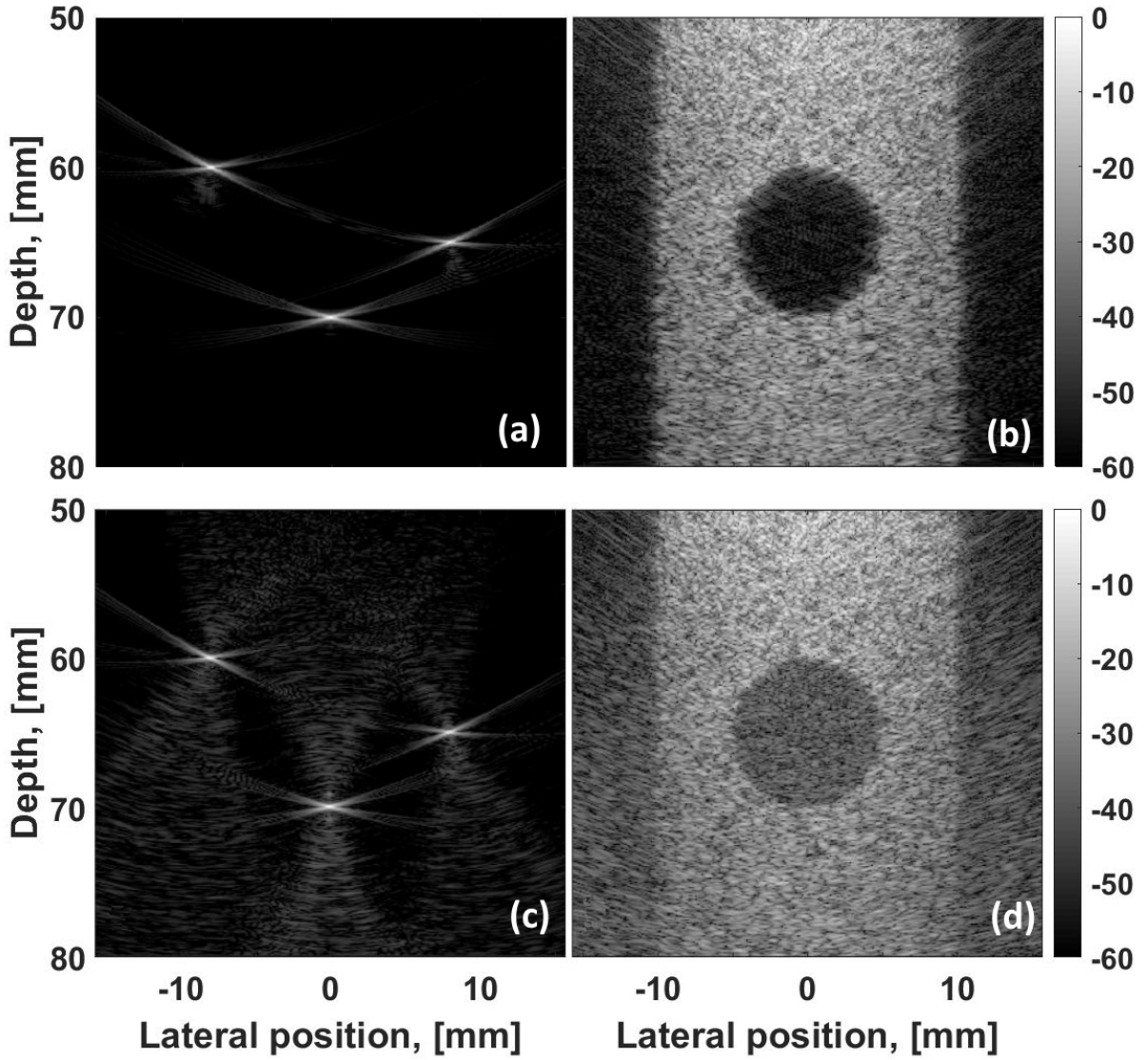

Figure 3.15: B-mode images obtained with two types of matrices $\boldsymbol{A}$ square and flat: (a) - Compounded image of the sparse medium obtained using the square $\boldsymbol{A}$ matrix, (b) - Compounded image of the cyst phantom obtained using the square $\boldsymbol{A}$ matrix, (d) - Compounded image of the sparse medium obtained using the flat $\boldsymbol{A}$ matrix, (e) - Compounded image of the cyst phantom obtained using the flat $\boldsymbol{A}$ matrix.

phantoms obtained using the simultaneous emission approach that does not provide any time gain ((a) and (b)) and using the simultaneous emission approach that provides a time gain of 20% ((c) and (d)). As expected, the effect of impaired estimation observed in Fig.3.14 generates noise in the final B-mode images. While the spatial resolution of the PSF remains constants, the estimation noise results in a drop in CNR value from $12.3dB$ to $7.25dB$ between the two B-mode images of the cyst phantom. This effect is even more significant if the time gain increases (as a result of the increase in the null space of the matrix $\boldsymbol{A}$) as it can be seen in Fig.3.16. Here, one can see that, indeed if no time gain is obtained the provided image quality is similar, however as the time increases the image quality provided by the simultaneous emission of plane waves decreases as a result of the direct kernel null-space Null($\boldsymbol{A}$).

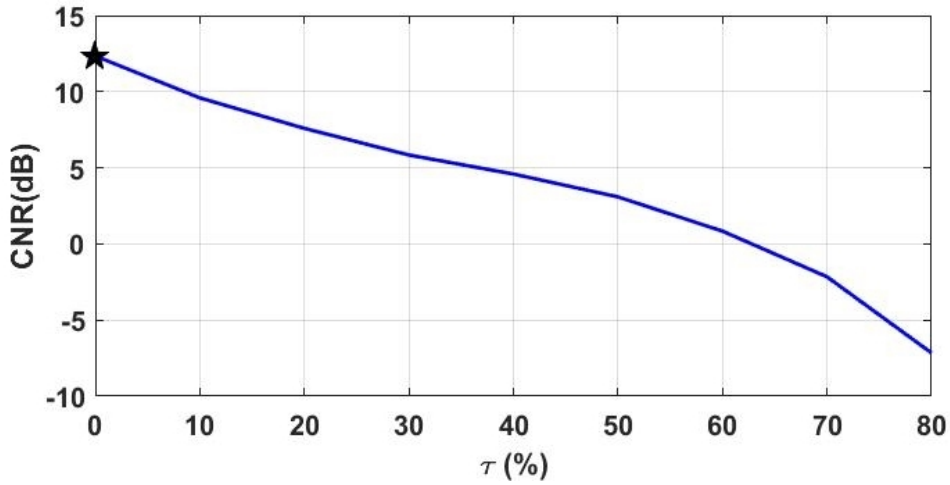

Figure 3.16: Evolution of the CNR as a function of the time gain τ provided by the simultaneous approach (solid blue line). The star represents the CNR value of the cyst B-mode image obtained using the conventional plane wave compounding method.

3.6 In vitro experiments results

The proposed method was also implemented on the research scanner Ula-Op 64. The probe described in Table 3.1 was used, but in this case only $N_{el} = 64$ elements were activated in emission and reception. The first objective was to acquire images of two types of mediums: wire submersed in water (sparse distribution of scatterers) and a cyst phantom (dense distribution of scatterers). The second objective was to compare the results obtained using two methods: classical plane wave imaging and simultaneous emission of plane waves.

In order to fall into the same conditions as the ones described in Subsection 3.4 (anechoic "Blind" and

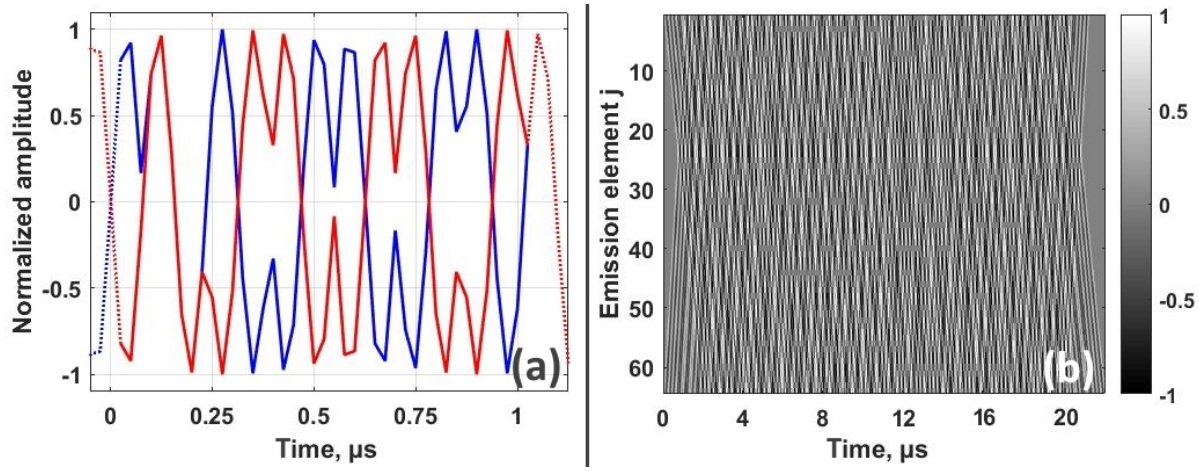

Figure 3.17: (a) - A segment of the waveforms $\boldsymbol{a}^1$ and $\boldsymbol{a}^2$, (b) - Excitations signals ${}_S\boldsymbol{a}_j | j \in [1..64]$. All the signal represented in this figure are sampled at $\nu_s = 50MHz$. The BPSK modulation frequency is $\nu_0 = 8.5MHz$.

"Perturbation" zones) the following protocol was followed:

1. Knowing that the echogenic part of the cyst phantom spans a depth of $\Delta z = 1.5\ cm$, we can deduce the length N_g of its pulse-echo impulse response $\boldsymbol{g}_i^k$ using (3.27). $N_g = 1400$ is obtained.
2. Since the length of the excitation signals N_a are tied to the length of the impulse response of the

medium N_g through (3.26), it was chosen to simultaneously emit only $N_{pwi} = 2$ plane waves ($\theta^1 = -7°$ and $\theta^2 = 4°$). This choice was made in order to limit the length of the excitation signals which first allows a smoother implementation on Ula-Op 64 and second limits the total energy emitted by the probe (thus reduces the risk of causing damage by heating). $N_a \geq (N_{pwi} - 1)N_g + 1 \approx 1400$ is obtained.

3. We generate two pseudo-orthogonal sequences and then BPSK modulate them to obtain $\boldsymbol{a}^1$ and $\boldsymbol{a}^2$. A segment of the waveforms $\boldsymbol{a}^1$ and $\boldsymbol{a}^2$ are shown in Fig.3.17(a).

4. Using $\boldsymbol{a}^1$ and $\boldsymbol{a}^2$ in (3.7), we can compute the signals ${}_S\boldsymbol{a}_j$ (Fig.3.17(b)).

5. ${}_S\boldsymbol{a}_j$ is emitted and ${}_S\boldsymbol{y}_i$ is modeled as seen in (3.8).

6. Since usually the RF data provided by the scanner is not necessarily recorded starting n_0, we can compute n_0 using (3.26) and crop ${}_S\boldsymbol{y}_i$ between n_0 and $n_0 + N_y$ (where $N_y = N_a + N_g - 1$).

7. Since the RF data provided by Ula-Op 64 contains a certain amount of noise, we can apply the same CNR based reasoning seen in Section 3.4, with an inversion using the Moore-Penrose pseudo inverse (3.29).

Fig.3.18(c) shows the evolution of the CNR as a function of the number of truncated singular values for the three estimated images i. e. $k = 1$, $k = 2$ and the compounded image ($\sum_{k=1}^{N_{pwi}=2}$). As it can be seen, all three curves present optimal points ($CNR_{-7°} = 5.6dB$, $CNR_{4°} = 5.3dB$ and $CNR_{final} = 6.02dB$) around $r_0 = 1200$ from a total of $N_y = 2800$ singular values (43%). The compounded image, obtained after truncation of the optimal number of singular values is shown in Fig.3.18(b). Here it can be observed that the CNR of the image obtained using the simultaneous emission is $1.8dB$ lower than the one provided by the conventional plane wave imaging. Since for this image (Fig. 3.18(b)) the hypothesis H3.1 is verified (that links the lengths of different vectors: excitations, pulse echo impulse responses, RF data), this means that no time gain is yet provided. This downgrade of the CNR can be thus explained, as shown in Section 3.4, by the fact that the RF data contains some acquisition noise (H3.2 not verified). This is why the star (which corresponds to the conventional imaging value of CNR), in Fig. 3.18(d), does not correspond with the value of CNR provided by the proposed method with no FAR gain (as opposite to Fig. 3.16, where H3.2 is verified). Moreover, in Fig. 3.18(d) it can be seen that the CNR value provided by the proposed method decreases when the value of the provided time gain increases. This is the effect of the increase in the size of the direct model null-space (Null($\boldsymbol{A}$)) that was described in Sub-section 3.3.3 and whose effects were shown in Section 3.5. Hence, here similar behavior of the CNR curve as the one presented in Fig. 3.16 is observed (CNR drop when τ increases).

Fig.3.19 shows the results obtained on wire phantom acquisitions. By comparing the PSF of the classical approach (Fig.3.19(a)) and the PSF of the proposed approach (Fig.3.19(b)), it may be observed that the provided spatial resolution is improved. This assessment is confirmed by the axial and lateral profiles of the PSFs shown in Fig.3.19(c) and Fig.3.19(d) respectively. Here, one can measure an improvement of 36.31% (from $189\mu m$ to $120\mu m$) in the axial resolution and of 19.75% (from $400\mu m$ to $321\mu m$) in the lateral resolution. This improvement in spatial resolution is expected since, in order to be able to drive the ultrasound probe using Ula-Op 64, the shortest signal that one can use as excitation signals in the classical emission method is a half cycle of a sinusoid centered at $\nu_0 = 8.5MHz$. On the other hand, the proposed method estimates the impulse responses of the medium for each plane wave insonification, thus the spatial resolution is improved. Finally, in Fig.3.19(c) it can be seen that the noise level in the reconstructed image is $20dB$ higher. As explained in Sub-subsection 3.4, this noise is a combination of the computation noise added by the singular value truncation and the amplified acquisition noise. Nonetheless, as shown in Fig.3.18(c), this level of noise is the lowest one can get in these conditions (excitations signals, acquisition noise).

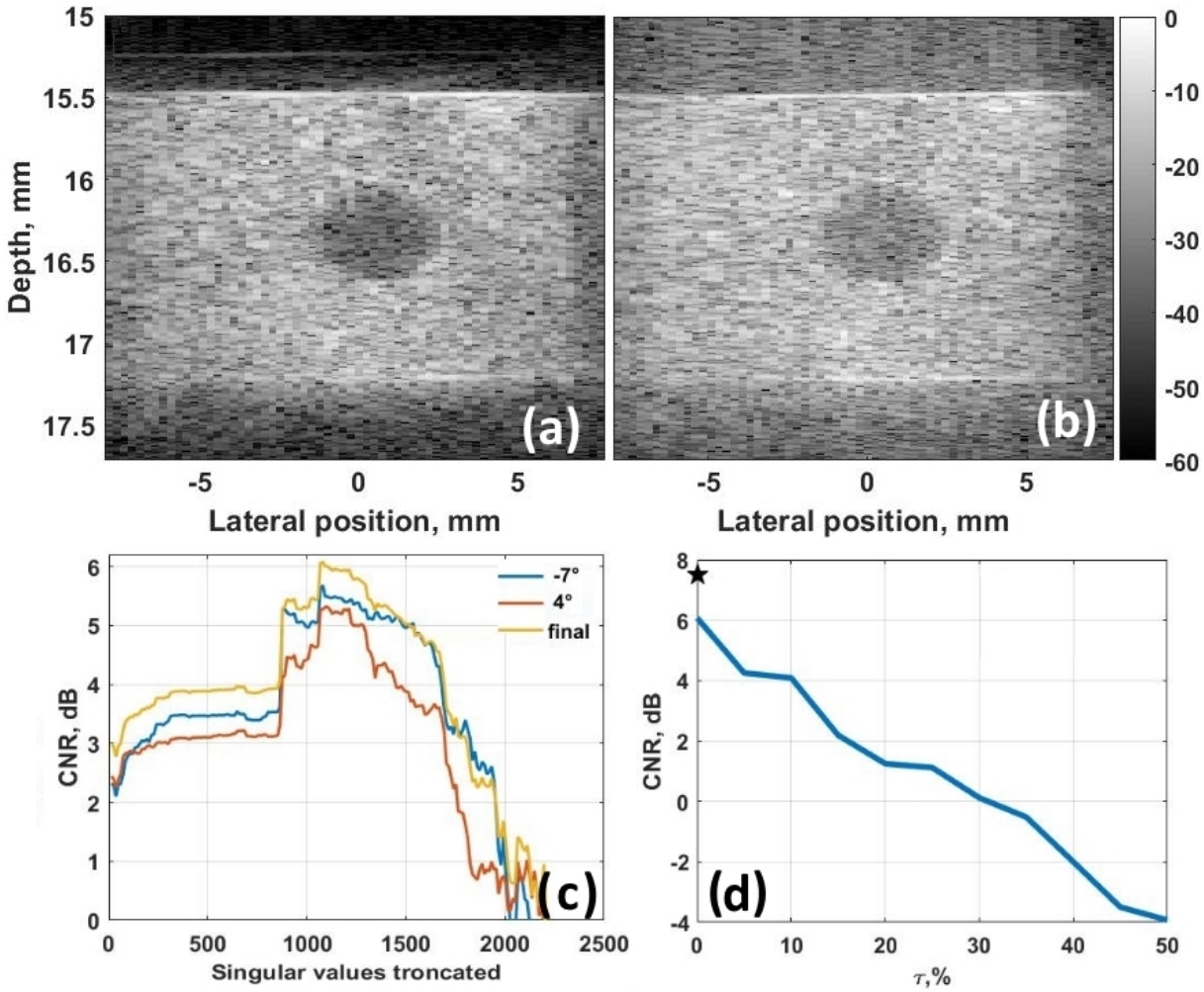

Figure 3.18: Cyst phantom results: (a) - Compounded image obtained using the successive emission of two plane waves, (b) - Compounded image (of best quality) obtained using the simultaneous emission of two plane waves, (c) - Evolution of cyst's CNR as a function of the number of truncated singular values (from a total of $N_y = 2800$).The blue and red lines represent the evolution of the CNR on the images $k = 1$ and $k = 2$ respectively. The green line represents the evolution of the CNR on the compounded image. (d) - Evolution of the cyst's CNR as a function of the time gain τ (3.34). With a star is represented the reference CNR, measured on the image obtained using successive insonifications of plane waves.

3.7 Summary

In this Chapter, an ultrasound imaging method that employs simultaneous emission of plane waves, was presented. Relying on the theoretical background stated in Chapter 2, the direct mathematical model of the ultrasound wave propagation / tissue interaction phenomena, was built. The properties of the resulting kernel were studied, and the necessary requirements on the type / size of the excitation signals, on the size of the imaged medium and on the type / size of the recorded RF data were deduced. It was shown that if these requirements are met, the obtained image quality is exactly the same as the one provided by the conventional imaging technique. It turns out that one of these requirements implies that, despite the simultaneous emission, the time gain provided by the proposed method is null when compared to the conventional plane wave imaging. It was shown, that is possible to violate all of these requirements, however, it was observed that the image quality drops when the provided time gain increases. Even though the choice of estimating the pulse echo impulse responses of the medium (corresponding to each emitted plane wave) using pseudo-inverse based methods has been made, as

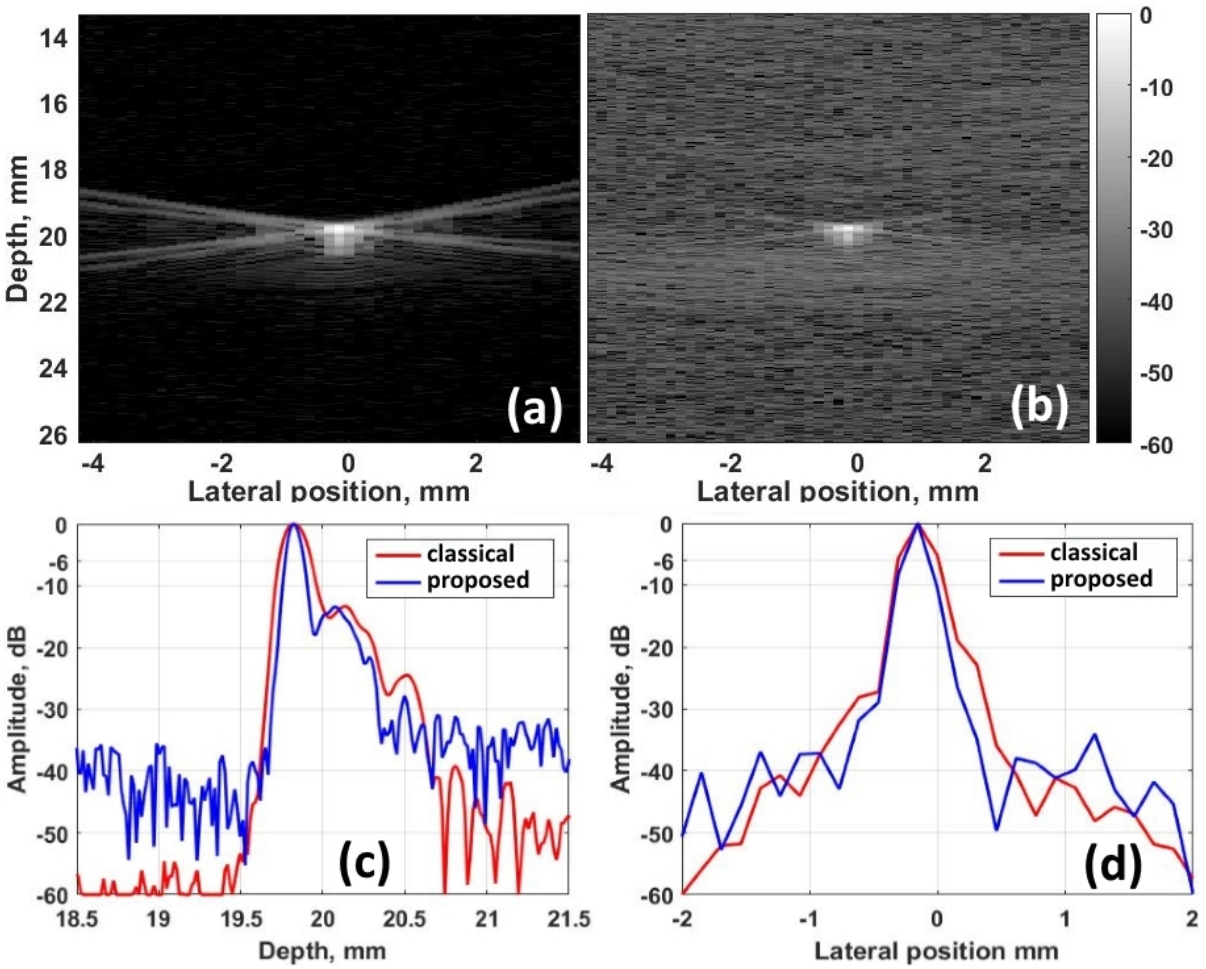

Figure 3.19: Wire phantom results: (a) - Compounded image obtained using the successive emission of two plane waves, (b) - Compounded image (of best quality) obtained using the simultaneous emission of two plane waves, (c) - Axial profiles of the PSFs showed in (a) and (b), (d) - Lateral profiles of the PSFs showed in (a) and (b).

shown in Appendix C, even more complex inversions that use regularization terms behave in the same when the time gain increases. Experimental results proved the feasibility of the proposed method, and once again confirmed the theoretical considerations demonstrated with the simulations. As it turns out, the trade-off between the image quality and frame rate is clearly reflected in the proposed framework, since it corresponds to the well-posedness of an inverse problem, which degrades as the time gain increases.

Thus at this point a novel challenge arises: is it possible to formally express the echoes generated by each plane wave as a function of a invariant entity (that most probably would be the medium TRF)? This would indeed allow to increase the time gain (by emitting more plane wave simultaneously) while not increasing the number of unknowns in the system (since the TRF is constant for all the plane waves emitted simultaneously).

4 Simultaneous Coded Ultrasound Imaging: Estimation of the Tissue Reflectivity Function

We detail in this Chapter an Advanced Model for Coded UltraSound imaging (AMCUS), a method that has the potential not only to increase the conventional plane wave imaging frame acquisition rate, but also to improve the provided image quality. The synopsis of the proposed solution is shown in Fig.4.1. As it can be observed in Fig.4.1(a), similar to the method presented in the previous Chapter, this approach relies on the simultaneous emission of plane waves. However, by comparing Fig.4.1(b) to Fig.3.4(b) and Fig.3.5, it can be seen that whereas the "Wave emission" and "Echo reception" blocks are similar for both methods, the "Wave propagation" and the "Image reconstruction" blocks were greatly changed for the method studied in this Chapter. First, in the "Wave Propagation" block, the pulse echo impulse responses $\boldsymbol{g}_i^k$ of the medium to a specific plane wave k are analytically expressed as a function of the medium TRF $\boldsymbol{\gamma}$ (dashed box in Fig. 4.1(b)). This twitch in the "Wave propagation" block implies also some modifications in the "Image reconstruction" module. Therefore, in order to solve the inherent problem of the echoes mixing in reception, here the filters $\boldsymbol{f}^k$ (corresponding to each excitation signal $\boldsymbol{a}^k$ and computed from each plane wave typical echo $\boldsymbol{e}_k = \boldsymbol{a}^k * \boldsymbol{h} * \boldsymbol{h}$) are used. All the filtered echoes $\hat{\boldsymbol{g}}_i^k$ are then used as the input of an inverse problem approach which provides the TRF estimation $\hat{\boldsymbol{\gamma}}$ as output.

This Chapter is organized as follows. First, we present the reason why this work is necessary and how it could improve the method showed in the previous Chapter. Then, relying on the ultrasound wave propagation theory described in Chapter 2, a linear mathematical model for the received signal by a punctual transducer in a scattering medium when another punctual transducer emits a signal, is built. The established model is then discretized in order to enable a matrix representation of the propagation phenomenon. Furthermore, the model is adapted to take into account the parameters of a real ultrasound probe used for acquisitions. Then, we give a general expression of the propagation model that can be applied to different acquisition schemes (using different ultrasound probes). We adapt our method in order to model the received backscattered echoes obtained using PW emission. Then, a coding technique that enables simultaneous emission of PW is proposed. The direct model is consequently adapted. Finally, an inverse problem approach is applied on the built direct model to obtain an estimation of the tissue reflectivity function. Results are presented and discussed.

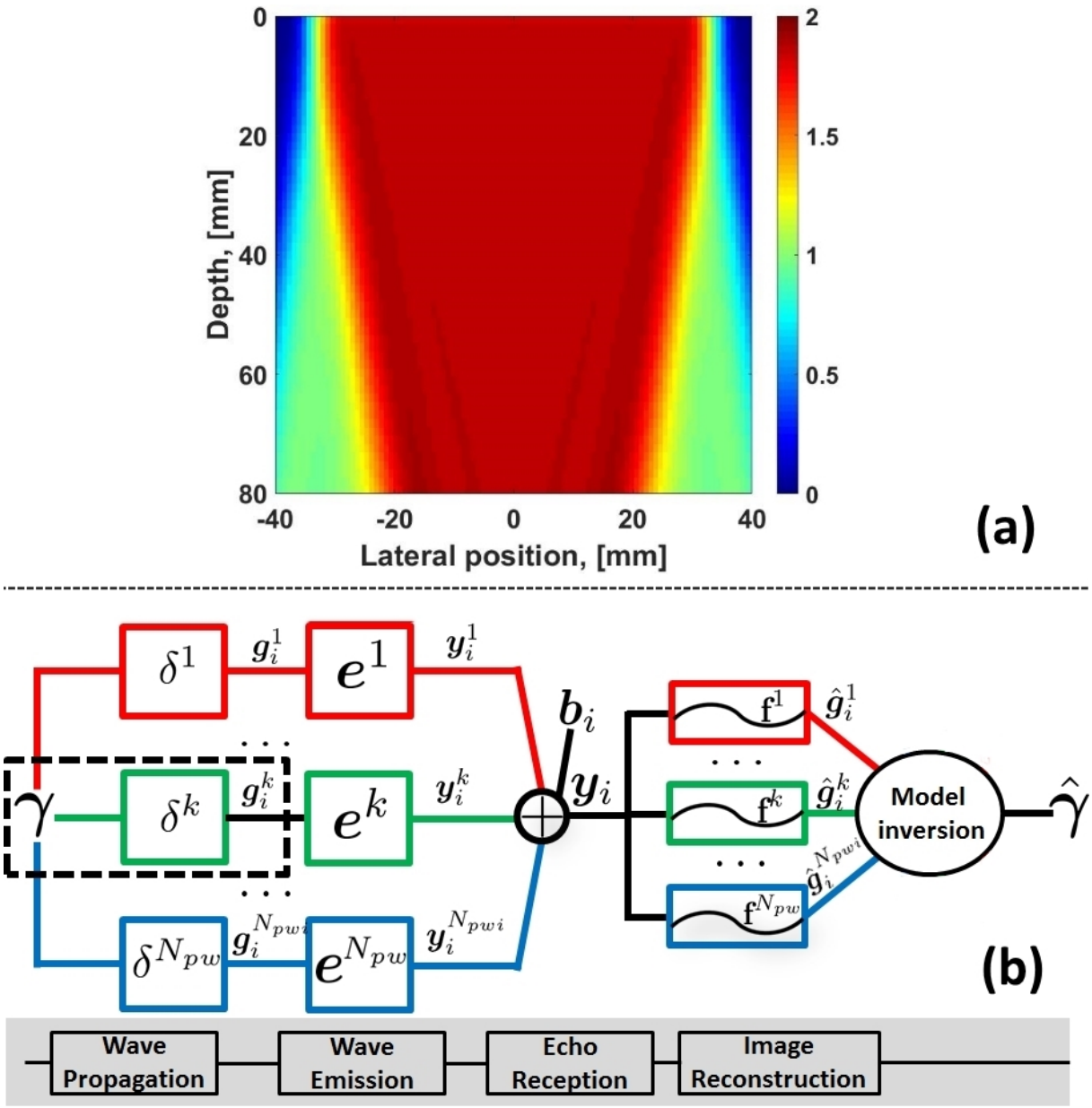

Figure 4.1: Representation of the proposed emission scheme for a given receiver i: (a) - The root mean square of the pressure field generated by the proposed emission scheme. (b) - Schematic representation of the proposed imaging approach (AMCUS). $\boldsymbol{\gamma}$ - tissue reflectivity function, δ^k - pulse excitation of the k^{th} wave, $\boldsymbol{g}_i^k$ - received echoes corresponding to the emission of δ^k (k^{th} wave), $\boldsymbol{e}^k = \boldsymbol{a}^k * \boldsymbol{h} * \boldsymbol{h}$ - typical waveform of the echo received when the excitation $\boldsymbol{a}^k$ was used, $\boldsymbol{a}^k$ - code carried by the k^{th} wave, $\boldsymbol{y}^k$ - received echoes after emission of $\boldsymbol{a}^k$, $\boldsymbol{y}_i$ - recorded echoes when N_{pw} plane waves are emitted simultaneously, $\boldsymbol{f}^k$ - optimal compression filter corresponding to the k^{th} wave, $\hat{\boldsymbol{g}}_i^k$ - estimation of $\boldsymbol{g}_i^k$ obtained from $\boldsymbol{y}_i$. Finally an estimation, $\hat{\boldsymbol{\gamma}}$, of the TRF $\boldsymbol{\gamma}$ is obtained by solving the inverse problem. The "Wave emission" and "Wave propagation" blocks switched positions just in order to simplify the representation.

4.1 On the need of an advanced direct model for the simultaneous emission of ultrasound waves

In this Section a simple simulation is developed in order to better understand the limitations of the method proposed in the previous Chapter. Furthermore, a thought experiment is proposed with the

intent to clarify how this method can be improved in order to provide both a faster frame acquisition rate and a better image quality.

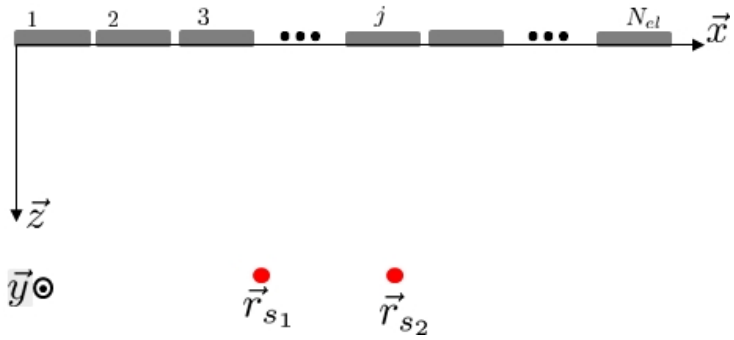

Figure 4.2: Simulation setup used to study the evolution of the impulse response of the medium to plane wave insonifications with wavefronts oriented in different directions. The specifications of the probe used here are detailed in Table 3.1. Two scatterers are placed at the positions $\vec{r}_{s_1} = (10.68, 0, 20)$ mm and $\vec{r}_{s_1} = (20.68, 0, 20)$ mm. Ten plane waves are emitted in directions θ^k between $-10°$ and $10°$.

Suppose the simulation setup shown in Fig.4.2 where a probe with $N_{el} = 64$ elements insonifies a medium with two scatterers placed at the positions $\vec{r}_{s_1} = (10.68, 0, 20)$ mm and $\vec{r}_{s_1} = (20.68, 0, 20)$ mm by emitting $N_{pwi} = 10$ plane waves in directions θ^k spanning from $\theta^1 = -10°$ to $\theta^{N_{pwi}} = 10°$.

In the previous Chapter was shown that the received echoes, if all the plane waves where emitted simultaneously, can be written as follows:

$$
\begin{aligned}
{}_S\boldsymbol{y}_i &= \boldsymbol{A} \cdot \boldsymbol{g}_i + \boldsymbol{b}_i \\
\text{with: } \boldsymbol{A} &= \begin{bmatrix} \boldsymbol{A}^1 & \boldsymbol{A}^2 & \cdots & \boldsymbol{A}^{N_{pwi}} \end{bmatrix} \\
\text{and } \boldsymbol{g}_i &= \begin{bmatrix} \boldsymbol{g}_i^1 \\ \boldsymbol{g}_i^2 \\ \vdots \\ \boldsymbol{g}_i^{N_{pwi}} \end{bmatrix}
\end{aligned}
\tag{4.1}
$$

where, if no additional hypothesis are made, the matrix $\boldsymbol{A}$ has $N_{pwi}(N_y + N_a - 1)$ columns and N_y lines. Under such conditions, the inverse problem based on (4.1) is heavily under-determined. As showed in Chapter 3, $\boldsymbol{A}^k$ are Toeplitz matrices built using the $\boldsymbol{a}^k$ excitations. In the previous Chapter, through a hypothesis that allow to reduce the number of unknowns in the problem and using a regularization term on the pulse echo impulse responses of the medium stored in $\boldsymbol{g}_i$, it was possible to achieve the same image quality and frame rate as the ones provided by the classical plane wave imaging. However as one was increasing the frame rate, the resulting image quality was dropping as a consequence of an ill-posed inverse problem. In the first column of the Fig.4.3 is shown the evolution of the impulse response of the medium $\boldsymbol{g}_1^k$ seen by the element $i = 1$ as a function of the plane wave emission angle θ^k. As one can see, for different angles, the impulse response of the medium changes significantly as a function of the emission angle, which means that the total vector $\boldsymbol{g}_1$ (4.1) cannot be regularized over θ, which would allow to decrease the number of unknowns. Now by looking at the second column of the Fig.4.3, it can be seen that even for the same angle $\theta^6 = 0$, the impulse responses $\boldsymbol{g}_i^6$ seen by different elements i of the transducer are different. This denies another possibility that could improve the well-posedness of the inverse problem which consists in the concatenation of the signals ${}_S\boldsymbol{y}_i$ received from different elements i in order to increase the total number of equation in the system.

At this point, one can imagine a simple thought experiment. To begin, consider an emission of a single plane wave k. Now suppose the existence of an vector $\boldsymbol{\chi}$ that would allow the following

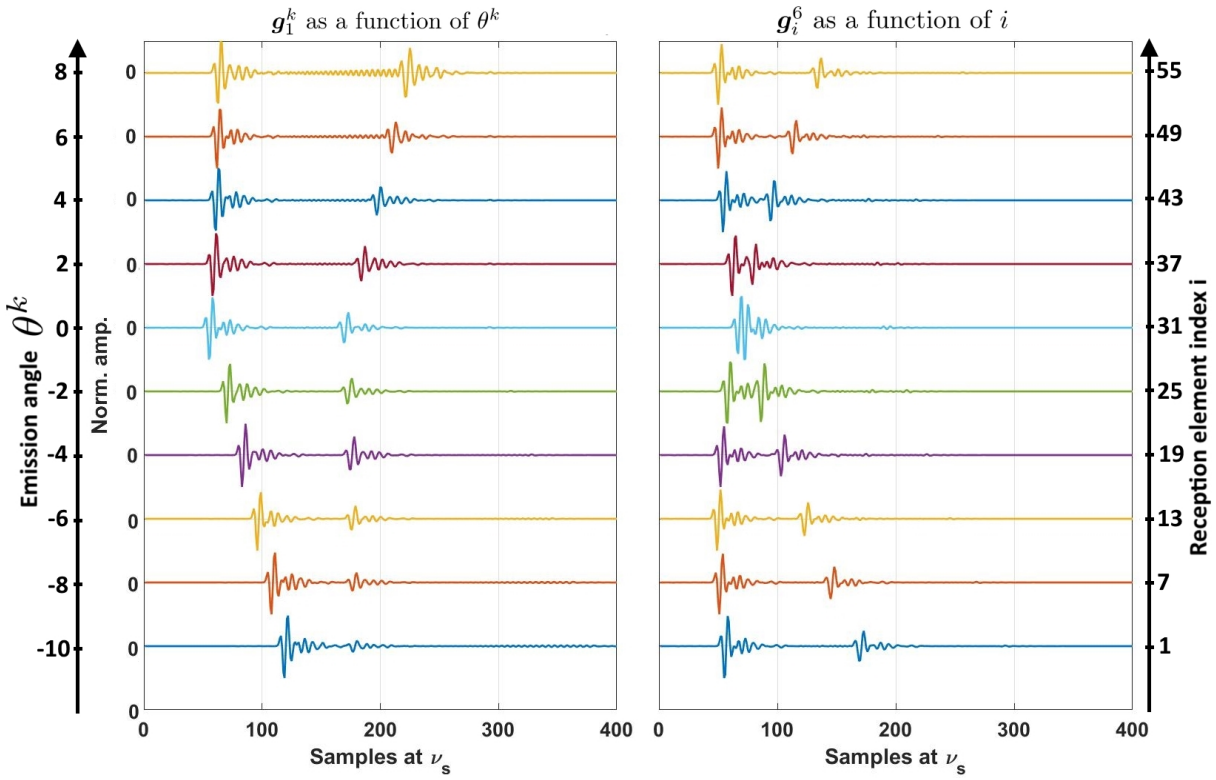

Figure 4.3: Evolution of the impulse responses of the medium resulted from the simulation whose setup is presented in Fig. 4.2. The first column represents the evolution of the impulse response of the medium $\boldsymbol{g}_1^k$ seen by the element $i = 1$ as a function of the ten emission angles θ^k. The second column represents the evolution of the impulse responses $\boldsymbol{g}_i^6$, when the emission angles is $\theta^6 = 0°$, as a function of the receiving element i.

formulation:

$$\boldsymbol{y}_i^k = \boldsymbol{A}^k \cdot \boldsymbol{C}_i^k \cdot \boldsymbol{\chi} + \boldsymbol{b}_i, \, \forall \, i \in [1..N_{el}] \tag{4.2}$$

where $\boldsymbol{y}_i^k$ are the signals received by the i^{th} element of the probe when the plane wave k is emitted. In (4.2) the matrix $\boldsymbol{C}_i^k$ relates $\boldsymbol{\chi}$ to $\boldsymbol{g}_i^k$ through $\boldsymbol{g}_i = \boldsymbol{C}_i^k \cdot \boldsymbol{\chi}$. At this point one cannot be sure that the inverse problem based on (4.2) is well-posed, however, since the vector $\boldsymbol{\chi}$ is constant for all the elements i, one could concatenate all the direct systems given by the N_{el} receiving elements in order to increase the total number of equations by a factor of N_{el}, while the number of unknowns (given by the size of the vector $\boldsymbol{\chi}$) remains constant.

Indeed a direct model such as (4.2) could improve significantly the well-posedness of the inverse problem in the context of plane wave propagation modeling. However, at this point several additional questions need to be answered: What does the vector $\boldsymbol{\chi}$ represent? How can we calculate the matrices $\boldsymbol{C}_i^k$? Is it sufficient, only with N_{el} concatenation of linear systems, to achieve a well posed inverse problem? In the following sections of this Chapter an answer to each of these questions will be carefully constructed.

4.2 On the vector χ, could it be the TRF?

To resume the reasoning started in the previous Section, here the main idea is to find a fitting vector $\boldsymbol{\chi}$ that will allow writing each pulse-echo impulse response of the medium to a plane wave insonification

as the following matrix product:

$$\boldsymbol{g}_i^k = \boldsymbol{C}_i^k \cdot \boldsymbol{\chi},\ \forall i \in [1..N_{el}] \tag{4.3}$$

In equations (2.31) and (2.32) of Chapter 2, complete analytical relations where deduced for the spatial impulse responses of the probe elements j and i in emission ($g_j(\vec{r},t)$) and reception ($g_i(\vec{r},t)$) respectively. As it was shown in (2.31)[1], for one pair of elements (j,i), the spatial impulse response at the point $\vec{r}$ of the medium can be computed as the temporal convolution between $g_j(\vec{r},t)$ and $g_i(\vec{r},t)$:

$$g_{ji}(\vec{r},t) = g_j(\vec{r},t) *_t g_i(\vec{r},t) \Longleftrightarrow$$

$$g_{ji}(\vec{r},t) = \left[\int_S \frac{1}{2\pi\|\vec{r}-\vec{r}_j-\vec{r}_S\|_2}\delta\Big(t - t_j - \frac{\|\vec{r}-\vec{r}_j-\vec{r}_S\|_2}{c_m}\Big)\mathrm{d}^2\vec{r}_S\right] *_t \left[\int_S \frac{1}{2\pi\|\vec{r}-\vec{r}_i-\vec{r}_S\|_2}\delta\Big(t - \frac{\|\vec{r}-\vec{r}_i-\vec{r}_S\|_2}{c_m}\Big)\mathrm{d}^2\vec{r}_S\right] \tag{4.4}$$

where t_j is the emission delay for the probe element j. At this point, by combining (2.34) and (4.4), it can be deduced that the pulse echo impulse response of the medium (that contains density inhomogeneities in the volume V) when the probe element j emits and the probe element i receives, can be written as follows:

$$g_{ji}(t) = \int_V \gamma(\vec{r})\Big[g_j(\vec{r},t) *_t g_i(\vec{r},t)\Big]\mathrm{d}^2\vec{r} \tag{4.5}$$

where $\gamma(\vec{r})$ represents the TRF value at the position $\vec{r}$. In (4.5) an appealing formulation starts to appear. In fact, one can observe that in the expression of $g_{ji}(t)$, two terms can be separated. The first term, represented by the convolution product $g_j(\vec{r},t) *_t g_i(\vec{r},t)$, can be evaluated for each position $\vec{r}$ inside the medium and it depends closely on the shape of the ultrasound elements (through their surface S and their positions $\vec{r}_j$ and $\vec{r}_i$). The second term however, which represents the tissue reflectivity function ($\gamma(\vec{r})$), is completely unknown and its recovery is the object of the ultrasound imaging process. Moreover, in (4.5) it can be seen that for different pairs of elements (j,i), the signal $g_{ji}(t)$ evolves since the positions $\vec{r}_j$ and $\vec{r}_i$ change. Nonetheless, since the imaged medium remains the same, the value of the TRF in each point of the medium $\vec{r}$ does not change from a pair of elements (j,i) to another. Thus, (4.5) can be reduced to:

$$g_{ji}(t) = (\mathsf{C}_{ji}\gamma)(t)$$
$$\text{with: } \big(\mathsf{C}_{ji}\gamma\big)(t) = \int_V \gamma(\vec{r})\Big[g_j(\vec{r},t) *_t g_i(\vec{r},t)\Big]\mathrm{d}^2\vec{r} \tag{4.6}$$

where C_{ji} is an integral operator which represents the spatial impulse response of the elements pair (j,i) at each point $\vec{r}$ of the medium. Now, one can observe that expressions (4.6) and (4.3) are very similar, with the only difference that one is in continuous time domain and the second is in the discrete time domain:

$$\boldsymbol{\chi} = \boldsymbol{\gamma} \tag{4.7}$$

Thus, it can be concluded that in (4.2) and (4.3) the vector $\boldsymbol{\chi}$ can be replaced by a discrete version of the TRF $\boldsymbol{\gamma}$. Moreover, it can be seen that the matrix $\boldsymbol{C}_{ji}$ is nothing else than a discrete version of the

[1] By contrast to the formulation shown in Chapter 2, here the choice to blend the emission delays t_j inside the medium spatial impulse responses $g_j(\vec{r},t)$ has been made.

integral operator C_{ji}.

4.3 On the far field approximation

In this Section, the hypothesis of far field propagation of the ultrasound wave, introduced in Sub-section 2.2.1, will be revised.

Before starting the study of the matrix $\mathbf{C}_{ji}$, consider the following simulation setup (Field II). The LA523E probe (Table 3.1) is used in emission and reception. Only one element ($(j,i) = (32,32)$) is active in emission and reception. The emission delay is null ($t_{32} = 0$ s). Seven pairs of emission / reception events are performed, each time the medium containing a single scatterer placed at different positions equally remote from the emission element by a distance of $\|\vec{r}_{s_q} - \vec{r}_{32}\|_2 = 20$ mm. The excitation signal and the acousto-electrical impulse responses of the probe elements were set to be Dirac impulsions. This simulation setup is presented in Fig.4.4(a). As it was shown in Sub-section 2.2.1, under the

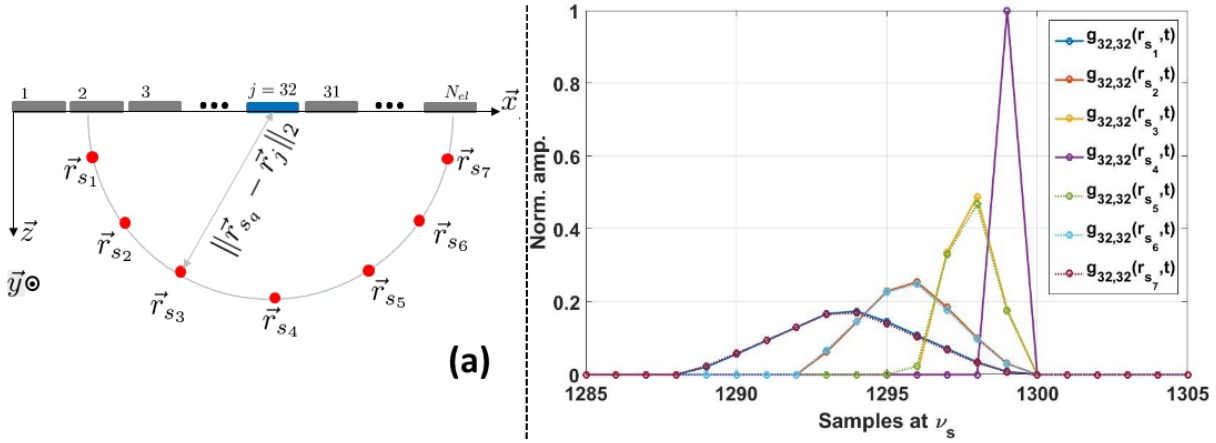

Figure 4.4: (a) - Simulation setup used to study the evolution of the spatial impulse response $g_{32,32}(\vec{r},t)$ as a function of the position $\vec{r}$. Only the element $j = i = 32$ is active in emission / reception. Seven different positions $\vec{r}_{s_q}$, uniformly distributed on an arc of radius $\|\vec{r}_{s_q} - \vec{r}_{32}\|_2 = 20$ mm centered in $\vec{r}_{32}$, where tested. (b) - Evolution of the spatial impulse response $g_{32,32}(\vec{r},t)$ as a function of the position $\vec{r}_{s_q}$. Here, all the impulse responses are normalized with respect to $g_{32,32}(\vec{r}_{s_4},t)$.

hypothesis of far field scattering, the pulse echo spatial impulse response in the point $\vec{r}$ when element j emits and element i receives can be written as follows:

$$g_{ji}(\vec{r},t) = g_j(\vec{r},t) *_t g_i(\vec{r},t) \underset{\text{far field}}{\approx} \frac{S^2 \delta\left(t - t_j - \frac{\|\vec{r}-\vec{r}_j\|_2 + \|\vec{r}-\vec{r}_i\|_2}{c_m}\right)}{4\pi^2 \|\vec{r}-\vec{r}_j\|_2 \|\vec{r}-\vec{r}_i\|_2} \tag{4.8}$$

By applying this formula to the simulation setup showed in Fig.4.4(a), one should obtain the following results. Since all the scatterers are equally spaced from the element $j = i = 32$, this implies that the term $S^2/\left(4\pi^2 \|\vec{r}_{s_q} - \vec{r}_j\|_2 \|\vec{r}_{s_q} - \vec{r}_i\|_2\right)$ is constant for all the seven scatterers q. Thus, one would expect in Fig.4.4(b) all the pulse echo spatial impulse responses $g_{32,32}(\vec{r}_{s_q},t)$ to have the same amplitude, which is clearly not the case in the simulation results. Moreover, the fact that all the scatterers are equally spaced from the element $j = i = 32$, using (4.8), one also can deduce that $g_{32,32}(\vec{r}_{s_q},t)$ should contain only a Dirac impulsion delayed by a lag of $\left(\|\vec{r}_{s_q} - \vec{r}_j\|_2 + \|\vec{r}_{s_q} - \vec{r}_i\|_2\right)/c_m = 25.98\ \mu s$ which corresponds to 1299 samples at $\nu_s = 50\ MHz$. However, this tendency, again, is not quite the same as the one observed in Fig.4.4(b). These simulation results show that only $g_{32,32}(\vec{r}_{s_4},t)$ falls perfectly under the previous predictions, however all the six other spatial impulse responses not only have their peaks earlier but also contain a sum of Dirac impulsions (instead of one), each delayed with a different lag. This suggests that the approximation made in (4.8) is not sufficiently accurate in order to model all

the scatterings inside the medium, in other words: the far field hypothesis is not respected for all the scatterers $\vec{r}_{s_q}$.

In order to understand the spatial pulse echo impulse responses showed in Fig.4.4(b), one should

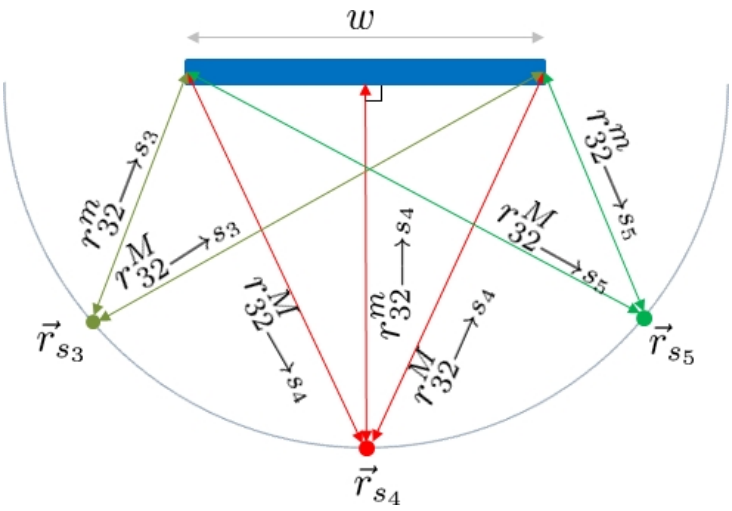

Figure 4.5: Zoom on the element $j = i = 32$ from the Fig.4.4(a). w represents the width of the element. $r^m_{32\to s_q}$ and $r^M_{32\to s_q}$ represent the shortest and the longest euclidean distances separating the probe element from the scatterer q.

consider the Huygens-Fresnel principle which states that every point on a wavefront is itself a source of spherical wavelets. Under such conditions, one can see the vibrating surface S of the probe element j (i in reception) as an infinity of points $u \in S_j$ (resp. $v \in S_i$) that are generating (resp. receiving), individually, spherical waves that propagate inside the medium. Now, since these points are infinitely small, their emitting waves have a far field behavior everywhere inside the medium. In such case, one can write their pulse spatial impulse response at the medium point $\vec{r}$ as follows:

$$\begin{cases} g_u(\vec{r},t) = \dfrac{\delta\left(t - t_u - \frac{\|\vec{r}-\vec{r}_u\|_2}{c_m}\right)}{2\pi\|\vec{r}-\vec{r}_u\|_2} \\ g_v(\vec{r},t) = \dfrac{\delta\left(t - \frac{\|\vec{r}-\vec{r}_v\|_2}{c_m}\right)}{2\pi\|\vec{r}-\vec{r}_v\|_2} \\ g_{uv}(\vec{r},t) = g_u(\vec{r},t) *_t g_v(\vec{r},t) = \dfrac{\delta\left(t - t_j - \frac{\|\vec{r}-\vec{r}_u\|_2 + \|\vec{r}-\vec{r}_v\|_2}{c_m}\right)}{4\pi^2\|\vec{r}-\vec{r}_u\|_2\|\vec{r}-\vec{r}_v\|_2} \end{cases} \tag{4.9}$$

where $\vec{r}_u$ and $\vec{r}_v$ are the positions of the points on the surfaces S_j (emission element) and S_i (reception element) respectively. In such conditions $t_u = t_j$. Now, the signal received by i can be seen as a continuous sum of all the signals received by each punctual receiver v, which receives respectively the continuous sum of all the signals emitted by each point source u. At this point, one can rewrite (4.4) as follows:

$$\begin{aligned} g_{ji}(\vec{r},t) &= \int_{S_j}\int_{S_i} \Big[g_u(\vec{r},t) *_t g_v(\vec{r},t) \Big] \, \mathrm{d}\vec{r}_v \, \mathrm{d}\vec{r}_u \iff \\ g_{ji}(\vec{r},t) &= \int_{S_j}\int_{S_i} \left[\frac{\delta\left(t - t_j - \frac{\|\vec{r}-\vec{r}_u\|_2 + \|\vec{r}-\vec{r}_v\|_2}{c_m}\right)}{4\pi^2\|\vec{r}-\vec{r}_u\|_2\|\vec{r}-\vec{r}_v\|_2} \right] \mathrm{d}\vec{r}_v \, \mathrm{d}\vec{r}_u \end{aligned} \tag{4.10}$$

In (4.10) one can observe that the pulse echo spatial impulse response of the medium at the point $\vec{r}$ can be seen as a continuous sum of Dirac impulsions.

Now consider the Fig.4.5, where a zoom on the element $j = i = 32$ from Fig.4.4(a) is represented. As one can observe, for each scatterer q one can find a point that is the closest to the scatterer position (at the distance $\|\vec{r} - \vec{r}_u\|_2 = r^m_{32\to s_q}$) and one point that is the furthest from the scatterer position (at the distance $\|\vec{r} - \vec{r}_u\|_2 = r^M_{32\to s_q}$). This implies that all the other Dirac impulsions will have a lag somewhere between the limits set by these two points: minimal arrival time $2r^m_{32\to s_q}/c_m$ and maximal arrival time $2r^M_{32\to s_q}/c_m$. Now, it turns out that for Fig.4.4(a) (zoomed-in in Fig.4.5) setup, $r^m_{32\to s_4} = 20\ mm$ and $r^M_{32\to s_4} = 20.0003\ mm$. These distances generate a minimal arrival time of 25.974 μs and a maximal arrival time of 25.978 μs. The difference between these two time lags is of 0.004 μs which corresponds to 0.2 samples at $\nu_s = 50\ MHz$. This is why $g_{32,32}(\vec{r}_{s_4}, t)$ appears as a Dirac impulsion in Fig.4.4(b). For the scatterer $q = 3$, the difference between the minimal and maximal propagation paths generate a time lag of 0.06 μs between the fastest and slowest arrivals. This corresponds to 3 samples at $\nu_s = 50\ MHz$ which again is coherent with $g_{32,32}(\vec{r}_{s_3}, t)$ curve showed in Fig.4.4(b). Since the positions of the scatterer $q = 3$ is exactly the same as the one of $q = 5$ similar behavior is obtained for $q = 5$. Using the same reasoning, 7 and 11 samples are obtained for $q = 2$ and $q = 1$ (by symmetry resp. $q = 6$ and $q = 7$).

Thus, it can be concluded that in order to faithfully approximate the spatial impulse response of the medium, one needs to account for the near field propagation / scattering of the emitted ultrasound waves. The consequence of this observation on the computation of the integral operator $\mathscr{C}_{ji}$ and its associated discrete counterpart $\boldsymbol{C}_{ji}$ is detailed in the next Section.

4.4 On the computation of the matrix $\boldsymbol{C}_{ji}$

In this Section the computation of the $\boldsymbol{C}_{ji}$ matrix is addressed. However, as it was deduced in the previous Section, the pulse echo impulse response of the medium to the element pair (j, i) can be seen as a superposition of such impulse responses of punctual sources (u, v). Thus, in order to obtain a formula for the computation of $\boldsymbol{C}_{ji}$, it would be more appropriate to start by computing the matrix $\boldsymbol{C}_{uv}$ which allows to model the pulse echo impulse of the medium when the punctual source u emits an ultrasound wave ($u \in S_j$) and the punctual source v receives ($v \in S_i$) its echoes.

4.4.1 Computation of the matrix $\boldsymbol{C}_{uv}$

In the previous Section, the relation (4.9) for the spatial impulse responses of the punctual transducers u and v in a medium point $\vec{r}$ has been deduced ($g_u(\vec{r}, t)$ and $g_v(\vec{r}, t)$ respectively). (4.9) gives also the pulse echo spatial impulse response at the medium point $\vec{r}$ when the transducer u emits and the transducer v receives the signal ($g_{uv}(\vec{r}, t)$). Thus, by applying (4.6) to (4.9), one can deduce the following expression:

$$\begin{gathered} g_{uv}(t) = (\mathsf{C}_{uv}\gamma)(t) \\ \text{with: } \big(\mathsf{C}_{uv}\gamma\big)(t) = \int_V \gamma(\vec{r})\Big[g_u(\vec{r}, t) *_t g_v(\vec{r}, t)\Big]\,\mathrm{d}^2\vec{r} \end{gathered} \tag{4.11}$$

where $g_{uv}(t)$ represents the pulse echo impulse response of the medium when u emits and v receives. C_{uv}, similar to C_{ji}, is an integral operator which represents the spatial impulse response of the point transducers pair (u, v) at each point $\vec{r}$ of the medium. As previously stated in Section 4.2, the matrix $\boldsymbol{C}_{uv}$ represents the discrete version of the operator C_{uv}. An essential question arises at this point: "How to discretize the integral operator C_{uv}?". A straightforward answer to this question is to adapt $\boldsymbol{C}_{uv}$ to the discretization that the domain $\gamma(\vec{r})$ and the codomain $g_{uv}(t)$ undergo. As it was shown in Chapter 2, the pulse echo impulse responses of medium to the emission / reception by the element pair (j, i) are discretized at the sampling frequency ν_s. This implies that the pulse echo impulse response of

the medium to the emission / reception by the punctual transducers pair (u, v) is also sampled at the frequency ν_s. For the $\gamma(\vec{r})$ domain however, no discretization appears naturally. Later in this section the choice of the medium discretization, will be addressed, however, for now, suppose a discretization with steps Δx and Δz in the directions $\vec{x}$ and $\vec{z}$ respectively. Following this discretization of the medium, a two dimensional grid $\mathbf{\Omega}$ is obtained (Fig.4.6(a)). Suppose for now that this grid has N_x and N_z nodes along the directions $\vec{x}$ and $\vec{z}$ respectively. It can be thus concluded that the discrete domain $\mathbf{\Omega}$ contains only $N_x \times N_z$ components $\boldsymbol{r} = (x_{\mathbf{\Omega}}, 0, z_{\mathbf{\Omega}}) \in \mathbf{\Omega}$. Therefore, the discrete counterpart of the TRF $\gamma(\vec{r})$ can be seen as a vector $\boldsymbol{\gamma}$ where each of its entry m represents the tissue scattering coefficient at the $\mathbf{\Omega}$ grid cell defined by $\boldsymbol{r}$ with:

$$m = \lfloor \frac{x_{\mathbf{\Omega}}}{N_x \Delta x} \rfloor N_z + \frac{z_{\mathbf{\Omega}}}{\Delta z} \tag{4.12}$$

Indeed, since each grid node $\boldsymbol{r}$ corresponds to a physical point inside the continuous medium, it can

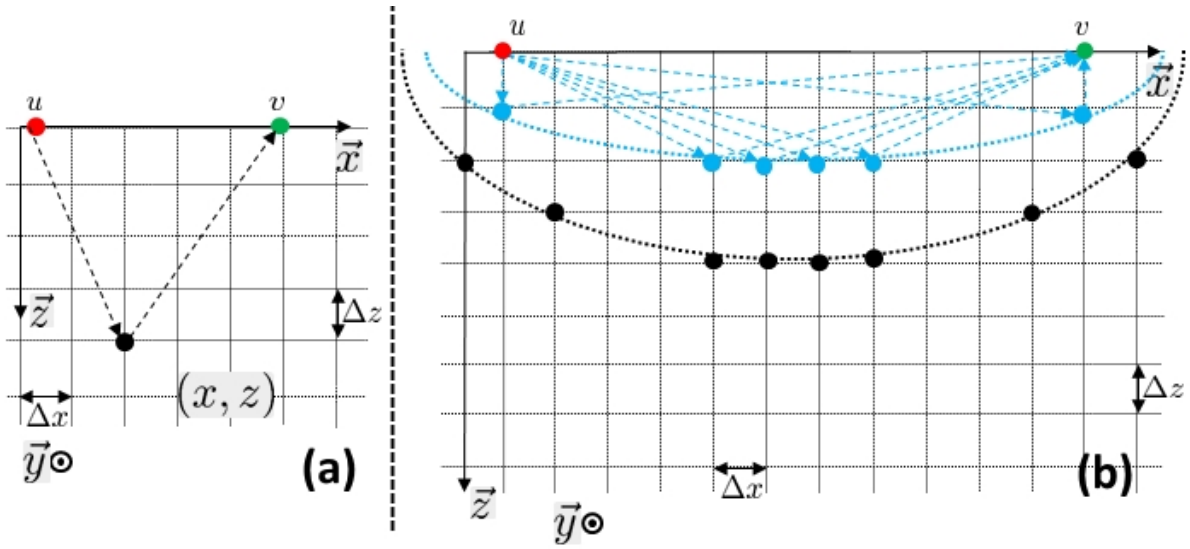

Figure 4.6: (a) - Proposed discretization for the imaged medium with steps Δx and Δz in the directions $\vec{x}$ and $\vec{z}$ respectively. The scatterers are supposed to be placed in the nodes of the generated grid. (b) - Representation of two sets of nodes $\vec{r}$ (blue and black points respectively) that contribute for two different samples n of the vector $\boldsymbol{g}_{uv}$. The curves that support this points are elliptical arcs.

be concluded that the value of the discrete TRF in $\boldsymbol{r}$ is equal to the value of the continuous TRF in $\boldsymbol{r}$ thus: $\boldsymbol{\gamma}[m] = \gamma(\boldsymbol{r})$. At this point one can adapt (4.11) to the new generated grid $\mathbf{\Omega}$. The following relation is obtained:

$$\begin{gathered} g_{uv}(t) = \sum_{\boldsymbol{r}\in\mathbf{\Omega}} \left[\frac{\delta\left(t - \frac{\|\boldsymbol{r}-\vec{r}_u\|_2 + \|\boldsymbol{r}-\vec{r}_v\|_2}{c_m}\right)}{4\pi^2 \|\boldsymbol{r}-\vec{r}_u\|_2 \|\boldsymbol{r}-\vec{r}_v\|_2} \boldsymbol{\gamma}[m] \right] \Longleftrightarrow \\ g_{uv}(t) = (\mathbf{C}_{uv}\boldsymbol{\gamma})(t) \quad \text{with: } \left(\mathbf{C}_{uv}\gamma\right)(t) = \sum_{\boldsymbol{r}\in\mathbf{\Omega}} \gamma(\boldsymbol{r}) \frac{\delta\left(t - \frac{\|\boldsymbol{r}-\vec{r}_u\|_2 + \|\boldsymbol{r}-\vec{r}_v\|_2}{c_m}\right)}{4\pi^2 \|\boldsymbol{r}-\vec{r}_u\|_2 \|\boldsymbol{r}-\vec{r}_v\|_2} \end{gathered} \tag{4.13}$$

As previously stated, during the RF data recording, the pulse echo impulse response of the medium is discretized at a rate ν_s. This means that each entry n of the vector $\boldsymbol{g}_{uv}$ represents a time instant $t = t_0 + n/\nu_s$ where t_0 represents the recording start time. By applying this effect to (4.13), it can be deduced that for each sample n only some echoes will contribute to the amplitude of this particular

sample. Indeed, in (4.13) it can be seen that:

$$\delta\left(t_0+\frac{n}{\nu_s}-\frac{\|\boldsymbol{r}-\vec{r}_u\|_2+\|\boldsymbol{r}-\vec{r}_v\|_2}{c_m}\right)=\begin{cases}1, \text{ if } \frac{\|\boldsymbol{r}-\vec{r}_u\|_2+\|\boldsymbol{r}-\vec{r}_v\|_2}{c_m}=t_0+\frac{n}{\nu_s}\\ 0, \text{ if } \frac{\|\boldsymbol{r}-\vec{r}_u\|_2+\|\boldsymbol{r}-\vec{r}_v\|_2}{c_m}\neq t_0+\frac{n}{\nu_s}\end{cases} \tag{4.14}$$

In Fig.4.6 are schematically represented two sets of nodes $\boldsymbol{r}$ (blue and black points respectively) that contribute for two different samples n of the vector $\boldsymbol{g}_{uv}$. As it can be seen, these points are placed on two arcs of ellipses whose foci are the points $\vec{r}_u$ and $\vec{r}_v$. These elliptical shapes of the curves are due to the fact that for a given sample n the distance between $\vec{r}_u$, $\boldsymbol{r}$ and $\vec{r}_v$ should be constant in order for the echo in $\boldsymbol{r}$ to contribute to the amplitude of this sample. This definition describes the behavior of points distributed along an elliptical shape. At this point it remains to find the matrix $\boldsymbol{C}_{uv}$ that allows linking the N_g long vector $\boldsymbol{g}_{uv}$ to the $N_x \times N_z$ long vector $\boldsymbol{\gamma}$. First, it can be deduced that the matrix $\boldsymbol{C}_{uv}$ has N_y lines and N_xN_z columns. Then, one can observe that since each column m of the matrix $\boldsymbol{C}_{uv}$ is related to a point $\boldsymbol{r}\in\boldsymbol{\Omega}$ through (4.12), for each point $\boldsymbol{r}$ the entries along only column m of $\boldsymbol{C}_{uv}$ will be modified as follows: m will be null everywhere except at the line n which corresponds to the time $n/\nu_s=(t-t_0)$ when the echo generated in $\boldsymbol{r}$ arrives at v. Therefore, this entry $[n,m]$ takes as value the geometrical spreading term $1/\left(4\pi^2\|\boldsymbol{r}-\vec{r}_u\|_2\|\boldsymbol{r}-\vec{r}_v\|_2\right)$. Thus, $\boldsymbol{C}_{uv}$ is built as follows:

$$\boldsymbol{C}_{uv}[n,m]=\begin{cases}\frac{1}{4\pi^2\|\boldsymbol{r}-\vec{r}_u\|_2\|\boldsymbol{r}-\vec{r}_v\|_2}, \text{ if } \frac{\|\boldsymbol{r}-\vec{r}_u\|_2+\|\boldsymbol{r}-\vec{r}_v\|_2}{c_m}=t_0+\frac{n}{\nu_s}\\ 0, \text{ if } \frac{\|\boldsymbol{r}-\vec{r}_u\|_2+\|\boldsymbol{r}-\vec{r}_v\|_2}{c_m}\neq t_0+\frac{n}{\nu_s}\end{cases} \tag{4.15}$$

While this method of $\boldsymbol{C}_{uv}$ computation is pretty straightforward, it contains an important drawback. In order to understand its origins, consider the Fig.4.6(b). Here it can be seen that some grid nodes do not belong to any elliptical arcs with foci inside $\vec{r}_u$ and $\vec{r}_v$, in other words: the arrival time for some points $\boldsymbol{r}$ of the grid $\boldsymbol{\Omega}$ falls between two samples n and $n+1$ of the vector $\boldsymbol{g}_{uv}$. A simple solution to this problem would be to set non null the entry sample n which is the closest to the arrival time t i.e. $n=\lfloor(t-t_0)\nu_s\rceil$ (where $\lfloor\,\rceil$ represents the nearest integer function). In order to conclude if this is a fitting solution, a good validation method is to study its effect on the received signal $\boldsymbol{y}_{uv}$, defined as follows:

$$\boldsymbol{y}_{uv}=\boldsymbol{e}*\boldsymbol{g}_{uv} \quad \text{with: } \boldsymbol{e}=\boldsymbol{a}*\boldsymbol{h}*\boldsymbol{h} \tag{4.16}$$

where $*$ represents the discrete convolution product, $\boldsymbol{a}$ is the waveform of the excitation signal (for u) and $\boldsymbol{h}$ are the acousto electrical impulse responses of the transducers u and v. For simplicity sake, in this example $\boldsymbol{e}$ is set to be a six cycles sinusoid tapered with a Hanning window. Fig.4.7 shows the received signals obtained for the case where the arrival time does not correspond perfectly with a integer sample at ν_s. The first one, $\boldsymbol{y}_{uv}$, is obtained using the simulation tool (Field II). The second signal, $\hat{\boldsymbol{y}}_{uv}$, is obtained using the matrix $\boldsymbol{C}_{uv}$ where the non aligning arrival times were shifted to the nearest integer values of n inside the pulse-echo impulse response of the medium $\boldsymbol{g}_{uv}$. As seen in Fig.4.7, only a small shift of 0.4 samples at $\nu_s=50\ MHz$ (which corresponds to 8 ns) had to be made in order to align the arrival time with the closest sample ($n=1299$) of $\boldsymbol{g}_{uv}$. However, as one can observe on the same figure, the computation error made reaches up to 40% of the reference received signal (computed using Field II) amplitude. Moreover, the measured energy of the error is only 7 dB lower than the energy of the reference received signal. These measurements combined with the visual assessment that one can make on the Fig.4.7, pushes to the conclusion that the construction of the $\boldsymbol{C}_{uv}$ matrix based on the nearest integer approximation (for the arrival time alignment with the $\boldsymbol{g}_{uv}$ samples) is not sufficient.

In order to find a better solution for the problem raised by the relation (4.15), one should first fix the objective that is to be achieved. Looking at the Fig.4.7, this objective should sound like: "Minimize the computational error between the reference signal $\boldsymbol{y}_{uv}$ and the modeled signal $\hat{\boldsymbol{y}}_{uv}$". Certainly, in some way, the nearest integer value used to obtain the results showed in Fig.4.7 tries also to achieve

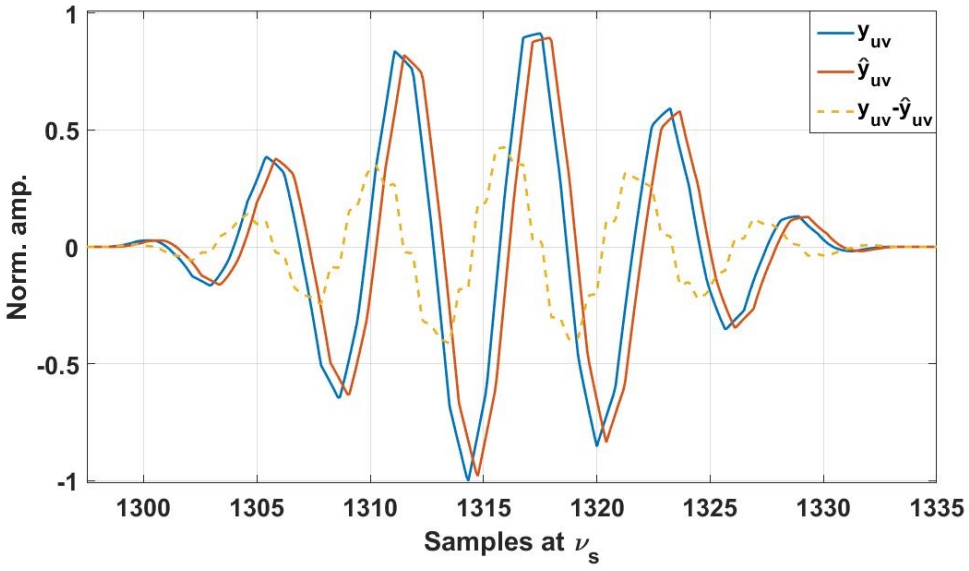

Figure 4.7: Results obtained on the case where the arrival time does not correspond perfectly with a integer sample at ν_s. $\boldsymbol{y}_{uv}$ is the simulated received signal and $\hat{\boldsymbol{y}}_{uv}$ is its counterpart computed using the matrix $\boldsymbol{C}_{uv}$. Here, $\boldsymbol{C}_{uv}$ is computed using the closest integer function in order to have on each column a non null entry. The sampling frequency is $\nu_s = 50\ MHz$. The dashed curve represents the computation error made due to the shift of the arrival time to the nearest value of n inside the pulse-echo impulse response of the medium $\boldsymbol{g}_{uv}$. In this case the arrival time is $t - t_0 = 1298.6/\nu_s$.

the previously stated objective (since if (4.15) is applied as it is, the null columns will generate null echoes and thus an error with a 0 dB discrepancy from the reference signal), however its performance is not optimal. Instead, here we propose to allow another degree of freedom for this optimization and we propose to use two coefficients α and β instead of one attributed to $n = \lfloor (t - t_0)/\nu_s \rceil$. Each of these coefficients will be associated to the samples $n = \lfloor (t - t_0)/\nu_s \rfloor$ and $n = \lceil (t - t_0)/\nu_s \rceil$ respectively and, depending on their value, will allow to minimize the Mean Square Error (MSE) between $\boldsymbol{y}_{uv}$ and $\hat{\boldsymbol{y}}_{uv}$. In such case, the novel relation that allows building the $\boldsymbol{C}_{uv}$ matrix is:

$$\boldsymbol{C}_{uv}[n,m] = \begin{cases} \frac{\alpha}{4\pi^2 \|\boldsymbol{r}-\vec{r}_u\|_2 \|\boldsymbol{r}-\vec{r}_v\|_2}, \text{ if } \left\lfloor \frac{\|\boldsymbol{r}-\vec{r}_u\|_2 + \|\boldsymbol{r}-\vec{r}_v\|_2}{c_m} \right\rceil = t_0 + \frac{n}{\nu_s} \\ \frac{\beta}{4\pi^2 \|\boldsymbol{r}-\vec{r}_u\|_2 \|\boldsymbol{r}-\vec{r}_v\|_2}, \text{ if } \left\lceil \frac{\|\boldsymbol{r}-\vec{r}_u\|_2 + \|\boldsymbol{r}-\vec{r}_v\|_2}{c_m} \right\rceil = t_0 + \frac{n}{\nu_s} \\ 0, \text{ elsewhere} \end{cases} \tag{4.17}$$

By writing the desired objective as a mathematical expression it can be deduced the optimization problem that allows computing the coefficients α and β:

$$\underset{(\alpha,\beta)}{\operatorname{argmin}} \left\| e(t) *_t \left[\delta\left(t - \frac{\|\boldsymbol{r}-\vec{r}_u\|_2 + \|\boldsymbol{r}-\vec{r}_v\|_2}{c_m}\right) - \alpha\delta\left(t - \left\lfloor \frac{\|\boldsymbol{r}-\vec{r}_u\|_2 + \|\boldsymbol{r}-\vec{r}_v\|_2}{c_m} \right\rceil\right) \right.\right. \\ \left.\left. -\beta\delta\left(t - \left\lceil \frac{\|\boldsymbol{r}-\vec{r}_u\|_2 + \|\boldsymbol{r}-\vec{r}_v\|_2}{c_m} \right\rceil\right) \right] \right\|_2 \tag{4.18}$$

The previous relation can be solved for (α, β) using a simplex search method [Lagarias et al., 1998] and is to be applied as many times as needed in order to compute the pair (α, β) for each point $\boldsymbol{r}_0$ for which there is a non alignment between the arrival time and the samples of the vector $\boldsymbol{g}_{uv}$.

For the case shown in Fig.4.7, the coefficients α and β computed using (4.18) are 0.4477 and 0.6546 respectively. Since each point $\boldsymbol{r}_0$ is treated one at the time, $\hat{\boldsymbol{y}}_{uv}$ can be seen as the sum of the two curves

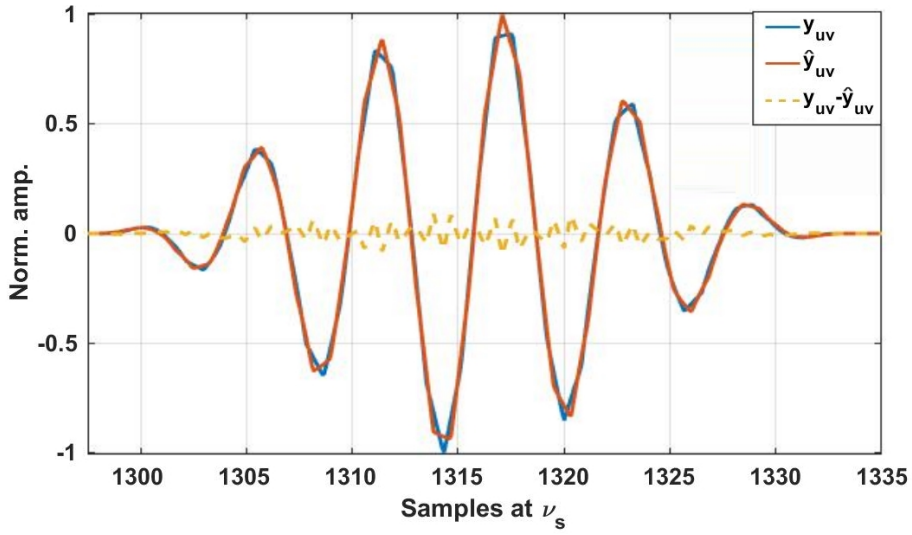

Figure 4.8: Results obtained on the case where the arrival time does not correspond perfectly with a integer sample at ν_s. Here, the relations (4.17) and (4.18) are used. $\boldsymbol{y}_{uv}$ is the simulated received signal and $\hat{\boldsymbol{y}}_{uv}$ is its counterpart computed using the matrix $\boldsymbol{C}_{uv}$. Here, $\boldsymbol{C}_{uv}$ is computed using (4.17). The sampling frequency is $\nu_s = 50\ MHz$. The dashed curve represents the computation error made.

A and B. This result is shown in Fig.4.8(b). Here one can observe that the modeled received signal $\hat{\boldsymbol{y}}_{uv}$ is very close to $\boldsymbol{y}_{uv}$. Indeed, the maximal amplitude of the error is only at 9.6% of the reference signal amplitude, the MSE is only of 0.001 (whereas in Fig.4.7 the MSE is 0.0073) and the energy of the computational error is 24.07 dB lower than the one of the reference signal. It can be thus concluded that the combination between the expressions (4.17) and (4.18) allows obtaining much better results than the combination between the expression (4.15) and the nearest integer function.

Thus, for the rest of this work (4.17) and (4.18) will be used in order to compute the $\boldsymbol{C}_{uv}$ matrix.

4.4.2 On the discretization of the imaged medium

In the previous Sub-section a method for the computation of the $\boldsymbol{C}_{uv}$ matrix has been deduced. However, the impact of the medium discretization on the reconstruction accuracy was not studied. Here, the impact of the medium partition size on the modeling error is addressed.

To understand the choice of the medium discretization steps Δx and Δz, consider the case shown in Fig.4.9. Here is represented a grid node $\boldsymbol{r}$, that generates an echo which arrives at the time sample n inside $\boldsymbol{g}_{uv}$. Since all the medium is sampled with the same steps $(\Delta x, \Delta z)$, each grid node $[n,m]$ (m computed from $\boldsymbol{r}$ using (4.12)) is surrounded by a rectangular cell of size Δz and Δx along the axial and lateral directions respectively. This cell, represented with a gray dashed line in Fig.4.9, has a surface $S_{c_{[n,m]}} = \Delta z \Delta x$ constant for all the nodes $[n,m]$. As it was shown in the previous Sub-section, when the medium is sampled, only the points $\vec{r}$ are modeled with the matrix $\boldsymbol{C}_{uv}$. This means that, the echo which is generated by any continuous medium point $\vec{r} \in S_{c_{[n,m]}}$ (red dots in Fig.4.9) is approximated with an echo generated by the discretized grid point $\boldsymbol{r}$ (green dot in Fig.4.9). Using (4.13), it can be deduced that:

$$
\begin{aligned}
g_{uv}(t) &= \frac{\delta\left(t - \frac{\|\vec{r}-\vec{r}_u\|_2 + \|\vec{r}-\vec{r}_v\|_2}{cm}\right)}{4\pi^2 \|\vec{r}-\vec{r}_u\|_2 \|\vec{r}-\vec{r}_v\|_2} \gamma(\vec{r}) \\
\mathrm{g}_{uv}(t) &= \frac{\delta\left(t - \frac{\|\boldsymbol{r}-\vec{r}_u\|_2 + \|\boldsymbol{r}-\vec{r}_v\|_2}{cm}\right)}{4\pi^2 \|\boldsymbol{r}-\vec{r}_u\|_2 \|\boldsymbol{r}-\vec{r}_v\|_2} \boldsymbol{\gamma}[m]
\end{aligned}
\tag{4.19}
$$

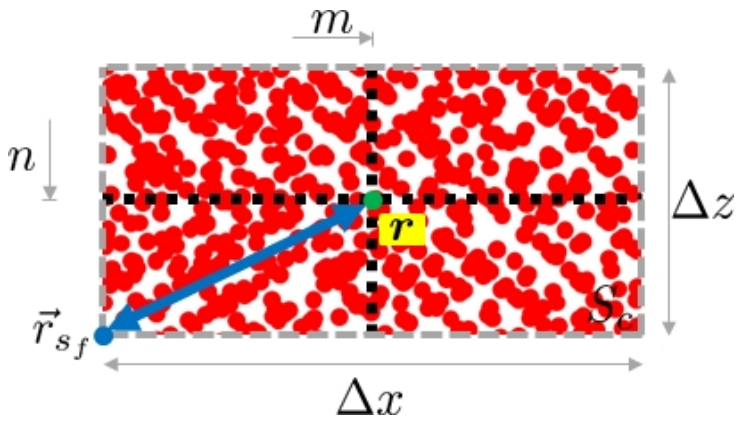

Figure 4.9: Zoom on a $\boldsymbol{\Omega}$ grid cell (of finite surface $S_{c_{[n,m]}}$) centered around the grid node $[n,m]$. The column m is computed using (4.12) and n is the time sample at which the echo generated at $\boldsymbol{r}$ arrives at v when u emits. Δz and Δx are the axial and lateral discretization steps for the imaged medium. $\vec{r}_{s_f} \in S_{c_{[n,m]}}$ is the position of the most remote scatterer from $\boldsymbol{r}$. During the modeling, $\vec{r}_{s_f}$ will be approximated with $\boldsymbol{r}$.

By comparing the continuous impulse response $g_{uv}(t)$ and its discrete space counterpart $\mathrm{g}_{uv}(t)$ in (4.19), it can be deduced that the error made by this approximation, has a similar effect as the one showed in Fig.4.7. In other words, by partitioning the medium, the echoes generated by the points $\vec{r}$ that do not fall directly on a grid nodes $\boldsymbol{r}$ are modeled with a small error, due to the shift between the arrival time of the echo generated in $\vec{r}$ and the one generated in $\boldsymbol{r}$. While there can be an infinity of time shifts between any point $\vec{r} \in S_{c_{[n,m]}}$ and $\boldsymbol{r}$, a maximal delay $t_{\vec{r}_f \longrightarrow \boldsymbol{r}}$ can be found. As it can be seen in Fig.4.9, $t_{\vec{r}_f \longrightarrow \boldsymbol{r}}$ depends on the maximal distance between the grid node (green dot) and the continuous medium point $\vec{r}_f$ (blue dot). This delay can be computed as follows:

$$t_{\vec{r}_f \longrightarrow \boldsymbol{r}} = \frac{2\sqrt{(\Delta z/2)^2+(\Delta x/2)^2}}{c_m} = \frac{\sqrt{(\Delta z)^2+(\Delta x)^2}}{c_m} \tag{4.20}$$

In the previous relation it can be clearly seen that $t_{\vec{r}_f \longrightarrow \boldsymbol{r}} \underset{(\Delta x,\Delta z)\longrightarrow(0,0)}{=} 0$. In other words, a potentially infinitesimal partition of the medium ($\Delta x \longrightarrow 0$ and $\Delta z \longrightarrow 0$) could indeed decrease significantly the modeling error (since at such spatial sampling rates $\boldsymbol{C}_{uv}$ would approach C_{uv}). However, this solution is not feasible because of two main reasons. In order to understand its drawbacks origins, let us define the following two relations:

$$N_x = \frac{w_{\boldsymbol{\Omega}}}{\Delta x} \quad \text{and:} \quad N_z = \frac{d_{\boldsymbol{\Omega}}}{\Delta z} \tag{4.21}$$

where $w_{\boldsymbol{\Omega}}$ and $d_{\boldsymbol{\Omega}}$ are the sizes of the imaged medium in the lateral and axial directions respectively. N_x and N_z are the number of $\boldsymbol{\Omega}$ columns and lines respectively. In (4.21) it can be seen that, as Δx and Δz approach zero, N_x and N_y increase. The inherent drawbacks of increasing N_x and N_z are that: first, it increases the number of unknowns inside the direct model and second, such small partitioning implies vectors $\boldsymbol{\gamma}$ and implicitly matrices $\boldsymbol{C}_{uv}$ of large sizes.

While indeed a small partitioning of the imaged medium could reduce the modeling error, its drawbacks imply serious computational problems. Thus, in order to keep the number of unknowns and the size of the involved matrices reasonable[2], in this work it was decided to fix the discretization

[2]Even though the computation of the $\boldsymbol{C}_i$ matrices will be detailed further, for the discretization steps $(\Delta x, \Delta z)$ (4.22) and the medium sizes $(w_{\boldsymbol{\Omega}}, d_{\boldsymbol{\Omega}}) = (1.5, 4)\ cm$, we can jump forward and say that the size of each matrix $\boldsymbol{C}_i$ is $N_y \times N_x N_z = 2597 \times 210438$. In a Matlab environment if stored in full, double precision such matrices can occupy up to 35Gb of memory. Furthermore later in this Chapter it will be shown that, in the total kernel Ψ this matrices $\boldsymbol{C}_i$ are concatenated for all the N_{el} receiving elements i and for multiple emissions N_{pwi}. Despite the fact that one can use the sparsity of the $\boldsymbol{C}_i$ matrices to optimize the resources, increasing the size of the involved matrices by a factor of $N_{el}N_{pwi}$) led us (given the highest amount of RAM memory at our disposal, 380Gb) to fix the spatial partition steps at this value and not lower.

steps at:

$$\Delta z = \frac{c_m}{\nu_s} \quad \text{and:} \quad \Delta x = 3\Delta z = \frac{3c_m}{\nu_s} \tag{4.22}$$

4.4.3 On the discretization of the probe elements

In Sections 4.2 and 4.3 it was shown that the Huygens - Fresnel principle can be used in order to model the pulse echo impulse response of the medium when a probe element emits and another receives the backscattered echoes. So far in this Section, the continuous and discrete relations that allow to link the backscattered echoes to the TRF in the case of punctual transducers were derived. Here, these concepts are combined. The objective is to obtain a continuous relation and its discrete counterpart that allow to model the received signals in the case where one probe element emits an ultrasound wave and another probe element receives its backscattered echoes.

Using (4.5), the expression for the signal received by the probe element i when j emits can be deduced:

$$\begin{gathered} y_{ji}(t) = e(t) *_t g_{ji}(t) = e(t) *_t \int_V \Big[g_j(\vec{r},t) *_t g_i(\vec{r},t) \Big] \gamma(\vec{r})\, \mathrm{d}^2\vec{r} \underset{\text{using (4.6)}}{\Longleftrightarrow} \\ y_{ji}(t) = e(t) *_t \big(\mathsf{C}_{ji}\gamma\big)(t) \end{gathered} \tag{4.23}$$

where $e(t) = a(t) *_t h(t) *_t h(t)$ can be seen as the continuous time counterpart of the recorded echoes waveform. At this point, by combining (4.6), (4.10) and (4.11), one can deduce the following expression for the integral operator C_{ji}:

$$\big(\mathsf{C}_{ji}\gamma\big)(t) = \int_{S_j}\int_{S_i} \big(\mathsf{C}_{uv}\gamma\big)(t)\, \mathrm{d}\vec{r}_v\, \mathrm{d}\vec{r}_u \tag{4.24}$$

Simply put, this relation models the Huygens-Fresnel principle in the continuous time / space domain. In Sub-section 4.4.1 it was shown how to compute the discrete counterpart of C_{uv} in the form of $\boldsymbol{C}_{uv}$. Here, this matrix can be used in order to find $\boldsymbol{C}_{ji}$ which is the discrete counterpart of C_{ji}. To do so, we propose the solution illustrated in Fig.4.10. As it can be seen here, the proposed approach consists in separating the total surface S of each probe element in smaller partitions of area S_{uv}. Consider the probe element j of width w and height $height$ shown in the left-side of Fig.4.10 whose origin is in $\vec{r}_j$. By dividing this element in N smaller partitions of width w_{uv} and height $height$ one can treat each generated subdivision as an independent transducer active in emission / reception. The positions $\vec{r}_v$ and $\vec{r}_u$ of the new partitions can be expressed as follows:

$$\vec{r}_v = \vec{r}_j + (v-1)\,\vec{w}_{uv} \quad \text{and} \quad \vec{r}_u = \vec{r}_i + (u-1)\,\vec{w}_{uv} \tag{4.25}$$

where $\vec{w}_{uv} = (w_{uv}, 0, 0)$ is a position vector along the $\mathcal{O}\vec{x}$ axis. Now, if the surfaces S_{uv} of the generated partitions are sufficiently small, then they can be considered punctual and their behavior can be modeled using the C_{uv} operators computed in Sub-section 4.4.1. In such case, (4.24) becomes:

$$\big(\mathsf{C}_{ji}\gamma\big)(t) = \sum_{v=1}^{N}\sum_{u=1}^{N} \big(\mathsf{C}_{uv}\gamma\big)(t) \tag{4.26}$$

Even though the surface of the probe elements was partitioned, (4.26) does not yet represent a discrete time / space counterpart of (4.24). To obtain this formula, it is sufficient to observe in (4.26) that C_{ji} and C_{uv} can be replaced with their discrete counterparts $\boldsymbol{C}_{ji}$ and $\boldsymbol{C}_{uv}$ respectively. Thus, the expression

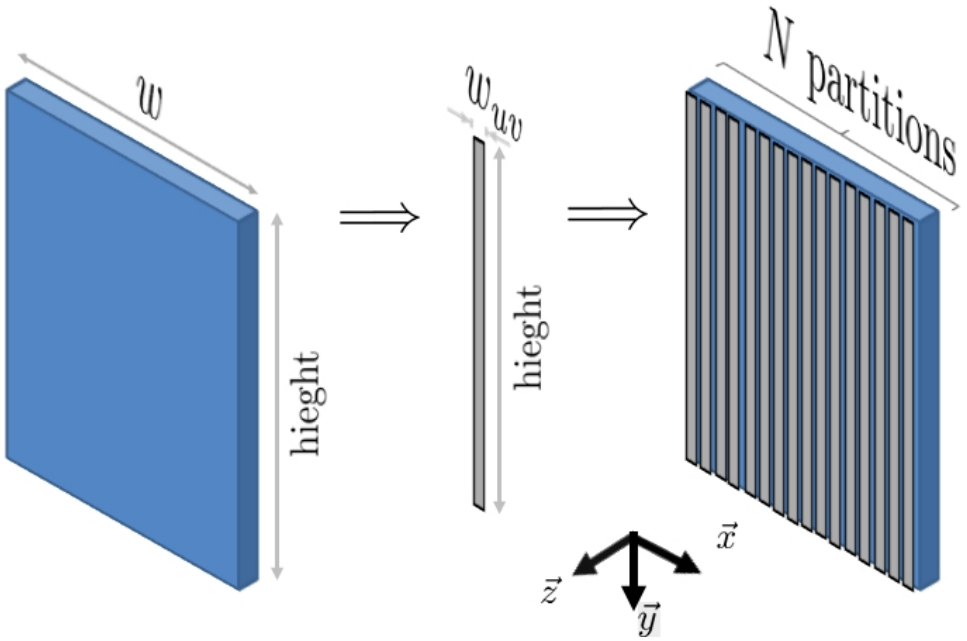

Figure 4.10: Schematic representation of the probe element discretization. On the left-side of the image is shown a probe element of width w and height $height$ whose surface is S. In the center of the image is shown a small partition of width w_{uv} and height $height$ whose surface S_{uv}. Finally in the left-side of the image is shown how the surface S of the probe element is divided in $N = w/w_{uv}$ smaller partitions of surface S_{uv}.

for the $\boldsymbol{C}_{ji}$ matrix can be written as follows:

$$\boldsymbol{C}_{ji} = \sum_{v=1}^{N}\sum_{u=1}^{N} \boldsymbol{C}_{uv} \tag{4.27}$$

Relying on (4.23) and (4.27), the expression for the recorded signal by the probe element j when i emits can be deduced:

$$\boldsymbol{y}_{ji} = \boldsymbol{e} * \boldsymbol{C}_{ji}\boldsymbol{\gamma} = \boldsymbol{e} * \left[\sum_{v=1}^{N}\sum_{u=1}^{N} \boldsymbol{C}_{uv}\boldsymbol{\gamma}\right] \tag{4.28}$$

To find the most fitting partition size for the probe element subdivision, consider the simulation setup shown in Fig.4.11(a) where an element of the LA523E (Table 3.1) is illustrated. A single scatterer is placed on a circle arc of radius 20 mm centered in the middle of the probe element j. First, the signal received by the $i = 32$ element when the element $j = 32$ emits is simulated using Field II. This signal $\boldsymbol{y}_{32,32}$ is showed in Fig.4.11(a). Second, $\boldsymbol{y}_{32,32}$ is approximated using (4.28) by employing two types of element partitioning: $w_{uv} = w$ (gives $\hat{\boldsymbol{y}}^{1}_{32,32}$) and $w_{uv} = w/20$ (gives $\hat{\boldsymbol{y}}^{20}_{32,32}$). As it can be observed in Fig.4.11(b), the signal modeled with $N = w/w_{uv} = 1$, while of similar shape as $\boldsymbol{y}_{32,32}$, presents however a significant modeling error. Indeed, one can measure an error ($\boldsymbol{y}_{32,32} - \hat{\boldsymbol{y}}^{1}_{32,32}$) that climbs at up to 40% of the reference signal amplitude and has an energy only 7 dB lower than the one of the reference signal. The MSE is 0.0213. Since, by setting $N = 1$ in (4.28), one replaces the matrix $\boldsymbol{C}_{ji}$ with $\boldsymbol{C}_{uv}$ (computed for far field), this result is expected and is the effect of the behavior seen in Fig.4.4(b). The experience illustrated in Fig.4.5 allowed to conclude that this is explained by the Huygens - Fresnel principle governing on the emission / reception elements surface. In fact, some points of this element are closer to the scatterer than others, which generates different arrival times and amplitudes for the echoes received by each punctual source of the receiving element surface. Thus a high modeling error is generated when computing $\hat{\boldsymbol{y}}^{1}_{32,32}$ since only one emission / reception punctual source is modeled

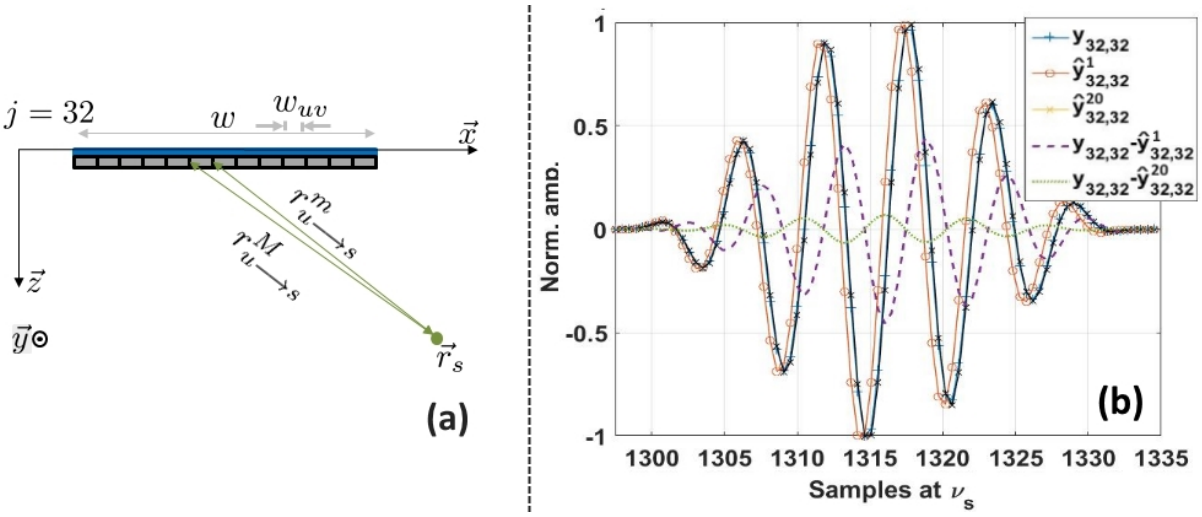

Figure 4.11: (a) - Simulation setup used to find the most fitting size for the element partition, (b) - Plots of the received signals recorded on the simulation setup shown in (a). $\boldsymbol{y}_{32,32}$ is the reference signal, obtained using Field II, $\hat{\boldsymbol{y}}^1_{32,32}$ and $\hat{\boldsymbol{y}}^{20}_{32,32}$ are the modeled signals obtained using the $\boldsymbol{C}_{32,32}$ matrix with $N = 1$ and $N = 20$ respectively.

(which corresponds to the center of the emission / reception element). However, as it was shown in (4.26), the Huygens - Fresnel principle can be modeled by splitting the surface of the emission / reception probe elements in smaller partitions. The reasoning that we implemented in order to find the right partition size for the element division is the following. In Fig.4.11(b) is clear that the high error $\boldsymbol{y}_{32,32} - \hat{\boldsymbol{y}}^1_{32,32}$ results from the fact that the echo waveform in $\hat{\boldsymbol{y}}^1_{32,32}$ is shorter (in the sense that it contains less non null samples) than the one present in $\boldsymbol{y}_{32,32}$. This effect itself is the result of the fact that $\hat{\boldsymbol{g}}^1_{32,32}$ contains less non null samples than $\boldsymbol{g}_{32,32}$. Thus, one can deduce that it is possible to improve the modeling error by making sure that there are the same number of non null samples in $\boldsymbol{g}_{32,32}$ and $\hat{\boldsymbol{g}}^N_{32,32}$. This can be achieved by choosing a width w_{uv} in such way so that for every medium point $\vec{r}$, the waves emitted / received by the element partitions behave in the far field conditions. To do so, first one can calculate the difference between the greatest ($r^M_{u\longrightarrow s}$) and the shortest ($r^m_{u\longrightarrow s}$) distance that separates the element u from any medium point $\vec{r}_s$ (Fig.4.11(a)):

$$d_{u\longrightarrow s} = r^M_{u\longrightarrow s} - r^m_{u\longrightarrow s} \tag{4.29}$$

Then, from the objective "There should be the same number of non null samples in $\boldsymbol{g}_{32,32}$ and $\hat{\boldsymbol{g}}^N_{32,32}$", one can deduce by contradiction the following necessary condition:

$$\frac{2d_{u\longrightarrow s}}{c_m} \leq \frac{1}{\nu_s} \Longleftrightarrow d_{u\longrightarrow s} \leq \frac{c_m}{2\nu_s} \tag{4.30}$$

In fact, if (4.30) is not verified, then the element partitions (u, v) model through $\boldsymbol{C}_{u,v}$ a spatial impulse response that should contain more non null samples (near field) with an impulse response that contains only one sample (far field). From Fig.4.11(a), it can be deduced that $d_{u\longrightarrow s}$ is maximal when $\vec{r}_s$ belongs to the $\vec{x}$ axis, meaning that $d_{u\longrightarrow s} = w_{uv}$. Therefore (4.30) becomes:

$$w_{uv} \leq \frac{c_m}{2\nu_s} \tag{4.31}$$

In Fig.4.11(b) is shown the modeled echo $\hat{\boldsymbol{y}}^{20}_{32,32}$ computed using a partition size $w_{uv} = w/N = w/20 \approx c_m/(2\nu_s)$. As it can be visually determined, $\hat{\boldsymbol{y}}^{20}_{32,32}$ is very similar to the reference signal $\boldsymbol{y}_{32,32}$. The modeling error $\boldsymbol{y}_{32,32} - \hat{\boldsymbol{y}}^{20}_{32,32}$ has an amplitude only of 7% compared to the one of the reference signal. Moreover, a MSE of 0.0032 is measured which means that the energy of the generated modeling error is 24 dB lower than the reference signal energy. Comparing the modeling error obtained on $\hat{\boldsymbol{y}}^1_{32,32}$ with

the one obtained on $\hat{\boldsymbol{y}}^{20}_{32,32}$, it can be deduced that, by splitting the emission / reception element in smaller partitions, a better modeling of the recorded data is achieved. In addition, an error 24 dB lower than the reference signal proves that the partition size computed using (4.31) allows a faithful modeling of the RF data.

4.5 The general forward model

To summarize the previous Section, a theoretical framework was developed that allows writing the recorded backscattered echoes by the element i when j emits as follows:

$$\mathbf{y}_{ji} = \boldsymbol{e} * \left[\sum_{v=1}^{N} \sum_{u=1}^{N} \boldsymbol{C}_{uv} \boldsymbol{\gamma} \right] = \boldsymbol{E} \cdot \boldsymbol{C}_{ji} \cdot \boldsymbol{\gamma} \tag{4.32}$$

In (4.32), the matrices $\boldsymbol{E}$ and $\boldsymbol{C}_{ji}$ are computed as follows:

$$\boldsymbol{C}_{ji} = \sum_{v=1}^{N} \sum_{u=1}^{N} \boldsymbol{C}_{uv}$$

$$\text{and: } \boldsymbol{E} = \begin{bmatrix} \boldsymbol{e}[N_e-1] & \boldsymbol{e}[N_e-2] & \cdots & \boldsymbol{e}[0] & 0 & \cdots & 0 & 0 & \cdots & 0 \\ 0 & \boldsymbol{e}[N_e-1] & \cdots & \boldsymbol{e}[1] & \boldsymbol{e}[0] & \cdots & 0 & 0 & \cdots & 0 \\ \vdots & \vdots & \ddots & \vdots & \vdots & \ddots & \vdots & \vdots & \ddots & \vdots \\ 0 & 0 & \cdots & \boldsymbol{e}[N_e-1] & \boldsymbol{e}[N_e-2] & \ddots & \boldsymbol{e}[0] & 0 & \cdots & 0 \\ 0 & 0 & \cdots & 0 & \boldsymbol{e}[N_e-1] & \ddots & \boldsymbol{e}[1] & \boldsymbol{e}[0] & \cdots & 0 \\ \vdots & \vdots & \ddots & \vdots & \vdots & \ddots & \vdots & \vdots & \ddots & \vdots \\ 0 & 0 & \cdots & 0 & 0 & \ddots & \boldsymbol{e}[N_e-1] & \boldsymbol{e}[N_e-2] & \cdots & \boldsymbol{e}[0] \end{bmatrix} \tag{4.33}$$

where the Toeplitz matrix[3] $\boldsymbol{E}$ is built using the echo waveform $\boldsymbol{e} = \boldsymbol{a} * \boldsymbol{h} * \boldsymbol{h}$ and $\boldsymbol{C}_{ji}$ is a matrix that models the wave forward / backward propagation inside the medium. N_e is the length of the echo waveform $\boldsymbol{e}$. Here, (4.32) is used as a building block in order to model the signal $\boldsymbol{y}_i^k$ recorded by an element of the probe when all the probe elements N_{el} are active in emission.

4.6 Validation of the forward model plane wave imaging

In Sub-section 2.2.1 (2.33) the following formula was deduced:

$$y_i(t) = w_i \sum_{j=1}^{N_{el}} w_j y_{ji}(t) + b_i(t) \tag{4.34}$$

where w_j and w_i are the emission and reception apodization windows respectively, $y_{ji}(t)$ are the received backscattered echoes by the element i when j emits[4] and $b_i(t)$ is the acquisition noise. 4.34 is the continuous time / space relation that links the received backscattered echoes at the element i when all the probe elements N_{el} are active in emission. As stated in Sub-section 2.2.1, (4.34) is a generic model. This means that this relation can be applied to any emission / reception scheme only by correspondingly adapting the emission delays t_j. Suppose now that the delay law t_j^k is used to

[3] $\boldsymbol{E}$ is similar to the matrix $\boldsymbol{A}^k$ computed in (3.5), the only difference being that, besides the excitation signal $\boldsymbol{a}$, $\boldsymbol{E}$ stores also the acousto electrical pulse echo impulse response of the probe:$\boldsymbol{h} * \boldsymbol{h}$.

[4] Note: Here, the $y_{ji}(t)$ signals are modeled in such way to include also the emission delays t_j.

generate an arbitrary (i.e. focused, plane or diverging) ultrasound beam k inside the medium. Using (4.34) it can be deduced that the received signal by the element i can be written as:

$$\begin{aligned} y_i^k(t) = w_i \sum_{j=1}^{N_{el}} w_j y_{ji}^k(t) + b_i(t) \underset{\text{Using (4.23)}}{=} w_i e(t) *_t g_i^k(t) + b_i(t) \\ \text{with: } g_i^k(t) = \sum_{j=1}^{N_{el}} w_j g_{ji}^k(t) \end{aligned} \tag{4.35}$$

where $g_i^k(t)$ is the pulse echo impulse response of the medium to the insonification k seen by the i^{th} element of the probe. By writing (4.35) in the discrete time domain one obtains the following relation for the recorded backscattered echoes by the probe element i:

$$\begin{aligned} \boldsymbol{y}_i^k = w_i \sum_{j=1}^{N_{el}} w_j \boldsymbol{y}_{ji}^k + \boldsymbol{b}_i = \boldsymbol{E}^k \cdot \boldsymbol{g}_i^k + \boldsymbol{b}_i \underset{\text{Using 4.32}}{=} \boldsymbol{E}^k \cdot \boldsymbol{C}_i^k \cdot \boldsymbol{\gamma} + \boldsymbol{b}_i \\ \text{with: } \boldsymbol{C}_i^k = w_i \sum_{j=1}^{N_{el}} w_j \boldsymbol{C}_{ji}^k = w_i \sum_{j=1}^{N_{el}} w_j \sum_{v=1}^{N} \sum_{u=1}^{N} \boldsymbol{C}_{uv}^k \end{aligned} \tag{4.36}$$

Simply put, the previous relation embodies the mathematical expression for the same color branches involved in the "Wave propagation" and "Wave emission" blocks of the Fig.4.1(b) also shown in Fig.4.11.

To assess the behavior of the developed model the emission / reception of a plane wave tilted in the

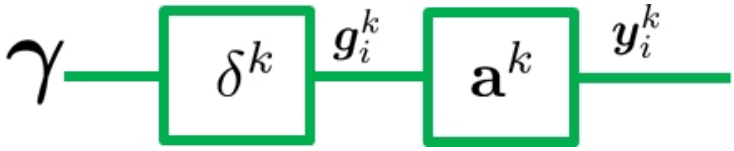

Figure 4.12: (a) - Schematic representation of the mathematical expression (4.36). The pulse echo impulse response of the medium to the insonification with the ultrasound beam k that carries a Dirac $\boldsymbol{\delta}^k$ impulsion is: $\boldsymbol{g}_i^k = \boldsymbol{C}_i^k \cdot \boldsymbol{\gamma}$. The convolution product between the excitation $\boldsymbol{a}^k$ and the impulse response $\boldsymbol{g}_i^k$ is modeled by the matrix product: $\boldsymbol{y}_i^k = \boldsymbol{E}^k \cdot \boldsymbol{C}_i^k \cdot \boldsymbol{\gamma}$.

direction $\theta^k = 10°$ (Fig.4.13(a)) was simulated using the Field II software. The excitation signal $\boldsymbol{a}^k$ used here (Fig.4.13(b)) is a slightly modified chirp[5] signal. The employed ultrasound probe is LA523E whose specifications are detailed in Table 3.1. Two mediums were studied in simulation. The first phantom

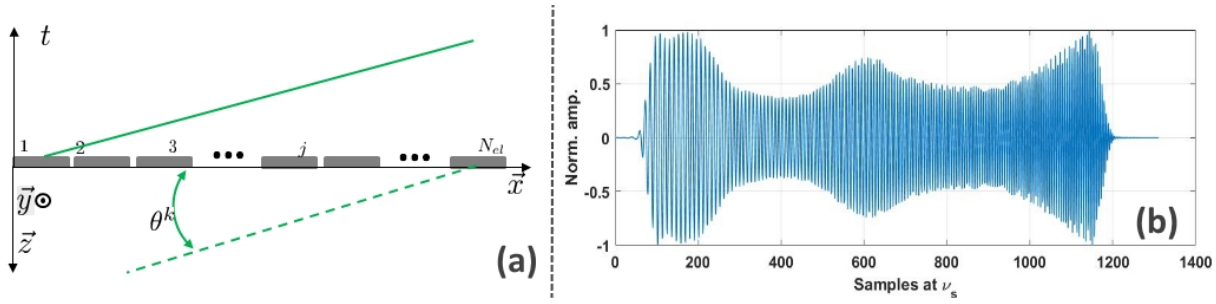

Figure 4.13: (a) - The LA523E (Table3.1) probe set to emit a plane wave in the direction $\theta^k = 10°$. (b) - Excitation signal $\boldsymbol{a}^k$ used to excite the ultrasound probe elements. $\nu_s = 50\ MHz$.

(Fig.4.14a), was a medium that contains 75 scatterers. The distance between each scatterer is 0.5 mm and 1.2 mm on the vertical and horizontal line respectively. The second medium (Fig.4.14b) has a

[5]This specific shape of the chirp envelope allows overcoming the negative effects of the band-limited ultrasound probe and will be discussed later in this Chapter.

scatterer distribution of 94 $scatt./mm^2$ and contains two hypo-echogenic cysts of 8 mm diameter. The direct model (4.36) was also used in order to generate the RF data for the two phantoms using

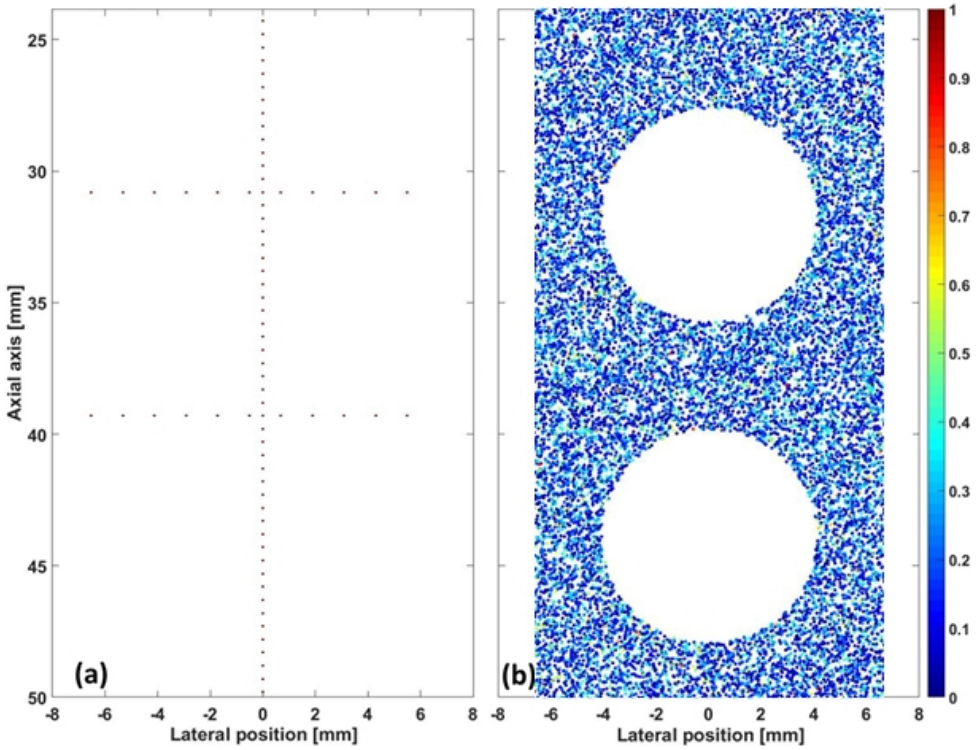

Figure 4.14: (a) - Physical position of the scatterers inside the simulated resolution phantom; (b) - Physical position of the scatterers inside the simulated cyst phantom.

the emission scheme showed in Fig.4.13(a). It is to be noted that the scatterers positions in the two phantoms are completely random in the sense that nothing insures that the scatterers fall perfectly on the $\mathbf{\Omega}$ grid nodes.

In Fig.4.15 are shown the RF datasets obtained on the sparse phantom (Fig.4.14(a)). By visual assessment one can deduce that both simulation data (Fig.4.15(a)) and modeled data (Fig.4.15(b)) are very similar. Indeed, the error $(\boldsymbol{y}_i^k - \hat{\boldsymbol{y}}_i^k)$ reaches only 8% of the maximal amplitude of the reference signal $\boldsymbol{y}_i^k$ (obtained using Field II). The total energy of the modeling error is 22.57 dB lower than the one of the reference signals. This result is coherent with the ones showed in Subsection 4.4.3 where the direct model performs slightly better (the error has 24 dB less energy than the signal). The RF datasets obtained on the cyst phantom (Fig.4.14(b)) are shown in Fig.4.16. Here again it can be seen that the reference RF dataset (Fig.4.16(a)) is close visually to the modeled RF dataset (Fig.4.16(b)). However, further investigations show that the modeling error $\boldsymbol{y}_i^k - \hat{\boldsymbol{y}}_i^k$ (Fig.4.16(c)) reaches 60% of the reference signal amplitude. This results in an error energy only 5.89 dB lower than the reference signal energy. This discrepancy between the RF data modeling error obtained on the sparse and cyst phantoms can be explained by the spatial discretization presented in Sub-section 4.4.2. In fact, as seen in this Sub-section, during the spatial discretization all the scatterers inside a cell of dimensions $(\Delta x, \Delta z)$ around a $\mathbf{\Omega}$ grid node $\boldsymbol{r}$ are modeled as one single scatterer that is placed at the position $\vec{r} = \boldsymbol{r}$. Now, for a sparse medium (as the one showed in Fig.4.14(a)), only one scatterer is present in the cell around the grid node $\boldsymbol{r}$ whose approximation generates a small modeling error. However, as the scatterer density increases the number of scatterers inside each cell follows the same tendency, each scatterer generating a small approximation error. The modeling errors showed in Fig.4.15(c) and Fig.4.16(c) are the interference of these approximations errors.

It can be thus concluded that the proposed forward model allows generating the received signals that one would receive if a plane wave was emitted in the medium. However, due to the spatial /

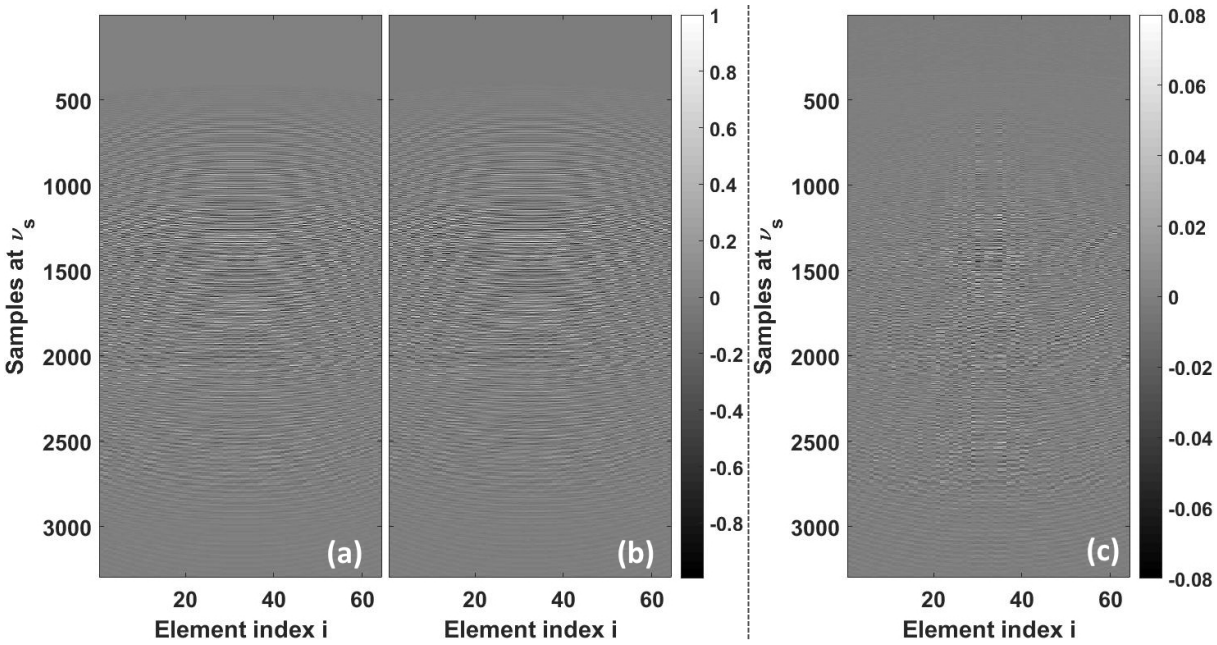

Figure 4.15: Sparse medium results. (a) - Recorded RF data obtained using the Field II program simulation: $\boldsymbol{y}_i^k$. (b) - RF data obtained using the direct model (4.36): $\hat{\boldsymbol{y}}_i^k$. For both of these images, each column i represents the signal recorded by the i^{th} element of the probe. (c) - Modeling error: $\boldsymbol{y}_i^k - \hat{\boldsymbol{y}}_i^k$.

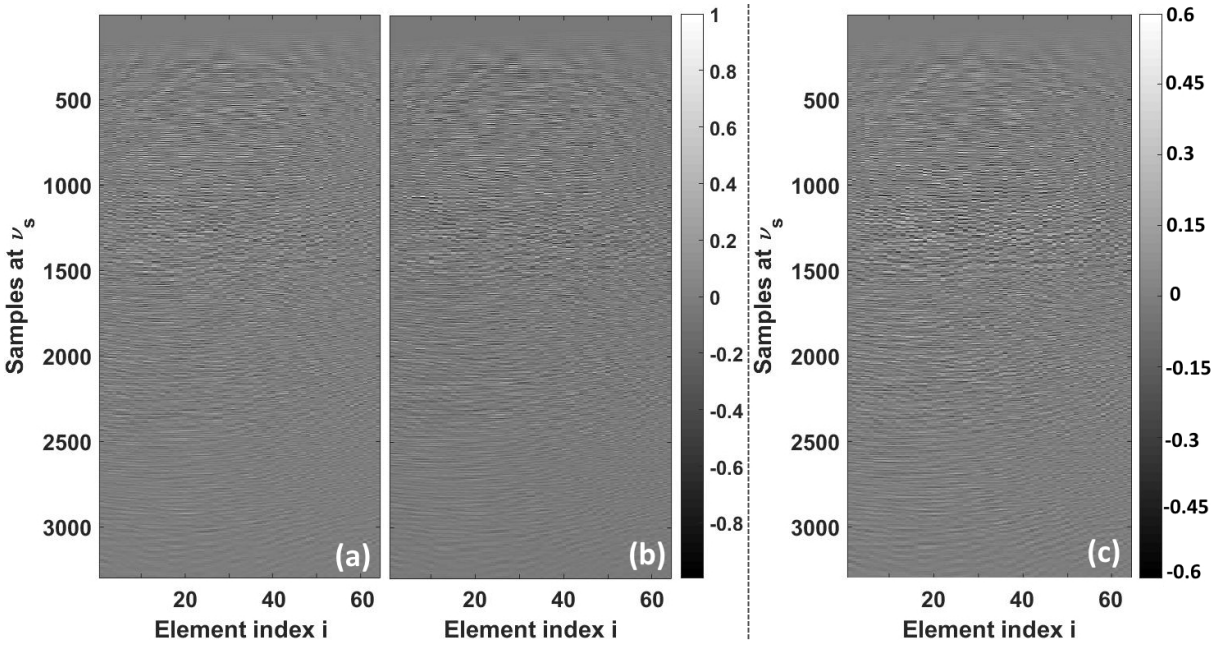

Figure 4.16: Cyst phantom results. (a) - Recorded RF data obtained using the Field II program simulation: $\boldsymbol{y}_i^k$. (b) - RF data obtained using the direct model (4.36): $\hat{\boldsymbol{y}}_i^k$. For both of these images, each column i represents the signal recorded by the i^{th} element of the probe. (c) - Modeling error: $\boldsymbol{y}_i^k - \hat{\boldsymbol{y}}_i^k$.

temporal discretization, the performance of the model depends on the scatterer density inside the TRF (sparse mediums generating very low modeling error and mediums with dense distribution of scatterers generating higher modelling errors). Nonetheless, since our final goal is to reconstruct the TRF itself, the fact that the RF data is not perfectly modeled, is not an important impediment as long as the final TRF estimation $\hat{\boldsymbol{\gamma}}$ corresponds with the reference TRF $\boldsymbol{\gamma}$. The TRF estimation will be presented in the following Sections.

4.7 On the simultaneous emission of encoded plane waves and echoes separation: the continuous AMCUS model

In this Section the direct model previously developed is adapted in order to include the temporal encoding of the plane waves. First, the need of temporal encoding is highlighted. Then, the continuous direct model is adapted in order to consider the temporal encoding of the plane waves. Finally, a method for the separation of the mixed backscattered echoes is detailed. The combination between the propagation model for a single plane wave, the temporal encoding and the echo separation concepts stands at the core of the Advanced Model for Coded UltraSound (AMCUS) imaging and represents the main contribution of this work.

4.7.1 Numerical issues linked to a single plane wave insonification

The natural question that comes to mind after building the direct model (4.36) shown in Section 4.5 is: "Is it possible to apply an inverse problem approach to (4.36)?". Here, this question will be addressed and, to jump forward, a need for a multiple plane wave insonification will be established.

To understand the limitation of an inverse problem approach based on the model (4.36) applied to a single plane wave insonification, it is convenient to start by studying the size of the involved $\mathbf{\Omega}$ grid (which imposes the length of the vector $\boldsymbol{\gamma}$, thus the number of unknowns in the system). Consider now the probe showed in Fig.4.17. To begin, suppose that the excitation signal is a Dirac impulsion $\delta(t)$. For

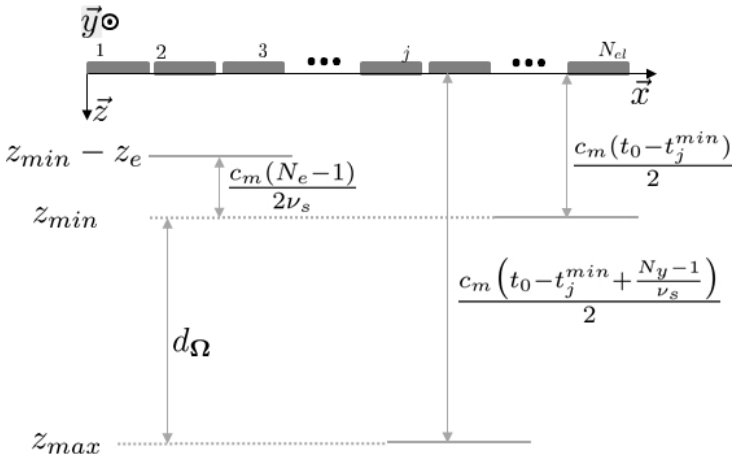

Figure 4.17: Representation of the scatterer depths whose echoes are potentially received during a RF data recording that starts at t_0 and ends at $t_0 + N_y/\nu_s$. $z_{min} - z_e$ is the minimal depth of a scatterer whose echoes are partially recorded. z_{min} is the minimal depth of a scatterer whose echoes are fully recorded. z_{max} is the maximal depth of a scatterer whose echoes are partially recorded.

the sake of computation simplicity, the hypothesis that the waves propagates in far field conditions will also be used here. In Sub-Section 2.2.1 (2.37), the following relation was given, to approximate the received echoes at any element i of the probe:

$$\begin{aligned} y_i(t) &\approx \int_V \gamma(\vec{r})\delta\big(t-\tau_i(\vec{r})\big)\,\mathrm{d}^2\vec{r} \\ \text{with: } \tau_i(\vec{r}) &\approx \min_{j\in[1..N_{el}]}\left(t_j + \frac{\|\vec{r}-\vec{r}_j\|_2}{c_m}\right) + \frac{\|\vec{r}-\vec{r}_i\|_2}{c_m} \end{aligned} \tag{4.37}$$

Thus, for $t = t_0$ the following equation holds:

$$y_i(t_0) \approx \int_V \gamma(\vec{r}) \delta\left(t_0 - \min_{j \in [1..N_{el}]} \left(t_j + \frac{\|\vec{r} - \vec{r}_j\|_2}{c_m} \right) + \frac{\|\vec{r} - \vec{r}_i\|_2}{c_m} \right) \mathrm{d}^2\vec{r} \tag{4.38}$$

Since $\delta(t)$ is non null only if $t = 0$ then it can be deduced from the previous relation that a potential (in the sense that $\gamma(\vec{r})$ can also be null at these positions) echo is recorded at t_0 from a scatterer placed at $\vec{r}_{min}$:

$$t_0 - \min_{j \in [1..N_{el}]} \left(t_j + \frac{\|\vec{r}_{min} - \vec{r}_j\|_2}{c_m} \right) + \frac{\|\vec{r}_{min} - \vec{r}_i\|_2}{c_m} = 0 \tag{4.39}$$

By imposing $\vec{r}_i = \vec{r}_j$ in (4.39) it can be deduced:

$$\begin{gathered} t_0 - \min_{j \in [1..N_{el}]} \left(t_j + \frac{z_{min}}{c_m} \right) + \frac{z_{\min}}{c_m} = 0 \Longleftrightarrow t_0 = t_j^{min} + \frac{2 z_{\min}}{c_m} \Longrightarrow \\ z_{\min} = \frac{c_m (t_0 - t_j^{\min})}{2} \end{gathered} \tag{4.40}$$

This relation links the minimal depth of the imaged medium to the time t_0 when the RF data starts to be recorded in the case where a Dirac impulsion is used as excitation. However, if the emitted signal is longer, scatterers that are at a lower depth than z_{min} have their echo recorded at t_0 (Fig.4.17). To deduce this depth one can use the following computational trick: apply the same analysis as in (4.38)-(4.40) for the last sample of the echo waveform $e(t)$ that is emitted by the probe element j. Since $\boldsymbol{e}$ has N_e samples, the last sample is emitted with a delay $t_e = (N_e - 1)/\nu_s$ after the first sample whose delay is $t_j^{\min}$. Thus, from (4.40) the following relation can be deduced:

$$\begin{gathered} z_{\min} - z_e = \frac{c_m (t_0 - t_j^{\min} - t_e)}{2} = \frac{c_m (t_0 - t_j^{\min} - \frac{N_e - 1}{\nu_s})}{2} \Longleftrightarrow \\ z_e = \frac{c_m (N_e - 1)}{2 \nu_s} \end{gathered} \tag{4.41}$$

In the same fashion as $z_{\min}$ and $z_{\min} - z_e$, the maximal depth $z_{\max}$ of the medium imaged when recording N_y long of RF data can be deduced. By switching t_0 in (4.38)-(4.40) with $t_0 + N_y/\nu_s$, the following expression is obtained:

$$z_{\max} = \frac{c_m (t_0 - t_j^{\min} + \frac{N_y - 1}{\nu_s})}{2} \tag{4.42}$$

Using (4.41) and (4.42) the depth $d_{\boldsymbol{\Omega}}$ of the image medium (and thus of the grid $\boldsymbol{\Omega}$) is deduced as follows:

$$d_{\boldsymbol{\Omega}} = z_{\max} - (z_{\min} - z_e) \Longleftrightarrow d_{\boldsymbol{\Omega}} = \frac{c_m (N_y + N_e)}{2 \nu_s} \tag{4.43}$$

Concerning the size of the imaged medium along the $\vec{x}$ axis, in this model [6], the region of interest of the medium will be supposed to span the total width of the ultrasound probe. Thus the width of the $\boldsymbol{\Omega}$ grid is:

$$w_{\boldsymbol{\Omega}} = N_{el}\, w + (N_{el} - 1)\, kerf \tag{4.44}$$

where w is the width of each probe element and $kerf$ is the space between two probe elements. At this point, using the grid cell size deduced in Sub-section 4.4.2, the number of grid nodes in $\boldsymbol{\Omega}$ can be

[6] Equal widths of the ultrasound probe and of the reconstructed medium were also used in the previous Chapters and is often the case for the linear array probes. This can be explained by the fact that the echoes generated in this region are more powerful, since the pressure field is stronger (Fig.3.1).

computed:

$$N_z = \frac{d_{\mathbf{\Omega}}}{\Delta z} + 1 = \frac{N_y + N_e}{2} + 1 \quad \text{and} \quad N_x = \frac{w_{\mathbf{\Omega}}}{\Delta x} + 1 = \frac{N_{el}\, w + (N_{el}-1)\, kerf}{c_m / \nu_s} + 1 \tag{4.45}$$

Thus, the length of the TRF vector $\boldsymbol{\gamma}$ is $N_z N_x$. Now, it turns out that here $N_z N_x$ is far greater than N_y since $\Delta x > pitch$ and $N_e \approx N_y/2$. This implies that the number of unknowns in the system given by (4.36) is underdetermined. As seen in the previous Chapter, solving such kind of inverse problems provides suboptimal solutions. To overcome the same issue in similar models [Besson et al., 2016, Besson et al., 2018] it was shown that is possible to concatenate the N_{el} systems (4.36) to increase the number of equations for the same number of unknowns (as discussed in Section 4.1). However, this is still not enough in order to have well determined system. The next step would be to emit successively a number $N_{pwi} = 3$ of plane wave insonifications[7] and then to concatenate the systems given by each emission / reception events. Despite its ability to increase the number of equations, this solution presents an important drawback that impairs the "fast" side of the acquisition rate. In fact, as shown in Sub-section 2.2.2, the acquisition time needed to gather all N_{pwi} observations is thus N_{pwi} times greater than the time needed to record the backscattered echoes from one plane wave emission. The unwanted effect of the increase in acquisition time is that, for fast transient events, the TRF changes so fast that for N_{pwi} successive emissions the TRF is not the same.

4.7.2 Temporal encoding for simultaneous emission of plane waves: the continuous time / space AMCUS

In order to overcome the problem stated in the previous Sub-section, we propose to emit the N_{pwi} plane waves simultaneously using quasi orthogonal encoding of the excitation signals $a^k(t)$ associated to each k^{th} plane wave. Here, the direct model is adapted in order to include the simultaneous emission of temporal encoded plane waves.

In Sub-section 3.2 (3.8), it was demonstrated that, in the case of simultaneous emission of N_{pwi} plane waves, one can write the total received signal ($y_i(t)$) at the element i as follows:

$$\begin{aligned} y_i(t) = w_i \sum_{j=1}^{N_{el}} \left[w_j h(t) *_{t\,S} a_j(t) *_t h(t) *_t \int_V \gamma(\vec{r})\, g_{ji}(\vec{r}, t)\, \mathrm{d}^2\vec{r} \right] + b_i(t) &\underset{\text{Using (3.7), (4.35)}}{\Longleftrightarrow} \\ y_i(t) = \sum_{k=1}^{N_{pwi}} e^k(t) *_t g_i^k(t) + b_i(t) = \sum_{k=1}^{N_{pwi}} y_i^k(t) + b_i(t) & \end{aligned} \tag{4.46}$$

As one can see in (4.46), the received signals $y_i(t)$ contain a mix of echoes associated to each simultaneously emitted plane wave k. To separate the contribution of each plane wave, we propose to use filters $f^k(t)$ adapted to the typical waveform of the plane wave echo $e^k(t)$. At this point, we can write the expression of the filtered backscattered echoes for each of the emitted plane wave k as follows:

$$\hat{g}_i^k(t) = f^k(t) *_t y_i(t) \tag{4.47}$$

where $\hat{g}_i^k(t)$ can be seen as an estimation of $g_i^k(t)$.

Supposing that all the excitations $a^k(t)$ occupy the same frequency bandwidth, in (4.47) the signal $\hat{g}_i^k(t)$ contains some noise related to the waveforms $e^l(t)$ ($l \neq k$) also called crosstalk. This noise can be evaluated by considering the case when all the N_{pwi} plane waves, carrying the codes $a^k(t)$, are emitted successively. In this case, the received signals $y_i^k(t)$ are not subject to crosstalk. Let us call $\overline{g}_i^k(t)$ the

[7] Since the number of simultaneously emitted plane waves depends on the spatial discretization steps and medium size, the detailed pipeline for the computation of N_{pwi} will appear in Section 4.10, where the simulation parameters will be presented.

corresponding estimation of $g_i^k(t)$, we have then:

$$\begin{aligned} y_i^k(t) &= e^k(t) *_t g_i^k(t) \\ \overline{g}_i^k(t) &= f^k(t) *_t y_i^k(t) \end{aligned} \tag{4.48}$$

Using (4.46), (4.47) and (4.48) we can deduce the expression of the crosstalk noise $\zeta_k(t)$:

$$\zeta^k(t) = \hat{g}_i^k(t) - \overline{g}_i^k(t) = \sum_{l=1, l\neq k}^{N_{pwi}} f^k(t) *_t e^l(t) *_t g_i^l(t) \tag{4.49}$$

In order to reduce $\zeta^k(t)$, one needs to find the optimal filters $f^k(t)$ given the excitation signals $a^l(t)$. Minimizing directly (4.49) is a complex problem and most importantly its solution depends directly on the imaged medium (through $g_i^l(t)$). Instead, we propose to minimize the following expression that is TRF invariant:

$$\zeta_r^k(t) = \sum_{l=1, l\neq k}^{N_{pwi}} f^k(t) *_t e^l(t) \tag{4.50}$$

The optimal filters $f^k(t)$ that minimize (4.50) are Wiener filters adapted to the waveforms $e^k(t)$ as follows:

$$F^k(\nu) = \frac{\left(E^k(\nu)\right)^*}{\left|E^k(\nu)\right|^2 + S(\nu)} \tag{4.51}$$

where $F^k(\nu)$ and $E^k(\nu)$ are the Fourier transforms of the corresponding temporal signals and $()^*$ represents the complex conjugate. The spectral density of the noise, $S(\nu)$, can be written as:

$$S(\nu) = \sum_{l=1, l\neq k}^{N_{pwi}} \left|E^l(\nu)\right|^2 \tag{4.52}$$

From (4.51) and (4.52), it can be seen that the signals $e^k(t)$ (and the corresponding compression filters $f^k(t)$) yielding the lowest amount of crosstalk need to be orthogonal or quasi orthogonal (high, pronounced main lobe for the convolution $f^k(t) *_t e^k(t)$ and low values of the product $f^l(t) *_t e^k(t)$, $l \neq k$).

As previously shown in Section 2.3, in ultrasound, different orthogonal excitations such as chirps or BPSK pseudo-orthogonal sequences have been proposed. Extensive research detailed in Appendix D, showed that the waveforms $e^k(t) = a^k(t) *_t h(t) *_t h(t)$ and the corresponding filters $f^k(t)$ that minimize the crosstalk (see (4.49)) consist in a mix between chirps and BPSK modulated m-sequences (see Fig.4.18a-c). As previously defined, each $e^k(t)$ represents the typical waveform of the backscattered echoes if the plane wave k was emitted. This implies that, in order to obtain such echoes as presented in Fig.4.18(a)-(c), we need to deduce the excitation signals $a^k(t)$. In order to compute $a^k(t)$, we propose the following pipeline:

(a) $e^1(t)$ is designed as a chirp waveform:

$$e^1(t) = \eta(t) \cos\left(2\pi(f_0 - \tfrac{B}{2} + \tfrac{B}{T}t)\,t\right) \tag{4.53}$$

where $B = 5.1MHz$ is the bandwidth of the pulse echo impulse response of the employed ultrasound probe (Table 3.1). $T = 18.55\mu s$ is the waveform duration and f_0 is the central frequency of the probe. $\eta(t)$ is a 20% Tukey window of duration T. The instantaneous frequency of the signal grows with time (4.53) thus $e^1(t)$ is called "up" chirp.

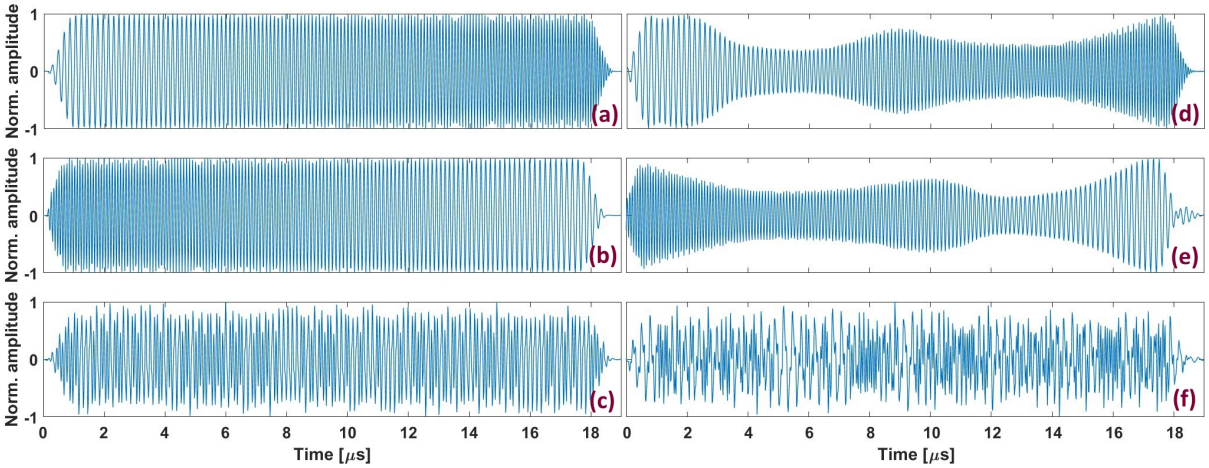

Figure 4.18: (a), (b), (c) - Example of a three orthogonal $e^k(t)$ signals. This set of waveforms contains an "up" chirp, a "down" chirp and a BPSK modulated m-sequence. (d), (e) and (f) - corresponding excitations $a^k(t)$ used to drive a transducer of pulse-echo impulse response $h(t)$ in order to obtain the waveforms $e^k(t)$ in reception.

(b) in the same way as $e^1(t)$, $e^2(t)$ is designed as a chirp waveform:

$$e^2(t) = \eta(t)\cos\left(2\pi(f_0 + \tfrac{B}{2} - \tfrac{B}{T}t)t\right) \tag{4.54}$$

Since the instantaneous frequency of $e^2(t)$ decreases with time, this signal is called "down" chirp.

(c) $e^3(t)$ is designed as a BPSK modulated pseudo-random sequence:

$$e^3(t) = \sum_{i=0}^{q-1} s_i \delta(t - iT_0) *_t \left[\cos\left(\tfrac{2\pi}{T_0}\right)\mathrm{rect}\left(\tfrac{t}{T_0}\right)\right] \tag{4.55}$$

where s is a m-sequence of length q, $T_0 = 1/f_0$ and $rect(t)$ is the rectangular function. In (4.55), the temporal convolution with a cosine function represents the BPSK modulation (at the central frequency of the probe) of the binary sequence s.

(d) the excitation signals $a^k(t)$ are deduced from the relation $e^k(t) = a^k(t) *_t h(t)$ using the following Wiener filter:

$$\begin{aligned} \Psi^k(\nu) &= \frac{\left(H^k(\nu)\right)^*}{\left|H(\nu)\right|^2 + \varsigma} \\ A^k(\nu) &= \Psi(\nu) *_t E^k(\nu) \end{aligned} \tag{4.56}$$

where the parameter ς can be empirically tuned in order to bypass zero division (outside the bandwidth of $h(t)$). This results in a better noise stability of (4.56).

The resulting excitation signals $a^k(t)$ that allow generating echoes of shape $e^k(t)$ (Fig.4.18(a)-(c)) are shown in Fig.4.18(d)-(f). These excitation signals allow overcoming the negative effects (main autocorrelation lobe broadening, compression side lobe level increase) of the pulse-echo impulse response of the probe (discussed in [Trots et al., 2004, Nowicki et al., 2007]) and were successfully implemented on chirps in [Oelze, 2007, Benane et al., 2018].

The optimal Wiener filters $f^k(t)$ are computed using (4.51). The matched filtering results of the $e^k(t)$ waveforms with the corresponding $f^k(t)$ filters are shown in Fig.4.19(a)-(c). This figure allows to observe how the optimal filters compress the echo waveforms. Indeed, the width at half height of the main lobe is equal for the three compressed pulses. Each crosstalk $\zeta_r^k(t)$, computed using (4.50),

is illustrated in Fig.4.19(d)-(f). It can be observed that $\zeta_r^k(t) < 0.18 \; \forall k \in \{1..3\}$ which means that for each plane wave k, the amplitude of the crosstalk noise never exceeds 18% of the amplitude of the compressed pulse.

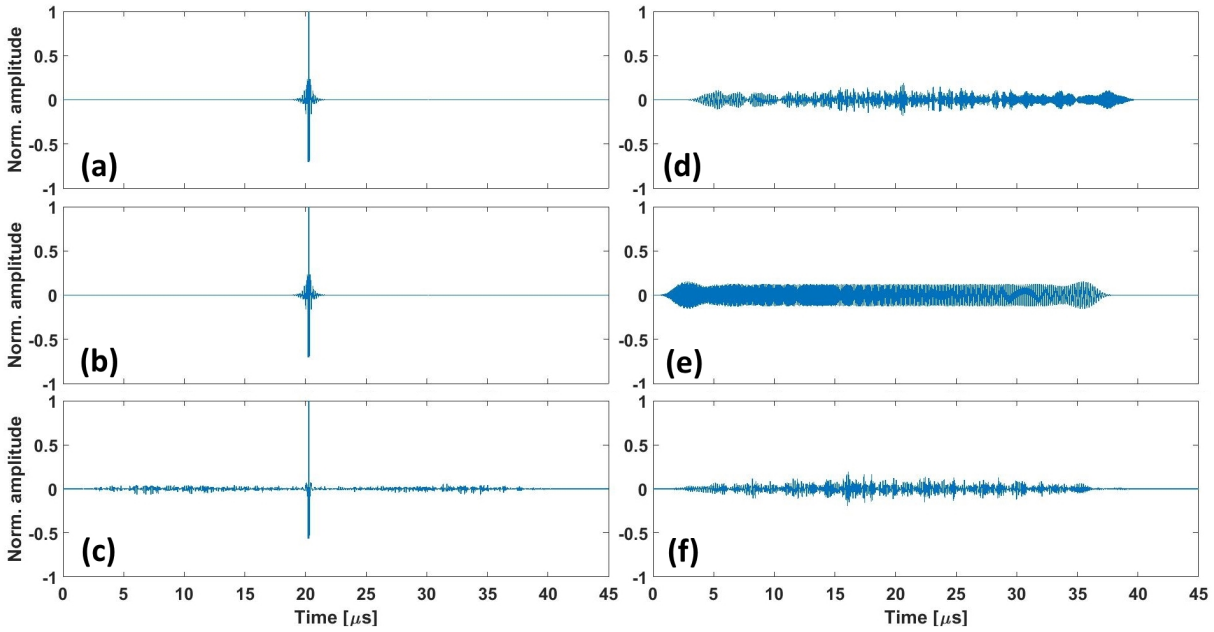

Figure 4.19: (a), (b), (c) - Results of compression of the waveforms $e^1(t)$, $e^2(t)$ and $e^3(t)$ using the filters $f^1(t)$, $f^2(t)$ and $f^3(t)$ respectively. (d), (e) and (f) - the crosstalk noise (realization of $\zeta_r^1(t)$, $\zeta_r^2(t)$, $\zeta_r^3(t)$ in equation (2.16)) generated during the compression of the waveforms $e^1(t)$, $e^2(t)$ and $e^3(t)$ respectively.

4.8 The time / space discretized AMCUS

In the previous Section, we detailed the analytical relations that link the received backscattered echoes to the simultaneously emitted coded plane waves and medium TRF. We also showed how to find optimal compression filters that allow echoes separation in reception. Here, we show the discrete time / space equivalent of AMCUS and we build the final kernel $\boldsymbol{\Psi}$.

The discrete time / space equivalent of the signal received by the i^{th} element of the probe, in the case of simultaneous plane wave imaging, can be deduced by applying (4.36) to (4.46) :

$$\begin{aligned} \boldsymbol{y}_i &= \sum_{k=1}^{N_{pwi}} \boldsymbol{y}_i^k = \sum_{k=1}^{N_{pw}} \boldsymbol{E}^k \cdot \boldsymbol{C}_i^k \cdot \boldsymbol{\gamma} = \underline{\boldsymbol{\Lambda}}_i \cdot \boldsymbol{\gamma} \\ \text{with: } \underline{\boldsymbol{\Lambda}}_i &= \sum_{k=1}^{N_{pwi}} \boldsymbol{\Lambda}_i^k \quad \text{and} \quad \boldsymbol{\Lambda}_i^k = \boldsymbol{E}^k \cdot \boldsymbol{C}_i^k \end{aligned} \tag{4.57}$$

The discrete expressions of the impulse responses estimation $\hat{g}_i^k(t)$ can be computed as follows:

$$\hat{\boldsymbol{g}}_i^k = \boldsymbol{F}^k \cdot \boldsymbol{y}_i = \boldsymbol{F}^k \cdot \underline{\boldsymbol{\Lambda}}_i \cdot \boldsymbol{\gamma} \tag{4.58}$$

where $\boldsymbol{F}^k$ are Toeplitz matrices built using the waveforms of the filters $\mathbf{f}^k$as follows:

$$\boldsymbol{F}^k = \begin{bmatrix} \boldsymbol{f}^k[0] & 0 & \cdots & 0 \\ \boldsymbol{f}^k[1] & \boldsymbol{f}^k[0] & \cdots & 0 \\ \vdots & \vdots & \ddots & \vdots \\ \boldsymbol{f}^k[N_a-1] & \boldsymbol{f}^k[N_f-2] & \cdots & \boldsymbol{f}^k[0] \\ 0 & \boldsymbol{f}^k[N_f-1] & \cdots & \boldsymbol{f}^k[1] \\ \vdots & \vdots & \ddots & \vdots \\ 0 & 0 & \cdots & \boldsymbol{f}^k[N_f-1] \end{bmatrix} \tag{4.59}$$

with $\boldsymbol{f}^k$ – the discrete time counterparts of $f^k(t)$ and N_f are their corresponding lengths. From (4.58), it can be deduced that each matrix $\mathbf{F}^k$ has N_y columns, the number of rows being set by the relation $N_y + N_f - 1$.

As discussed in Section 4.1 and later in Sub-section 4.7.1, since $\hat{\boldsymbol{g}}_i^k$ depends only on the interaction between the plane wave k and the medium (exempting the crosstalk $\zeta^k(t)$), the observation space can be built by concatenating the vectors $\hat{\boldsymbol{g}}_i^k$ for all the receiving elements N_{el} and all the plane waves N_{pwi}:

$$\tilde{\boldsymbol{g}} = \left[\hat{\boldsymbol{g}}_1^1 \| \hat{\boldsymbol{g}}_2^1 \| \cdots \| \hat{\boldsymbol{g}}_{N_{el}}^1 \| \cdots \| \hat{\boldsymbol{g}}_1^{N_{pw}} \| \hat{\boldsymbol{g}}_2^{N_{pw}} \| \cdots \| \hat{\boldsymbol{g}}_{N_{el}}^{N_{pw}}\right] \tag{4.60}$$

where $\boldsymbol{g}_1 \| \boldsymbol{g}_2$ represents the concatenation along the columns of the vectors $\boldsymbol{g}_1$ and $\boldsymbol{g}_2$. In these conditions, using (4.58), we can write the total AMCUS kernel and the corresponding linear system as follows:

$$\begin{gathered} \boldsymbol{\Psi} = \left[\boldsymbol{F}^1 \cdot \underline{\boldsymbol{\Lambda}}_1 \| \cdots \| \boldsymbol{F}^1 \cdot \underline{\boldsymbol{\Lambda}}_{N_{el}} \| \cdots \| \boldsymbol{F}^{N_{pw}} \cdot \underline{\boldsymbol{\Lambda}}_1 \| \cdots \| \boldsymbol{F}^{N_{pw}} \cdot \underline{\boldsymbol{\Lambda}}_{N_{el}}\right] \\ \tilde{\boldsymbol{g}} = \boldsymbol{\Psi} \cdot \boldsymbol{\gamma} \end{gathered} \tag{4.61}$$

Since each matrix $\boldsymbol{F}^k$ is of size $(N_y + N_f - 1) \times N_y$ and each matrix $\underline{\boldsymbol{\Lambda}}_k$ is of size $N_y \times N_x N_z$ this results in a kernel $\boldsymbol{\Psi}$ of size $N_{pw} N_{el}(N_y + N_f - 1) \times N_x N_z$. The full pipeline of AMCUS is showed in Fig.4.20. Here one can immediately observe the relation $\tilde{\boldsymbol{g}} = \boldsymbol{\Psi} \cdot \boldsymbol{\gamma}$ that appears between the filtered backscattered echoes and the tissue reflectivity function. Furthermore, it can be seen that the kernel $\boldsymbol{\Psi}$ models simultaneously the "Wave Emission", "Wave propagation", "Echo reception" blocks and even a small part of the inverse problem in the "Image reconstruction" block. In fact, the echo separation filters $\boldsymbol{F}^k$ (used to build $\boldsymbol{\Psi}$) can be seen as the first step towards the inversion of the propagation model that links the TRF $\boldsymbol{\gamma}$ to the observations $\boldsymbol{y}_i$.

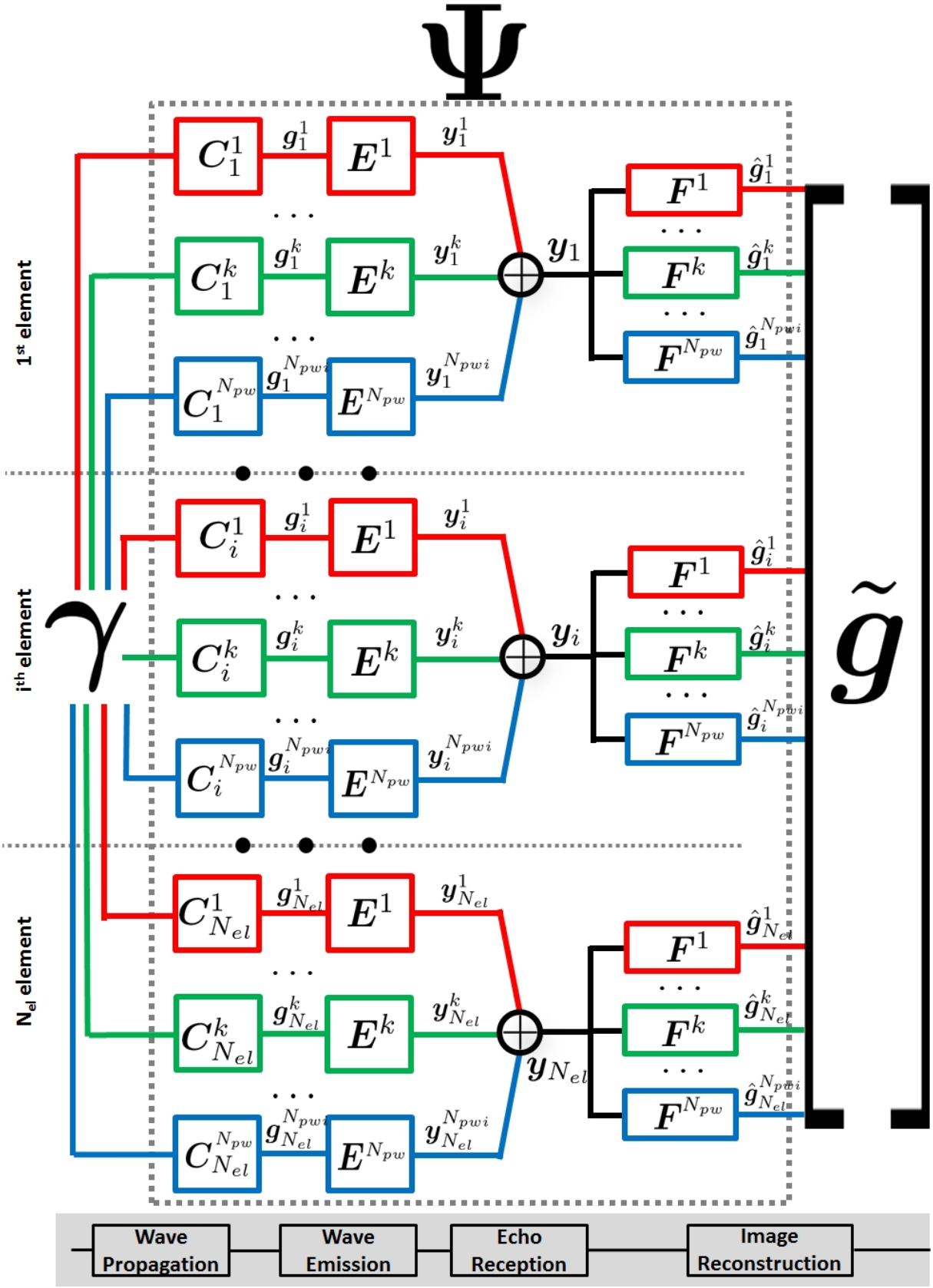

Figure 4.20: The complete AMCUS pipeline. The red, green and blue colors represent the $N_{pwi} = 3$ plane waves that are emitted simultaneously inside the medium.

4.9 AMCUS: Inverse problem statement

In this Section is addressed the part of the "Image reconstruction" block that allows to go from the filtered backscattered echoes $\tilde{\boldsymbol{g}}$ to the TRF estimation $\hat{\boldsymbol{\gamma}}$.

The AMCUS model (4.61), developed in the previous Section, was written without considering the noise. However, as seen in Sections 4.4, 4.5 and 4.7, the $\boldsymbol{C}_i^k$ matrices generate modeling errors which can be seen as an additive noise superposed to the observations $\boldsymbol{y}_i^k$ and thus on the vector $\tilde{\boldsymbol{g}}$. In the presence of modeling numerical noise $\boldsymbol{b}$, (4.61) becomes:

$$\tilde{\boldsymbol{g}} = \boldsymbol{\Psi}\boldsymbol{\gamma} + \boldsymbol{b} \tag{4.62}$$

As seen in Sub-section 3.3.1, a straightforward way to solve the problem (4.62) would be to minimize the square error term: $\|\boldsymbol{\Psi}\boldsymbol{\gamma} - \tilde{\mathbf{g}}\|_2^2$ where $\|\ \|_2$ represents the l_2 norm. In this case, under the condition that $\boldsymbol{\Psi}$ is well-conditioned, the solution would be $\hat{\boldsymbol{\gamma}} = \boldsymbol{\Psi}^\dagger \tilde{\boldsymbol{g}}$ where $\boldsymbol{\Psi}^\dagger$ is the Moore-Penrose pseudo-inverse of $\boldsymbol{\Psi}$. However, in Sub-section 3.3.2 it was also shown that the quality of the $\hat{\boldsymbol{\gamma}}$ estimation depends closely on the kernel $\boldsymbol{\Psi}$ condition number $K(\boldsymbol{\Psi})$. Thus it is convenient to first study the behavior of $K(\boldsymbol{\Psi})$. In Section 4.7, we showed that the filters $f^k(t)$ are adapted to quasi orthogonal waveforms $e^k(t)$. This means that $f^k(t)$ are also almost orthogonal and the resulting Toeplitz matrices $\boldsymbol{F}^k$ verify $(\boldsymbol{F}^k)^T\boldsymbol{F}^k \approx \boldsymbol{I}$, $\forall k \in \{1..N_{pw}\}$ where $(\,)^T$ is the transpose operator and $\boldsymbol{I}$ is the identity matrix. We can use the Gram matrix rank property in order to deduce the rank $\varrho_{\boldsymbol{\Psi}}$ of the matrix $\boldsymbol{\Psi}$:

$$\varrho_{\boldsymbol{\Psi}} = \varrho_{(\boldsymbol{\Psi})^T\boldsymbol{\Psi}} \tag{4.63}$$

Using (4.61), we can deduce the analytical expression for the matrix product $(\boldsymbol{\Psi})^T\boldsymbol{\Psi}$:

$$\begin{gathered}(\boldsymbol{\Psi})^T\boldsymbol{\Psi} = \sum_{k=1}^{N_{pwi}}\sum_{i=1}^{N_{el}}(\underline{\boldsymbol{\Lambda}}_i)^T(\boldsymbol{F}^k)^T\boldsymbol{F}^k\underline{\boldsymbol{\Lambda}}_i \approx \sum_{k=1}^{N_{pwi}}\xi^k\sum_{i=1}^{N_{el}}(\underline{\boldsymbol{\Lambda}}_i)^T\underline{\boldsymbol{\Lambda}}_i \approx \boldsymbol{\Xi}\sum_{k=1}^{N_{pwi}}\xi^k \\ \text{with: } \begin{cases} \xi^k = \|\boldsymbol{f}^k\|_2 \\ \boldsymbol{\Xi} = \sum_{i=1}^{N_{el}}(\underline{\boldsymbol{\Lambda}}_i)^T\underline{\boldsymbol{\Lambda}}_i \end{cases}\end{gathered} \tag{4.64}$$

Since $\varrho_{\underline{\boldsymbol{\Lambda}}_i} \leq N_y$, we can use the subadditivity property of the matrix rank to write:

$$\varrho_{\boldsymbol{\Xi}} \leq \sum_{i=1}^{N_{el}}\varrho_{(\underline{\boldsymbol{\Lambda}}_i)^T\underline{\boldsymbol{\Lambda}}_i} \leq N_{el}N_y \tag{4.65}$$

Combining (4.63), (4.64) and (4.65) we obtain:

$$\varrho_{\boldsymbol{\Psi}} \leq \varrho_{\boldsymbol{\Xi}} \leq N_{el}N_y \tag{4.66}$$

Given that the kernel $\boldsymbol{\Psi}$ is of size $N_{pwi}N_{el}(N_y+N_f-1)\times N_xN_z$, the result of (4.66) implies that $\boldsymbol{\Psi}$ is not full rank which means, by definition, that its condition number $K(\boldsymbol{\Psi})$ is very high ($\sim 10^{22}$). In such case, a straightforward inversion of the kernel, based on the pseudo-inverse, would provide a degraded estimation $\hat{\boldsymbol{\gamma}}$, due to the amplification of noise $\mathbf{b}$. This problem can be overcome by constraining the solution space through a regularization term [Beck and Teboulle, 2009]. The TRF can be then estimated as:

$$\hat{\boldsymbol{\gamma}} = \underset{\boldsymbol{\gamma}}{\operatorname{argmin}}\{\|\boldsymbol{\Psi}\boldsymbol{\gamma} - \tilde{\boldsymbol{g}}\|_2^2 + \lambda\|\boldsymbol{\gamma}\|_p\} \tag{4.67}$$

where $\|\ \|_p$ represents the l_p norm and the scalar λ allows a trade-off between the data attachment and the regularization term.

Finding a general regularization term in (4.67) is an open problem in the ultrasound domain, where

in the approaches that use inverse problems in order to estimate the TRF, the norm l_p and the weight λ, are usually adapted in function of the TRF [David et al., 2015, Besson et al., 2016, Besson et al., 2018]. Here we propose to use $l_p = l_1$, the weight λ being empirically adapted as a function of the expected TRF. The complete pipeline of the inverse problem approach implemented in the "Image reconstruction" block is shown in Fig.4.21. As it can be seen here, the part that allows solving (4.67) and thus obtaining an estimation of the tissue reflectivity function from the filtered backscattered echoes is the Fast Iterative Shrinkage Thresholding Algorithm(FISTA). A detailed description of FISTA is presented in Appendix B. Similar to [Besson et al., 2018], the FISTA stopping criterion was set to be the drop of the relative difference (between successive estimations) of the TRF under 10^{-3}.

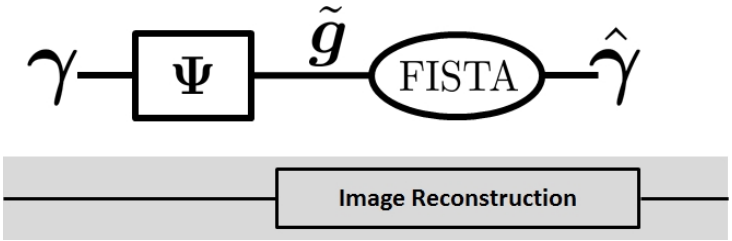

Figure 4.21: The inverse problem part of the "Image reconstruction" block that allows obtaining an estimation of the TRF from the filtered backscattered echoes. In this work, the Fast Iterative Shrinkage-Thresholding Algorithm (FISTA) is used to invert the AMCUS.

4.10 AMCUS: Inverse problem results on Field II generated data

In this Section, we detail the results obtained when solving the inverse problem based on AMCUS. First, its performance on a simulated wire phantom is assessed then the results obtained on a simulated cyst phantom are presented. In order to assess the performance of AMCUS, the obtained results were compared with the ones provided by the classical reconstruction algorithm DAS (2.36) using consecutive transmissions (2.55). The ultrasound probe LA523E (Table 3.1) was used for emission reception of the ultrasound waves. The phantoms showed in Fig.4.14 were used in order to assess the AMCUS performance to return the TRF estimation on mediums with different scatterer densities. The discretization parameters used in order to build our direct model are presented in Table 4.1. Here, t_0 corresponds to the starting time for the recording of the backscattered echoes.

Parameter	**Value**
Sampling frequency f_s	61.6 MHz
No. of element subdivision N	10
Axial resolution Δz	25 μm
Lateral resolution Δx	61.25 μm
$\boldsymbol{\Omega}$ start depth	20 mm
$\boldsymbol{\Omega}$ end depth	61.2 mm
t_0	26.2 μs

Table 4.1: Time / Space discretization parameters

Using the relation (4.21) and the size of the medium given in Table 4.1, one can deduce that the size of the $\boldsymbol{\Omega}$ grid is $N_x \times N_z = 257 \times 1648$. This implies that the total amount of unknowns (length of the TRF $\boldsymbol{\gamma}$ vector) in the system is $N_x \times N_z = 423536$. Imaging a $w_{\boldsymbol{\Omega}} = 4.12\ cm$ deep medium implies that the recorded data needs to be $N_y = 3300$ long (computed using (3.4)). In other words, each element i of the probe provides 3300 equations. Now, for one plane wave emission / reception there are $N_{el} = 64$ active elements in receptions which give a total amount of $N_{el} \times N_y = 211200$ equations. It can be

observed that $N_x \times N_z > N_{el} \times N_y$ ($N_x \times N_z/(N_{el} \times N_y) > 2$). Thus, in order to have at least the same number of equations ($N_{el} \times N_y$) as there are unknowns in the system, we decided to force $N_{pwi} = 3$. The emission angles are $\theta_k \in \{-10°, 0°, 10°\}$. To each plane wave was assigned an excitation signal $\boldsymbol{a}^k$ shown in Fig.4.18(d)-(f).

4.10.1 Wire phantom results

Fig. 4.22 displays the B-mode images of the reference TRF (a), estimated TRF using AMCUS (b) and estimated TRF using DAS (c). Firstly, one can notice that $\hat{\boldsymbol{\gamma}}_{AMCUS}$ is very similar to $\boldsymbol{\gamma}$ which shows that the proposed direct model and its inversion is capable to converge towards a stable solution. Indeed, the obtained axial and lateral resolution at $-6\ dB$ (Table 4.2) estimated on the B-mode images are exactly the same (axial resolution: 25 μm, lateral resolution: 61.25 μm). This is due to the fact that for both images the size of the scatterers does not exceed the size of the pixel which is set by the discretization parameters shown in Table 4.1. In the $\hat{\boldsymbol{\gamma}}_{DAS}$ B-mode image, we can distinguish the expected TRF, but the axial and lateral resolutions of the targets are much larger (axial resolution: 192.5 μm, lateral resolution: 455 μm) than the values obtained with AMCUS. This effect can be clearly noticed on the wires closely placed (e. g. at 39 mm, the three central points are indistinguishable with DAS) while the AMCUS separates these targets as in the reference TRF. In addition to the respective gain in axial and lateral resolutions between $\hat{\boldsymbol{\gamma}}$ and $\hat{\boldsymbol{\gamma}}_{DAS}$, AMCUS does not yield the artifacts visible in DAS B-mode image (in this case, around $-26\ dB$).

Metric	$\boldsymbol{\gamma}$	$\hat{\boldsymbol{\gamma}}_{AMCUS}$	$\hat{\boldsymbol{\gamma}}_{DAS}$
Axial resolution	25 μm	25 μm	192.5 μm
Lateral resolution	61.25 μm	61.25 μm	455 μm

Table 4.2: Axial and lateral resolution measured on the wire phantom for the point placed at the position $r = (0, 0, 23.9)\ mm$

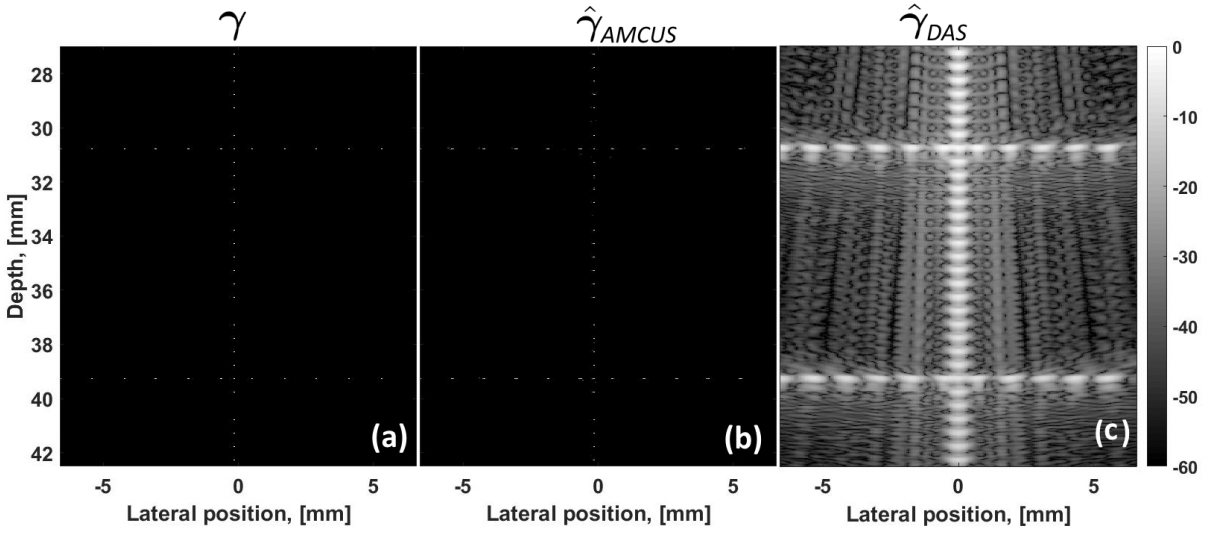

Figure 4.22: B-mode images of the wire TRF: (a) - reference ($\boldsymbol{\gamma}$); (b) - estimated using the proposed approach ($\hat{\boldsymbol{\gamma}}_{AMCUS}$). For FISTA algorithm: $\lambda = 0.01$; (c) - estimated using DAS algorithm ($\hat{\boldsymbol{\gamma}}_{DAS}$). Note that for $\boldsymbol{\gamma}$ and $\hat{\boldsymbol{\gamma}}$ the B-mode images are obtained by log-compressing directly the TRF functions while for $\hat{\boldsymbol{\gamma}}_{DAS}$ an additional step of envelope detection is applied before log-compression.

Given that $\boldsymbol{\gamma}$ contains identical targets (same dimensions, same amplitudes) we also verified if the

estimated TRFs preserve this property. The reconstructed TRF images obtained from the wire phantom shown in Fig.4.23, provide the local Point Spread Function (PSF) of the reconstruction schemes / systems associated to the AMCUS and the DAS. As shown in Fig. 4.23, the shape of the PSF obtained using DAS changes as a function of depth and lateral position of the scatterer. On the other hand, the PSFs inside $\hat{\boldsymbol{\gamma}}$ do not change drastically between the scatterers and are very similar to the expected PSFs contained by the reference TRF. The small evolution of the PSF obtained for $\hat{\boldsymbol{\gamma}}$ between the first and second scatterer has a relative amplitude of $-19\ dB$ and does not change the values of the measured axial and lateral resolutions.

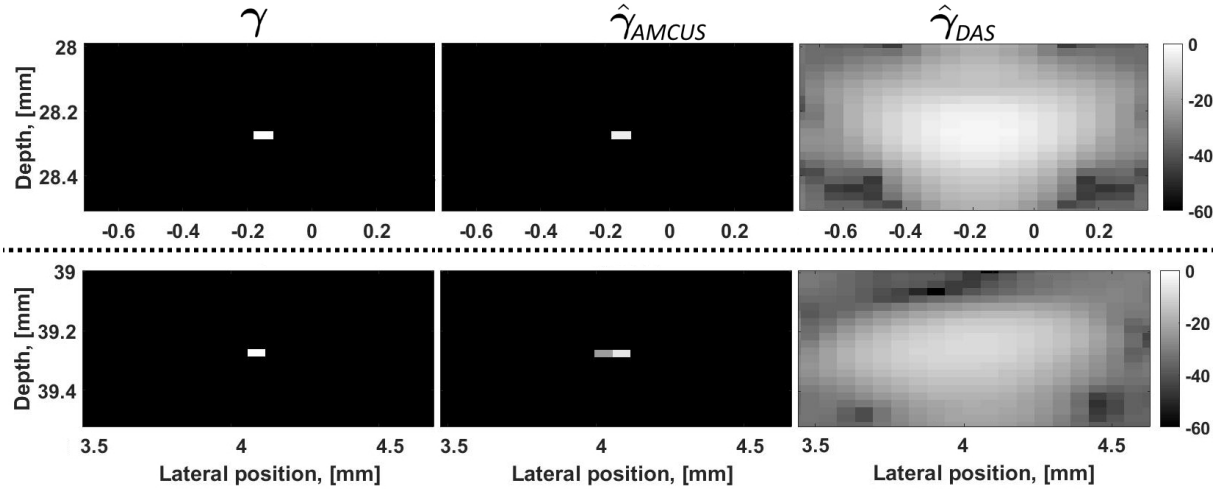

Figure 4.23: Reference punctual scatterers in the wire phantom ($\boldsymbol{\gamma}$) and the corresponding PSFs obtained with the proposed method ($\hat{\boldsymbol{\gamma}}_{AMCUS}$) and DAS ($\hat{\boldsymbol{\gamma}}_{DAS}$). The first row concerns the scatterer at $r = (-1.75, 0, 28.275)$ mm. The second row concerns the scatterer at $r = (4.1, 0, 39.275)$ mm.

4.10.2 Cyst phantom results

The B-mode images of the estimated TRF for the cyst phantom are shown in Fig.4.24. Here again, it can be observed that the AMCUS yields a B-mode image more similar to the reference than the one obtained with DAS. Knowing that the cysts are completely anechoic, one can see that the artifacts (previously observed on the wire phantom image) generate reconstruction noise inside the cysts that alters the TRF estimation. AMCUS also generates some noise inside the anechoic regions, however this noise is very sparse and visually less important (lower in amplitude). These observations are confirmed by the calculation of the SNR inside the anechoic regions, where the obtained value measured on $\hat{\boldsymbol{\gamma}}_{AMCUS}$ is 7.8 dB higher than the one measured on $\hat{\boldsymbol{\gamma}}_{DAS}$ (Table 4.3).
In Fig. 4.24, it can also be seen that the speckle inside $\hat{\boldsymbol{\gamma}}$ image is more similar to the one of $\boldsymbol{\gamma}$. This observation is coherent with the axial / lateral resolutions and PSFs observed on the wire phantom. DAS reconstruction, however, provides an estimate of the TRF with a much coarse speckle. This tendency is also visible on the the $Ax.AC_x$ and $Lat.AC_z$ (computed using (2.39)) plots showed in Fig. 4.25a and Fig. 4.25b respectively. In Fig. 4.25a, it can be seen that the $Ax.AC_x$ for $\hat{\boldsymbol{\gamma}}_{AMCUS}$ and $\boldsymbol{\gamma}$ are almost the same with a Width at Half Maximum (WHM) of 55.1 μm while the WHM for $\hat{\boldsymbol{\gamma}}_{DAS}$ is of 239 μm. A small degradation (9.2 μm) on the WHM for the $Lat.AC_z$ between $\hat{\boldsymbol{\gamma}}_{AMCUS}$ and $\boldsymbol{\gamma}$ is observed in Fig. 4.25b, however this value is much better than the one provided by the DAS approach (increase of 1710 μm). The $Ax.AC_x$ and $Lat.AC_z$ WHMs are summarized in Table 4.3.

The previously mentioned similarity between B-mode images of $\boldsymbol{\gamma}$ and $\hat{\boldsymbol{\gamma}}_{AMCUS}$ was also confirmed by the measurement of the Speckle Consistency (SC defined in (2.40)) (Fig. 4.26). As it can be seen, the SC main lobe is thinner (axially and laterally) for $\hat{\boldsymbol{\gamma}}_{AMCUS}$ B-mode image compared to the one of $\hat{\boldsymbol{\gamma}}_{DAS}$

Metric	γ	$\hat{\gamma}_{AMCUS}$	$\hat{\gamma}_{DAS}$
$Ax.AC_x$ WHM	55.1 μm	55.1 μm	239 μm
$Lat.AC_z$ WHM	130.7 μm	139.9 μm	1850 μm
SNR	∞ dB	21.3 dB	13.5 dB

Table 4.3: Image quality metrics evaluated on the cyst phantom

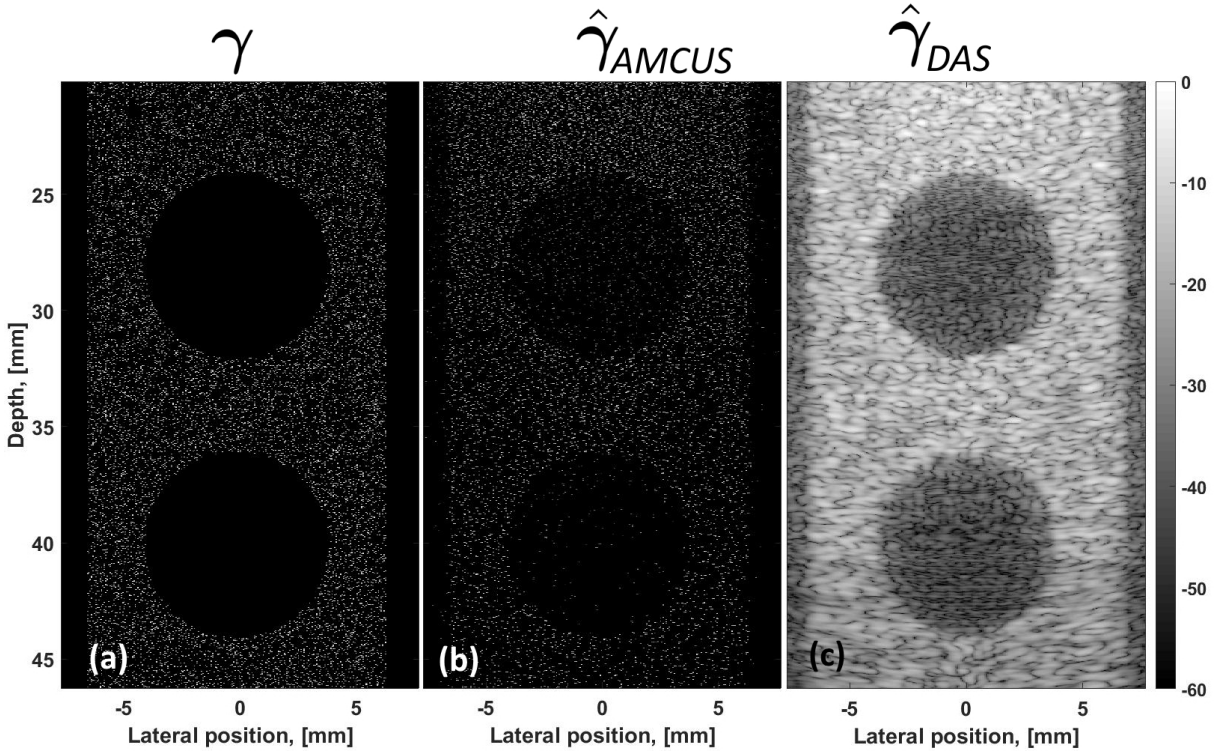

Figure 4.24: B-mode images of the cyst TRF: (a) - reference ($\boldsymbol{\gamma}$); (b) - estimated using the proposed approach ($\hat{\boldsymbol{\gamma}}_{AMCUS}$). For FISTA algorithm: $\lambda = 0.000075$; (c) - estimated using DAS algorithm ($\hat{\boldsymbol{\gamma}}_{DAS}$). Note that for $\boldsymbol{\gamma}$ and $\hat{\boldsymbol{\gamma}}$ the B-mode images are obtained by log-compressing directly the TRF functions while for $\hat{\boldsymbol{\gamma}}_{DAS}$ an additional step of envelope detection is applied before log-compression.

image, which means that the speckle in $\hat{\boldsymbol{\gamma}}$ is closer to the reference than the speckle in $\hat{\boldsymbol{\gamma}}_{DAS}$. These visual assessments are also backed by the measurements of the WHM of these *SC* main lobes. Indeed, we measure an axial WHM of 53.1 μm, 83.6 μm and 213.7 μm for $\boldsymbol{\gamma}$, $\hat{\boldsymbol{\gamma}}_{AMCUS}$ and $\hat{\boldsymbol{\gamma}}_{DAS}$ respectively. The corresponding lateral WHMs are 104.1 μm, 122.3 μm and 364.4 μm.

4.11 Discussion

In the previous Sections, we presented a general direct model that links the recorded radio-frequency data to the excitations signals, geometrical / acousto-electrical properties of the ultrasound probe and tissue reflectivity function. The general model was adapted to the concept of plane wave imaging, where the obtained results showed a relative error under 10% (for individual, sparse scatterers) when compared to the reference data (computed using the Field II program). However, due to its origin, this error has the tendency to increase if the scatterer density increases. As shown in Section 4.4, 4.5 and 4.7, this error can be reduced by refining the partitioning of the ultrasound probe elements and of the imaged medium.

In order to decrease the frame acquisition time, a simultaneous coded emission of plane waves was

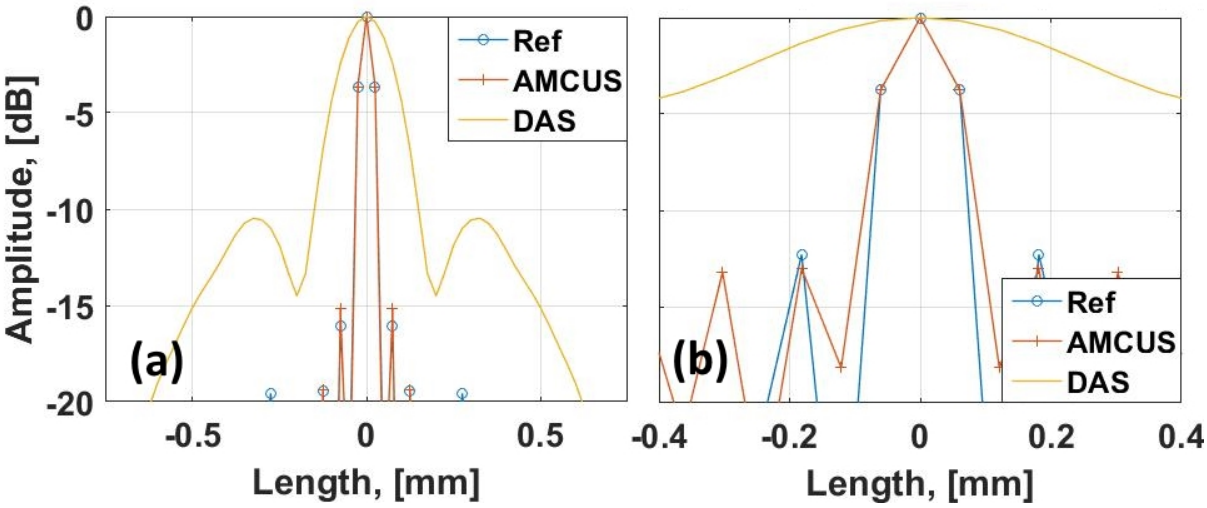

Figure 4.25: (a) - Axial Auto-Correlation lengths for $\boldsymbol{\gamma}$ (Ref), $\hat{\boldsymbol{\gamma}}_{AMCUS}$ $(AMCUS)$ and $\hat{\boldsymbol{\gamma}}_{DAS}$ (DAS). These metrics are evaluated for the axial line that passes trough $x = 5\ mm$; (b) - Lateral Auto-Correlation lengths for $\boldsymbol{\gamma}$ (Ref), $\hat{\boldsymbol{\gamma}}_{AMCUS}$ $(AMCUS)$ and $\hat{\boldsymbol{\gamma}}_{DAS}$ (DAS). These metrics are evaluated for the horizontal line that passes trough $z = 35\ mm$.

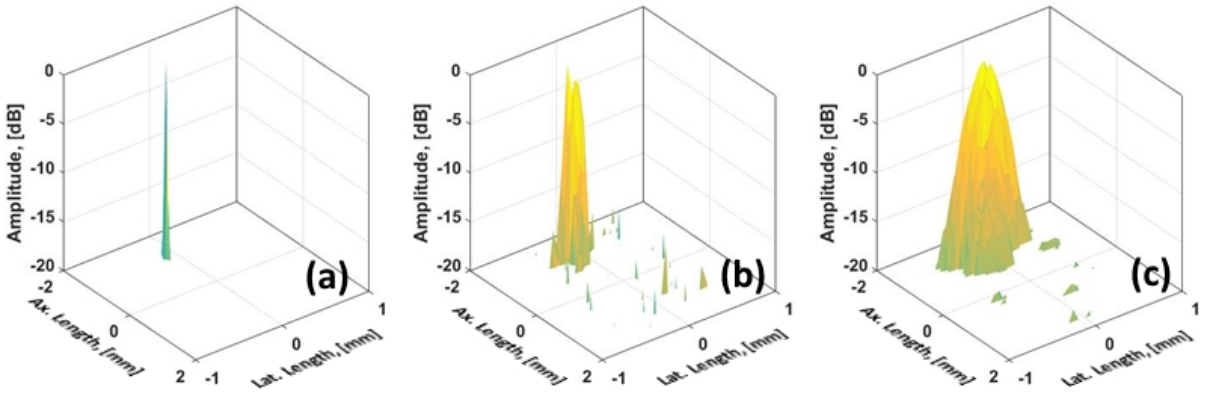

Figure 4.26: SC results measured on: (a) - $\boldsymbol{\gamma}$, (b) - $\hat{\boldsymbol{\gamma}}_{AMCUS}$ and (c) - $\hat{\boldsymbol{\gamma}}_{DAS}$. For the SC computation (2.40), the patch $\boldsymbol{p}_\gamma$ has a size of $2 \times 2\ mm^2$ centered at the position $\vec{r} = (-4, 0, 26)\ mm$ inside the reference $\boldsymbol{\gamma}$ image (before log-compression) Fig.4.24(a).

proposed and the direct model was accordingly adapted. Three plane waves were emitted simultaneously inside the medium in order to obtain a well determined direct model. The proposed excitation signals were a mix of two linear chirps (with increasing and decreasing instantaneous frequencies respectively) and one phase shift keyed pseudo-random binary sequence. We also decided to compensate the effect of the band-limited pulse-echo impulse response of the ultrasound probe in order to better preserve the large bandwidth and orthogonality properties of these signals. Thus, the obtained maximal value of the cross-correlation / auto-correlation ratio (between the excitation signals) did not exceed 17%. Besides, as the proposed direct model accounts for the crosstalk noise (therefore its effect is compensated during the inversion of the direct model), the obtained estimation of the TRF was not influenced.

Simulation results on a wire phantom showed that the axial and lateral resolutions are improved by a factor of more than six, when compared to classical reconstruction algorithm (DAS). Such improvements are linked to the fact that the proposed modeling (AMCUS) is not based upon the classical DAS assumptions (a Dirac pulse as excitation signal, an ultrasound probe of infinite bandwidth and a far field scatterings). An exhaustive study of the discretization step impact has shown that the provided

spatial resolution followed exactly the size of the grid cells (of the discretized medium), thus we can affirm that a smaller discretization would provide a better image resolution. We also observed that the PSFs inside the proposed TRF estimation is quasi-constant as a function of the scatterer depth and lateral position (contrary to the DAS PSF). This behavior was expected, since in AMCUS the refined discretization of the emitting / receiving elements allowed to model the spatial impulse response of the probe. Finally, the spatial stability of the PSF and the provided image resolution allowed to obtain a very similar TRF B-mode image compared to the reference. The previous results together with the visual assessment show a clear resemblance between the AMCUS estimated TRF and the reference. Despite the fact that, as seen in Section 4.6, the forward model performance decreases with the increase of the scatterer density, the results obtained on the simulated cyst phantom are very promising. In fact, the measurements on the axial and lateral autocorrelation widths at half maximum also showed an improvement provided by AMCUS, when compared to DAS (more than 3 and 12-fold, respectively). The drastic improvement in lateral autocorrelation width at half maximum (that exceeds heavily the boost in lateral resolution) can be explained by the fact that, for a coherent compounding of only three plane wave images, the obtained speckle size in the lateral direction is much larger than its size in the axial direction. This observations are also supported by the speckle consistency measurements which show a shrinking of the main inter-correlation peak in the axial and lateral direction (by a factor of 1.5 and 1.9 respectively), when compared to the obtained values on the DAS image.

5 General conclusion

The work presented in this manuscript extends the concept of ultrafast ultrasound imaging. More precisely, through a mix of techniques such as plane wave imaging, multiple-input / multiple-output systems and inverse problems, the proposed method allows to reconstruct images of much better quality than the ones obtained with classical imaging approaches, from data acquired only from one emission / reception event.

Firstly, a general theoretical formalism of the acoustic wave propagation phenomenon was developed. This allowed to link the electrical signal received by a piezoelectric transducer to the source excitation signal. The theoretical concepts thus developed were used to review the existing acquisition schemes. It was demonstrated that imaging methods which require less emission / reception events provide a lower image quality than the ones which require more emission / reception events. The general objective of this work was then deduced from this observation. Different ways of temporal encoding of the excitation signals were outlined as a mean to improve the image quality. A technique called coded synthetic transmit aperture, that mixes concepts from telecommunication systems and ultrasound imaging to boost the frame acquisition rate, was presented. It was shown that a more in depth study of this method is required in order to fully understand its limits. Such a study was done in the second chapter of this manuscript.

In the first contribution of this work, a technique that relies on the simultaneous emission of temporal encoded plane waves was developed. Relying on the theoretical background previously established, a direct mathematical model of the ultrasound plane wave propagation / tissue interaction phenomena, was built. The properties of the resulting direct model were studied, and the necessary requirements on the type / size of the excitation signals, on the size of the imaged medium and on the size of the recorded RF data were deduced. It was shown that if these requirements are met, the obtained image quality is exactly the same as the one provided by the conventional imaging technique. Moreover, it was demonstrated that these requirements imply that, despite the simultaneous emission, the time gain provided by the proposed method is null when compared to the conventional plane wave imaging. In addition, it was observed that if the necessary conditions are not met, the image quality drops significantly when the provided frame acquisition rate increases. Experimental results proved the feasibility of the proposed method, and once again confirmed the theoretical considerations demonstrated with the simulations. Such conclusion raised a certain number of questions, one of the most important being to know whether it is possible to formally express the echoes generated by each plane wave as a function of a invariant entity. These questions were the core objectives of the second contribution of my thesis.

Perhaps the most valuable input of this work to the ultrasound imaging field was the theoretical development and simulation validation of an imaging method that has the potential not only to increase the frame acquisition rate, but also to improve the provided image quality of the conventional plane

wave imaging. Relying on the drawbacks of the coded synthetic aperture and plane wave imaging methods, the need for a more complex direct kernel that allows to model the ultrasound wave propagation / tissue interaction was demonstrated. Consequently, an advanced model that links the received backscattered echoes to the Tissue Reflectivity Function (TRF) was deduced. It was shown that the inverse problem based on the kernel built for an unique plane wave emission is heavily ill-posed. The Advanced Model for Coded UltraSound imaging (AMCUS) was designed, which relies on the core principle of the first contribution, and consists in the combination of such concepts as the simultaneous emission of coded plane waves and the advanced direct model. The general requirements, that the excitation signals / compression filters associated with each simultaneously emitted plane wave need to meet, were stated. For the TRF estimation, a regularized inverse problem was proposed, where the prior information on the TRF was set to be its sparsity. Furthermore, AMCUS performance was tested in simulation. Phantoms with sparse and dense distributions of scatterers were tested and it was observed, that due to the limitation in the temporal / spatial partition size, AMCUS provides synthetic RF data with a modeling error that depends on the scatterer density. Nonetheless, the quality of the TRF estimation, obtained by inverting AMCUS, was still better than the one provided by the classical reconstruction algorithms for a frame rate increased by a factor of three (for the simulated case studied here).

6 Discussion: current deadlocks and possible extensions

6.1 On the computational time and resources

One of the questions that will probably arise in the mind of every person during the lecture of this work, is in a certain way linked to the computation time required for the AMCUS based reconstruction of the TRF to first build the forward kernel and then solve the inverse problem. These questions have all the rights to exist, since in a world where ultrasound methods are widely known mostly thanks to their "real time" feature, a method that provides B-mode images "off-line" can be less appealing. To be fair, the AMCUS based TRF estimation is computational much more heavy than the delay and sum algorithm and even more than the Fourier domain migrations of the radio frequency data. In fact, despite using the advantages of the sparse matrices and vectorized computation in the MATLAB environment, building the direct AMCUS kernel is an operation that can take up to couple dozen of hours. As shown in Sub-section 4.4.2, the matrices involved in the computation of the AMCUS forward model can reach several hundreds gigabytes which implies that even charging the kernel into the operative memory can takes up to one hour. Finally, the last part of the TRF reconstruction using AMCUS, which is the estimation layer (using FISTA), reaches the stopping criteria in about four hours. In the defense of our method we can state that, at this stage, the most computational heavy part of our method which is direct model generation, for a given probe and region of interest inside the medium, is only to be built once and then it can be applied to any RF data acquired with this particular probe on this particular region of interest. This reduces greatly the computational time, however it remains still in the range of several hours. While such computation time is still far away from the concept of "real time", the quality of the proposed TRF estimation should at least motivate us as researchers to optimize the computation time to begin with. Thus, a way to tackle this issue could consist in combining AMCUS with the "matrix free" framework [Besson et al., 2018] developed by the group led by Jean-Philippe Thiran at the EPFL. The "matrix free" concept consists in the generation of the direct / inverse model "on the fly" and relies on parallel computations (on GPU) to achieve very low computation times. Such an improvement will not only allow to work more freely with AMCUS, but will also approach (in terms of computation time) AMCUS based TRF estimation to the reconstruction algorithms such as delay and sum.

6.2 On the AMCUS performance

Going back to the Sub-sections 4.4.2 and 4.4.3, where the choice on the size of the discretization steps for the imaged medium and the probe elements was made, one can rightfully affirm that the AMCUS performance would increase if these steps where refined. However, smaller partition steps imply bigger

matrices involved in the generation of the AMCUS forward kernel, which would immediately increase the computation time. Thus, in an attempt to decrease the computational time through "matrix free" computation, in the acceptable limits, refining the medium / probe elements discretization steps would be a feasible idea to increase the performance of AMCUS.

Here, one can also discuss the choice of the regularization parameters used for the AMCUS inversion. In fact, in this manuscript we presented results obtained using only a l_1 type regularization because it is the prior information term that works the best. However this choice is not uncommon for the ultrasound community, a high number of inverse problem based reconstruction methods using the same term to achieve the final results. Indeed, such an important assumption is not always adapted to the imaged medium which explains the decrease in TRF estimation quality on cyst phantoms. However, as long as a more precise model for the scatterer distribution inside the medium is not available, the l_1 norm provides the better results. A possible way of deducing such models would be first to reconstruct the image using classical algorithms and then from these TRF estimation, deduce the scatterer distribution and then inject it in the AMCUS inversion. While such method of scatterer distribution computation would be greatly impaired by the speckle inside the TRF estimation (using classical methods), such method could still provide a good prior on the scatterer amplitude and density and has the potential to improve the performance of the AMCUS based estimation of the TRF. Indeed, a more adapted prior information would increase the performance of other kernel based reconstruction methods in the same time. However, in this context, the advantages of AMCUS are that first it represents faithfully the ultrasound wave emission / propagation / reception and second it provides much more data thanks to the simultaneous emission of encoded waves.

6.3 On the generality of the AMCUS based reconstruction

Another point that we made in Section 4.5 is that AMCUS and by consequence the TRF estimation based on AMCUS, can be adapted to any emission / reception scheme. While the results presented in this manuscript show only the AMCUS performance on plane wave imaging and simultaneous plane wave imaging, the work that has been done as an extension of AMCUS showed its ability to adapt to classical synthetic transmit aperture and to temporally encoded synthetic transmit aperture. Moreover, the AMCUS based reconstruction showed promising results by achieving image qualities far better than the one provided by the classical reconstruction algorithms. This is a first step towards the statement of the AMCUS generality, the next step being to adapt it to acquisition schemes based on narrow beams such as focused imaging, multi-line acquisition and multi-line transmission. Such imaging schemes would indeed better fit the AMCUS based reconstruction since, thanks to the focused emissions, not only the received signals would contain a far lower noise level but one will also be able to reduce the size of the region of interest in the medium (by doing so, reducing the number of unknowns in the inverse problem associated with AMCUS). Another interesting path to explore would be to assess the AMCUS performance when all the probe elements emit, with random delays, arbitrary waveforms thus generating wavefronts of no particular shape. Such method would not only be the ultimate proof of AMCUS generality but also would pave the way towards novel types of imaging methods.

6.4 On the practical implementation of AMCUS based reconstruction

A limitation of our work on the AMCUS based reconstruction is the lack of experimental results. While one can argue that the modeling noise can be seen as an acquisition noise, this imitates poorly the radio frequency signals obtained from actual phantom experiments. However, recent experimental implementation of AMCUS based reconstruction in a synthetic aperture imaging scheme showed promising results. Thus, a natural extension of this work would be to experimentally implement AMCUS on an ultrasound scanner using the plane wave imaging scheme. For the experimental

implementation, the pipeline shown in Chapter 4 can be used. Another important requirement for the AMCUS experimental implementation is that the geometrical / acousto-electrical properties of the ultrasound probe should be known in order to build the forward kernel. Since the system resources required for the AMCUS based reconstruction are without any doubt far above what one gets on an research ultrasound scanner, an off-line computation of AMCUS / inversion should be done. Another aspect that is to be analyzed when implementing time encoded excitation signals is the scanner ability to generate arbitrary waveforms. Thanks to the linear amplifiers used to drive the probe elements, the implementation of AMCUS method on a Ula-Op system would be straightforward, the excitation signals used in simulation being also adapted for the Ula-Op emission. However, on a scanner that uses tri-state voltage sources to supply the probe the probe elements, the AMCUS implementation may be more challenging.

Another aspect of the real phantom experiments that could cause a decrease in the performance of the AMCUS based reconstruction are the phenomena of nonlinear propagation of acoustic waves and the frequency dependent tissue attenuation. While the non-linear effect is difficult to compensate for, regarding attenuation, in the light of our recent work where we showed the ability of pulse compression technique to adapt to the attenuation [Benane et al., 2017], there is a way to consequently adapt AMCUS. In fact, the tissue attenuation can be modeled at by its impulse response, thus for a wave propagating from a certain distance, the effect of attenuation on a Dirac pulse is perfectly deterministic. As we showed in Chapter 4, AMCUS is strongly based on the impulse responses of all the points inside the medium, thus adding the attenuation impulse response to a particular point inside the medium should not be a challenging task.

6.5 On the extension to 3D ultrasound imaging

With the ever-growing understanding of the interaction between the ultrasound wave and the soft tissue inside human bodies and with the need to improve the quality of the provided diagnostic, a growing field inside the ultrasound research is the development of fast 3D imaging methods. While in this manuscript we described the AMCUS forward kernel only for linear ultrasound probes that acquire data from only plane inside the medium, this framework can be easily extended to a distribution of transducer elements along a 2D grid that receive echoes from a 3D region of interest inside the medium. The problem that arises here, is closely linked to the one discussed in Section 6.1, and consists in an important increase in the computational time and required system resources. Thus, such an extension of this work is to be foreseen in the long term.

Manuscript Summary in French Part II

7 Introduction

7.1 Contexte

Il ne fait aucun doute que le coût relativement faible des échographes, la procédure rapide et la capacité d'imager des tissus biologiques mous ont permis à l'échographie de devenir l'un des outils de diagnostic médical les plus courants. En outre, les ondes acoustiques utilisées pour l'imagerie ultrasonore n'étant pas très énergétiques, elles n'ont pas d'effet biologique sur le tissu insonifié. Ainsi, dans un large éventail d'applications telles que cardiologie, angiologie, obstétrique, musculo-squelettique, l'échographie est un outil d'examen clé. Malheureusement, l'imagerie ultrasonore présente encore des inconvénients par rapport à d'autres techniques d'imagerie médicale (telles que la tomographie par rayons X et l'imagerie par résonance magnétique), principalement en termes de qualité d'image et de détails fournis. Néanmoins, sa capacité à fournir des images en temps réel permet d'étudier le mouvement des tissus, d'effectuer des modalités d'imagerie telles que le Doppler à ondes pulsées / continues et même de suivre le mouvement des ondes de cisaillement par ultrasons. Cependant, dans le souci d'améliorer les performances de ces techniques, une meilleure qualité d'image par ultrasons est requise, ce qui peut être réalisé facilement au détriment de la cadence d'acquisition d'images. Ce compromis profond entre la qualité d'image fournie et le temps d'acquisition est l'un des plus difficiles verrous de la recherche dans le domaine de l'échographie et son dépassement pourrait mener à des meilleures performances des applications existantes [Hansen et al., 2014] et même à des nouvelles utilisations de l'échographie [Tanter and Fink, 2014].

Plus précisément, ces travaux viennent étendre le concept d'insonification par ondes ultrasonores planes. L'imagerie par ondes planes représente une technique d'acquisition dite ultra-rapide et permettant d'atteindre des cadences d'acquisition de plusieurs milliers d'images par seconde. Cette méthode repose sur des émissions / réceptions de faisceau a front d'onde plan afin de reconstituer simultanément des images complètes du milieu. Cependant, l'absence de focalisation du faisceau d'émission nuit considérablement à la qualité d'image fournie notamment par rapport aux techniques d'imagerie à base des faisceaux focalisés. Une sommation cohérente des images reconstituées après l'émission / réception d'ondes planes dépointées peut être utilisée afin d'améliorer la qualité de l'image finale ainsi obtenue, mais cette amélioration se fait au détriment de la cadence d'acquisition.

7.2 Objective

Ce travail de thèse porte sur l'amélioration du compromis précédemment indiqué entre la qualité d'image et la cadence d'acquisition. En combinant des concepts tels que l'imagerie par ondes planes, les systèmes à entrées multiples / sorties multiples et les problèmes inverses, ce travail vise à acquérir simultanément des images ultrasonores du tissu insonifié, ce qui permet d'augmenter la cadence

d'acquisition sans réduire la qualité de l'image fournie.

7.3 Plan de la thèse

Ce manuscrit est divisé en quatre chapitres:

- **Introduction** – Dans ce Chapitre, un bref résumé des applications de l'imagerie échographique est donné de même que ses avantages. Le problème que ce travail adresse est indiqué et les objectifs de la thèse sont formulés. Un résumé succinct de ce manuscrit est également fourni.
- **Principes d'acoustique et d'imagerie par ultrasons** – Le contexte théorique de la propagation des ondes acoustiques est fixé ici. De plus, sur la base de cette formulation, les schémas d'acquisition ultrasonore conventionnels sont revus et les métriques habituelles qui quantifient la qualité de l'image sont introduites. Nous résumons ici également les approches déjà existantes visant à surmonter le compromis entre qualité d'image et cadence d'acquisition d'images.
- **Codage temporel pour augmenter la cadence d'acquisition d'images** – Ce chapitre présente la première contribution de ce travail. Tout d'abord, il détaille le contexte théorique d'une approche d'imagerie par ultrasons basée sur un modèle réduit de propagation des ondes ultrasonores codées temporellement dans les tissus mous. Ensuite, la simulation et les résultats in vitro sont présentés et discutés, les avantages / limites de la méthode étant soulignés.
- **Un modèle avancé pour l'imagerie ultrasonore codée (AMCUS)** – les performances d'une approche d'imagerie basée sur un modèle avancé de propagation des ondes ultrasonores sont présentées dans ce chapitre. Tout d'abord, le modèle direct général est construit. Ensuite, le modèle avancé est associé au concept de codage temporel des ondes ultrasonores et son adaptation à un schéma d'acquisition ultra-rapide spécifique est illustrée. En outre, une approche par problème inverse est proposée afin de reconstruire l'image du milieu insonifié. Les performances du modèle direct et de la méthode de reconstruction sont évaluées au moyen de simulations numériques.

8 Principes d'acoustique et d'imagerie par ultrasons

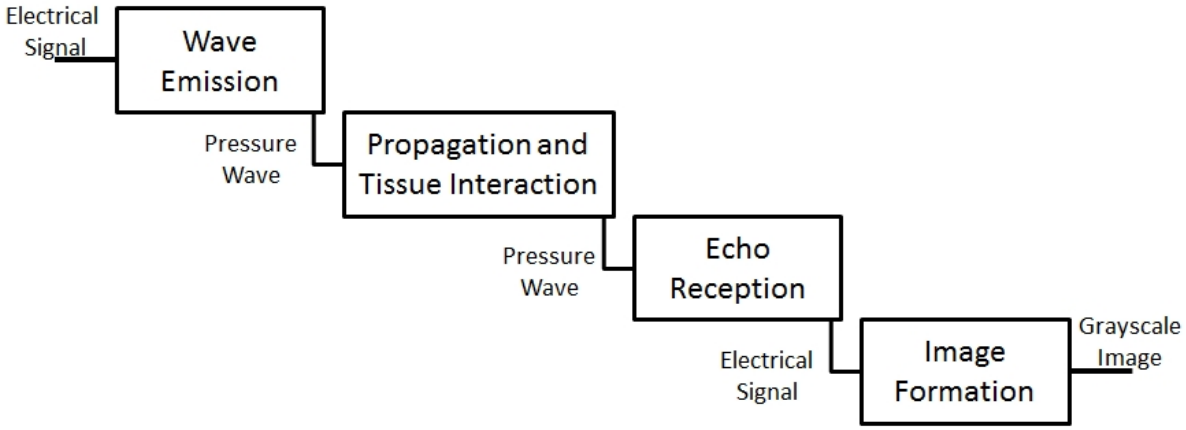

Figure 8.1: Le pipeline conventionnel pour la formation d'images par ultrasons.

Le processus conventionnel d'imagerie ultrasonore est présenté dans la Fig. 8.1. Ici, ce pipeline est traité en intégralité et chaque bloc est détaillé afin de mieux comprendre le contexte de ce travail. Le but étant de présenter un cadre général permettant de décrire tous les schémas d'acquisition ultrasonores existants: ondes focalisées / planes / divergentes. Sur la base de ce cadre, sont présentées les modifications déjà existantes pour chacun des blocs de la Fig. 8.1 visant à surmonter le compromis entre la qualité d'image / la cadence d'acquisition d'image. En plus de son objectif de généraliser la modélisation de tous les schémas d'acquisition existants, le cadre développé ici permettra également de mieux comprendre les contributions présentées dans les prochains Chapitres.

8.1 Principe de propagation des ondes ultrasonores

Le phénomène de propagation des ondes acoustiques représente le principal composant (voir Fig. 8.1) sur lequel reposent toutes les techniques d'imagerie échographiques existantes et les méthodes développées dans cette thèse n'y font pas exception. Dans cette section, le principe de ce phénomène est expliqué. Ainsi, est définie la base pour la compréhension des méthodes d'imagerie échographique déjà existantes ainsi que celles proposées dans cette thèse.

Comme indiqué précédemment, l'échographie utilise des ondes acoustiques à faible énergie pour insonifier ce qui est supposé être un tissu biologique mou au repos [Jensen, 1991, Schmerr Jr, 2014]. Dans ces conditions, on peut supposer qu'avant la génération de l'onde, le milieu insonifié à chaque point (défini par le vecteur de position $\vec{r} = (x_r, y_r, z_r)$) a une pression moyenne P_0 et une densité $\rho_0(\vec{r})$

[Jensen, 1991, Jensen, 1999]. Bien que le milieu puisse être in-homogène, ce qui signifie que $\rho_0(\vec{r})$ peut varier, pour les tissus mous au repos, la pression est supposée constante. Dans ces conditions, la petite perturbation générée par l'onde acoustique génère de légères ondulations $p_1(\vec{r},t)$ et $\rho_1(\vec{r},t)$ respectivement dans les champs de pression et densité. Ainsi, pour un point $\vec{r}$, la nouvelle pression et densité peuvent être écrites [Jensen, 1991, Morse et al., 1969] comme suit:

$$\begin{array}{l} P(\vec{r},t) = P_0 + p_1(\vec{r},t) \\ \rho(\vec{r},t) = \rho_0(\vec{r}) + \rho_1(\vec{r},t) \end{array} \text{ with } \begin{cases} p_1(\vec{r},t) << P_0 \\ \rho_1(\vec{r},t) << \rho_0(\vec{r}) \end{cases} \tag{8.1}$$

8.1.1 Équation d'onde linéaire

En s'appuyant sur les lois de conservation de la masse et de la quantité du mouvement, démontrées dans l'Annexe A, on montre qu'il existe une relation étroite entre l'évolution spatio-temporelle des champs de pression et de densité. Cette relation est écrite comme suit:

$$\nabla^2 p_1(\vec{r},t) - \frac{1}{c_m^2}\frac{\partial^2 p_1(\vec{r},t)}{\partial t^2} = -\frac{2\Delta c_0(\vec{r})}{c_m^3}\cdot\frac{\partial^2 p_1(\vec{r},t)}{\partial t^2} + \frac{1}{\rho_m}\nabla\big[\Delta\rho_0(\vec{r})\big]\cdot\nabla p_1(\vec{r},t) \tag{8.2}$$

où c_m et ρ_m sont respectivement la vitesse de propagation du son et la densité des tissus mous au repos. $\Delta\rho_0(\vec{r})$ et $\Delta c_0(\vec{r})$ sont respectivement les variations locales des grandeurs précédemment énoncées. On remarque que dans (8.2), le côté gauche de l'équation représente l'évolution de la pression en fonction du temps et de l'espace tandis que le côté droit représente le comportement des ondes lorsqu'elles rencontrent des in-homogénéités tissulaires sous la forme de variations dans la vitesse de la propagation du son et dans la densité $\Delta c_0(\vec{r})$ et $\Delta\rho_0(\vec{r})$ respectivement. Cette relation est appelée l'équation de la propagation des ondes acoustiques à l'intérieur de milieux non homogènes. Pour un milieu parfaitement homogène, l'équation (8.2) est écrite:

$$\nabla^2 p_1(\vec{r},t) - \frac{1}{c_m^2}\frac{\partial^2 p_1(\vec{r},t)}{\partial t^2} = 0 \tag{8.3}$$

8.1.2 Diffusion des ondes de pression

Dans la section précédente, deux équations modélisant la propagation des ondes acoustiques à l'intérieur de tissus mous in-homogènes (8.2) et homogènes (8.3) ont été déduites. Ici, l'effet de la diffusion de l'onde acoustique est présenté et la pression d'échos en un point donné du milieu, est calculée. L'objet d'étude de cette Section est la configuration montrée dans la Fig.8.2(a), où une onde acoustique est émise en $\vec{r}_0$, elle se disperse dans le volume in-homogène V et est reçue en $\vec{r}_1$.

Comme montré dans (8.2), s'il y a une variation dans le champ de densité, une diffusion des ondes de pression est générée. Ce phénomène est considéré comme une génération d'un nouveau champ de pression $p_s(\vec{r}_1, t_{\vec{r}_1})$ au point $\vec{r}_1$. Dans ces conditions, une perturbation de la pression totale $p_1(\vec{r}_1, t_{\vec{r}_1})$, à tout point $\vec{r}_1$ à l'intérieur du milieu, peut être considérée comme une superposition d'un champ de pression incident $p_i(\vec{r}_1, t_{\vec{r}_1})$ (lié à l'onde acoustique incidente) et d'un champ de pression dispersée $p_s(\vec{r}_1, t_{\vec{r}_1})$ (lié aux échos):

$$p_1(\vec{r}_1, t_{\vec{r}_1}) = p_i(\vec{r}_1, t_{\vec{r}_1}) + p_s(\vec{r}_1, t_{\vec{r}_1}) \tag{8.4}$$

Le calcul détaillé dans cette Section permet d'arriver à une relation mathématique qui lie la pression dispersée $p_s(\vec{r}_1, t_{\vec{r}_1})$ en tout point de mesure $\vec{r}_1$ à la pression incidente $p_i(\vec{r}_1, t_{\vec{r}_1})$. En s'appuyant sur

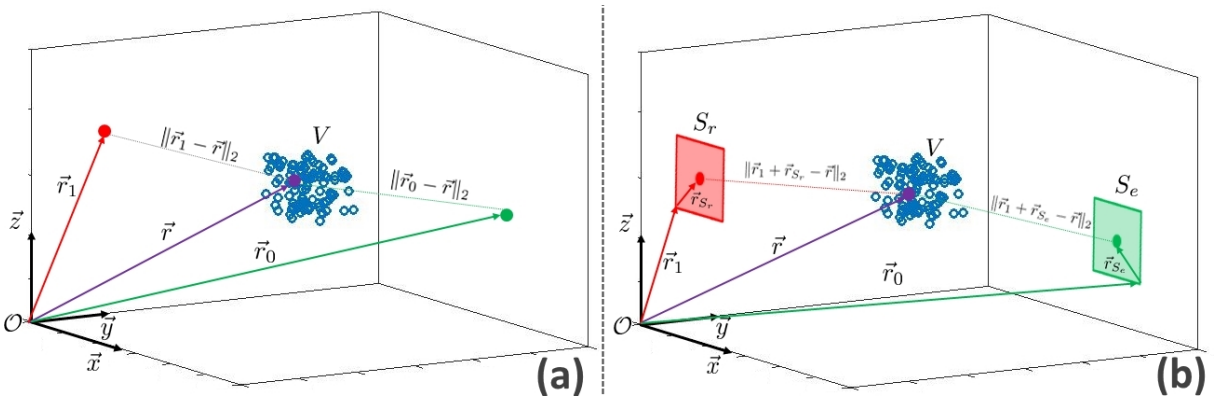

Figure 8.2: (a) - Représentation schématique d'un milieu et de son système de coordonnées associé. Le milieu est partout homogène sauf dans le volume V où il contient des in-homogénéités de densité (bleu). Le point de calcul de la pression dispersée est $\vec{r}_1$. Le point de génération de l'onde à l'intérieur du milieu est $\vec{r}_0$. L'onde acoustique est émise en $\vec{r}_0$, elle se disperse en V et est reçue en $\vec{r}_1$. (b) - Représentation schématique d'un milieu homogène contenant un volume V avec des in-homogénéités de densité. Deux transducteurs sont immergés dans le milieu. S_e est la surface plane qui génère une onde de pression dans le milieu. Ainsi, l'onde acoustique se propage dans des conditions de champ libre, elle atteint V où elle se disperse puis est reçue par S_r.

l'approximation de Born-Neumann (premier ordre), cette relation est écrite de la manière suivante:

$$p_s(\vec{r}_1, t_{\vec{r}_1}) = \int_V \int_t \mathcal{G}_p(\vec{r}_1, t_{\vec{r}_1} | \vec{r}, t) \left[-\frac{2\Delta c_0(\vec{r})}{c_m^3} \cdot \frac{\partial^2 p_i(\vec{r}, t)}{\partial t^2} + \frac{1}{\rho_m} \nabla \left[\Delta \rho_0(\vec{r}) \right] \cdot \nabla p_i(\vec{r}, t) \right] \mathrm{d}t \, \mathrm{d}^3\vec{r}$$
$$\text{avec: } \mathcal{G}_p(\vec{r}_1, t_{\vec{r}_1} | \vec{r}, t) = \frac{1}{4\pi \|\vec{r}_1 - \vec{r}\|_2} \delta\left(t - t_{\vec{r}} - \frac{\|\vec{r}_1 - \vec{r}\|_2}{c_m} \right) \tag{8.5}$$

où $\mathcal{G}_p(\vec{r}_1, t_{\vec{r}_1} | \vec{r}, t)$ est la fonction de Green [Jensen, 1991, Morse et al., 1969]. La relation (8.5) permet

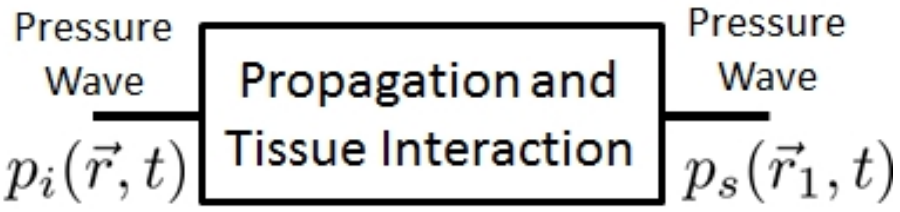

Figure 8.3: Le bloc "Propagation / Interaction milieu" avec ses entrées / sorties expliquées dans les Sections 8.1.1-8.1.2.

de calculer la pression des échos générés dans le volume V, lorsque V est insonifié avec un champ de pression incidente $p_i(\vec{r}, t)$. À ce stade, le bloc "Propagation / Interaction milieu" (Fig. 8.1) est terminé et sa nouvelle représentation est représentée dans la Fig. 8.3. Ainsi, cette Section présente une description complète du phénomène physique de propagation des ondes acoustiques dans les tissus mous homogènes / in-homogènes.

8.1.3 Deux transducteurs plan

L'objet d'étude de cette Section sont les deux blocs "Emission de l'onde" et "Réception des échos" du pipeline de formation de l'image échographique (Fig. 8.1). L'objectif principal étant de savoir comment l'onde acoustique incidente $p_i(\vec{r}, t)$ est générée et quelle est la signature électrique de l'onde

de pression rétro-diffusée $p_s(\vec{r}_1, t)$. Le cas de deux transducteurs piézoélectriques planaires immergés dans un milieu in-homogène (Fig. 8.2(b)) est analysé.

Comme on le voit dans (8.5), pour le cas affiché dans la Fig. 8.2(a), l'onde diffusée générée dans le volume V dépend de la pression incidente $p_1(\vec{r}, t)$ (généré par une source ponctuelle placée à $\vec{r}_0$). Dans le cas de la Fig. 8.2(b), la source (resp. le récepteur) est une surface plane d'aire S_e (resp. S_r). Supposons que le milieu entourant les transducteurs soit homogène (pression P_0 et densité ρ_m) et que lors de la vibration, les deux surfaces restent parallèles à leur position initiale. Dans de telles conditions, on en déduit que les vitesses de vibration $\mathcal{V}_{S_e}(t)$ (resp. $\mathcal{V}_{S_r}(t)$) ne changent pas en fonction de la position sur les surfaces S_e (resp. S_r). De plus, le milieu étant homogène entre la surface S_e et le volume V, l'onde acoustique émise se propage en champ libre entre S_e et V et vérifie (8.3). Maintenant, pour résoudre (8.3) dans le cas d'un transducteur plan, dans [Tupholme, 1969, Stepanishen, 1971] a été proposé d'utiliser le potentiel de vitesse $\psi(\vec{r}, t)$ de l'onde acoustique à l'intérieur du volume V. En milieu homogène, $\psi(\vec{r}, t)$ satisfait la relation suivante:

$$\nabla^2\psi(\vec{r}, t) - \frac{1}{c_m^2}\frac{\partial^2\psi(\vec{r}, t)}{\partial t^2} = 0 \tag{8.6}$$

Le calcul détaillé dans cette Section permet de trouver la solution générale de l'équation (8.6), qui peut s'écrire sous la forme suivante:

$$\begin{aligned} \psi(\vec{r}, \vec{r}_0, t) &= \int_S \int_t \mathcal{V}_{S_e}(t)\mathcal{G}_\psi(\vec{r}, t|\vec{r}_0 + \vec{r}_{S_e}, t_{\vec{r}_0})\,\mathrm{d}t_{\vec{r}_0}\,\mathrm{d}^2\vec{r}_{S_e} \\ \text{avec: } \mathcal{G}_\psi(\vec{r}, t|\vec{r}_0 + \vec{r}_{S_e}, t_{\vec{r}_0}) &= \frac{1}{2\pi\|\vec{r}-\vec{r}_0-\vec{r}_{S_e}\|_2}\delta\Big(t - t_{\vec{r}_0} - \frac{\|\vec{r}-\vec{r}_0-\vec{r}_{S_e}\|_2}{c_m}\Big) \end{aligned} \tag{8.7}$$

où $\vec{r}_0$ (resp. $\vec{r}_1$) sont les points les plus proches de la surface S_e (resp. S_r) de l'origine du système de coordonnées $\mathcal{O}$. Le vecteur de position $\vec{r}_{S_e}$ (resp. $\vec{r}_{S_r}$) est choisi de telle sorte que tout point décrit par $\vec{r}_0 + \vec{r}_{S_e}$ (resp. $\vec{r}_1 + \vec{r}_{S_r}$) appartiennent à la surface S_e (resp. S_r). Dans (8.7), $\psi(\vec{r}, \vec{r}_0, t)$ est interprété comme la valeur du potentiel de vitesse au point $\vec{r}$, généré par la vibration de la surface S_e à la position $\vec{r}_0$. La somme continue sur tous les points de la surface vibrante S_e dans (8.7) représente le principe de Huygens - Fresnel. En d'autres termes, $\psi(\vec{r}, \vec{r}_0, t)$ est vu comme une superposition d'un nombre infini d'ondes sphériques générées par un nombre infini des points sur la surface S_e. Comme dans (8.7) $\mathcal{V}_{S_e}(t)$ est constant pour tout $\vec{r}_{S_e}$, (8.7) est réécrit comme suit:

$$\begin{aligned} \psi(\vec{r}, \vec{r}_0, t) &= \int_t \mathcal{V}_{S_e}(t)\left[\int_S \mathcal{G}_\psi(\vec{r}, t|\vec{r}_0 + \vec{r}_{S_e}, t_{\vec{r}_0})\,\mathrm{d}^2\vec{r}_{S_e}\right]\mathrm{d}t_{\vec{r}_0} \Longleftrightarrow \\ \psi(\vec{r}, \vec{r}_0, t) &= \int_t \mathcal{V}_{S_e}(t)\,g_{S_e}(\vec{r}, t - t_{\vec{r}_0})\,\mathrm{d}t_{\vec{r}_0} \\ \text{avec: } g_{S_e}(\vec{r}, t - t_{\vec{r}_0}) &= \int_S \mathcal{G}_\psi(\vec{r}, t|\vec{r}_0 + \vec{r}_{S_e}, t_{\vec{r}_0})\,\mathrm{d}^2\vec{r}_{S_e} \Longleftrightarrow \\ g_{S_e}(\vec{r}, t - t_{\vec{r}_0}) &= \int_S \frac{1}{2\pi\|\vec{r}-\vec{r}_0-\vec{r}_{S_e}\|_2}\delta\Big(t - t_{\vec{r}_0} - \frac{\|\vec{r}-\vec{r}_0-\vec{r}_{S_e}\|_2}{c_m}\Big)\,\mathrm{d}^2\vec{r}_{S_e} \end{aligned} \tag{8.8}$$

À ce stade, on observe que dans (8.8) le terme $g_{S_e}(\vec{r}, t - t_{\vec{r}_0})$ ne dépend pas des propriétés physiques du milieu et ne prend en compte que la géométrie de la source émettrice (S_e) et le point où le potentiel de vitesse est calculé ($\vec{r}$). Ainsi, $g_{S_e}(\vec{r}, t - t_{\vec{r}_0})$ est appelée la réponse impulsionnelle spatiale de la source S_e en émission [Jensen, 1991, Jensen, 1999, Jensen and Svendsen, 1992]. Les calculs développés montrent que la pression $p_i(\vec{r}, t)$ peut être déduite par la relation (8.8) comme suit [Jensen, 1991,

Stepanishen, 1971, Jensen and Svendsen, 1992]:

$$p_i(\vec{r},t) = \rho_m \frac{\partial \psi(\vec{r},\vec{r}_0,t)}{\partial t} = \rho_m \frac{\partial \mathcal{V}_{S_e}(t)}{\partial t} *_t g_{S_e}(\vec{r},t) \tag{8.9}$$

Les équations (8.5) et (8.9) représentent le champ de pression diffusé mesuré en tout point du milieu $\vec{r}_1$ et le champ de pression incidente en tout point du milieu $\vec{r}$ respectivement.

À cette étape, on définit la force totale $\mathcal{U}_{S_r}(t_{\vec{r}_1})$ exercée par l'onde acoustique sur la surface S_r et on montre qu'elle peut être calculée de la manière suivante:

$$\begin{gathered}\mathcal{U}_{S_r}(t_{\vec{r}_1}) = \frac{1}{2}\int_V \mathcal{F}\, p_i(\vec{r},t) *_t g_{S_r}(\vec{r},t_{\vec{r}_1})\,\mathrm{d}^3\vec{r} \\ \text{avec: } \begin{cases} \mathcal{F} = -\frac{2\Delta c_0(\vec{r})}{c_m^3}\cdot\frac{\partial^2}{\partial t^2} + \frac{1}{\rho_m}\nabla\big[\Delta\rho_0(\vec{r})\big]\cdot\nabla \\ g_{S_r}(\vec{r},t_{\vec{r}_1}-t) = \int_S \frac{1}{2\pi\|\vec{r}-\vec{r}_1-\vec{r}_{S_r}\|_2}\delta\Big(t_{\vec{r}_1}-t-\frac{\|\vec{r}-\vec{r}_1-\vec{r}_{S_e}\|_2}{c_m}\Big)\,\mathrm{d}^2\vec{r}_{S_e} \end{cases}\end{gathered} \tag{8.10}$$

où le signal $g_{S_r}(\vec{r},t)$ représente la réponse impulsionnelle spatiale du transducteur vibrant S_r au point $\vec{r}$ du milieu [Jensen, 1991, Jensen, 1999, Jensen and Svendsen, 1992]. (8.10) est l'expression de la force totale exercée sur le transducteur récepteur et représente la somme sur tout le volume V de la réflexion de chaque diffuseur convolué avec la réponse impulsionnelle spatiale du transducteur. Ensuite, on montre que en combinant (8.9) et (8.10), l'expression pour la force $\mathcal{U}_{S_r}(t_{\vec{r}_1})$ peut être écrite comme suit [Jensen, 1991, Jensen, 1999, Jensen and Svendsen, 1992]:

$$\begin{gathered}\mathcal{U}_{S_r}(t) = \frac{\rho_m}{2c_m^2}\frac{\partial^3 \mathcal{V}_{S_e}(t)}{\partial t^3} *_t \int_V \left[-\frac{2\Delta c_0(\vec{r})}{c_m} + \frac{\Delta\rho_0(\vec{r})}{\rho_m}\right] g_{er}(\vec{r},t)\,\mathrm{d}^3\vec{r} \\ \text{avec: } g_{er}(\vec{r},t) = g_{S_e}(\vec{r},t) *_t g_{S_r}(\vec{r},t)\end{gathered} \tag{8.11}$$

où $g_{er}(\vec{r},t)$ est la réponse impulsionnelle spatiale du point $\vec{r}$ lorsque le transducteur S_e émet et que S_r reçoit.

Enfin, l'expression de la force totale exercée par l'onde acoustique sur la surface du transducteur S_r (8.11) est utilisée pour obtenir le signal électrique généré par ce transducteur [Jensen, 1999, Stepanishen, 1971] :

$$\begin{aligned} y_{S_r}(t) = h_{S_r}(t) *_t \mathcal{U}_{S_r}(t) = \frac{\rho_m}{2c_m^2} h_{S_r}(t) *_t \frac{\partial^3 \mathcal{V}_{S_e}(t)}{\partial t^3} *_t \int_V \left[-\frac{2\Delta c_0(\vec{r})}{c_m} + \frac{\Delta\rho_0(\vec{r})}{\rho_m}\right] g_{er}(\vec{r},t)\,\mathrm{d}^3\vec{r} \iff \\ y_{S_r}(t) = h_{S_r}(t) *_t \mathcal{U}_{S_r}(t) = h_{S_r}(t) *_t a(t) *_t h_{S_e}(t) *_t \int_V \left[-\frac{2\Delta c_0(\vec{r})}{c_m} + \frac{\Delta\rho_0(\vec{r})}{\rho_m}\right] g_{er}(\vec{r},t)\,\mathrm{d}^3\vec{r} \end{aligned} \tag{8.12}$$

où $a(t)$ représente l'excitation électrique du transducteur émetteur (S_e). Dans (8.12), $h_{S_e}(t)$ et $h_{S_r}(t)$ sont respectivement les réponses impulsionnelles acousto-électriques des transducteurs émetteurs et récepteurs. Le terme $-2\Delta c_0(\vec{r})/c_m + \Delta\rho_0(\vec{r})/\rho_m$ ne dépend que des in-homogénéités de la densité et il représente le coefficient de réflexion du point $\vec{r}$ dans le volume V.

8.1.4 Résumé

Dans cette Section, le pipeline affiché dans la Fig. 8.4 a été détaillé. Une étude théorique complète du phénomène de propagation des ondes acoustiques a permis de relier le signal électrique reçu par un

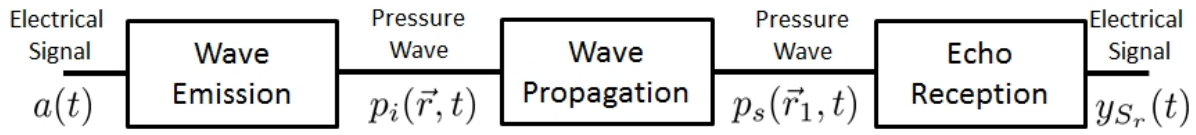

Figure 8.4: Résultat de la Sous-section 8.1. Le signal électrique de sortie $y_{S_r}(t)$ est modélisé en fonction de la géométrie du transducteur, des in-homogénéités du milieu et du signal électrique d'entrée $a(t)$.

transducteur piézoélectrique au signal d'excitation de la source. La formalisation employée a permis de relier les signaux suivants:

- signal d'excitation du transducteur source
- réponse impulsionnelle acousto-électrique des transducteurs source et récepteur
- in-homogénéités de la densité moyenne et de la vitesse de propagation du son
- réponse impulsionnelle spatiale des transducteurs source et récepteur.

Les hypothèses suivantes ont dû être faites pour obtenir la relation finale:

- avant l'insonification, le milieu est complètement immobile, impliquant un champ de pression constant et un champ de densité avec des petites in-homogénéités
- les perturbations à l'intérieur des champs de pression et de densité induits par la propagation des ondes acoustiques sont très faibles par rapport aux valeurs moyennes de ces champs
- approximation Born-Neumann du premier ordre qui n'impose que des réflexions uniques de l'onde incidente de pression
- les réponses impulsionnelles spatiales des transducteurs varient lentement sur de petits volumes à l'intérieur du milieu.

8.2 Imagerie ultrasonore

Ici, les processus conventionnels d'imagerie ultrasonore sont détaillés. Tout d'abord, les différentes parties impliquées dans le processus d'échographie sont présentées, puis la relation entre le pipeline affiché dans la Fig. 8.4 et la reconstruction de l'image est montrée. De plus, les métriques permettant de quantifier les performances de l'approche d'imagerie sont listées et leur utilité est expliquée. Ainsi, lorsque finalement les différentes méthodes d'échographie sont présentées, elles sont comparées en fonction des valeurs fournies par les métriques de performance.

8.2.1 Contexte général

Comme le montre la Fig. 8.5, le processus conventionnel d'imagerie par ultrasons comporte quatre parties:

- L'utilisateur – est la personne responsable de l'acquisition des données. Normalement, l'utilisateur définit un certain nombre de paramètres (qui seront décrits plus en détail dans ce chapitre) tels que: type de formation de faisceau d'émission, forme des signaux d'excitation, profondeur d'imagerie, fréquence de répétition d'impulsion, nombre d'images acquises, etc. Ces paramètres définissent le type d'acquisition et ont un impact primordial sur la qualité de l'image fournie. Les images échographiques (pour les scanners cliniques et de recherche) sont renvoyées à l'utilisateur. Les échographes de recherche ont également la possibilité de retourner à l'utilisateur

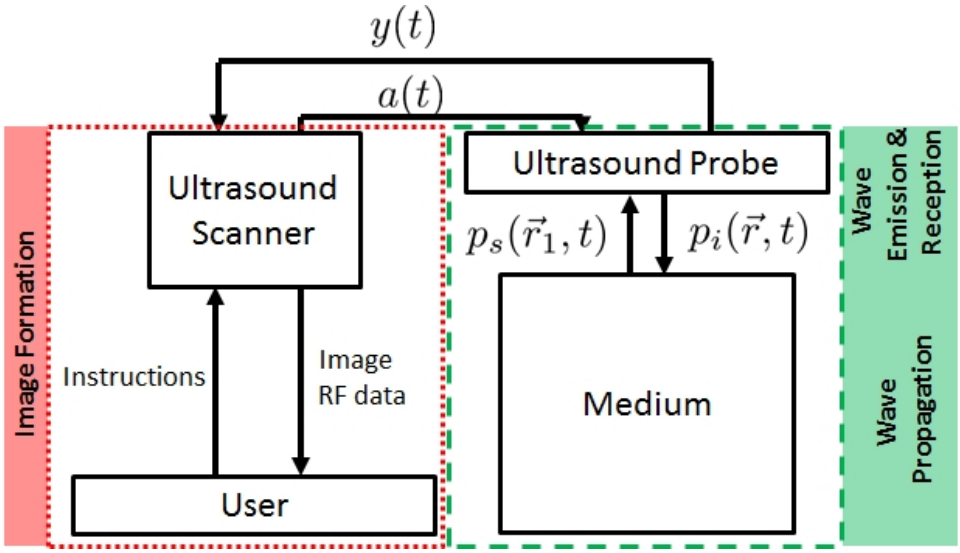

Figure 8.5: Représentation schématique des différentes parties impliquées dans le processus d'imagerie ultrasonore et des tâches effectuées par chaque partie. En se basant sur les instructions de l'utilisateur, l'échographe génère un ensemble de signaux d'excitation $a(t)$ qui sont transformés dans des ondes acoustiques $p_i(\vec{r},t)$ par la sonde. Ces ondes se propagent à l'intérieur du milieu et les échos diffusés $p_s(\vec{r}_1,t)$ sont reçus par la sonde, qui les transforme en signaux électriques $y(t)$. Les données RadioFréquence (RF) $y(t)$ sont utilisées par l'échographe pour reconstruire l'image échographique.

les données RadioFréquence (RF) (données brutes utilisées pour reconstruire les images). Les données RF peuvent être post-traitées en utilisant des algorithmes spécifiques en fonction de l'application.

- L'échographe – a pour fonction de traiter les paramètres définis par l'utilisateur et de piloter en conséquence les éléments de la sonde. Ainsi, le scanner envoie des signaux électriques à la sonde pendant la phase "Emission d'onde" et reçoit des signatures électriques des échos rétro-diffusés, pendant la phase "Réception d'échos". Pour les approches d'imagerie conventionnelles, l'échographe peut être configuré au niveau logiciel / matériel afin de reconstruire des images échographiques (pour les scanners cliniques et de recherche). Cependant, l'option permettant aux utilisateurs de bénéficier des données brutes d'acquisition est uniquement disponible pour les échographes de recherche.

- La sonde – est responsable de la conversion directe et inverse de l'énergie électrique en énergie mécanique pendant les phases «Emission d'onde» et «Réception d'échos» respectivement. Cette fonction est réalisée principalement grâce à un certain nombre d'éléments électroacoustiques (Fig. 8.6) situés sur la tête de la sonde.

- Le milieu – représente l'objet d'étude de l'échographie. C'est le support de la "Propagation des ondes" et ses in-homogénéités de densité génèrent des échos qui sont ensuite captés par la sonde et reconstruits en une image échographique.

Avant d'aller plus en détails sur les approches d'imagerie, on parle de la manière dont le pipeline affiché dans la Fig. 8.4 est utilisé dans le processus de formation d'images par ultrasons. Comme le montre la Fig. 8.6, une sonde linéaire conventionnelle est constituée de plusieurs éléments identiques (de même surface $S = S_r = S_e$ et de même réponse impulsionnelle acousto électrique en émission et en réception $h(t)$). Ces éléments sont écartés d'une distance constante appelée $kerf$ (au nombre: N_{el}) et sont disposés en ligne. Pendant la phase de "l'Emission de l'onde", chaque élément j de la sonde est excité par l'échographe en utilisant un signal électrique $a_j(t)$. Ensuite, pendant la phase de "Réception

d'échos", la même sonde reçoit les échos rétro-diffusés, ainsi chaque élément i de la sonde enregistre un signal électrique $y_i(t)$. La relation entre le signal reçu $y_i(t)$ et le signal émis $a_j(t)$, est modélisée par

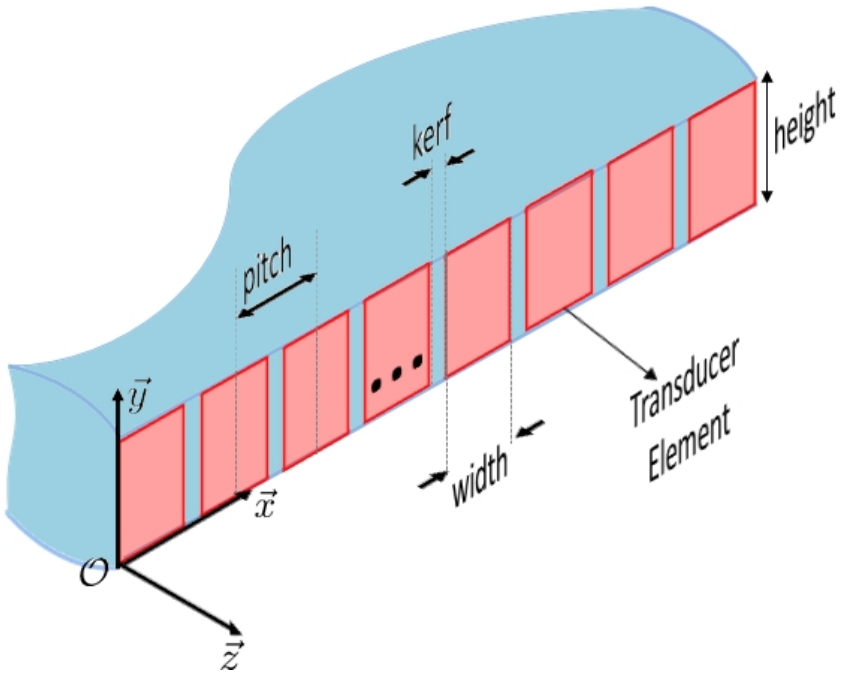

Figure 8.6: Représentation schématique de la sonde. Chaque élément de la sonde (rouge) représente un transducteur capable de convertir (dans le sens directe / inverse) de l'énergie électrique en énergie mécanique (vibrations). L'architecture présentée ici est typique pour une sonde linéaire.

le pipeline montré dans la Fig. 8.4. Le phénomène de N_{el} émissions simultanées d'ondes acoustiques est modélisée en supposant que les phénomènes suivants sont linéaires: l'émission des ondes par les éléments transducteurs, la propagation des ondes à l'intérieur du milieu imagé et la réception des échos par les éléments transducteurs. En adaptant les réponses impulsionnelles spatiales $g_{S_e}(\vec{r},t)$ (8.8) et $g_{S_r}(\vec{r},t)$ (8.10) à une paire (j,i) d'éléments, on obtient les expressions suivantes:

$$g_{S_e}(\vec{r},t) = \delta(t-t_j) *_t g_j(\vec{r},t)$$

$$g_{S_r}(\vec{r},t) = \delta(t-t_i) *_t g_i(\vec{r},t)$$

$$\text{avec:} \begin{cases} g_j(\vec{r},t) = \displaystyle\int_S \frac{1}{2\pi\|\vec{r}-\vec{r}_j-\vec{r}_S\|_2}\delta\Big(t-\frac{\|\vec{r}-\vec{r}_j-\vec{r}_S\|_2}{c_m}\Big)\,\mathrm{d}^2\vec{r}_S \\ g_i(\vec{r},t) = \displaystyle\int_S \frac{1}{2\pi\|\vec{r}-\vec{r}_i-\vec{r}_S\|_2}\delta\Big(t-\frac{\|\vec{r}-\vec{r}_i-\vec{r}_S\|_2}{c_m}\Big)\,\mathrm{d}^2\vec{r}_S \end{cases} \tag{8.13}$$

où t_j et t_i sont les retards à l'émission et à la réception respectivement. La relation (8.13) est introduite ici uniquement pour la modélisation. Elle permet de définir les réponses impulsionnelles spatiales $g_j(\vec{r},t)$ et $g_i(\vec{r},t)$ du transducteur j et i respectivement (qui ne dépendent que de la géométrie des éléments transducteurs et du point $\vec{r}$) à partir de la temporisation t_j et t_i. Il est rappelée ici une autre hypothèse importante sur laquelle repose l'imagerie échographique: la diffusion des ondes acoustiques se produit dans le champ lointain de l'élément transducteur [Thomenius, 1996, Lockwood et al., 1998]. Dans de telles conditions, les réponses impulsionnelles spatiales $g_j(t)$, $g_i(t)$ et $g_{ji}(t)$ sont approximés

comme suit:

$$\begin{cases} g_j(\vec{r},t) = \int\limits_S \dfrac{1}{2\pi\|\vec{r}-\vec{r}_j-\vec{r}_S\|_2}\delta\Big(t-\dfrac{\|\vec{r}-\vec{r}_j-\vec{r}_S\|_2}{c_m}\Big)\,\mathrm{d}^2\vec{r}_S \approx \dfrac{S\delta\Big(t-\frac{\|\vec{r}-\vec{r}_j\|_2}{c_m}\Big)}{2\pi\|\vec{r}-\vec{r}_j\|_2} \\ g_i(\vec{r},t) = \int\limits_S \dfrac{1}{2\pi\|\vec{r}-\vec{r}_i-\vec{r}_S\|_2}\delta\Big(t-\dfrac{\|\vec{r}-\vec{r}_i-\vec{r}_S\|_2}{c_m}\Big)\,\mathrm{d}^2\vec{r}_S \approx \dfrac{S\delta\Big(t-\frac{\|\vec{r}-\vec{r}_i\|_2}{c_m}\Big)}{2\pi\|\vec{r}-\vec{r}_i\|_2} \\ g_{ji}(\vec{r},t) = g_j(\vec{r},t) *_t g_i(\vec{r},t) = \dfrac{S^2\delta\Big(t-\frac{\|\vec{r}-\vec{r}_j\|_2+\|\vec{r}-\vec{r}_i\|_2}{c_m}\Big)}{4\pi^2\|\vec{r}-\vec{r}_j\|_2\|\vec{r}-\vec{r}_i\|_2} \end{cases} \tag{8.14}$$

Alors que, comme est montré plus loin dans cette Section, les délais d'émission dépendent du schéma d'acquisition, les délais de réception sont classiquement fixés à 0 ($t_i = 0$). En utilisant (8.14), le signal électrique total reçu par l'élément i de la sonde lorsque tous les éléments émettent est écrit comme suit:

$$y_i(t) = w_i \sum_{j=1}^{N_{el}} w_j y_{ji}(t) + b_i(t) \tag{8.15}$$

Dans (8.15), les termes w_j et w_i sont des coefficients de pondération appliqués respectivement aux signaux électriques émis et reçus afin de modifier le champ de pression à l'intérieur du milieu imagé [Capon, 1969, Holfort et al., 2009, Tong et al., 2014]. Ces termes varient spatialement en fonction de l'élément émetteur / récepteur et sont généralement choisis entre les fenêtres suivantes: porte (rectangulaire), Hanning, Tuckey.

$$\begin{gathered} y_i(t) \underset{\text{Avec (8.12)}}{=} w_i \sum_{j=1}^{N_{el}} \Big[w_j h(t) *_t a_j(t) *_t h(t) *_t \int\limits_V \gamma(\vec{r}) g_{ji}(\vec{r},t)\,\mathrm{d}^2\vec{r}\,\Big] + b_i(t) \\ \text{et: } y_{ji}(t) = h(t) *_t a(t) *_t h(t) *_t \int\limits_V \gamma(\vec{r}) g_{ji}(\vec{r},t)\,\mathrm{d}^2\vec{r} \end{gathered} \tag{8.16}$$

En fonction du schéma d'émission, les signaux d'excitation $a_j(t)$ sont retardés de telle sorte qu'une onde ultrasonore inclinée / focalisée / divergente est émise à l'intérieur du milieu, donc les signaux $a_j(t)$ contiennent déjà les retards d'émission t_j. Dans (8.15), $b_i(t)$ représente un bruit d'acquisition additif. La carte de réflectivité du tissu (TRF[1]) $\gamma(\vec{r})$, utilisée dans la définition des signaux reçus dans (8.15), représente le coefficient de réflectivité à chaque position $\vec{r}$ du milieu. En comparant (8.16) et (8.12) on en déduit:

$$\gamma(\vec{r}) = -\frac{2\Delta c_0(\vec{r})}{c_m} + \frac{\Delta\rho_0(\vec{r})}{\rho_m} \tag{8.17}$$

Compte tenu de la distribution spatiale des éléments de la sonde, la relation précédente, comme est montré plus loin dans cette Section, permet d'orienter un faisceau uniquement dans un plan Π (où chaque point $\vec{r}$ a une coordonnée $y = 0$ constante), les signaux enregistrés $y_i(t)$ sont la signature électrique des échos rétro-diffusés du plan Π du milieu imagé.

Reconstruction de l'image

Alors que dans la littérature il existe un grand nombre de méthodes de reconstruction d'image qui opèrent soit dans le domaine temps / espace [Wright, 1985, Shoup and Hart, 1988, Montaldo et al., 2009,

[1] TRF est l'abrégé pour "Tissue Reflectivity Function"

David et al., 2015] soit dans le domaine des fréquences temporelles / spatiales [Nagai, 1985, Lu, 1997, Garcia et al., 2013, Zhang et al., 2016], l'algorithme conventionnel de reconstruction repose sur la sommation cohérente des échos rétro-diffusés (appelé DAS[2]). L'estimation DAS de la TRF est obtenue en utilisant la relation suivante:

$$\begin{aligned} \hat{\gamma}_{DAS}(\vec{r}) &= \sum_{i=1}^{N_{el}} y_i(\tau_i(\vec{r})) \\ \text{avec: } \tau_i(\vec{r}) &= \frac{1}{c_m} \min_{j\in[1..N_{el}]} \left[c_m t_j + \|\vec{r} - \vec{r}_j\|_2 \right] + \frac{1}{c_m} \|\vec{r} - \vec{r}_i\|_2 \end{aligned} \tag{8.18}$$

où $\tau_i(\vec{r})$ représente le temps de vol nécessaire pour que l'onde se propage entre l'émission / réflexion dans le point du milieu $\vec{r}$ / reception au i^{eme} élément de la sonde. Comme on peut le voir, pour tout schéma d'émission, ce délai peut être approximé par la somme de deux termes. Le terme le plus à droite ($|\vec{r} - \vec{r}_i|_2 / c_m$) est le délai de propagation en arrière et représente le temps nécessaire à un écho, généré dans le point $\vec{r}$, pour atteindre l'élément récepteur i. Le terme de gauche ($\min_{j\in[1..N_{el}]} \left[c_m t_j + \|\vec{r} - \vec{r}_j\|_2 \right] / c_m$), représente le temps nécessaire pour que le point $\vec{r}$ soit atteint par toute onde sphérique émise par un élément j. Dans la littérature, cela se présente sous différentes formes (en fonction du schéma d'émission) l'idée principale étant de calculer le temps nécessaire pour que le front d'onde total généré par l'émission de la sonde atteigne le point $\vec{r}$ [Montaldo et al., 2009]. Cependant, comme cela est montré plus loin dans cette Section, puisque les retards d'émission t_j sont générés de telle manière que le front d'onde désiré est créé en émission, la fonction "min" dans le calcul du retard de propagation (8.18) n'est plus nécessaire (car $c_m t_j + \|\vec{r} - \vec{r}_j\|_2$ devient constant pour tout j). Il est clair que cette relation est mieux adaptée pour le champ proche (par rapport aux expressions complètes): en effet, la méthode DAS suppose que l'onde est déjà dans le champ lointain donc les retards classiques sont légèrement décalés.

Dans cette Section, le principe et le formalisme de la méthode de reconstruction d'image DAS a été détaillée. Enfin, sur l'image 2D $\hat{\gamma}_{DAS}(\vec{r})$ obtenue après l'application du DAS, une extraction de l'enveloppe et une compression logarithmique sont effectuées afin d'obtenir une image en niveaux de gris dont l'intensité peut varier entre $-\infty$ et 0. L'image finale est souvent appelée image B-mode[3] et, lorsqu'elle est affichée, une échelle d'intensité à dynamique limitée est généralement utilisée (par exemple, entre $-60\ dB$ et $0\ dB$ ou entre $-50\ dB$ et $0\ dB$).

À ce stade, le dernier bloc du processus d'imagerie ultrasonore est détaillé (Fig. 8.1). Dans la Fig. 8.7 sont représentées des images B-mode typiques que l'on peut obtenir par acquisition ultrasonore.

Quantificateurs de qualité d'image

Dans cette Section les métriques classiques utilisées pour la quantification de la qualité de l'image ultrasonore sont présentées. Pour résumer brièvement, les concepts suivants sont présentés:

- Résolution spatiale – définie comme la capacité du système à discerner deux diffuseurs dans la direction parallèle / perpendiculaire du faisceau ultrasonore utilisé pour l'imagerie.
- La longueur d'autocorrelation axiale / latérale – sont utilisées pour quantifier la largeur du speckle (texture granulaire dans la Fig.8.7)
- SNR[4] – qui permet de mesurer la quantité du bruit dans l'images B-mode
- CNR[5] – qui permet de quantifier le contraste dans l'image B-mode

[2]Abrégé pour "Delay And Sum"
[3]Abrégé de "mode Brillance"
[4]Abrégé pour "Signal to Noise Ratio"
[5]Abrégé pour "Contrast to Noise Ratio"

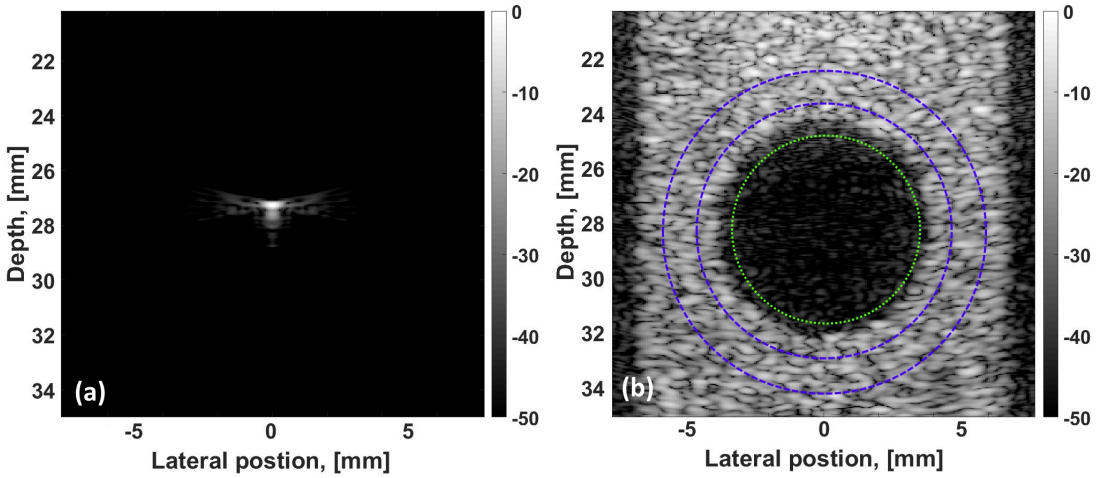

Figure 8.7: Images B-mode typiques: (a) - d'un fantôme de résolution et (b) - d'un kyste anéchoïque. La ligne verte en pointillé représente la zone de l'image où le SNR est mesurée et la zone d'arrière-plan pour le calcul du CNR. La zone entre les deux lignes bleues en pointillés représente la région d'intérêt pour le calcul du CNR.

- $eSNR$[6] – qui permet de quantifier la quantité du bruit dans le signal brut RF
- FAR[7] – qui donne le nombre des images échographiques acquises par unité de temps.

8.2.2 Méthodes d'acquisition

Dans cette section sont présentés les principes des méthodes d'imagerie les plus utilisées dans l'échographie. Pour chaque méthode, est détaillée sa relation avec le pipeline montré dans la Fig. 8.1 (et décrit dans les Section 8.1 et 8.2.1). De plus, les avantages de chaque technique sont soulignés en présentant l'évolution des métriques de quantification de la qualité d'image (définies dans la Section 8.2.1). À travers l'évolution du FAR, les notions de schémas d'acquisition "rapide" et "ultrarapide" sont introduites. Enfin, est présentée une comparaison générale entre les qualités d'image fournies par les méthodes "lentes" et "ultrarapides". Le compromis inhérent entre le FAR et une meilleure résolution d'image, CNR, SNR est mis en évidence.

Imagerie échographiques focalisée (FUI)

FUI est la méthode conventionnelle d'acquisition d'images ultrasonores largement utilisée dans les scanners médicaux [Briguet et al., 2014]. Comme son nom l'indique, elle repose sur l'émission des faisceaux ultrasonores focalisés à l'intérieur du milieu imagé [Drukarev et al., 1993]. Considérons une sonde linéaire avec N_{el} éléments et un séparation inter-éléments $\wp$ (Fig. 8.8(a)). Pour acquérir des images FUI en utilisant cette sonde, d'abord, un ensemble de points du milieu $\vec{r}_{f_k} | \; k \in [1..N_l]$ où les faisceaux seront focalisés, doit être fixé. Ensuite, pour focaliser toutes les N_{el} ondes sphériques émises (par chaque élément de la sonde) au point du milieu $\vec{r}_{f_k}$, il faut compenser la différence de temps de parcours entre toutes les positions des éléments ($\vec{r}_j$) et le point focal $\vec{r}_{f_k}$. Le calcul détaillé des délais d'émission, des signaux émis, des signaux reçus ainsi que du FAR est donné dans cette Section. À travers ces calculs et à travers un exemple synthétique est montré que malgré la qualité très bonne de l'image fournie, FUI est une technique lente (au sens du FAR) d'imagerie.

[6] Abrégé pour "echo Signal to Noise Ratio"
[7] Abrégé pour "Frame Acquisition Rate"

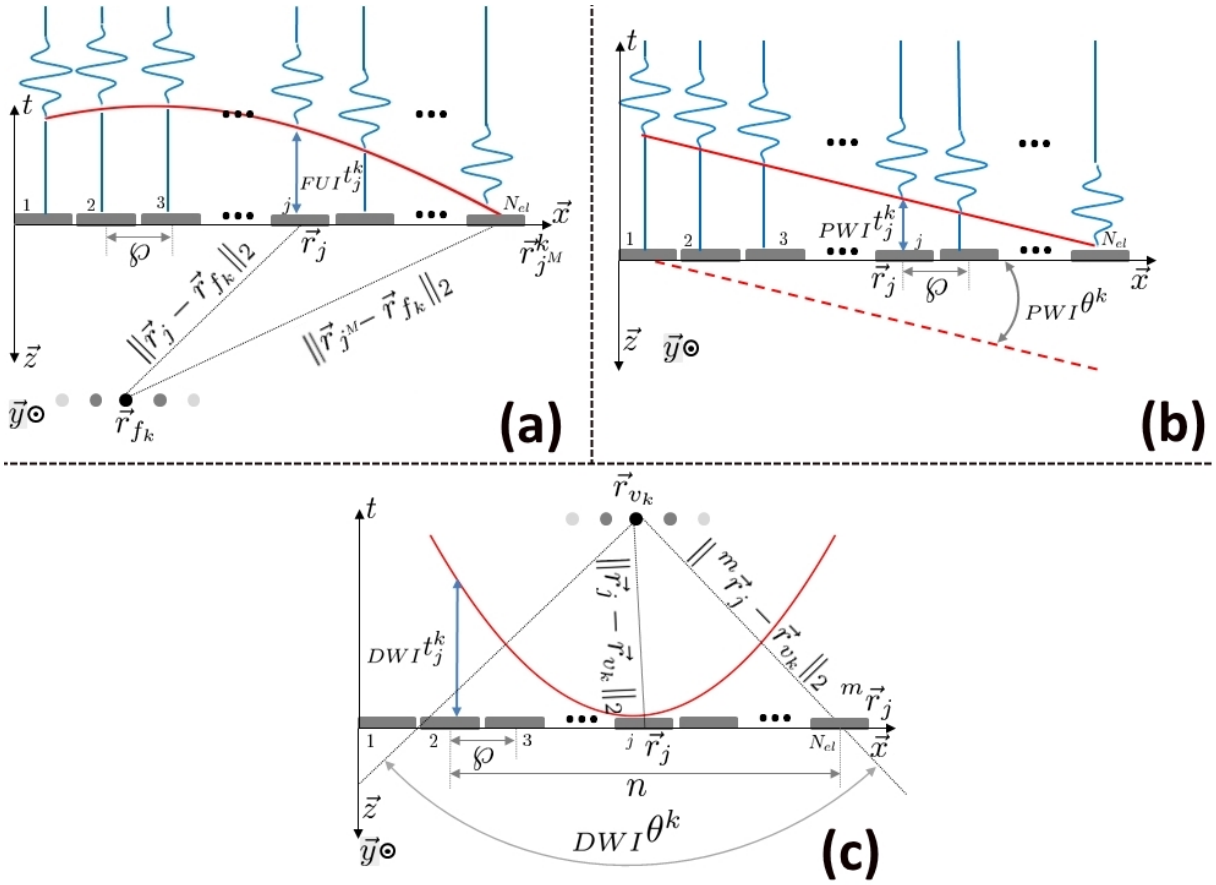

Figure 8.8: (a) - La sonde excitée par des signaux sinusoïdaux $a(t)$, retardée à l'élément j avec une durée ${}_{FUI}t_j^k$ pour émettre un faisceau focalisé à la position $\vec{r}_{f_k}$ ($z_{f_k} > 0$). La ligne rouge représente l'évolution de ${}_{FUI}t_j^k$ en fonction de j. (b) - La sonde excitée par des signaux sinusoïdaux $a(t)$, retardée à l'élément j avec une durée ${}_{PWI}t_j^k$ afin d'émettre une onde plane dans la direction ${}_{PWI}\theta^k$. La ligne rouge continue représente l'évolution de ${}_{PWI}t_j^k$ en fonction de j et la ligne rouge en pointillés représente la forme d'onde émise. (c) - Schéma d'une sonde qui émet une onde divergente. En rouge sont représentés les retards ${}_{DWI}t_j^k$ utilisés pour générer une source virtuelle à la position $\vec{r}_{v_k} | z_{v_k} < 0$. L'ouverture angulaire générée est ${}_{DWI}\theta^k$.

Multi Line Transmit (MLT)

Le schéma d'acquisition MLT s'appuie fortement sur le principe de FUI. Il consiste en l'émission simultanée de N_{MLT} faisceaux focalisés dans N_{MLT} points $\vec{r}_{f_k}$ [Mallart and Fink, 1992, Drukarev et al., 1993, Badescu et al., 2017, Tong et al., 2014]. En MLT, une image B-mode complète est reconstruite après N_l / N_{MLT} événements d'émission / de réception / de reconstruction. Cela implique que MLT est plus rapide que FUI, mais comme montré dans cette Section, la qualité de l'image fournie par MLT est dégradée. Ici, est démontré que cette dégradation vient de l'interférence entre les faisceaux émis simultanément.

Imagerie par onde plane (PWI)

Comme FUI et MLT, PWI s'appuie aussi sur la superposition linéaire des ondes sphériques (générées par chaque élément j de la sonde). Cependant, dans ce cas, les ondes sphériques sont générées de telle manière que le front d'onde qui se propage à l'intérieur du milieu est un plan [Sandrin et al., 1999, Tanter et al., 2002, Sandrin et al., 2002] (ligne rouge en pointillés sur la Fig. 8.8(b)).

Dans la Fig.8.8(b) est montrée une sonde ultrasonore configurée pour l'émission d'une onde plane dans la direction ${}_{PWI}\theta^k$. Dans cette Section le calcul explicite des délais d'émission, des signaux émis, des signaux reçus ainsi que du FAR est donné. On conclue ici que si l'on accepte une légère perte de qualité d'image, l'imagerie à ondes planes peut fournir une amélioration du FAR d'un facteur 10.

Imagerie par onde divergente et imagerie à synthèse d'ouverture (DWI et STA)

DWI et STA sont deux méthodes d'imagerie qui utilisent des insonifications du milieu par ondes divergentes afin de reconstruire des images B-mode complètes après une seule émission / réception. Bien que dans la littérature il existe un grand nombre de variantes DWI [Hasegawa and Kanai, 2011, Papadacci et al., 2014, Zhang et al., 2016, Porée et al., 2016] et STA [Jensen et al., 2006], le processus utilisé pour générer une image B-mode est généralisé dans cette Section. Dans la Fig.8.8(c) est montrée une sonde ultrasonore configurée pour l'émission d'une onde divergente avec une source virtuelle à la position $\vec{r}_{v_k}|z_{v_k} < 0$ et une ouverture angulaire générée de ${}_{DWI}\theta^k$. Les calculs développés dans cette Section de la thèse montrent que, similaire au PWI, DWI fournit des qualités d'image proches de FUI lorsque N_{dwi} est élevé. Cependant, pour un nombre élevé d'ondes divergentes utilisées pour la composition, la cadence d'acquisition de l'image finale diminue, ce qui montre encore une fois le compromis inhérent entre le FAR et une bonne qualité d'image. Selon l'application, il existe différentes approches DWI. Cependant, toutes ces méthodes d'imagerie peuvent être considérées comme une variante de l'approche présentée dans cette Section. Ainsi, en fixant le nombre d'éléments actifs et en déplaçant la position de la source virtuelle le long de différents motifs (cercles, ellipses), le champ de pression généré peut être modifié afin d'insonifier le milieu de différentes manières. La variation classique de l'imagerie par synthèse d'ouverture (STA) peut également être considérée comme une variation du schéma d'émission décrit dans cette Section. Le STA classique consiste en des émissions successives, avec un seul élément, d'ondes divergentes à l'intérieur du milieu [Jensen et al., 2006]. Après chaque émission / réception, une image de faible qualité est reconstruite et ces images sont finalement combinées (après l'émission par l'ensemble des éléments de la sonde). Enfin, des variations de STA qui sont exactement les mêmes que l'approche DWI existent [Karaman et al., 1998].

Résumé sur les méthodes d'imagerie

Method / Metric	FUI	MLT	PWI	DWI
FAR	⊖	⊕	⊕	⊕
Ax. res.	⊕	⊕	⊕	⊕
Lat. res.	⊕	⊖	⊖	⊖
Ax. cor.	⊕	⊕	⊕	⊕
Lat. cor.	⊕	⊖	⊖	⊖
SNR	⊕	⊖	⊖	⊖
CNR	⊕	⊖	⊖	⊖
eSNR	⊕	⊖	⊖	⊖

Figure 8.9: Évolution qualitative des métrique de qualité d'image pour les différentes approches d'imagerie présentées dans la section 8.2.2

Dans la Fig.8.9 est montrée un diagramme qui résume les performances des différentes méthodes d'imagerie présentées dans cette Section. Comme on peut l'observer ici, la meilleure qualité d'image

est obtenue grâce au schéma d'acquisition conventionnel (focalisé). On peut également observer que les méthodes d'imagerie qui offrent une cadence d'acquisition plus rapide impliquent une diminution de la qualité de l'image fournie.

8.3 Codage temporel pour augmenter le rapport signal sur bruit des échos

8.3.1 Généralités

Jusqu'à présent l'évolution de la qualité d'image en fonction du FAR a été présentée. Cependant, pour une méthode d'acquisition donnée, ses performances peuvent également être altérées par le bruit à l'intérieur des données RF. Le but de cette Section est de présenter brièvement l'impact du bruit sur la qualité de l'image et surtout de montrer comment le codage temporel des signaux d'excitation permet de surmonter les effets indésirables.

En développant l'expression de l'$eSNR$, on montre dans cette Section, que dans le contexte de l'imagerie échographique la seule manière qui permet d'améliorer l'$eSNR$ est en augmentant la longueur des signaux d'excitation $a(t)$. Cependant, de telles excitations nuisent fortement à la résolution spatiale de l'image. Pour résoudre ce compromis, une solution réaliste et réalisable consiste à utiliser une classe particulière de signaux $^\circ a(t)$ qui, malgré leur longue durée, peuvent être filtrés afin de compresser leur énergie sur une courte durée. Dans la Fig. 8.10, est montré comment le bloc

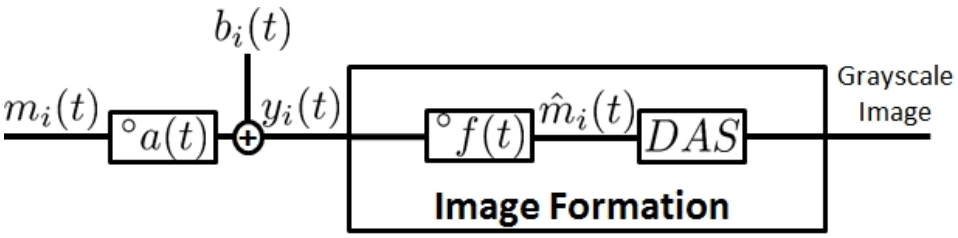

Figure 8.10: Représentation schématique du bloc "Reconstruction d'image" du processus d'imagerie échographique utilisant des signaux d'excitation $^\circ a(t)$ qui permettent d'augmenter l'$eSNR$.

"Reconstruction de l'image" peut être modifié afin de compresser l'énergie du signal d'excitation $^\circ a(t)$. Principalement, la seule différence entre le bloc classique de "Reconstruction de l'image" et celui présenté dans la Fig. 8.10 est que, ici, une étape supplémentaire de filtrage $^\circ f(t)$ a été ajouté. Dans cette Section sont montrés aussi les calculs permettant de calculer les filtres $^\circ f(t)$ optimaux. La relation suivante est déduite:

$$^\circ F(\nu) = \frac{^\circ A^*(\nu)}{^\circ A(\nu)\,^\circ A^*(\nu) + \frac{\mathbb{E}\left\{|B_i(\nu)|^2\right\}}{\mathbb{E}\left\{|M_i(\nu)|^2\right\}}} = \frac{^\circ A^*(\nu)}{|^\circ A(\nu)|^2 + \frac{1}{eSNR_{M_i}(\nu)}} = \begin{cases} \frac{1}{^\circ A(\nu)}, \; 1/eSNR_{M_i}(\nu) << |^\circ A(\nu)|^2 \\ ^\circ A^*(\nu), \text{ sinon} \end{cases} \tag{8.19}$$

où les majuscules représentent les transformées de Fourier (FT) des signaux temporels correspondants (par exemple, pour un signal arbitraire $s(t)$, sa transformée de Fourier est définie comme $S(\nu) = \mathrm{FT}(s)$)). Dans (8.19), $F^*(\nu)$ (resp. $A^*(\,u)$) représente le conjugué complexe du signal $F(\nu)$ (resp. $A(\nu)$). $eSNR_{M_i}(\nu)$ représente le rapport signal sur bruit de l'écho (pour chaque bande de fréquence ν) dans le cas où une impulsion a été utilisée comme signal d'excitation (à condition que le bruit ait la même variance que dans l'acquisition avec l'excitation $^\circ a(t)$). Maintenant, comme on peut le voir dans (8.19), si le bruit d'acquisition est très faible ($1/eSNR_{M_i}(\nu) << |^\circ A(\nu)|^2$), $^\circ F(\nu)$ devient un filtre inverse, ce qui signifie que la résolution fournie est optimale. Cependant, si le bruit augmente, $^\circ F(\nu)$ devient plus proche d'un filtre adapté. Cette famille de filtres est appelée Wiener [Wiener et al., 1949].

En effet, dans le cas où aucun bruit n'est présent (ou il est très faible), le filtre inverse fournirait une résolution spatiale optimale sans aucun bruit de fond (généré par $B_i(v)$), puisque l'estimation $\hat{M}_i(v)$ correspond parfaitement à $M_i(v)$ (dans Fig.8.10). Dans de tels cas, tout signal d'excitation serait applicable à l'acquisition. Cependant, dans tous les autres cas, où $^\circ F(v)$ est intermédiaire entre un filtre inverse et un filtre adapté, les signaux qui ont un "bon" produit d'autocorrélation (défini comme: $^\circ a(t) *_t {}^\circ a(-t)$) conviennent. Par "bon", dans cette application est implicite que la densité spectrale de puissance (définie comme $^\circ A(v)\,^\circ A^*(v) = \mathrm{FT}\{^\circ a(t) *_t {}^\circ a(-t)\}$) est constante, ce qui implique que le produit d'autocorrélation génère un lobe principal très mince et que les lobes secondaires sont faibles par rapport au lobe principal. Bien avant leur application aux ultrasons, de tels signaux étaient déjà mis en œuvre dans des systèmes RADAR et de télécommunication pour atteindre les mêmes objectifs finaux [Skolnik, 1962, Siebert, 1988, Prasad and Ojanpera, 1998, Nathanson et al., 1991]. Ces signaux peuvent être divisés en deux groupes principaux en fonction de leur schéma de génération: les signaux BPSK (Binary Phase Shift Keyed) et les signaux LFM (Linear Frequency Modulated) (appelés aussi chirps). Les propriétés ainsi que les principes d'implémentation de chacune de ces deux groupes (et leurs variations) sont présentés dans cette Section.

8.4 Codage temporel pour augmenter la cadence d'acquisition d'images

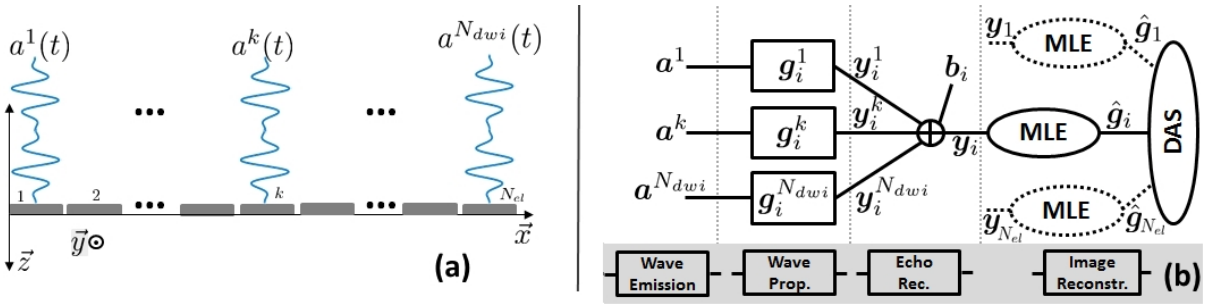

Figure 8.11: (a) - Représentation schématique de l'émission STA codé, (b) - Pipeline de l'approche d'imagerie STA codée. MLE et DAS signifient respectivement: "estimateur du maximum de vraisemblance" et "Delay And Sum" (algorithme de reconstruction de l'image).

Comme indiqué dans la Section précédente, les premières méthodes utilisant des signaux modulés en amplitude / fréquence avaient pour seul objectif d'augmenter l'$eSNR$ des signaux reçus. Plus tard, des excitations codées ayant comme but d'augmenter le FAR ont commencé à être utilisées dans les schémas d'acquisition échographiques (inspirées par les approches à accès multiple par répartition en fréquence et code (FDMA et CDMA) largement utilisées dans les systèmes de télécommunication [Black and Black, 1994, Prasad and Ojanpera, 1998, Jonassen et al., 2008]). En termes simples, dans les systèmes de télécommunication, FDMA et CDMA permettent à plusieurs paires d'utilisateurs de communiquer sur une ressource partagée (généralement un canal) sans interférence ni perte d'information. Comme leur nom l'indique, ceci est réalisé soit en divisant la bande passante totale du canal en sous-bandes passantes (chaque paire communiquant via son sous-canal) soit en attribuant à chaque paire un code d'étalement spécifique utilisé en émission et en réception (le code de chaque paire étant orthogonal aux autres, l'interférence entre les paires est réduite). En établissant une parallèle entre les systèmes échographiques et les systèmes de télécommunication, on peut donc en conclure que des approches similaires peuvent être appliquées aux ultrasons pour augmenter les FAR. Supposons les équivalences suivantes entre les systèmes de télécommunication $\Longleftrightarrow$ échographie: canal $\Longleftrightarrow$ milieu imagé, message $\Longleftrightarrow$ signal d'excitation, paire d'utilisateurs (ou paire d'antennes utilisateur) $\Longleftrightarrow$ sonde en émission et sonde en réception. Dans ces conditions, le processus d'imagerie ultrasonore (qui, comme il a été montré dans la Section 8.2, essaye de reconstruire le TRF du milieu) peut être considéré comme un équivalent des méthodes d'estimation du canal, largement utilisées dans les télécommunications [Zhao and Huang, 1997, Torlak and Xu, 1997, Coleri et al., 2002, Kang et al., 2003]. Ainsi, en

s'appuyant sur ce principe, un schéma d'acquisition ultrasonore qui utilise l'émission simultanée d'ondes acoustiques codées pour augmenter la fréquence d'images du STA classique, a été développé dans [Gran and Jensen, 2004, Gran et al., 2004, Gran and Jensen, 2008, Kotowick et al., 2013], .

Par rapport à l'approche STA conventionnelle, la méthode STA codée utilise l'émission simultanée de N_{dwi} ondes ultrasonores divergentes, chacune portant un signal BPSK $a^k(t)$ (Fig. 8.11(a)). Dans cette Section est montré que les blocs "Emission de l'onde", "Propagation et interaction avec le milieu" et " Réception d'échos" peuvent être modélisés par le système linéaire suivant:

$$\boldsymbol{y}_i = \sum_{k=1}^{N_{dwi}} \boldsymbol{a}^k *_t \boldsymbol{g}_i^k + \boldsymbol{b}_i = \begin{bmatrix} \boldsymbol{A}^1 & \boldsymbol{A}^2 & \cdots & \boldsymbol{A}^{N_{dwi}} \end{bmatrix} \cdot \begin{bmatrix} \boldsymbol{g}_i^1 \\ \boldsymbol{g}_i^2 \\ \vdots \\ \boldsymbol{g}_i^{N_{dwi}} \end{bmatrix} + \boldsymbol{b}_i \tag{8.20}$$

où les symboles en gras représentent les versions échantillonnées des signaux suivants: le signal total reçu à l'élément i de la sonde ($y_i(t)$) et la réponse impulsionnelle du milieu lorsque l'élément k émet et que i reçoit ($g_i^k(t)$). Dans (8.20), $\boldsymbol{A}^k$ sont des matrices de convolution construites à partir des signaux $\boldsymbol{a}^k$ correspondants.

Ensuite, avant de procéder à la reconstruction DAS, dans cette Section est montré comment à partir de (8.20) obtenir des estimations de la réponse impulsionnelle du milieu lorsque l'élément k émet et que i reçoit. Cette étape est appelée MLE (Fig.8.11(b)) et permet de calculer tous les signaux $\hat{g}_i^k(t)$ depuis (8.20), en se basant sur le fait que le bruit $\boldsymbol{b}_i$ est gaussien. Ainsi, on obtient:

$$\begin{gathered} \hat{\boldsymbol{g}}_i = \left(\boldsymbol{A}^T \cdot \boldsymbol{A}\right)^{-1} \cdot \boldsymbol{A}^T \cdot \boldsymbol{y}_i \\ \text{with: } \hat{\boldsymbol{g}}_i = \begin{bmatrix} \hat{\boldsymbol{g}}_i^1 \\ \hat{\boldsymbol{g}}_i^2 \\ \vdots \\ \hat{\boldsymbol{g}}_i^{N_{dwi}} \end{bmatrix} \text{ and } \boldsymbol{A} = \begin{bmatrix} \boldsymbol{A}^1 & \boldsymbol{A}^2 & \cdots & \boldsymbol{A}^{N_{dwi}} \end{bmatrix} \end{gathered} \tag{8.21}$$

où $\boldsymbol{A}^T$ représente la transposition de la matrice $\boldsymbol{A}$ et $\left(\boldsymbol{A}^T \cdot \boldsymbol{A}\right)^{-1} \cdot \boldsymbol{A}^T$ représente sa pseudo-inverse.

Dans la Fig. 8.12(a) sont montrées les images obtenues en utilisant la STA codée et classique dans

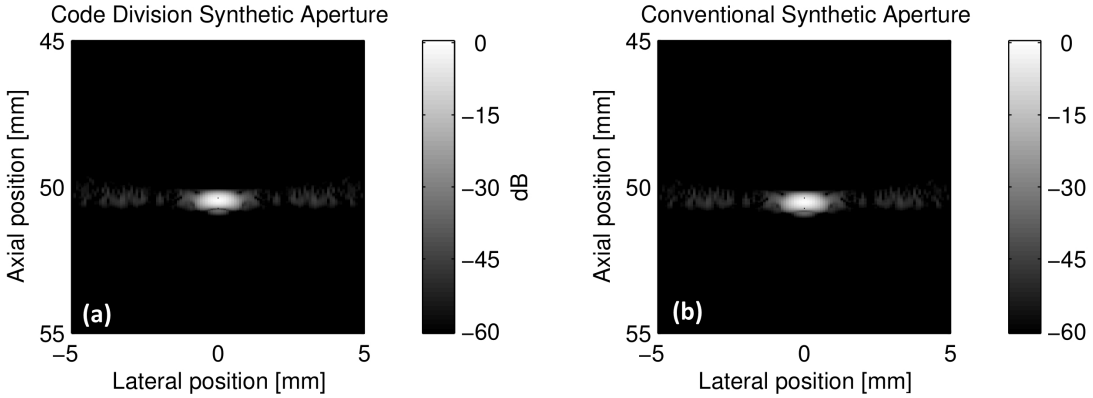

Figure 8.12: Images B-mode obtenues avec: (a) - STA codée, (b) - STA classique (avec comme excitation une impulsion de Dirac). Ceci est une reproduction fidèle de la Fig.4 publiée dans [Gran et al., 2004].

une simulation Field II [Jensen and Svendsen, 1992, Jensen, 1996]. On peut voir que, comparé au STA classique (Fig. 8.12 (b)), aucune différence entre les deux images B-mode ne peut pas être évaluée. Comme expliqué dans cette Section, cela résulte du fait que la STA codée permet d'estimer les données RF que l'on obtiendrait si des impulsions de Dirac étaient utilisées comme excitation dans une STA

conventionnelle. Enfin, comme N_{dwi} ondes divergentes sont émises simultanément et que leurs échos sont séparés en réception par MLE, cela signifie que théoriquement, la STA codée augmente le FAR d'un facteur de N_{dwi} (par rapport à STA conventionnelle). Cependant, comme le montre ce Chapitre, le $eSNR$ des techniques STA (DWI) est le plus faible comparé à d'autres approches d'imagerie (par exemple, ultrasons focalisés et à ondes planes). Est-ce que cette méthode est stable à une telle quantité de bruits? Cette méthode peut-elle être appliquée à d'autres types de schémas d'acquisition autres que les STA? Quelles sont les hypothèses à formuler pour que cette méthode fonctionne correctement? Comment choisir les signaux d'excitation? Peut-il être implémenté sur un échographe? À ce stade, pour répondre à toutes ces questions, une étude plus approfondie de la méthode doit être effectuée.

8.5 Résumé

Dans ce Chapitre, le principe de propagation des ondes acoustiques a été détaillé. Les hypothèses sur lesquelles reposent les méthodes conventionnelles d'imagerie échographique ont été présentées et les modèles mathématiques correspondants ont été construits pour chacun des schémas d'acquisition conventionnels. En outre, l'évolution de la qualité d'image fournie en fonction du temps d'acquisition a été décrite et le compromis entre la qualité d'image et la cadence d'acquisition d'images a été souligné. Les différents types de signaux d'excitation couplés aux techniques de filtrage correspondantes et leurs avantages ont été présentés. Leur impact sur la qualité de l'image ultrasonore a été discuté. Enfin, il a été montré comment ces signaux spécifiques d'excitation peuvent être utilisés dans une approche d'imagerie qui peut théoriquement augmenter la cadence d'acquisition d'images. Cette méthode innovante repose sur des émissions simultanées et sur la séparation d'échos en utilisant des approches de problèmes inverses. Cependant, malgré son intérêt théorique, cette méthode n'a pas été complètement validée et une étude plus détaillée doit être réalisée pour en percevoir ses limites. Cela sera fait dans le prochain Chapitre, en abordant sa compatibilité avec un schéma d'acquisition par onde plane. Le choix du PWI à la place du FUI en tant que schéma d'acquisition provient du fait que pour chaque tir, PWI fournit des images complètes du milieu et que, quand composées, ces images ont une qualité comparable à celle des images FUI tout en utilisant moins de tirs (Sous-section 8.2.2).

9 Imagerie ultrasonore codée: estimation de la réponse impulsionnelle du tissu à une onde plane

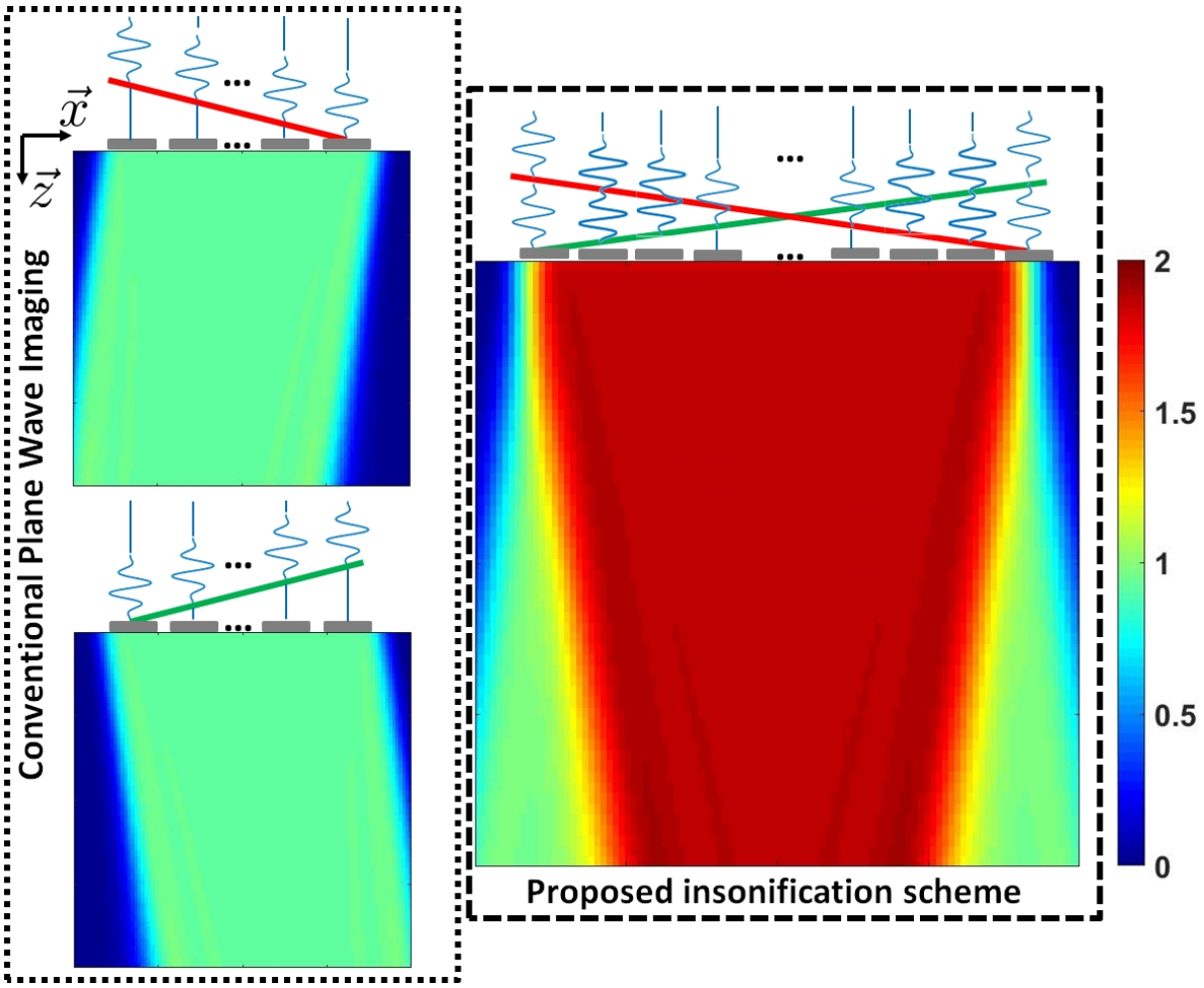

Figure 9.1: Représentation du schéma d'émission proposé. Alors que pour l'imagerie classique par onde plane (canevas pointillé), chaque onde plane (correspondant aux lois de retard d'émission rouge et vert) est émise successivement, la solution proposée ici (canevas ligne discontinue) consiste en une émission simultanée des ondes planes. La palette de couleurs représente la moyenne quadratique des champs de pression générés par les différentes émissions.

Dans ce Chapitre, est détaillée une méthode permettant, sous certaines conditions, d'augmenter la cadence d'acquisition d'images de l'approche classique d'échographie par ondes planes. Le synoptique

de la solution proposée est illustré dans la Fig. 9.1. Comme on peut le constater, alors que dans l'imagerie classique par onde plane (canevas pointillé), chaque onde plane (correspondant aux lois de retard d'émission rouge et vert) est émise successivement, la solution proposée ici (canevas ligne pointillée) consiste en une émission simultanée d'ondes planes. Cela signifie que chaque diffuseur du milieu est insonifié en même temps par deux fronts d'onde (rouge et vert), ce qui implique qu'il génère une onde rétro-diffusée qui est un mélange d'échos que le même diffuseur générerait si chaque onde plane était émise successivement. Ici le problème inhérent consistant à séparer le mélange des échos à l'intérieur des données reçues afin de discriminer la contribution de chaque onde plane est traité. Tout d'abord, on construit le modèle direct permettant d'écrire les échos rétro-diffusés reçus en fonction des signaux émis et en fonction des réponses impulsionnelles du milieu à chaque onde plane. Deuxièmement, on propose une méthode permettant d'estimer les réponses impulsionnelles du milieu à partir des données reçues en s'appuyant sur le modèle direct construit. On étudie également l'impact des différents paramètres de modélisation sur l'estimation. Deux hypothèses sont énoncées:

H3.1 Les zones "Blind" and "Perturbation" [1] sont complètement anéchoïques.

H3.2 Aucun bruit d'acquisition n'est superposé aux données RF.

On étudie la performance de la méthode lorsque ces hypothèses sont vérifiées et violées. De plus, on presente et on discute des résultats de simulation et d'acquisition in vitro. Enfin, on souligne les avantages et les inconvénients de la méthode proposée.

Ce travail est une extension de l'idée présentée dans [Pages et al., 2015], et ces différents éléments ont été publié dans
[Bujoreanu et al., 2017b, Bujoreanu et al., 2017a, Bujoreanu et al., 2017c].

9.1 Insonification par une seule onde plane

Avant d'entrer dans les détails du modèle direct pour l'émission simultanée d'ondes planes (canevas en ligne pointillée sur la Fig. 9.1), on construit d'abord le modèle direct pour l'émission d'une seule onde plane. La sonde configurée pour l'émission d'une seule onde plane est représentée dans la Fig.9.2(a). Dans cette Section sont montrés les relations qui permettent de générer les signaux d'excitation pour ce schéma d'émission. Ainsi, on montre que le signal reçu par l'élément i de la sonde peut s'écrire comme suit:

$$\boldsymbol{y}_i^k = \boldsymbol{a}^k *_t \boldsymbol{g}_i^k \tag{9.1}$$

où $\boldsymbol{a}^k$ est le signal portée par l'onde plane k, $\boldsymbol{y}_i$ est les signal enregistré par l'élément i de la sonde et $\boldsymbol{g}_i^k$ est la réponse impulsionnelle du milieu à l'onde plane k vue par l'élément i. Ensuite une écriture de (9.1) sur la forme d'un produit matriciel est proposée. Le système suivant est obtenu:

$$\boldsymbol{y}_i^k = \boldsymbol{A}^k \cdot \boldsymbol{g}_i^k \tag{9.2}$$

où $\boldsymbol{A}^k$ est une matrice de Toeplitz générée à partir des signaux d'excitation $\boldsymbol{a}^k$. La représentation schématique du modèle directe ainsi créé est représentée dans la Fig.9.2(b) .

[1] La définition de ces régions est introduite plus tard dans ce Chapitre.

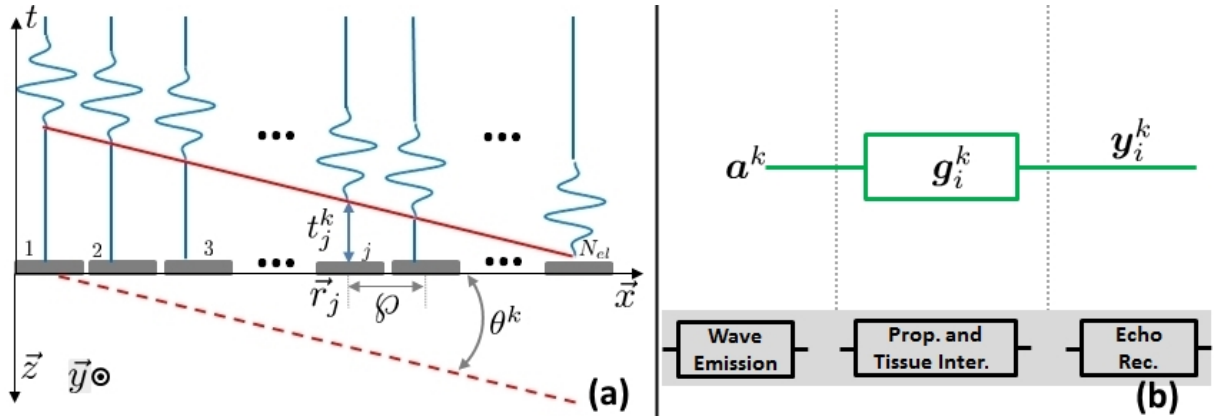

Figure 9.2: Principe de l'imagerie conventionnelle par onde plane: (a) - La sonde excitée par des impulsions sinusoïdaux $a^k(t)$, retardés à l'élément j avec une durée t_j^k pour émettre une onde plane dans la direction θ^k. La ligne rouge continue représente l'évolution de t_j^k en fonction de j et la ligne rouge en pointillés représente le front d'onde émis. (b) - Le modèle direct construit pour l'insonification à une seule onde plane. On peut voir que le bloc "Emission de l'onde" est modélisée uniquement par la forme d'onde du signal d'excitation $\boldsymbol{a}^k$. Le bloc "Propagation et Interaction milieu" est modélisé par la réponse impulsionnelle du milieu à l'onde plane k, vue par l'élément i de la sonde $\boldsymbol{g}_i^k$. Le signal $\boldsymbol{y}_i$ enregistré par l'élément i de la sonde (dans un cas d'acquisition sans bruit) est modélisé comme la convolution entre la forme d'onde d'excitation $\boldsymbol{a}^k$ et la réponse impulsionnelle $\boldsymbol{g}_i^k$ du milieu à l'onde plane k.

9.2 Insonification simultanée par plusieurs ondes planes

Dans cette Section on montre que résoudre directement (9.2) pour $\boldsymbol{g}_i^k(t)$ n'est pas optimal car le problème inverse est mal posé. Comme l'émission successive des ondes planes n'est pas une solution optimale en termes de cadence d'imagerie (car elle augmente le temps d'acquisition), ici on propose d'émettre les ondes planes simultanément.

Dans cette Section la démarche nécessaire pour calculer les signaux d'excitation pour chacun des éléments j de la sonde est donnée. La sonde en configuration d'émission simultanée des ondes planes est montrée dans la Fig.9.3(a). Comme on peut le voir dans la Fig.9.3(a), pour émettre simultanément N_{pwi} ondes planes il faut utiliser une superposition des signaux d'excitations que l'on utiliserait pour émettre successivement chaque onde plane:

$$ {}_S a_j(t) = \sum_{k=1}^{N_{pwi}} a_j^k(t) = \sum_{k=1}^{N_{pwi}} a^k(t - t_j^k) \tag{9.3} $$

À cette étape, en combinant la définition des signaux d'excitation (9.3) avec l'expression générale des échos reçus (2.33), on peut déduire la relation qui lie les données RF (dans le cas d'une émission codée simultanée) aux N_{pwi} signaux d'excitation $a^k(t)$ et aux N_{pwi} réponses impulsionnelles du milieu $g_i^k(t)$:

$$ {}_S\boldsymbol{y}_i = \sum_{k=1}^{N_{pwi}} \boldsymbol{y}_i^k + \boldsymbol{b}_i = \sum_{k=1}^{N_{pwi}} \boldsymbol{A}^k \cdot \boldsymbol{g}_i^k + \boldsymbol{b}_i \tag{9.4} $$

Une représentation schématique de la relation précédente est montrée sur la Fig. 9.3(b). Comme on peut le voir ici, la "caractéristique" simultanée de l'émission est modélisée dans le bloc "Réception d'échos", qui modélise le signal total reçu ${}_S\boldsymbol{y}_i$ par une superposition linéaire des signaux $\boldsymbol{y}_i^k$ (Fig. 9.2(b)) que l'on recevrait si chaque onde plane était émise successivement. En se basant sur les propriétés du

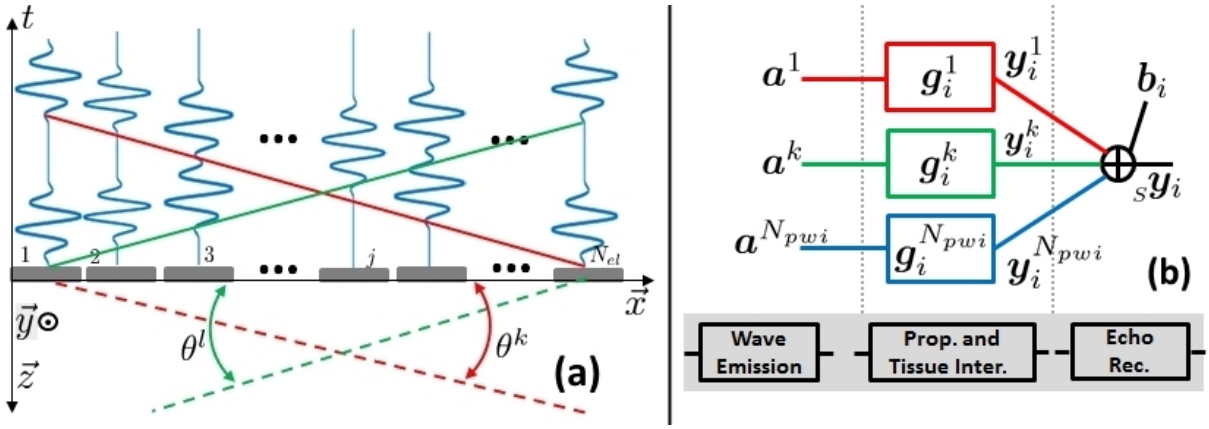

Figure 9.3: Principe de l'émission simultanée d'ondes planes: (a) - La sonde est excitée par une superposition des signaux d'excitation que l'on utiliserait pour émettre successivement chaque onde plane. Ici, un exemple d'émission simultanée de deux ondes planes est affiché. Les délais d'excitation qui suivent la ligne rouge continue produisent un front d'onde qui se propage dans la direction θ^k et les retards qui suivent la ligne verte continue génèrent un front d'onde qui se propage dans la direction θ^l. (b) - Le modèle direct construit pour l'émission simultanée de N_{pwi} ondes planes. On peut voir que pour chaque onde plane k, les blocs "Emission de l'onde" et "Propagation et interaction tissu" sont modélisés de manière identique à la Fig. 9.2(b). La "caractéristique" simultanée de la méthode apparaît dans la modélisation du bloc "Réception d'échos". Cette couche représente le signal total reçu ${}_S\boldsymbol{y}_i$ en tant qu'une superposition linéaire des signaux $\boldsymbol{y}_i^k$ que l'on recevrait si chaque onde plane était émise successivement. $\boldsymbol{b}_i$ représente un bruit additif d'acquisition. Ici, chaque couleur (sauf le noir) met en évidence le pipeline suivi d'une onde plane spécifique: $k = 1 \Longleftrightarrow$ red, $k \Longleftrightarrow$ green and $k = N_{pwi} \Longleftrightarrow$ blue.

produit matriciel, on réécrit (9.4) comme suit:

$$
\begin{gathered}
{}_S\boldsymbol{y}_i = \boldsymbol{A}\cdot\boldsymbol{g}_i + \boldsymbol{b}_i \\
\text{avec: } \boldsymbol{A} = \begin{bmatrix} \boldsymbol{A}^1 & \boldsymbol{A}^2 & \cdots & \boldsymbol{A}^{N_{pwi}} \end{bmatrix} \text{ et } \boldsymbol{g}_i = \begin{bmatrix} \boldsymbol{g}_i^1 \\ \boldsymbol{g}_i^2 \\ \vdots \\ \boldsymbol{g}_i^{N_{pwi}} \end{bmatrix}
\end{gathered}
\tag{9.5}
$$

Où $\boldsymbol{A}$ est une matrice avec N_y lignes et $N_{pwi}(N_y + N_a - 1)$ colonnes et $\boldsymbol{g}_i$ est un vecteur de taille $N_{pwi}N_g$.

9.3 Élaboration du problème inverse

Dans la Section précédente a été construit un modèle direct qui, dans le cas de l'émission simultanée des ondes planes, relie les échos rétro-diffusés reçus aux formes d'onde émises et aux réponses impulsionnelles du milieu à chacune des ondes planes. L'objectif ici est de présenter comment séparer la réponse impulsionnelle du milieu à chacune des ondes planes à l'aide du modèle direct généré. Ainsi, dans cette Section est détaillé le bloc "Image Reconstruction" affiché dans la Fig. 9.4.

Comme on peut le voir sur la Fig. 9.4, le bloc "Reconstruction de l'image" prend en entrée les données RF enregistrées qui contiennent N_{el} vecteurs ${}_S\boldsymbol{y}_i$. Afin de séparer la contribution de chaque onde plane à l'intérieur de ces signaux, ici est implémentée une étape d'estimation ("Est" dans la Fig. 9.4). Après l'estimation séparée de N_{el} vecteurs $\hat{\boldsymbol{g}}_i$, la relation (9.5) est utilisée pour trouver chaque réponse impulsionnelle du milieu. Pour faire ceci, on divise les N_{el} vecteurs $\hat{\boldsymbol{g}}_i$ en N_{el} ensembles de

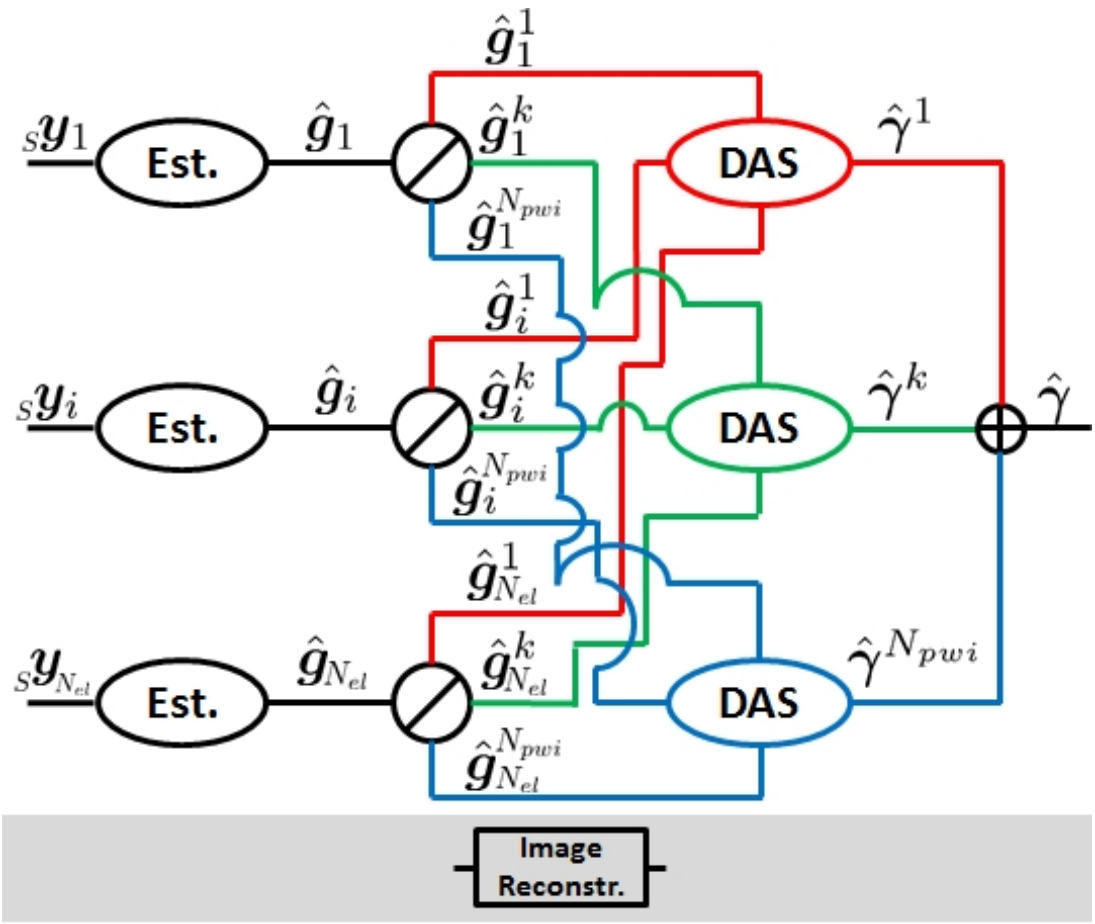

Figure 9.4: Le bloc "Image Reconstruction" de la méthode d'imagerie proposée. Une fois les données RF ${}_S\boldsymbol{y}_i$ reçues (après émission simultanée des ondes planes), le signal reçu par chaque élément de la sonde passe par une étape permettant de séparer les échos pour chaque onde plane ("Est"). Après cette étape d'estimation, chacun des N_{el} vecteur $\boldsymbol{g}_i$ est divisé ($\oslash$) dans N_{pwi} vecteurs $\boldsymbol{g}_i^k$ (représentés avec des différentes couleurs) qui représentent la réponse impulsionnelle du milieu à l'onde plane k, vue par l'élément i de la sonde. Les N_{pwi} ensembles de N_{el} vecteurs $\boldsymbol{g}_i^k$ sont passés par l'algorithme DAS afin de reconstruire l'image correspondante $\boldsymbol{\gamma}^k$. Enfin, les N_{pwi} images $\boldsymbol{\gamma}^k$ sont ajoutées de manière cohérente pour obtenir l'image finale $\hat{\boldsymbol{\gamma}}$. Ici, chaque couleur (sauf le noir) met en évidence le pipeline suivi par une onde plane spécifique: $k = 1 \Longleftrightarrow$ rouge, $k \Longleftrightarrow$ vert et $k = N_{pwi} \Longleftrightarrow$ bleu.

N_{pwi} vecteurs. Ces signaux sont ensuite utilisés comme entrée pour une étape DAS afin de trouver une image de la TRF $\boldsymbol{\gamma}^k$. Comme vu dans la Section 2.2.2, les N_{pwi} images $\boldsymbol{\gamma}^k$ sont ensuite sommées pour obtenir l'image finale $\hat{\boldsymbol{\gamma}}$.

9.3.1 La couche d'estimation

Dans le pipeline détaillé ci-dessus, on peut observer que, une fois que les N_{el} ensembles de N_{pwi} vecteurs $\hat{\boldsymbol{g}}_i^k$ ont été isolés, le traitement proposé suit le même chemin que l'imagerie classique par ondes planes. Ainsi, l'étape la plus importante du traitement proposé est la couche "Est.". Ici, on montre qu'une solution au problème inverse basé sur (9.5) est:

$$\hat{\boldsymbol{g}}_i = (\boldsymbol{A}^T \cdot \boldsymbol{A})^{-1} \cdot \boldsymbol{A}^T \cdot {}_S\boldsymbol{y}_i \tag{9.6}$$

où $\hat{\boldsymbol{g}}_i$ est l'estimation du vecteur $\boldsymbol{g}_i$. La relation précédente représente l'estimateur conventionnel utilisé pour minimiser l'erreur au sens des moindres carrés sur le terme d'attache aux données $\| {}_S\boldsymbol{y}_i - \boldsymbol{A}\cdot\boldsymbol{g}_i\|_2^2$ [Beck and Teboulle, 2009]. Pour prédire le comportement de cet estimateur en fonction des différents paramètres de modélisation (par exemple: signaux d'excitation, temps d'enregistrement, bruit d'acquisition, etc.), une analyse du noyau $\boldsymbol{A}$ est faite dans cette Section. Cette étude est basée sur la décomposition en valeurs singulières de la matrice $\boldsymbol{A}$:

$$\boldsymbol{A} = \boldsymbol{U}\cdot\boldsymbol{S}\cdot\boldsymbol{V}^T \tag{9.7}$$

où $\boldsymbol{U}$ et $\boldsymbol{V}$ sont deux matrices orthonormées de tailles respectives $N_y \times N_y$ et $N_{pwi}(N_y+N_a-1)\times N_{pwi}(N_y+N_a-1)$. $\boldsymbol{S}$ est une matrice diagonale qui contient les valeurs singulières σ_i de $\boldsymbol{A}$.

9.3.2 Sur le conditionnement du problème inverse et sur le choix des signaux d'excitation

Dans cette Section est étudié l'impact du bruit d'acquisition sur la qualité d'estimation du vecteur $\boldsymbol{g}_i$. À travers des calculs détaillés, est montré que la qualité d'estimation dépend de la matrice $\boldsymbol{V}\cdot\boldsymbol{S}^{-1}\cdot\boldsymbol{U}^T$. Plus précisément, la relation suivante est donnée, pour fixer les limites de l'erreur d'estimation:

$$\begin{gathered}\frac{1}{K(\boldsymbol{A})}\frac{\|\boldsymbol{b}_i\|_2}{\|{}_S\boldsymbol{y}_i\|_2} \leq \frac{\|\delta\hat{\boldsymbol{g}}_i\|_2}{\|\hat{\boldsymbol{g}}_i\|_2} \leq K(\boldsymbol{A})\frac{\|\boldsymbol{b}_i\|_2}{\|{}_S\boldsymbol{y}_i\|_2} \\ \text{avec: } K(\boldsymbol{A}) = \frac{\sigma_1}{\sigma_{N_y}}\end{gathered} \tag{9.8}$$

où $K(\boldsymbol{A})$ est appelé le conditionnement de la matrice $\boldsymbol{A}$. (9.8) montre que, si le conditionnement de $\boldsymbol{A}$ est très élevé, même pour des petites valeurs du bruit ($\|\boldsymbol{b}_i\|_2 << \|\boldsymbol{y}_i\|_2$), la variation ($\|\delta\hat{\boldsymbol{g}}_i\|_2$) sur la solution estimée ($\hat{\boldsymbol{g}}_i$) peut devenir très importante. Ainsi, pour stabiliser l'estimation par rapport au bruit, on déduit qu'il faut avoir une matrice $\boldsymbol{A}$ avec un petit conditionnement, idéalement, avec $K(\boldsymbol{A}) = 1$.

On démontre ensuite que pour avoir un noyau $\boldsymbol{A}$ avec un faible conditionnement, l'inter-corrélation des N_{pwi} signaux d'excitation doit être très faible. Comme indiqué dans la Section 2.3, la famille de codes pseudo-aléatoires modulés en phase (BPSK) possèdent ces propriétés. Ainsi, en utilisant le conditionnement du noyau $\boldsymbol{A}$, il a été montré que les formes d'onde $a^k(t)$ que doit porter chaque onde plane k doivent être des séquences pseudo-aléatoires modulées en phase. Pour le reste de ce Chapitre, seuls ces types de signaux sont étudiés.

9.3.3 Sur le problème inverse bien posé

Un autre aspect néfaste du modèle direct (9.5) est que le problème inverse associé est sous-déterminé. En d'autres termes: le système contient plus d'inconnues (échantillons dans $\boldsymbol{g}_i$) que d'équations (échantillons dans ${}_S\boldsymbol{y}_i$). En utilisant le noyau de la matrice $\boldsymbol{A}$, dans cette Section est montré que plus il manque d'équations dans (9.5) pire l'estimation $\hat{\boldsymbol{g}}_i$ devient. Pour résoudre ce problème, une hypothèse est introduite sur la capacité de la TRF de générer des échos dans les zones "Blind" et de "Perturbation". Ainsi, en supposant que le milieu est anéchoïque dans les zones "Blind" et de "Perturbation", on démontre que quelle que soit la direction θ^k de l'onde plane, la réponse impulsionnelle $g_i^k(t)$ générée par le milieu est toujours de longueur finie N_g. Ensuite, on en déduit que pour que la matrice $\boldsymbol{A}$ soit carrée, il faut vérifier la relation suivante:

$$(N_g+N_a-1) \geq (N_{pwi}N_g) \Longleftrightarrow N_a \geq (N_{pwi}-1)N_g+1 \tag{9.9}$$

où N_a est la longueur du signal d'excitation $\boldsymbol{a}^k$. Cette relation implique que pour imager des milieux plus profonds, la durée de l'excitation doit augmenter et inversement, pour des milieux moins profonds

les signaux d'excitation peuvent être plus courts.

9.4 Étude du comportement du problème inverse vis-à-vis du bruit

En vérifiant les hypothèses introduites dans les Sections précédentes (1. sur la nature et la longueur des signaux d'excitation, 2. sur l'échogénicité du milieu dans les zones "Blind" et de "Perturbation") ici la qualité d'image reconstruite est étudiée en simulation. Les simulations ont été effectuées avec l'outil Field II [Jensen, 1996, Jensen and Svendsen, 1992]. La sonde LA523E (dont les paramètres sont montrés dans le Tableau 9.1) a été utilisée.

Dans la Fig. 9.5 sont affichés les résultats de l'inversion des données RF bruitées en non-bruitées

Parameter	**Value**
No. des éléments actifs N_{el}	128
Largeur de l'élément w	215 μm
Kerf	30 μm
Pitch $\wp$	245 μm
hauteur $height$	6 mm
Fréquence centrale ν_0	8.5 MHz
Largeur d'ouverture $N_{el}\wp$	3.14 cm
Fréquence d'échantillonnage ν_s	50 MHz

Table 9.1: Spécifications de la sonde LA523E

respectivement. Comme on peut le voir, si aucun traitement supplémentaire n'est pas appliqué à la pseudo-inverse $(\boldsymbol{A}^T\cdot\boldsymbol{A})^{-1}\cdot\boldsymbol{A}^T$, l'estimation ${}_n\hat{\boldsymbol{g}}^1_{64}$ (obtenue à partir des RF bruités) est loin de la référence $\hat{\boldsymbol{g}}^1_{64}$ (obtenue à partir de données RF sans bruit). Comme indiqué précédemment dans la Section 9.3.2, ceci est le résultat de l'amplification du bruit d'acquisition. En fait, la pseudo-orthogonalité des signaux

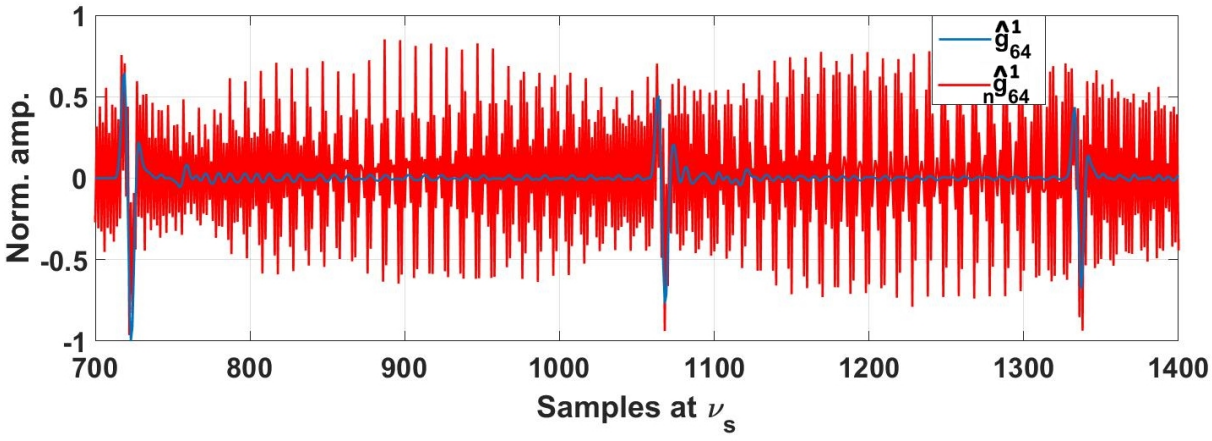

Figure 9.5: Comparaison entre l'estimation $\hat{\boldsymbol{g}}^1_{64}$ (ligne bleue) obtenue à partir des données ${}_S\boldsymbol{y}_{64}$ non-bruitées et estimation ${}_n\hat{\boldsymbol{g}}^1_{64}$ (ligne rouge continue) obtenue à partir des données ${}_S\boldsymbol{y}_{64}$ qui contiennent du bruit ($eSNR = 30dB$).

$\boldsymbol{a}^k$ n'assure pas complètement que $K(\boldsymbol{A}) = 1$, donc une méthode supplémentaire d'amélioration du conditionnement de $\boldsymbol{A}$ est nécessaire. Ainsi, pour encore diminuer le conditionnement de $\boldsymbol{A}$, la méthode implémentée dans cette Section repose sur la troncature des valeurs singulières de $\boldsymbol{A}$. Étant donnée la définition du conditionnement de $\boldsymbol{A}$ (9.8), on peut observer que si la plus petite valeur singulière de $\boldsymbol{A}$ augmente, le conditionnement de la matrice s'améliore. Ceci est réalisé en forçant

dans $\boldsymbol{S}^{-1}$ toutes les valeurs singulières $\sigma_r^{-1} | r \in (r_0..r_{N_y}]$ à être égales à zéro [Quarteroni et al., 2008]:

$$\boldsymbol{S}^{\dagger} = \text{diag}\begin{bmatrix}\sigma_1^{-1} & \sigma_2^{-1} & \cdots & \sigma_{r_0}^{-1} & 0 & \cdots & 0\end{bmatrix} \tag{9.10}$$

Le processus d'annulation des valeurs singulières au-delà d'une valeur arbitraire est appelé troncature des valeurs singulières. Dans ces conditions, le conditionnement du nouveau problème devient $K_{r_0}(\boldsymbol{A}) = \sigma_1/\sigma_{r_0}$ et la pseudo-inverse de $\boldsymbol{A}$ est écrite comme suit:

$$\boldsymbol{A}^{\dagger} = \boldsymbol{V} \cdot \boldsymbol{S}^{\dagger} \cdot \boldsymbol{U}^{T} \tag{9.11}$$

Cependant, dans cette Section est démontré que en ajustant le conditionnement par la troncature des valeurs singulières, une erreur de calcul inversement proportionnelle aux valeurs singulières tronquées est induite. Cette erreur augmente très vite quand les valeurs singulières les plus petites sont tronquées (celles qui permettent de diminuer le plus le conditionnement).

Dans la Fig. 9.6 (a) est affichée l'évolution en fonction du nombre de valeurs singulières tronquées de

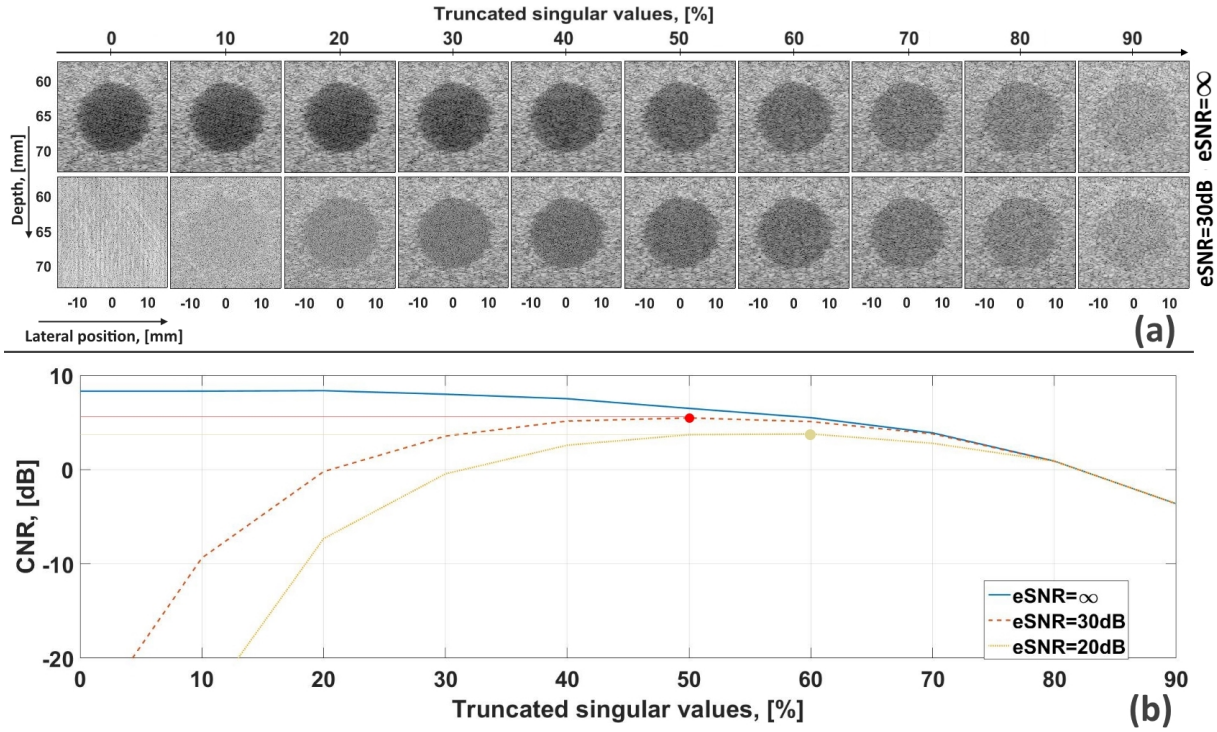

Figure 9.6: (a) - Évolution en fonction du nombre de valeurs singulières tronquées de la qualité des images reconstruites à partir de données RF sans bruit (ligne du haut) et bruitées (ligne en bas, $eSNR = 30dB$). La plage dynamique est de $60dB$. En commençant par la première colonne, où 0% des valeurs singulières sont tronquées, entre deux colonnes consécutives 10% plus de valeurs singulières sont tronquées. (b) - Évolution du CNR (mesuré sur les kystes de (a)) en fonction du nombre des valeurs singulières tronquées. La ligne bleue continue est obtenue lorsque des données RF sans bruit sont utilisées, la ligne rouge non continue est obtenue lorsque des données RF bruitées ($eSNR = 30dB$) sont utilisées. La ligne verte en pointillés est obtenue lorsque des données RF avec un $eSNR$ de $20dB$ sont utilisées.

la qualité des images reconstruites à partir de données RF sans bruit (ligne du haut) et bruitées (ligne en bas, $eSNR = 30dB$) en fonction du nombre de valeurs singulières tronquées. On observe que, dans le cas d'une acquisition sans bruit (ligne du haut), la qualité de l'image se dégrade progressivement avec le nombre des valeurs singulières tronquées. Cependant, sur la courbe obtenue à partir des données RF bruitées, la qualité d'image est optimale pour un certain nombre des valeurs singulières tronquées à partir duquel la qualité se dégrade progressivement. Comme montré dans cette Section,

ceci est l'effet de l'erreur de calcul introduite par la troncature des valeurs singulières. On peut donc en conclure que quel que soit le niveau de bruit à l'intérieur des données RF, il y aura toujours une valeur optimale du nombre de valeurs singulières tronquées qui fournira la meilleure qualité d'image possible. Cependant, comme on peut le déduire de la Fig.9.6(b), la meilleure qualité d'image possible est différente entre deux estimations provenant de jeux de données RF avec différents niveaux de bruit (qualité d'image supérieure obtenue à partir de données RF moins bruitées).

9.5 Comportement du problème inverse par rapport à la cadence d'imagerie

Dans la Section 9.4, il a été démontré que lorsque les hypothèses H3.1 et H3.2 sont vérifiées, la qualité de l'image fournie par l'approche proposée est exactement la même que celle fournie par la méthode conventionnelle (où les signaux d'excitation sont des impulsions courtes). Ainsi, la seule métrique restante permettant de discriminer les deux méthodes est le FAR. Ainsi, dans cette Section, l'évolution de la qualité de l'image (fournie par la méthode proposée) en fonction du gain en FAR fourni est étudiée.

Tout d'abord, on définit le gain en temps d'acquisition τ. τ, fournit par l'émission simultanée d'ondes planes par rapport à l'émission successive conventionnelle est calculé comme suit:

$$\begin{aligned} \tau &= \frac{{}_C t_{rec} - {}_S t_{rec}}{{}_C t_{rec}} \cdot 100\% \\ \text{avec: } {}_C t_{rec} &= N_{pwi}\, {}_{PWI} t_{rec} \end{aligned} \tag{9.12}$$

où ${}_C t_{rec}$ est le temps total nécessaire pour enregistrer tous les échos des ondes planes émises successivement et ${}_{PWI} t_{rec}$ est le temps nécessaire pour enregistrer les échos générés par une onde plane. ${}_S t_{rec}$ est le temps nécessaire pour enregistrer les échos générés lorsque les N_{pwi} ondes planes sont émises simultanément.

Les calculs développés montrent que en ne respectant pas l'hypothèse H3.1, pour le même nombre d'ondes planes N_{pwi}, la méthode proposée peut atteindre des FAR plus élevés que la méthode classique d'acquisition par ondes planes. On en déduit aussi une autre approche pour augmenter le FAR, qui consiste à diminuer la longueur N_a des signaux d'excitation pour la même longueur N_g de la réponse impulsionnelle du milieu (compromettant ainsi l'inégalité $N_a \geq (N_{pwi}-1)N_g+1$). Cependant, en utilisant l'une ou l'autre de ces solution pour l'augmentation du FAR, une zone "Perturbation" ou à la fois une zone "Blind" et une zone de "Perturbation" sont créées, ce qui donne un modèle direct sous-déterminé (qui implique, comme vu dans la Section précédente une qualité d'image dégradée).

Dans la Fig. 9.7 sont montrées les images B-mode obtenues sur une fantôme de résolution et sur une fantôme de kyste. Le schéma d'acquisition est l'émission simultanée des $N_{pwi} = 5$ ondes planes. Fig. 9.7(a) et (b) sont obtenues quand la méthode ne fournit aucun gain en FAR ($\tau = 0\%$). Fig. 9.7(a) et (b) sont obtenues quand la méthode fournit un gain en FAR de 20% ($\tau = 20\%$). Comme prouvé théoriquement, on observe que si $\tau = 0\%$ alors la qualité de l'image fournie est optimale et si $\tau = 20\%$ la qualité de l'image est dégradée. La dégradation est subie que par le CNR et le SNR comme résultat de l'augmentation de la dimension du noyau[2] de la matrice $\boldsymbol{A}$. Cependant, la résolution spatiale fournie par l'approche reste constante. La dégradation de la qualité d'image est encore plus importante si le gain en FAR augmente. Cet effet est montré sur la Fig. 9.7. Ici, on peut voir que, en effet, si aucun gain de temps n'est fourni, la qualité d'image obtenue est similaire avec la référence (méthode classique d'imagerie par onde plane). Cependant, lorsque le gain en temps augmente, la qualité d'image fournie par l'émission simultanée d'ondes planes diminue en raison de la diminution du nombre d'équations par rapport au nombre d'inconnues dans le système.

[2]Ici "le noyau" signifie l'espace créé par les vecteurs dont le produit avec $\boldsymbol{A}$ donne le vecteur nul.

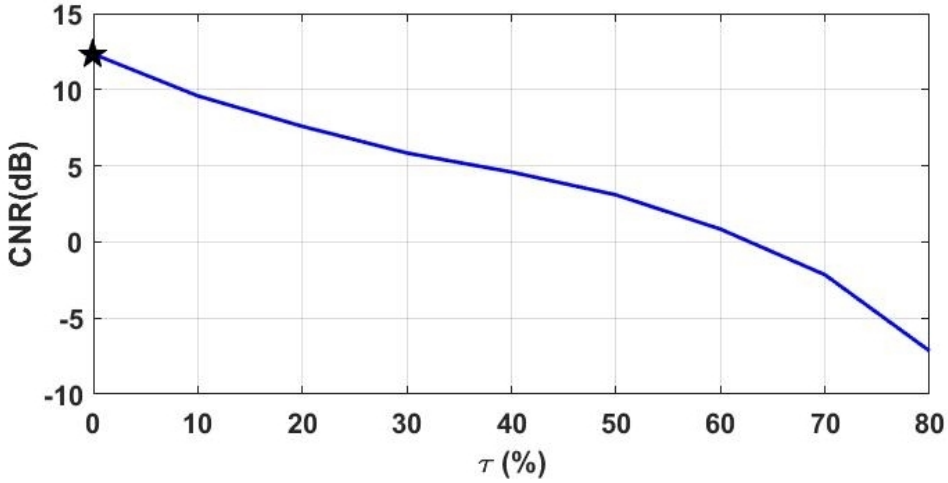

Figure 9.7: Évolution du CNR en fonction du gain de temps τ fourni par l'approche simultanée (ligne bleue pleine). L'étoile représente la valeur du CNR de l'image B-mode du kyste obtenue en utilisant la méthode classique d'imagerie par onde plane.

9.6 Résultats des expériences in vitro

La méthode proposée a également été implémentée sur le scanner de recherche Ula-Op 64. La sonde décrite dans le Tableau 9.1 a été utilisée, mais dans ce cas, seulement $N_{el} = 64$ éléments ont été activés en émission et en réception. Le premier objectif a été d'acquérir des images sur deux types de milieux: fil immergé dans de l'eau (distribution parcimonieuse des diffuseurs) et fantôme kyste (distribution dense des diffuseurs). Le deuxième objectif a été de comparer les résultats obtenus en utilisant deux méthodes: l'imagerie classique (successive) par ondes planes et l'émission simultanée d'ondes planes.

Dans cette Section premièrement est détaille le protocole de l'implémentation d'imagerie ultrasonore par émission simultanée des ondes planes codées. Fig. 9.8(c) montre l'évolution du CNR en fonction du nombre des valeurs singulières tronquées pour les trois images estimées: $k = 1$, $k = 2$ et l'image finale ($\sum_{k=1}^{N_{pwi}=2}$). Comme on peut le voir, les trois courbes présentent des points optimaux ($CNR_{-7^\circ} = 5,6dB$, $CNR_{4^\circ} = 5,3dB$ et $CNR_{final} = 6.02dB$) autour de $r_0 = 1200$ à partir d'un total de $N_y = 2800$ valeurs singulières (43%). L'image finale, obtenue après la troncature du nombre optimal de valeurs singulières, est représentée sur la Fig. 9.8(b). On observe ici que le CNR de l'image obtenue en utilisant l'émission simultanée est inférieur de 1,8dB à celui fourni par l'imagerie conventionnelle par onde plane. Puisque pour cette image (Fig. 9.8(b)) l'hypothèse H3.1 est vérifiée (qui relie les longueurs des différents vecteurs: excitations, réponses impulsionnelles d'écho d'impulsion, données RF), cela signifie qu'aucun gain en temps n'est encore fourni. Cette chute du CNR peut donc être expliquée, comme indiqué dans la Section 9.4, par le fait que les données RF contiennent du bruit d'acquisition (H3.2 non vérifié). C'est pourquoi l'étoile (qui correspond à la valeur du CNR fournie par l'imagerie classique), dans la Fig. 9.8(d), ne correspond pas à la valeur du CNR fournie par la méthode proposée sans gain en termes de cadence d'imagerie (comme opposé à Fig. 9.7, où H3.2 est vérifié). De plus, sur la Fig. 9.8(d), on peut voir que le CNR fourni par la méthode proposée diminue lorsque la valeur du gain en temps augmente. C'est l'effet de l'augmentation de la taille de l'espace nul du modèle direct (Null($\boldsymbol{A}$)) qui a été décrit dans la Sous-section 9.3.3 et dont les effets ont été montrés dans Section 9.5. Par conséquent, on observe ici un comportement similaire entre cette courbe du CNR et celle présentée dans la Fig. 9.7 (chute du CNR lorsque τ augmente).

Fig. 9.9 montre les résultats obtenus après les acquisitions sur le fantôme de résolution. En comparant les deux images finales reconstruites, on observe que la résolution spatiale est améliorée. Cette observation est confirmée par les profils axiaux et latéraux des diffuseurs montrés respectivement dans la Fig. 9.9 (c) et dans la Fig. 9.9 (d). Ici, on mesure une amélioration de 36.31% (de 189μm à

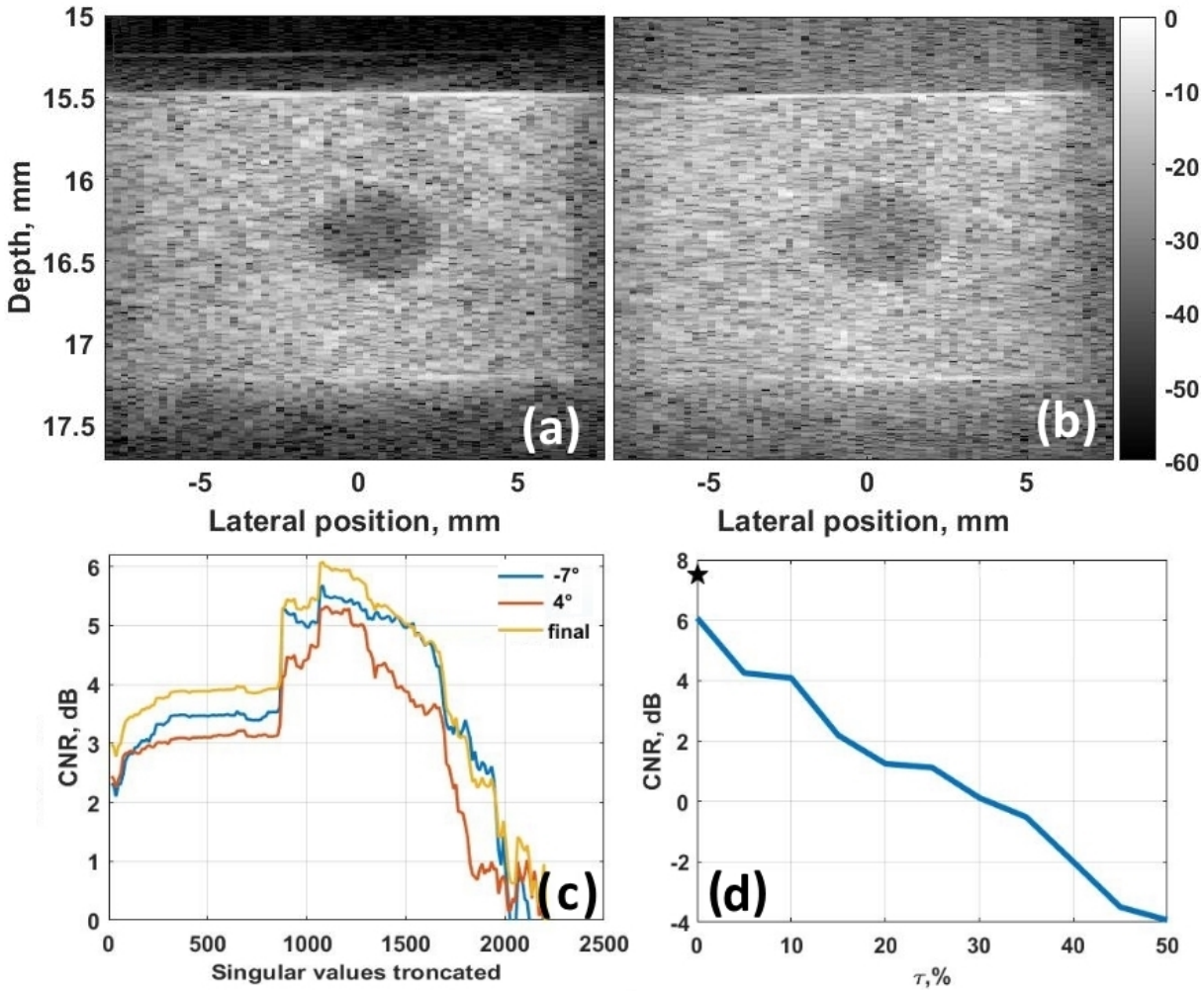

Figure 9.8: Résultats obtenus sur le fantôme du kyste: (a) - Image finale obtenue avec la méthode d'imagerie classique par onde plane, (b) - Image finale (de meilleure qualité) obtenue avec l'émission simultanée des $N_{pwi} = 2$ ondes planes, (c) - Évolution du CNR du kyste en fonction du nombre des valeurs singulières tronquées (d'un total de $N_y = 2800$). Les lignes bleue et rouge représentent l'évolution du CNR sur les images $k = 1$ et $k = 2$ respectivement. La ligne verte représente l'évolution du CNR sur l'image finale. (d) - Èvolution du CNR du kyste en fonction du gain en temps τ (9.12). Le CNR de référence représenté par une étoile est mesuré sur l'image finale obtenue à l'aide des insonifications successives par ondes planes.

120μm) dans la résolution axiale et de 19.75% (de 400μm à 321μm) dans la résolution latérale. Cette amélioration de la résolution spatiale est attendue car, pour pouvoir piloter la sonde à l'aide du Ula-Op 64, le signal le plus court que l'on puisse utiliser dans la méthode d'émission classique est un demi-cycle d'une sinusoïde centrée à $\nu_0 = 8,5MHz$. D'autre part, la méthode proposée (simultanée) estime les réponses impulsionnelles du milieu pour chaque insonification par onde plane, ce qui améliore la résolution spatiale. Enfin, sur la Fig. 9.9(c), on peut voir que le niveau de bruit dans l'image reconstruite est 20dB plus élevé dans le cas où la méthode d'émission simultanée a été utilisée. Comme expliqué dans la Sous-section 9.4, ce bruit est une combinaison du bruit de calcul (ajouté par la troncature des valeurs singulières) et du bruit d'acquisition amplifié (par le conditionnement de la matrice $\boldsymbol{A}$). Néanmoins, comme le montre la Fig. 9.8(c), ce niveau de bruit est le plus bas possible dans ces conditions (signaux d'excitations, bruit d'acquisition).

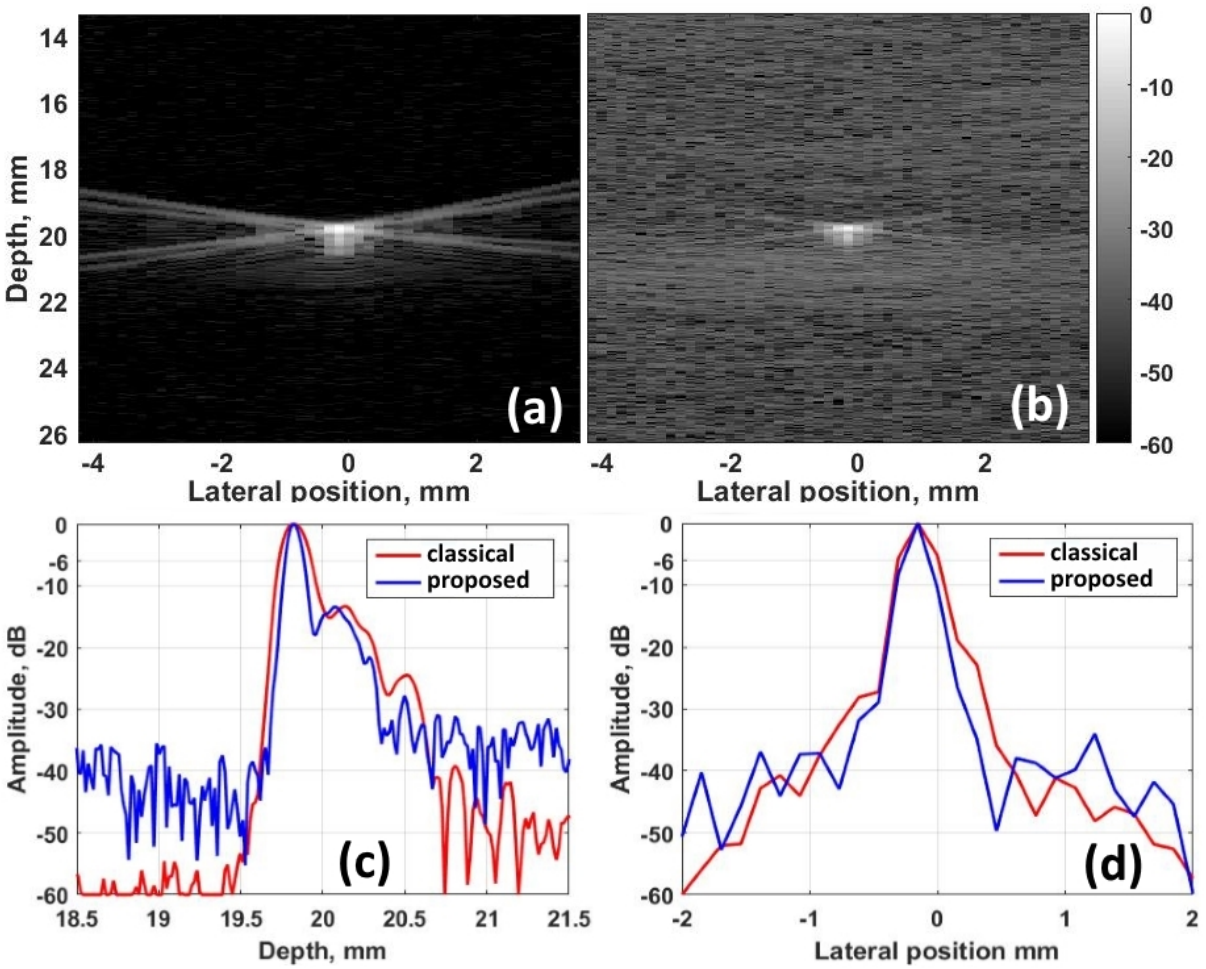

Figure 9.9: Résultats obtenus sur le fantôme fil: (a) - Image finale obtenue par émission successive des deux ondes planes, (b) - Image finale obtenue par émission simultanée des deux ondes planes, (c) - Profils axiaux des diffuseurs reconstruits dans les figures (a) et (b), (d) - Profils latéraux des diffuseurs reconstruits dans les figures (a) et (b).

9.7 Résumé

Dans ce Chapitre, une méthode d'imagerie échographique a été présentée qui utilise l'émission simultanée d'ondes planes. Le modèle mathématique direct des phénomènes de propagation des ondes ultrasonores et d'interaction tissulaire a été fondé en utilisant les principes théoriques exposés dans le Chapitre 8. Les propriétés de la matrice du système ont été étudiées et les hypothèses nécessaires concernant le type / la taille des signaux d'excitation, la taille du milieu imagé et le type / la taille des données RF enregistrées ont été déduites. Il a été démontré que si ces hypothèses sont satisfaites, la qualité d'image obtenue est exactement la même que celle fournie par la technique d'imagerie conventionnelle. Il s'avère que l'une de ces hypothèses implique que, malgré l'émission simultanée, le gain de temps fourni par la méthode proposée est nul par rapport à l'imagerie par onde plane classique. Il a été montré que ces hypothèses peuvent être corrompues, mais que, dans ce cas là, la qualité d'imagerie augmentent en même que le gain en cadence d'acquisition. Même si le choix d'estimer les réponses impulsionnelles du milieu (correspondant à chaque onde plane émise) à l'aide de méthodes basées sur la pseudo-inverse a été effectué, comme le montre l'Annexe C, les termes de régularisation se comportent de la même manière lorsque le gain de temps augmente. Les résultats expérimentaux ont prouvé la faisabilité de la méthode proposée et ont confirmé une fois de plus les considérations théoriques démontrées avec les simulations. En fin de compte, le cadre proposé

reflète clairement le compromis entre la qualité de l'image et la cadence d'acquisition d'images, car la reconstruction d'une image complète à partir de moins des données RF correspond au problème inverse mal posé. Ainsi, un nouveau défi se pose à ce stade: est-il possible d'exprimer les échos générés par chaque onde plane en fonction d'une entité invariante (qui serait très probablement la TRF du milieu)? Cela permettrait en effet d'augmenter le gain de temps (en émettant plus d'ondes planes simultanément) sans augmenter le nombre d'inconnues dans le système (puisque la TRF est constante pour toutes les ondes planes émises simultanément).

10 Imagerie ultrasonore codée: estimation de la TRF

Dans ce Chapitre, une méthode qui permet non seulement d'augmenter la cadence d'acquisition de l'imagerie par onde plane classique, mais également d'améliorer la qualité de l'image fournie est détaillée. Le synopsis de la solution proposée est illustré sur la Fig. 10.1. Comme on peut l'observer dans la Fig. 10.1(a),de manière similaire à la méthode présentée dans le Chapitre précédent, cette approche repose sur l'émission simultanée d'ondes planes. Cependant, en comparant la Fig. 10.1(b) à la Fig. 3.4(b) et la Fig. 3.5, on peut voir que même si les blocs "Wave emission" et "Echo reception" sont similaires pour les deux méthodes, les blocs "Wave Propagation" et "Image Reconstruction" sont beaucoup plus avancés dans cette approche. Tout d'abord, dans le bloc "Wave Propagation", les réponses impulsionnelles ($\boldsymbol{g}_i^k$) du milieu à une onde plane spécifique k sont exprimées analytiquement en fonction de la TRF du milieu $\boldsymbol{\gamma}$ (zone en pointillés sur la Fig. 10.1(b)). Cette modification dans le bloc "Wave propagation" implique également quelques modifications dans le module "Image reconstruction". Par conséquent, pour résoudre le problème inhérent au mélange des échos en réception, ici on utilise les filtres $\boldsymbol{f}^k$ (correspondant à chaque signal d'excitation $\boldsymbol{a}^k$). Tous les échos filtrés $\hat{\boldsymbol{g}}_i^k$ sont alors utilisés comme entrée pour une approche "problème inverse" qui fournit en sortie une estimation de la TRF ($\hat{\boldsymbol{\gamma}}$). Ce Chapitre est organisé comme suit. Tout d'abord, la raison pour laquelle ce travail est nécessaire et comment il pourrait améliorer la méthode décrite dans le Chapitre précédent est présentée. Ensuite, en se basant sur la théorie de la propagation des ondes ultrasonores décrite au Chapitre 2, on construit un modèle mathématique linéaire du signal reçu par un transducteur ponctuel dans un milieu lorsqu'un autre transducteur ponctuel émet un signal. Ensuite, le modèle établi est discrétisé afin de permettre une représentation matricielle du phénomène de propagation. De plus, ce modèle est adapté pour prendre en compte les paramètres d'une sonde ultrasonore quelconque. Ensuite, une expression générale du modèle de propagation qui peut être appliqué à différents schémas d'acquisition (utilisant différentes sondes) est donnée. La méthode est adaptée afin de modéliser les échos rétro-diffusés obtenus à l'aide de l'émission par onde plane. Ensuite, une technique de codage permettant l'émission simultanée des ondes planes est proposée. Le modèle direct est par conséquent adapté. Enfin, pour obtenir une estimation de la TRF, une approche par problème inverse est appliquée au modèle direct construit. Des résultats sont présentés et discutés.

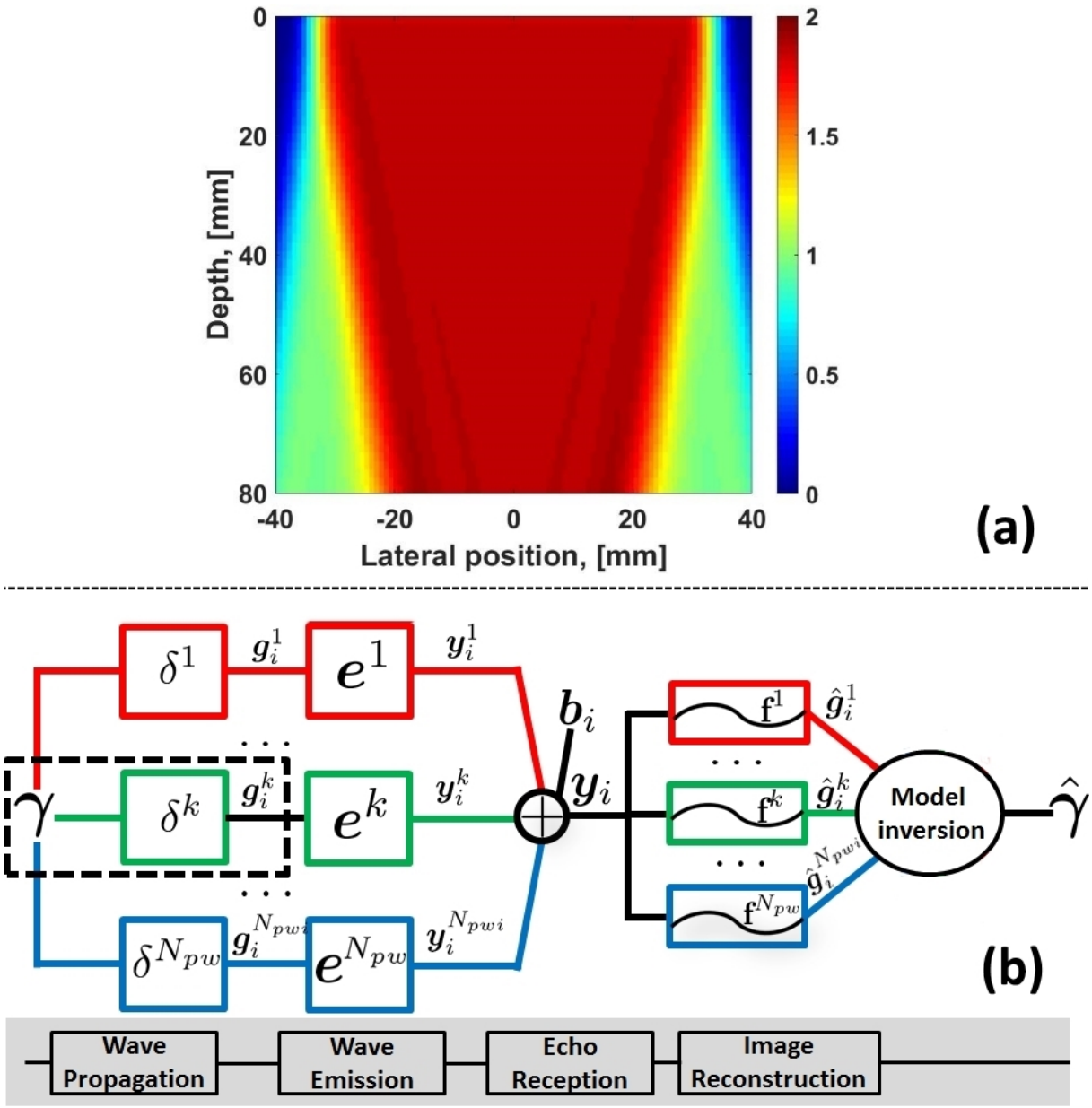

Figure 10.1: Représentation du schéma d'émission proposé: (a) - La moyenne quadratique du champ de pression généré par le schéma d'émission proposé. (b) - Représentation schématique de l'approche d'imagerie proposée (AMCUS). $\boldsymbol{\gamma}$ - la TRF, δ^k - courte excitation électrique utilisée pour l'onde k, $\boldsymbol{g}_i^k$ - échos reçus correspondant à l'émission de δ^k (onde k), $\boldsymbol{a}^k$ - code porté par l'onde k, $\boldsymbol{y}^k$ - échos reçus après émission de $\boldsymbol{a}^k$, $\boldsymbol{y}_i$ - échos enregistrés lorsque les N_{pwi} ondes planes sont émises simultanément, $\boldsymbol{f}^k$ - filtre de compression optimal correspondant à l'onde k, $\hat{\boldsymbol{g}}_i^k$ - estimation de $\boldsymbol{g}_i^k$ obtenue à partir de $\boldsymbol{y}_i$. Enfin, une estimation $\hat{\boldsymbol{\gamma}}$, de la TRF $\boldsymbol{\gamma}$ est obtenue en résolvant le problème inverse. Les blocs "Wave emission" et "Wave Propagation" ont été inter-changés pour faciliter la représentation schématique.

10.1 Sur la nécessité d'un modèle direct avancé

Dans cette Section, une simulation simple est développée afin de mieux comprendre les limites de la méthode proposée dans le Chapitre précédent. En outre, une expérience de pensée est proposée dont le but est de clarifier comment cette méthode peut être améliorée afin de fournir à la fois une cadence d'acquisition plus rapide et une meilleure qualité d'image.

Les résultats obtenus à l'aide de la simulation montrent que pour des angles différents, la réponse

impulsionnelle du milieu change significativement, ce qui signifie que dans le vecteur total $\boldsymbol{g}_i$ aucune régularisation particulière ne peut pas être trouvée (tels que des segments répétés) qui permettraient de diminuer le nombre d'inconnues. De plus, on observe que même pour un angle d'émission constant, les réponses impulsionnelles vues par des éléments i différents de la sonde changent. Cela annule une autre possibilité qui pourrait améliorer le fait que le problème inverse soit mal posé. Une telle solution consisterait dans la concaténation des signaux ${}_S\boldsymbol{y}_i$ reçus par des différents éléments i afin d'augmenter le nombre total d'équations dans le système.

À ce stade, une expérience de pensée simple est proposée. Pour commencer, on considère une émission d'une seule onde plane k. Après, on suppose l'existence d'un vecteur $\boldsymbol{\chi}$ qui permettrait la formulation suivante:

$$\boldsymbol{y}_i^k = \boldsymbol{A}^k \cdot \boldsymbol{C}_i^k \cdot \boldsymbol{\chi} + \boldsymbol{b}_i, \, \forall i \in [1..N_{el}] \tag{10.1}$$

où $\boldsymbol{y}_i^k$ sont les signaux reçus par l'élément i de la sonde acoustique lorsque l'onde plane k est émise. Dans (10.1), la matrice $\boldsymbol{C}_i^k$ relie $\boldsymbol{\chi}$ à $\boldsymbol{g}_i^k$ par la relation suivante: $\boldsymbol{g}_i^k = \boldsymbol{C}_i^k \cdot \boldsymbol{\chi}$. Car on ne peut pas être sûr que le problème inverse basé sur (10.1) est bien posé, comme le vecteur $\boldsymbol{\chi}$ est constant pour tous les éléments i, on pourrait concaténer tous les systèmes directs donnés par les N_{el} éléments récepteurs afin d'augmenter le nombre total d'équations d'un facteur N_{el}, pour le même nombre d'inconnues (donné par la taille du vecteur $\boldsymbol{\chi}$).

En effet, un modèle direct tel que (10.1) pourrait améliorer de manière significative le problème inverse dans le contexte de la modélisation de la propagation des ondes planes. Cependant, à ce stade, plusieurs questions supplémentaires doivent être posées: Qu'est-c'est le vecteur $\boldsymbol{\chi}$? Comment on peut calculer les matrices $\boldsymbol{C}_i^k$? Est-ce suffisant, seulement avec la concaténation des N_{el} systèmes linéaires d'obtenir un problème inverse bien posé? Dans les Sections suivantes de ce Chapitre, une réponse à chacune de ces questions est soigneusement élaborée.

10.2 Sur le vecteur χ

Ici, l'idée principale est de trouver un vecteur approprié $\boldsymbol{\chi}$ qui permettra d'écrire chaque réponse impulsionnelle du milieu à une insonification sous forme du produit matriciel suivant:

$$\boldsymbol{g}_i^k = \boldsymbol{C}_i^k \cdot \boldsymbol{\chi}, \, \forall i \in [1..N_{el}] \tag{10.2}$$

En s'appuyant sur le cadre théorique développé dans le Chapitre 2, ici on démontre que la réponse impulsionnelle du milieu quand l'élément j émet et l'élément i reçoit s'écrit comme suit:

$$g_{ji}(t) = (\mathsf{C}_{ji}\gamma)(t)$$

$$\text{avec: } \begin{cases} (\mathsf{C}_{ji}\gamma)(t) = \displaystyle\int_V \gamma(\vec{r}) \Big[g_j(\vec{r},t) *_t g_i(\vec{r},t) \Big] \, \mathrm{d}^2\vec{r} \\ g_j(\vec{r},t) = \displaystyle\int_S \frac{1}{2\pi \|\vec{r} - \vec{r}_j - \vec{r}_S\|_2} \delta\Big(t - t_j - \frac{\|\vec{r} - \vec{r}_j - \vec{r}_S\|_2}{c_m} \Big) \, \mathrm{d}^2\vec{r}_S \\ g_i(\vec{r},t) = \displaystyle\int_S \frac{1}{2\pi \|\vec{r} - \vec{r}_i - \vec{r}_S\|_2} \delta\Big(t - \frac{\|\vec{r} - \vec{r}_i - \vec{r}_S\|_2}{c_m} \Big) \, \mathrm{d}^2\vec{r}_S \end{cases} \tag{10.3}$$

où C_{ji} est un opérateur intégral qui représente la réponse impulsionnelle spatiale de la paire d'éléments (j,i) à chaque point $\vec{r}$ du milieu. $g_j(\vec{r},t)$ et $g_i(\vec{r},t)$ sont les réponses impulsionnelles de la paire (j,i) au point $\vec{r}$ du milieu. On observe que les expressions (10.3) et (10.2) sont très similaires, la seule différence étant que l'un est dans le domaine temporel continu et la seconde est dans le domaine temporel discret. On en conclut que dans (10.1) et (10.2) le vecteur $\boldsymbol{\chi}$ peut être remplacé par une

version discrète de la TRF $\boldsymbol{\gamma}$. De plus, on observe que la matrice $\boldsymbol{C}_{ji}$ n'est rien d'autre qu'une version discrète de l'opérateur intégral C_{ji}.

10.3 Sur l'approximation du champ lointain

Dans cette Section, est révisée l'hypothèse de propagation en champ lointain de l'onde ultrasonore introduite dans la Sous-section 2.2.1.

À travers des calculs théoriques, vérifiés en simulation, on démontre que l'hypothèse de propagation de l'onde acoustique en champ lointain ne permet pas de modéliser précisément les échos reçus. On démontre que la réponse impulsionnelle de la paire (j,i) au point $\vec{r}$ modélisée comme suit n'est pas assez précise:

$$g_{ji}(\vec{r},t) = g_j(\vec{r},t) *_t g_i(\vec{r},t) \underset{\text{champ lointain}}{\approx} \frac{S^2\delta\left(t-t_j-\frac{\|\vec{r}-\vec{r}_j\|_2+\|\vec{r}-\vec{r}_i\|_2}{c_m}\right)}{4\pi^2\|\vec{r}-\vec{r}_j\|_2\|\vec{r}-\vec{r}_i\|_2} \tag{10.4}$$

Pour mieux approximer les signaux RF, on propose de modéliser le principe de Huygens - Fresnel qui est présent en émission et en réception sur les surfaces des éléments j et i. Ainsi, on introduit le concept des sources ponctuelles (v,u) disposées sur les surfaces des éléments (j,i). Après, on écrit leur réponses spatiales comme suit:

$$\begin{cases} g_u(\vec{r},t) = \dfrac{\delta\left(t-t_u-\frac{\|\vec{r}-\vec{r}_u\|_2}{c_m}\right)}{2\pi\|\vec{r}-\vec{r}_u\|_2} \\ g_v(\vec{r},t) = \dfrac{\delta\left(t-\frac{\|\vec{r}-\vec{r}_v\|_2}{c_m}\right)}{2\pi\|\vec{r}-\vec{r}_v\|_2} \\ g_{uv}(\vec{r},t) = g_u(\vec{r},t) *_t g_v(\vec{r},t) = \dfrac{\delta\left(t-t_j-\frac{\|\vec{r}-\vec{r}_u\|_2+\|\vec{r}-\vec{r}_v\|_2}{c_m}\right)}{4\pi^2\|\vec{r}-\vec{r}_u\|_2\|\vec{r}-\vec{r}_v\|_2} \end{cases} \tag{10.5}$$

où $\vec{r}_u$ et $\vec{r}_v$ sont les positions des points (u,v) sur les surfaces S_j (élément d'émission j) et S_i (élément de réception i) respectivement. Or, le signal reçu par i peut être vu comme une somme continue de tous les signaux reçus par chaque récepteur ponctuel v, qui reçoit respectivement la somme continue de tous les signaux émis par chaque source ponctuelle u. Ceci permet de modéliser le principe de Huygens - Fresnel et d'écrire $g_{ji}(\vec{r},t)$ sous la forme:

$$\begin{aligned} g_{ji}(\vec{r},t) &= \int_{S_j}\int_{S_i}\Big[g_u(\vec{r},t) *_t g_v(\vec{r},t)\Big]\,\mathrm{d}\vec{r}_v\,\mathrm{d}\vec{r}_u \iff \\ g_{ji}(\vec{r},t) &= \int_{S_j}\int_{S_i}\left[\frac{\delta\left(t-t_j-\frac{\|\vec{r}-\vec{r}_u\|_2+\|\vec{r}-\vec{r}_v\|_2}{c_m}\right)}{4\pi^2\|\vec{r}-\vec{r}_u\|_2\|\vec{r}-\vec{r}_v\|_2}\right]\mathrm{d}\vec{r}_v\,\mathrm{d}\vec{r}_u \end{aligned} \tag{10.6}$$

10.4 Sur le calcul de la matrice $\boldsymbol{C}_{ji}$

Dans cette Section, le calcul de la matrice $\boldsymbol{C}_{ji}$ est adressé. Cependant, comme cela a été déduit dans la Section précédente, la réponse impulsionnelle du milieu à la paire d'éléments (j,i) peut être vue comme une superposition des réponses impulsionnelles des sources ponctuelles (u,v). Ainsi, pour calculer $\boldsymbol{C}_{ji}$, on commence par le calcul de la matrice $\boldsymbol{C}_{uv}$ (ce qui permet de modéliser la réponse impulsionnelle du milieu lorsque la source ponctuelle u émet une onde ultrasonore ($u \in S_j$) et que la source ponctuelle v reçoit ($v \in S_i$) ses échos).

10.4.1 Calcul de la matrice C_{uv}

Dans la Section précédente, la relation (10.5) pour les réponses impulsionnelles spatiales des transducteurs ponctuels u et v dans un point $\vec{r}$ ont été déduites ($g_u(\vec{r},t)$ et $g_v(\vec{r},t)$ respectivement). Ainsi, en appliquant (10.3) à (10.5), on obtient l'expression suivante:

$$\begin{aligned} g_{uv}(t) &= (\mathsf{C}_{uv}\gamma)(t) \\ \text{avec: } \mathsf{C}_{uv} &= \int_V \Big[g_u(\vec{r},t) *_t g_v(\vec{r},t) \Big] \mathrm{d}^2\vec{r} \end{aligned} \tag{10.7}$$

où $g_{uv}(t)$ représente la réponse impulsionnelle du milieu lorsque u émet et que v reçoit. C_{uv}, similaire à C_{ji}, est un opérateur intégral qui représente la réponse impulsionnelle spatiale de la paire des transducteurs ponctuels (u,v) à chaque point $\vec{r}$ du milieu. Comme indiqué dans la Section 10.2, la matrice $\boldsymbol{C}_{uv}$ représente la version discrète de l'opérateur C_{uv}. Une question essentielle se pose à cette étape: "Comment discrétiser l'opérateur intégral C_{uv}?". Comme il a été montré dans le Chapitre 2, les réponses impulsionnelles du milieu à l'émission / réception par la paire d'éléments (j,i) sont discrétisées à la fréquence d'échantillonnage ν_s. Ceci implique que la réponse impulsionnelle du milieu à l'émission / réception par la paire de transducteurs ponctuels (u,v) est également échantillonnée à la fréquence ν_s. Cependant, pour le domaine $\gamma(\vec{r})$, aucune discrétisation n'apparaît naturellement. Dans la suite de cette Section, le choix de la discrétisation du milieu est abordé, mais pour le moment est supposée une discrétisation par pas Δx et Δz dans les directions $\vec{x}$ et $\vec{z}$ respectivement. Suite à cette discrétisation du milieu, une grille bidimensionnelle $\boldsymbol{\Omega}$ de taille $N_z \times N_x$ est obtenue. On peut donc en conclure que le domaine discret $\boldsymbol{\Omega}$ ne contient que $N_x \times N_z$ entrées $\boldsymbol{r} = (x_{\boldsymbol{\Omega}}, 0, z_{\boldsymbol{\Omega}}) \in \boldsymbol{\Omega}$. Par conséquent, la contrepartie discrète de TRF $\gamma(\vec{r})$ est vue comme un vecteur $\boldsymbol{\gamma}$ où chacune de ses entrées m représente le coefficient de réflexion acoustique du tissus au nœud $\boldsymbol{r}$ de la grille $\boldsymbol{\Omega}$ défini par:

$$m = \Big\lfloor \frac{x_{\boldsymbol{\Omega}}}{N_x \Delta x} \Big\rfloor N_z + \frac{z_{\boldsymbol{\Omega}}}{\Delta z} \tag{10.8}$$

Utilisant la grille $\boldsymbol{\Omega}$, dans cette Section on développe les calculs qui permettent d'arriver a la relation suivante pour le calcul des matrice $\boldsymbol{C}_{ji}$:

$$\boldsymbol{C}_{uv}[n,m] = \begin{cases} \frac{\alpha}{4\pi^2 \|\boldsymbol{r}-\vec{r}_u\|_2 \|\boldsymbol{r}-\vec{r}_v\|_2}, \text{ si } \left\lfloor \frac{\|\boldsymbol{r}-\vec{r}_u\|_2 + \|\boldsymbol{r}-\vec{r}_v\|_2}{c_m} \right\rfloor = t_0 + \frac{n}{\nu_s} \\ \frac{\beta}{4\pi^2 \|\boldsymbol{r}-\vec{r}_u\|_2 \|\boldsymbol{r}-\vec{r}_v\|_2}, \text{ si } \left\lceil \frac{\|\boldsymbol{r}-\vec{r}_u\|_2 + \|\boldsymbol{r}-\vec{r}_v\|_2}{c_m} \right\rceil = t_0 + \frac{n}{\nu_s} \\ 0, \text{ ailleurs} \end{cases} \tag{10.9}$$

où n est l'index de la ligne et m est l'index de la colonne. t_0 est le temps de début de sauvegarde des signaux RF. α et β sont deux coefficients dont la formule de calcul est présentée dans cette Section. Les résultats de l'implémentation de cette méthode montrent que la modélisation des signaux reçus à l'aide de (10.9) permet d'atteindre une erreur de modélisation dont l'énergie est $24dB$ plus petite que l'énergie du signal attendu.

10.4.2 Sur la discrétisation du milieu

Dans la Sous-section précédente, une méthode de calcul de la matrice $\boldsymbol{C}_{uv}$ a été déduite. Cependant, l'impact de la discrétisation du milieu sur la précision de la reconstruction n'a pas été étudié. Ici, l'impact de la taille de la partition du milieu sur l'erreur de modélisation est résolu.

Dans la Fig. 10.2 est représenté un nœud $\boldsymbol{r}$ de grille $\boldsymbol{\Omega}$, qui génère un écho qui arrive à l'échantillon

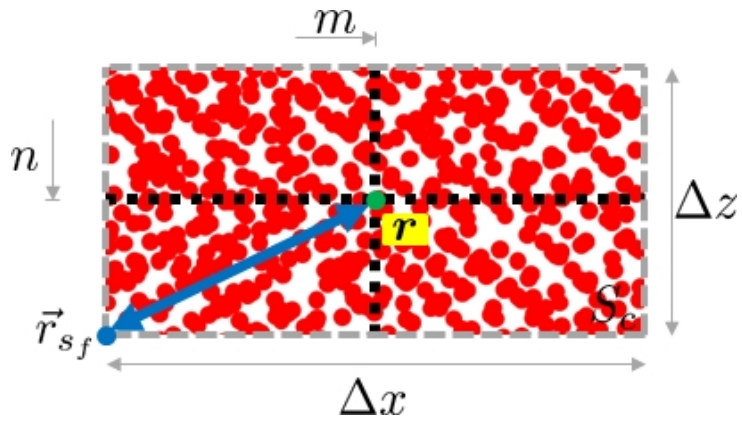

Figure 10.2: Zoom sur une cellule de $\boldsymbol{\Omega}$ (de surface finie $S_{c_{[n,m]}}$) centrée autour du nœud $[n,m]$ de la grille. La colonne m est calculée en utilisant (10.8) et n est l'échantillon du temps auquel l'écho généré dans $\boldsymbol{r}$ arrive à v lorsque u émet. Δz et Δx sont les pas de discrétisation axial et latéral du milieu imagé. $\vec{r}_{s_f} \in S_{c_{[n,m]}}$ est la position du diffuseur le plus distant de $\boldsymbol{r}$. Lors de la modélisation, $\vec{r}_{s_f}$ est approximé avec $\boldsymbol{r}$.

de temps n dans $\boldsymbol{g}_{uv}$. Puisque tout le milieu est échantillonné avec les mêmes pas $(\Delta x, \Delta z)$, chaque nœud de la grille $[n,m]$ (m calculé à partir de $\boldsymbol{r}$ en utilisant (10.8)) est entouré d'une cellule rectangulaire de taille Δz et Δx respectivement dans les directions axiale et latérale. Cette cellule, représentée par une ligne pointillée grise sur la Fig. 10.2, a une surface $S_{c_{[n,m]}} = \Delta z \Delta x$ constante pour tous les nœuds $[n,m]$.

Ici on montre que tous les diffuseurs qui se trouvent à des positions aléatoires $\vec{r} \in S_{c_{[n,m]}}$ (représentes en rouge dans la Fig.10.2) ont leurs échos approximés par l'écho du nœud central de la cellule $[n,m]$. On en déduit que $g_{uv}(t)$ est modélisé par sa version discrétisé $\boldsymbol{g}_{uv}(t)$. Les deux expressions obtenues sont:

$$\begin{aligned} g_{uv}(t) &= \frac{\delta\left(t - \frac{\|\vec{r}-\vec{r}_u\|_2 + \|\vec{r}-\vec{r}_v\|_2}{c_m}\right)}{4\pi^2 \|\vec{r}-\vec{r}_u\|_2 \|\vec{r}-\vec{r}_v\|_2} \gamma(\vec{r}) \\ \boldsymbol{g}_{uv} &= \frac{\delta\left(t - \frac{\|\boldsymbol{r}-\vec{r}_u\|_2 + \|\boldsymbol{r}-\vec{r}_v\|_2}{c_m}\right)}{4\pi^2 \|\boldsymbol{r}-\vec{r}_u\|_2 \|\boldsymbol{r}-\vec{r}_v\|_2} \boldsymbol{\gamma}[m] \end{aligned} \tag{10.10}$$

En comparant la réponse impulsionnelle continue $g_{uv}(t)$ et sa version discrète dans (10.10), on peut en déduire que l'erreur faite par cette approximation a un effet similaire à celui montré dans la Sous-section 10.4.1. En d'autres termes, en partitionnant le milieu, les échos générés par les points $\vec{r}$ qui ne tombent pas directement sur un nœud $\boldsymbol{r}$ de grille sont modélisés avec une petite erreur due au décalage entre le temps d'arrivée de l'écho généré dans $\vec{r}$ et celui d'écho généré dans $\boldsymbol{r}$. On déduit que le décalage temporel maximal est:

$$t_{\vec{r}_f \longrightarrow \boldsymbol{r}} = \frac{2\sqrt{(\Delta z/2)^2 + (\Delta x/2)^2}}{c_m} = \frac{\sqrt{(\Delta z)^2 + (\Delta x)^2}}{c_m} \tag{10.11}$$

De (10.11) on déduit que la plus petite erreur de modélisation est obtenue quand $\Delta x \longrightarrow 0$ et $\Delta z \longrightarrow 0$. Cependant, avoir des tels petits pas de discrétisation du milieu implique que le nombre d'inconnues dans le problème est grand et aussi que les tailles des matrices impliquées explosent. Ainsi, afin de maintenir raisonnable le nombre d'inconnues et la taille des matrices impliquées, il a été décidé dans ce travail de fixer les pas de discrétisation aux valeurs suivantes:

$$\Delta z = \frac{c_m}{\nu_s} \quad \text{and:} \quad \Delta x = 3\Delta z = \frac{3c_m}{\nu_s} \tag{10.12}$$

10.4.3 Sur la discrétisation des éléments de la sonde

Dans les Sections 10.2 et 10.3, il a été montré que le principe de Huygens-Fresnel peut être utilisé pour modéliser la réponse impulsionnelle du milieu lorsqu'un élément de sonde émet et qu'un autre reçoit les échos. Jusqu'à présent, dans cette Section, on a déduit les relations continues et discrètes qui permettent de relier les échos rétro-diffusés à la TRF dans le cas de transducteurs ponctuels. Ici, ces concepts sont combinés. L'objectif est d'obtenir une relation continue et sa version discrète permettant de modéliser les signaux reçus dans le cas où un élément de la sonde émet une onde ultrasonore et qu'un autre élément de la sonde reçoit ses échos rétro-diffusés.

On déduit que le signal reçu par j quand i émet peut être écrit comme suit:

$$\begin{aligned} y_{ji}(t) &= e(t) *_t \left(\mathsf{C}_{ji}\gamma\right)(t) \\ \text{avec: } \mathsf{C}_{ji} &= \int_{S_j}\int_{S_i} \mathsf{C}_{uv}\, \mathrm{d}\vec{r}_i\, \mathrm{d}\vec{r}_j \end{aligned} \tag{10.13}$$

En termes simples, cette relation modélise le principe de Huygens-Fresnel dans les domaines continu de temps et d'espace. Pour discrétiser (10.13), on propose la solution illustrée dans la Fig. 10.3. Comme

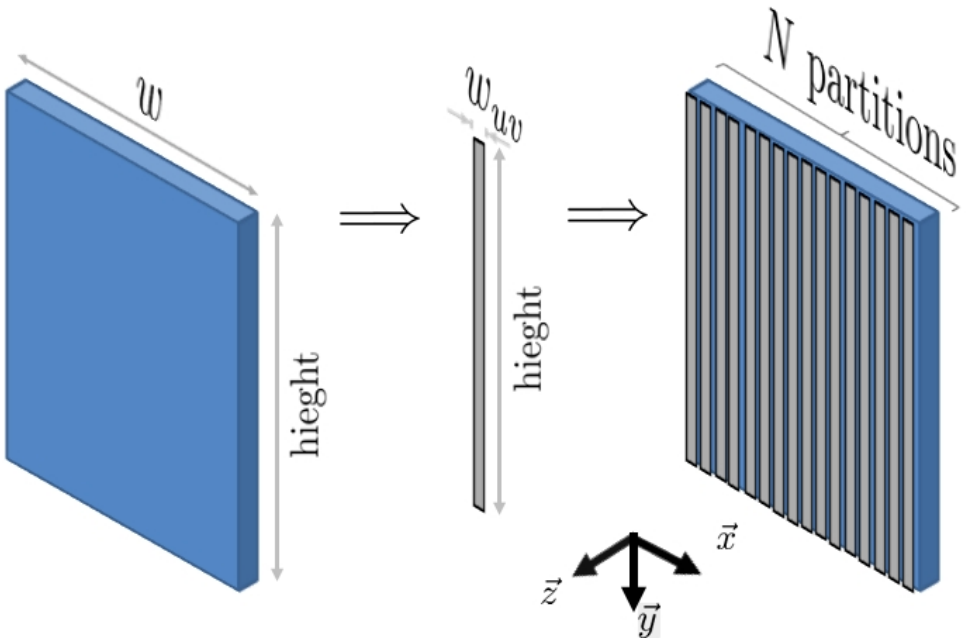

Figure 10.3: Représentation schématique de la discrétisation d'un élément de la sonde. Sur le côté gauche de l'image est représenté un élément de largeur w et de hauteur $height$ dont la surface est S. Au centre de l'image est représentée une petite partition de largeur w_{uv} et de hauteur $height$ dont la surface vaut S_{uv}. Enfin, dans la partie gauche de l'image, on voit comment la surface S de l'élément est divisée en $N = w/w_{uv}$ partitions plus petites de surface S_{uv}.

on peut le voir ici, l'approche proposée consiste à séparer la surface totale S de chaque élément en partitions plus petites de surface S_{uv}. Ainsi, en divisant chaque élément en N partitions plus petites de largeur w_{uv} et de hauteur $height$, on traite chaque subdivision générée comme un transducteur ponctuel indépendant actif en émission / réception. Pour le signal reçu par l'élément i quand j émet,

la relation suivante est obtenue:

$$\begin{gathered} \boldsymbol{y}_{ji} = \boldsymbol{e} * \boldsymbol{C}_{ji}\boldsymbol{\gamma} = \boldsymbol{e} * \left[\sum_{v=1}^{N} \sum_{u=1}^{N} \boldsymbol{C}_{uv}\boldsymbol{\gamma} \right] \\ \text{avec: } \boldsymbol{C}_{ji} = \sum_{v=1}^{N} \sum_{u=1}^{N} \boldsymbol{C}_{uv} \end{gathered} \tag{10.14}$$

Dans cette Sous-section est présenté aussi une étude qui permet de trouver la taille optimale w_{uv} de la partition des éléments:

$$w_{uv} \leq \frac{c_m}{2v_s} \tag{10.15}$$

(10.14) ainsi que le pas de partition (10.15) permettant de modéliser le signal reçu avec une erreur dont l'énergie est $24dB$ plus petite que l'énergie des échos générés.

10.5 Sur le calcul de la matrice C_i

Pour résumer les Sections précédentes, un cadre théorique a été développé qui permet d'écrire les échos rétro-diffusés enregistrés par l'élément i lorsque j émet:

$$\mathbf{y}_{ji} = \boldsymbol{e} * \left[\sum_{v=1}^{N} \sum_{u=1}^{N} \boldsymbol{C}_{uv}\boldsymbol{\gamma} \right] = \boldsymbol{E} \cdot \boldsymbol{C}_{ji} \cdot \boldsymbol{\gamma}$$

$$\text{avec: } \begin{cases} \boldsymbol{C}_{ji} = \displaystyle\sum_{v=1}^{N} \sum_{u=1}^{N} \boldsymbol{C}_{uv} \\ \boldsymbol{E} = \begin{bmatrix} \boldsymbol{e}[N_e-1] & \boldsymbol{e}[N_e-2] & \cdots & \boldsymbol{e}[0] & 0 & \cdots & 0 & 0 & \cdots & 0 \\ 0 & \boldsymbol{e}[N_e-1] & \cdots & \boldsymbol{e}[1] & \boldsymbol{e}[0] & \cdots & 0 & 0 & \cdots & 0 \\ \vdots & \vdots & \ddots & \vdots & \vdots & \ddots & \vdots & \vdots & \ddots & \vdots \\ 0 & 0 & \cdots & \boldsymbol{e}[N_e-1] & \boldsymbol{e}[N_e-2] & \ddots & \boldsymbol{e}[0] & 0 & \cdots & 0 \\ 0 & 0 & \cdots & 0 & \boldsymbol{e}[N_e-1] & \ddots & \boldsymbol{e}[1] & \boldsymbol{e}[0] & \cdots & 0 \\ \vdots & \vdots & \ddots & \vdots & \vdots & \ddots & \vdots & \vdots & \ddots & \vdots \\ 0 & 0 & \cdots & 0 & 0 & \ddots & \boldsymbol{e}[N_e-1] & \boldsymbol{e}[N_e-2] & \cdots & \boldsymbol{e}[0] \end{bmatrix} \end{cases} \tag{10.16}$$

où la matrice de Toeplitz $\boldsymbol{E}$ est construite en utilisant la forme typique d'onde de l'écho $\boldsymbol{e} = \boldsymbol{a} * \boldsymbol{h} * \boldsymbol{h}$ et $\boldsymbol{C}_{ji}$ est une matrice qui modélise la propagation aller / retour de l'onde à l'intérieur du milieu. Ici, (10.16) est utilisé comme un bloc de construction pour modéliser le signal $\boldsymbol{y}_i^k$ enregistré par un élément de la sonde lorsque tous les N_{el} éléments de la sonde sont actifs en émission. La relation suivante est obtenue:

$$\begin{gathered} \boldsymbol{y}_i^k = w_i \sum_{j=1}^{N_{el}} w_j \boldsymbol{y}_{ji}^k + \boldsymbol{b}_i = \boldsymbol{E}^k \cdot \boldsymbol{g}_i^k + \boldsymbol{b}_i \underset{\text{Avec 10.16}}{=} \boldsymbol{E}^k \cdot \boldsymbol{C}_i^k \cdot \boldsymbol{\gamma} + \boldsymbol{b}_i \\ \text{où: } \boldsymbol{C}_i^k = w_i \sum_{j=1}^{N_{el}} w_j \boldsymbol{C}_{ji}^k = w_i \sum_{j=1}^{N_{el}} w_j \sum_{v=1}^{N} \sum_{u=1}^{N} \boldsymbol{C}_{uv}^k \end{gathered} \tag{10.17}$$

où w_j et w_i sont respectivement les fenêtres d'apodisation d'émission et de réception. En termes simples, la relation précédente représente l'expression mathématique des branches de même couleur impliquées dans les blocs "Propagation des ondes" et "Emission d'onde" de la Fig. 10.1(b).

Dans la Fig. 10.4 est donné un exemple des données RF obtenues quand le milieu insonifié contient

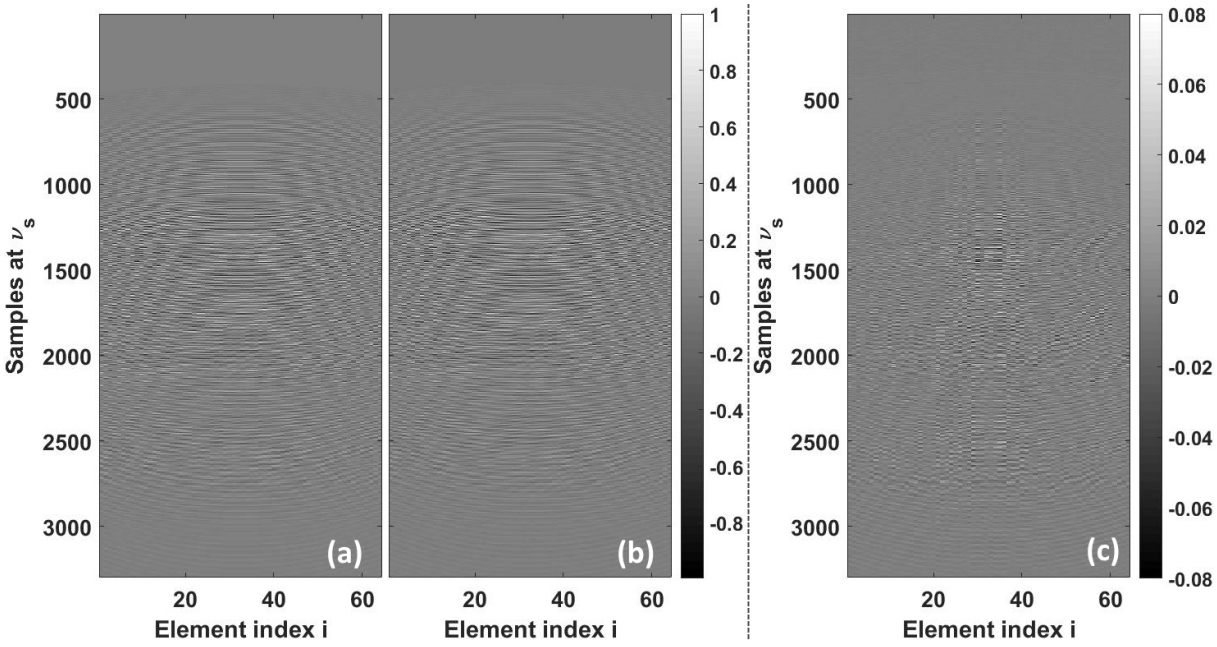

Figure 10.4: Résultats obtenus sur un milieu avec une densité faible des diffuseurs. (a) - Données RF obtenues avec Field II: $\boldsymbol{y}_i^k$. (b) - Données RF obtenues avec le modèle directe (10.17): $\hat{\boldsymbol{y}}_i^k$. Pour ces deux images, chaque colonne i représente le signal enregistré par l'élément i de la sonde. (c) - Erreur de modélisation: $\boldsymbol{y}_i^k - \hat{\boldsymbol{y}}_i^k$. On note la différence d'échelle entre les deux images (a) et (b) et l'erreur.

une densité très petite de diffuseurs. Visuellement, on en déduit que les deux données de simulation (Fig. 10.4(a)) et les données modélisées avec (10.17) (Fig. 10.4(b)) sont très similaires. En effet, l'erreur ($\boldsymbol{y}_i^k - \hat{\boldsymbol{y}}_i^k$) n'atteint que 8% de l'amplitude maximale du signal de référence $\boldsymbol{y}_i^k$ (obtenu en utilisant le logiciel Field II). Le MSE a une valeur de $4,59$, ce qui donne une énergie totale de l'erreur de modélisation $22.5769dB$ plus petite que celle du signal de référence. Ces résultats sont cohérents avec ceux présentés dans la Sous-section 10.4.3 où le modèle direct est légèrement meilleur. Les ensembles de données RF obtenus sur le fantôme de kyste (avec une densité haute des diffuseurs) sont montrées dans la Fig. 10.5. Ici encore, on peut voir que les données RF de référence (Fig. 10.5(a)) sont proche visuellement des données RF modélisées (Fig. 10.5(b)). Cependant, l'erreur de modélisation $\boldsymbol{y}_i^k - \hat{\boldsymbol{y}}_i^k$ (Fig. 10.5(c)) atteint 60% de l'amplitude du signal de référence. Le MSE mesuré est de 35.214, ce qui donne une énergie d'erreur de seulement $5.89dB$ inférieure à l'énergie du signal de référence. On observe que l'on fait plus d'erreur de modélisation si le milieu contient un nombre très grand des diffuseurs. Ceci est expliqué par l'effet de la discrétisation spatiale présentée dans la Sous-section 10.4.2. En fait, comme on le voit dans cette Sous-section, pendant la discrétisation spatiale, tous les diffuseurs à l'intérieur d'une cellule de dimensions $(\Delta x, \Delta z)$ autour d'un nœud $\boldsymbol{r}$ de $\boldsymbol{\Omega}$ sont modélisés comme un seul diffuseur placé à la position $\vec{r} = \boldsymbol{r}$. Maintenant, pour un milieu avec un nombre réduit des diffuseurs, un seul diffuseur est présent dans la cellule autour du nœud de grille $\boldsymbol{r}$ dont l'approximation génère un petit erreur de modélisation. Cependant, à mesure que la densité des diffuseur augmente, le nombre de diffuseurs à l'intérieur de chaque cellule suit la même tendance, chaque diffuseur générant une petite erreur d'approximation. Les erreurs de modélisation montrées dans la Fig. 10.4(c) et dans la Fig. 10.5(c) représentent l'interférence de ces erreurs d'approximation.

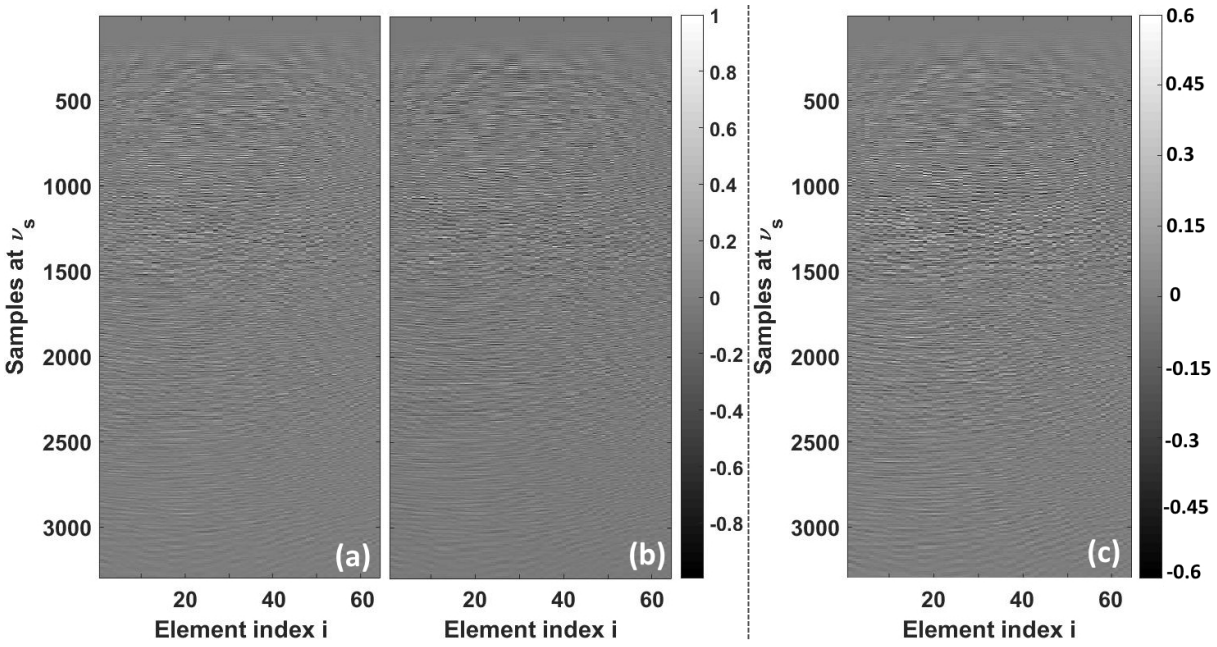

Figure 10.5: Résultats obtenus sur un milieu avec une densité haute des diffuseurs: (a) - Données RF obtenues avec Field II: $\boldsymbol{y}_i^k$. (b) - Données RF obtenues avec le modèle directe (10.17): $\hat{\boldsymbol{y}}_i^k$. Pour ces deux images, chaque colonne i représente le signal enregistré par l'élément i de la sonde. (c) - Erreur de modélisation: $\boldsymbol{y}_i^k - \hat{\boldsymbol{y}}_i^k$. On note la différence d'échelle entre les deux images (a) et (b) et l'erreur.

10.6 Sur l'émission simultanée des ondes planes codées et sur la séparation des échos: le modèle AMCUS continu

Dans cette Section, le modèle direct précédemment développé est adapté pour inclure le codage temporel des ondes planes. Tout d'abord, le besoin de codage temporel est mis en évidence. Ensuite, le modèle direct continu est adapté pour tenir compte du codage temporel des ondes planes. Enfin, est détaillée une méthode de séparation des échos mixés rétro-diffusés. La combinaison entre le modèle de propagation pour une onde plane unique, les concepts de codage temporel et de séparation des échos sont au cœur de l'imagerie AMCUS (Advanced Model for Coded UltraSound) et représente la principale contribution de ce travail.

10.6.1 Le problème de l'insonification par une seule onde plane

La question naturelle qui vient à l'esprit après la construction du modèle direct (10.17) présenté dans la Section 10.5 est: "Est-il possible d'inverser (10.17)? ". Ici, cette question est abordée et le besoin pour l'insonification multiple du milieu est montré.

En utilisant les paramètres de discrétisation obtenus dans la Sous-section (10.4.2) ici on démontre que le nombre de nœuds dans la grille du milieu est beaucoup plus grand que le nombre d'équations (donnée par le nombre d'échantillons dans le signal reçu par chaque élément de la sonde) dans le système (10.17). Ceci implique que le problème inverse basé sur (10.17) est mal-posé et que sa solution n'est pas optimale. Pour augmenter le nombre des équations dans le système, il est proposé de concaténer les signaux reçus par tous les éléments de la sonde après une seule émission d'onde plane. Cependant ceci ne résout pas complètement le problème. Ainsi le besoin d 'insonification multiple est atteint.

10.6.2 Encodage temporel pour l'émission simultanée des ondes planes: AMCUS en temps / espace continu

Dans la Sous-section précédente a été démontré que pour avoir un problème inverse bien posé, on a besoin d'une insonification multiple par ondes planes. Cependant, comme montré dans la Section 2.2.2, si ces insonifications sont faites de manière consécutive, la cadence d'acquisition des images diminue. Afin de surmonter ce problème, nous proposons d'émettre simultanément les N_{pwi} ondes planes en utilisant un codage quasi orthogonal des signaux d'excitation $a^k(t)$ associé à chaque onde plane k. Ici, le modèle direct est adapté pour inclure l'émission simultanée d'ondes planes codées temporellement.

Les calculs développés ici, montrent que pour $N_{pwi} = 3$ les signaux d'excitation $a^k(t)$ (Fig.10.6)(a)-

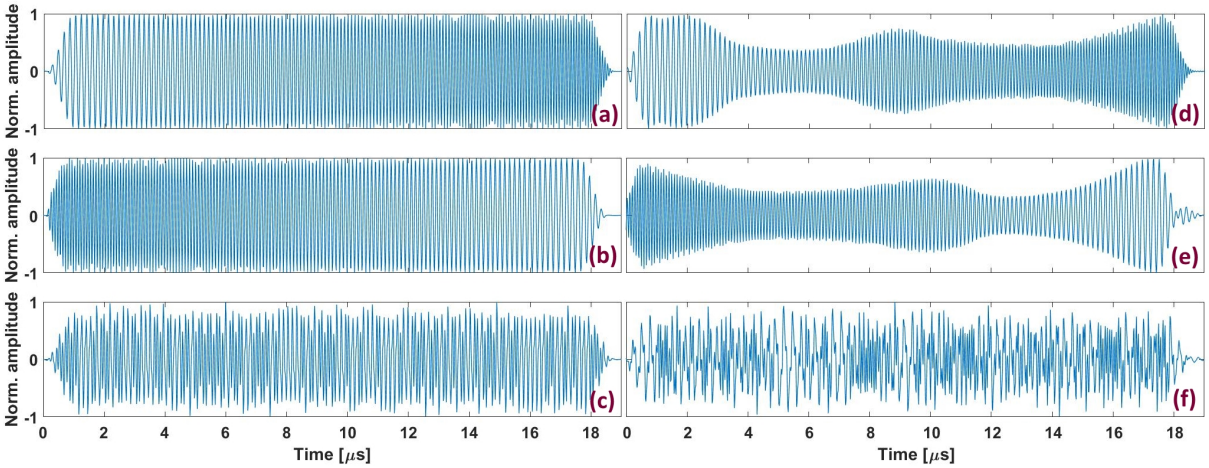

Figure 10.6: (a), (b), (c) - Exemple de $N_{pwi} = 3$ signaux $e^k(t)$ quasi-orthogonaux. Ces signaux sont composés d'un chirp avec une fréquence instantanée croissante, d'un chirp avec une fréquence instantée décroissante et d'une m-séquence modulée en phase. (d), (e) and (f) - Les signaux d'excitations $a^k(t)$ correspondant. Une fois que les signaux $a^k(t)$ sont émis et les échos sont reçus, les formes d'onde enregistrées peuvent être définies comme $e^k(t) = h(t) *_t a^k(t) *_t h(t)$.

(c) doivent être générés en utilisant le pipeline suivant:

(a) le signal $e^1(t)$ est défini comme suit:

$$e^1(t) = \eta(t)\cos\left(2\pi(f_0 - \tfrac{B}{2} + \tfrac{B}{T}t)\,t\right) \tag{10.18}$$

où $B = 5.1MHz$ est la largeur de bande de la réponse impulsionnelle de la sonde ultrasonore utilisée (Tableau 3.1). $T = 18.55\mu s$ est la durée de la forme d'onde et f_0 est la fréquence centrale de la sonde. $\eta(t)$ est une fenêtre de Tukey (20%) de durée T. Comme dans (10.18), la fréquence instantanée du chirp augmente, on l'appelle chirp "montant" ((Fig.10.6)(d)).

(b) de la même manière que $e^1(t)$, créer $e^2(t)$:

$$e^2(t) = \eta(t)\cos\left(2\pi(f_0 + \tfrac{B}{2} - \tfrac{B}{T}t)\,t\right) \tag{10.19}$$

ici on observe que la fréquence instantanée diminue donc le chirp crée est appelé "descendant" ((Fig.10.6)(e)).

(c) $e^3(t)$ est une m-séquence modulée en phase ((Fig.10.6)(f)):

$$e^3(t) = \sum_{i=0}^{q-1} s_i\delta(t - iT_0) *_t \left[\cos\left(\tfrac{2\pi}{T_0}\right)\mathrm{rect}\left(\tfrac{t}{T_0}\right)\right] \tag{10.20}$$

où s est une m-séquence de longueur q, $T_0 = 1/f_0$ et rect(t) est une fenêtre rectangulaire. Dans (10.20), la convolution temporelle entre la m-séquence et la fonction cosinus représente la modulation en phase (BPSK).

(d) enfin on déduit les signaux d'excitation $a^k(t)$ de la relation $e^k(t) = a^k(t) *_t h(t) *_t h(t)$ en utilisant le filtre de Wiener suivant:

$$\begin{aligned} \Psi^k(\nu) &= \frac{\left(H^k(\nu)H^k(\nu)\right)^*}{\left|H(\nu)H^k(\nu)\right|^2 + \varsigma} \\ A^k(\nu) &= \Psi(\nu) *_t E^k(\nu) \end{aligned} \tag{10.21}$$

où le paramètre ς est fixé de telle manière pour rendre (10.21) stable au bruit.

Les filtres optimaux $f^k(t)$ (correspondant à chaque forme d'onde $e^k(t)$) qui permettent de séparer les échos reçus tout en minimisant le bruit "crosstalk" sont aussi déduits.

10.7 AMCUS discrétisé en temps et espace

Dans la Section précédente, ont été détaillées les relations analytiques qui lient les échos rétro-diffusés reçus aux ondes planes codées émises simultanément et à la TRF du milieu. Nous avons également montré comment trouver des filtres de compression optimaux permettant la séparation des échos en réception. Ici, nous montrons l'équivalent temps / espace discret d'AMCUS et nous construisons le noyau final $\mathbf{\Psi}$.

Le pipeline complet d'AMCUS est montré dans la Fig. 10.7. On peut immédiatement observer la relation $\tilde{\boldsymbol{g}} = \mathbf{\Psi} \cdot \boldsymbol{\gamma}$ qui apparaît entre les échos rétro-diffusés filtrés et la fonction de réflectivité du tissu ($\boldsymbol{\gamma}$). De plus, on peut voir que le noyau $\mathbf{\Psi}$ modélise simultanément les blocs "Wave Emission", "Wave propagation", "Echo reception" et même une petite partie du problème inverse dans le bloc "Image reconstruction". En fait, les filtres de séparation d'écho $\boldsymbol{F}^k$ (utilisés pour construire $\mathbf{\Psi}$) peuvent être considérés comme le premier pas vers l'inversion du modèle de propagation qui lie la TRF $\boldsymbol{\gamma}$ aux observations $\boldsymbol{y}_i$.

10.8 AMCUS: Énoncé du problème inverse

Dans cette Section est abordée la partie du bloc "Image reconstruction" qui permet de passer des échos rétro-diffusés filtrés $\tilde{\boldsymbol{g}}$ à l'estimation de la TRF $\hat{\boldsymbol{\gamma}}$.

On commence par démontrer que le noyau $\mathbf{\Psi}$ du modèle direct est mal conditionné. Ensuite on conclue qu'une méthode simple d'inversion, basée sur la psudo-inverse de $\mathbf{\Psi}$ donnera des estimations sous-optimales à cause de l'amplification du bruit (surtout de modélisation). Ainsi, on décide d'implémenter une autre méthode d'inversion, et on propose d'utiliser [Beck and Teboulle, 2009]:

$$\hat{\boldsymbol{\gamma}} = \underset{\boldsymbol{\gamma}}{\operatorname{argmin}}\{\|\mathbf{\Psi}\boldsymbol{\gamma} - \tilde{\boldsymbol{g}}\|_2^2 + \lambda\|\boldsymbol{\gamma}\|_p\} \tag{10.22}$$

où $\|\|_p$ représente la norme l_p et le scalaire λ permet un compromis entre le terme d'attache aux données et le terme de régularisation.

Trouver un terme général de régularisation dans (10.22) est un problème ouvert dans le domaine des ultrasons, où dans les approches utilisant des problèmes inverses pour estimer la TRF, la norme l_p et le poids λ sont généralement adaptés en fonction de la TRF [David et al., 2015, Besson et al., 2016, Besson et al., 2018]. Nous proposons ici d'utiliser $l_p = l_1$, le poids λ étant empiriquement adapté en fonction de la TRF attendue. Le pipeline complet de l'approche problème inverse implémentée dans le bloc "Image reconstruction" est montré dans la Fig. 10.8. Comme on peut le voir ici, la partie qui

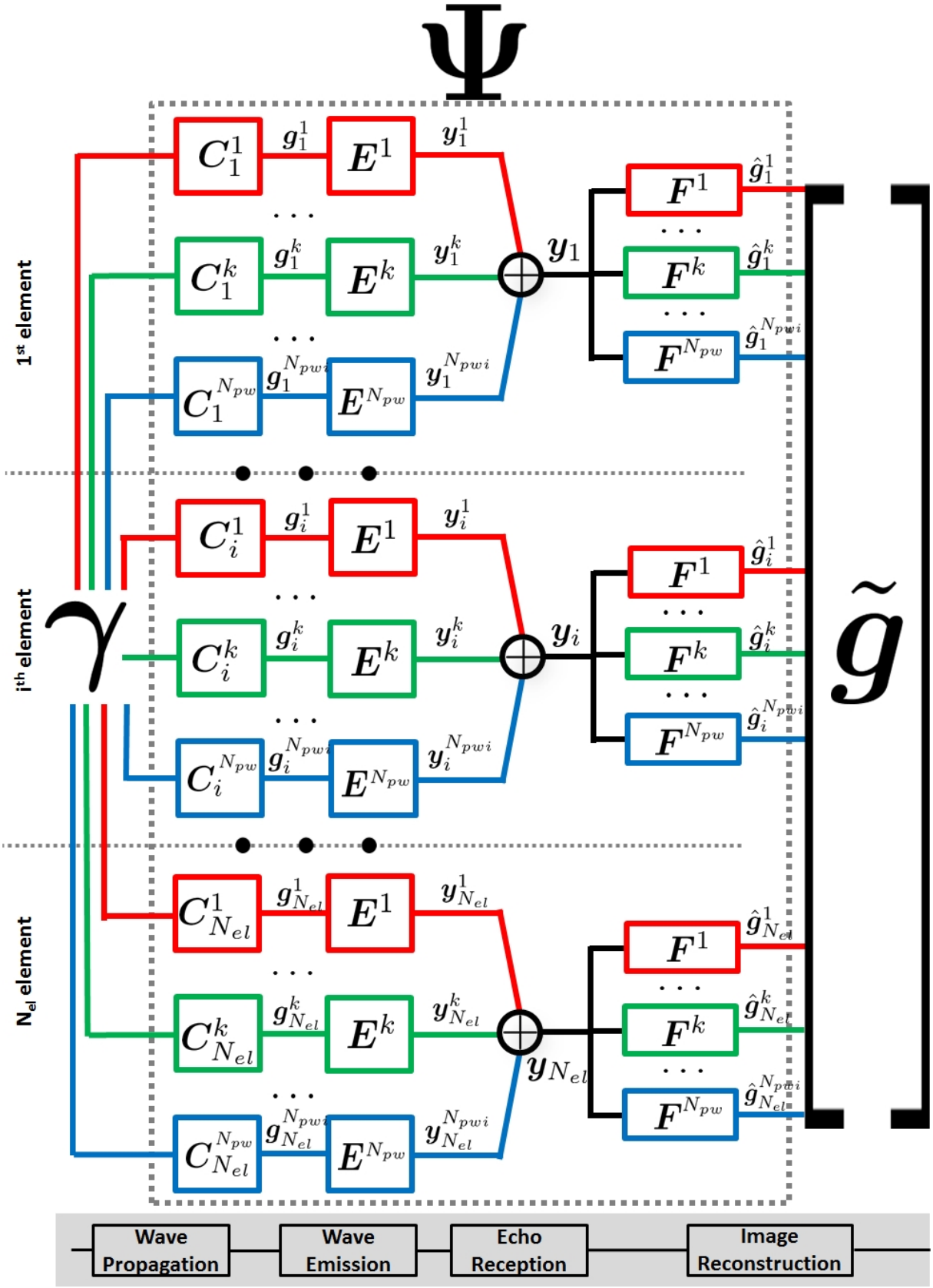

Figure 10.7: Le pipeline complet AMCUS. Les couleurs rouge, vert et bleu représentent les $N_{pwi} = 3$ ondes planes émises simultanément dans milieu.

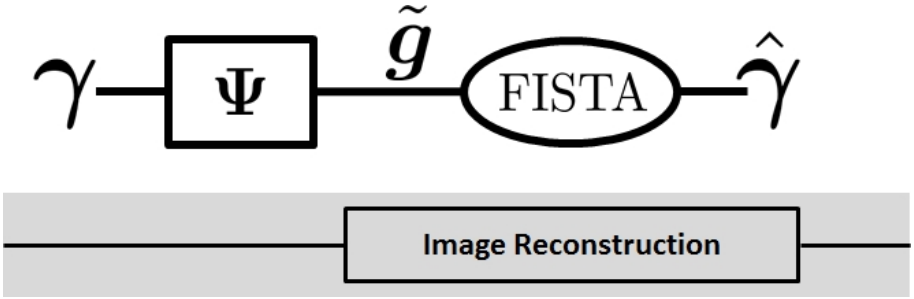

Figure 10.8: La partie "problème inverse" du bloc "Image reconstruction" qui permet d'obtenir une estimation de la TRF à partir des échos rétro-diffusés filtrés. Dans ce travail, l'algorithme Fast Iterative Shrinkage-Thresholding Algorithm (FISTA) est utilisé pour inverser l'AMCUS.

permet de résoudre (10.22) et d'obtenir ainsi une estimation de la TRF à partir des échos rétro-diffusés filtrés est l'algorithme FISTA.

10.9 AMCUS: Résultats de l'inversion

Dans cette Section, sont détaillés les résultats obtenus lors de la résolution du problème inverse basé sur AMCUS. Tout d'abord, ses performances sur un fantôme parcimonieux est évaluée puis les résultats obtenus sur un fantôme dense sont présentés.

10.9.1 Résultats sur fantôme parcimonieux

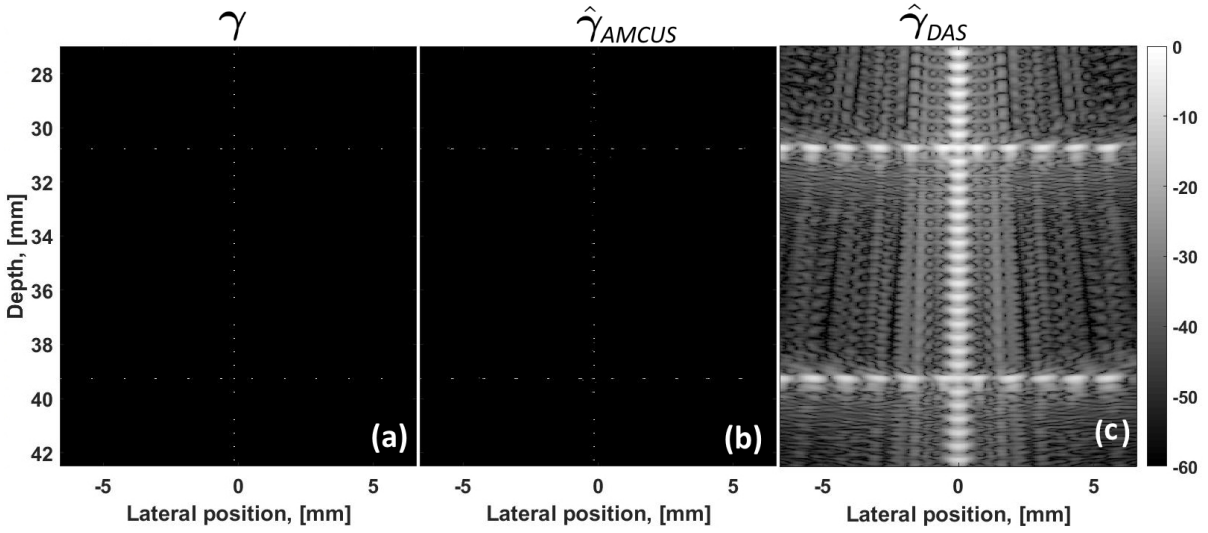

Figure 10.9: Images B-mode obtenues sur le fantôme parcimonieux: (a) - la référence ($\boldsymbol{\gamma}$); (b) - estimée avec AMCUS ($\hat{\boldsymbol{\gamma}}$); (c) - estimée avec DAS ($\hat{\boldsymbol{\gamma}}_{DAS}$). À noter que pour $\boldsymbol{\gamma}$ et $\hat{\boldsymbol{\gamma}}$ les images B-mode sont obtenues après la log-compression directe des résultats de l'inversion, tandis que pour $\hat{\boldsymbol{\gamma}}_{DAS}$ avant la log-compression une étape d'extraction d'enveloppe a été ajoutée.

Fig. 10.9 affiche les images B-mode de la TRF de référence (a), TRF estimée en utilisant AMCUS (b) et TRF estimée en utilisant DAS (c). Tout d'abord, on remarque que $\hat{\boldsymbol{\gamma}}$ est très similaire à $\boldsymbol{\gamma}$, ce qui montre que le modèle direct proposé et son inversion sont capables de converger vers une solution stable. En effet, la résolution axiale et latérale estimée sur les images B-mode est exactement la même (résolution axiale: 25μm, résolution latérale: 61,25 μm). Dans l'image B-mode $\hat{\boldsymbol{\gamma}}_{DAS}$, on peut distinguer la TRF attendue, mais les résolutions axiales et latérales des cibles sont moins bonnes (résolution axiale:

192.5 μm, résolution latérale: 455μm) que les valeurs obtenues avec AMCUS. En plus du gain respectif en résolutions axiale et latérale entre $\hat{\boldsymbol{\gamma}}$ et $\hat{\boldsymbol{\gamma}}_{DAS}$, AMCUS ne produit pas les artefacts visibles dans l'image B-mode DAS (dans ce cas, autour de $-26dB$).

10.9.2 Résultats sur fantôme dense

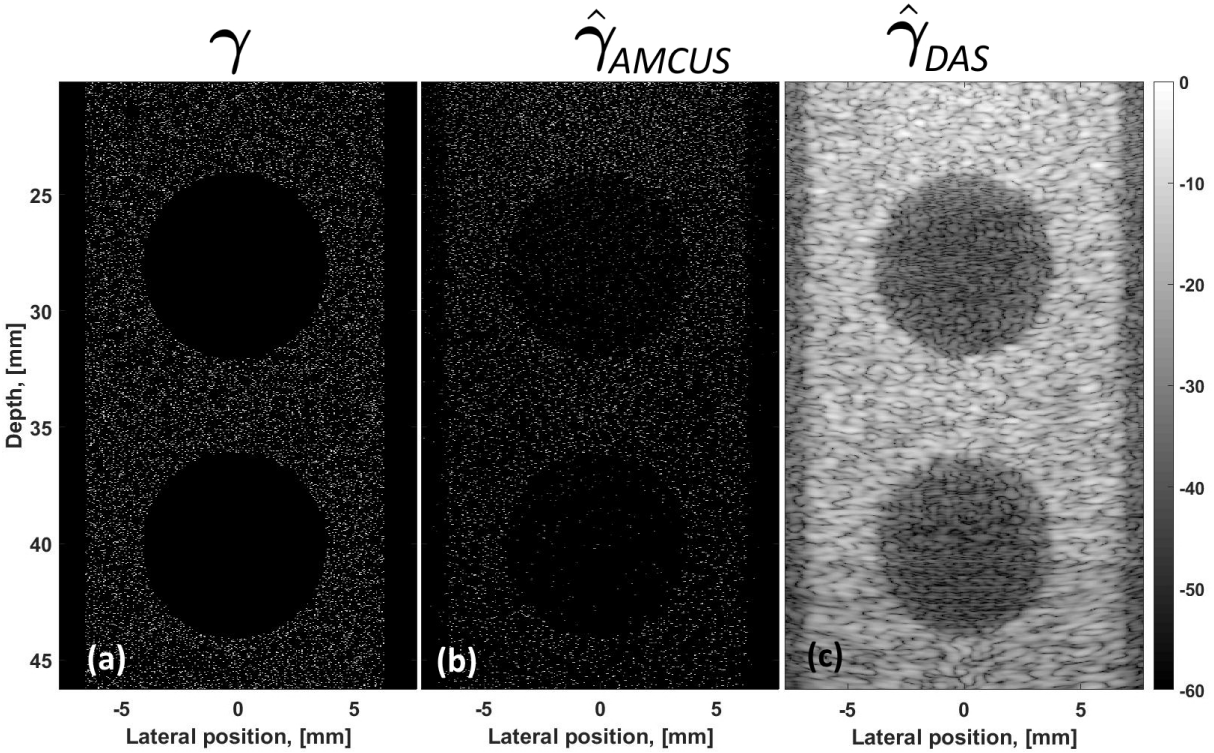

Figure 10.10: Images B-mode obtenues sur le fantôme dense: (a) - la référence ($\boldsymbol{\gamma}$); (b) - estimée avec amcus ($\hat{\boldsymbol{\gamma}}$); (c) - estimée avec DAS ($\hat{\boldsymbol{\gamma}}_{DAS}$). À noter que pour $\boldsymbol{\gamma}$ et $\hat{\boldsymbol{\gamma}}$ les images B-mode sont obtenues après la log-compression directe des résultats de l'inversion, tandis que pour $\hat{\boldsymbol{\gamma}}_{DAS}$ avant la log-compression une étape d'extraction d'enveloppe a été ajoutée.

Les images B-mode de la TRF estimée pour le fantôme dense sont montrées dans la Fig. 10.10. Là encore, on peut observer que l'inversion d'AMCUS produit une image B-mode plus proche de la référence que celle obtenue avec DAS. Sachant que les kystes sont complètement anéchoïques, on peut voir que les artefacts (précédemment observés sur l'image du fantôme parcimonieux) génèrent un bruit de reconstruction à l'intérieur des kystes qui dégrade la qualité de l'estimation de la TRF. AMCUS génère également du bruit dans les régions anéchoïques, mais ce bruit est faible et visuellement moins important (amplitude inférieure). Ces observations sont confirmées par le calcul du SNR dans les régions anéchoïques, où la valeur obtenue sur $\hat{\boldsymbol{\gamma}}$ est de $7,8dB$ plus élevée que celle mesurée sur $\hat{\boldsymbol{\gamma}}_{DAS}$.

Dans la Fig. 10.10, on peut également voir que la texture de l'image à l'intérieur de l'image $\hat{\boldsymbol{\gamma}}$ ressemble plus à celui de $\boldsymbol{\gamma}$. Cette observation est cohérente avec les résolutions axiales / latérales observés sur le fantôme parcimonieux. La reconstruction DAS fournit cependant une estimation de la TRF avec un speckle très grossier. Cette tendance est également visible sur les tracés de $Ax.AC$ et de $Lat.AC$ montrés respectivement sur la Fig. 10.11(a) et la Fig. 10.11(b). Dans la Fig. 10.11(a), on peut voir que $Ax.AC$ pour $\hat{\boldsymbol{\gamma}}$ et $\boldsymbol{\gamma}$ sont presque les mêmes avec une largeur à mi-hauteur (WHM) de 55.1μm tandis que le WHM pour $\hat{\boldsymbol{\gamma}}_{DAS}$ est de 239μm. Une légère dégradation (9.2μm) sur le WHM pour le $Lat.AC$ entre $\hat{\boldsymbol{\gamma}}$ et $\boldsymbol{\gamma}$ est observée dans la Fig. 10.11(b), cependant, cette valeur est bien meilleure que celle fournie par l'approche DAS (augmentation de 1710μm). La similarité mentionnée précédemment entre les images B-mode de $\boldsymbol{\gamma}$ et $\hat{\boldsymbol{\gamma}}$ a également été confirmée par la mesure de la cohérence du speckle

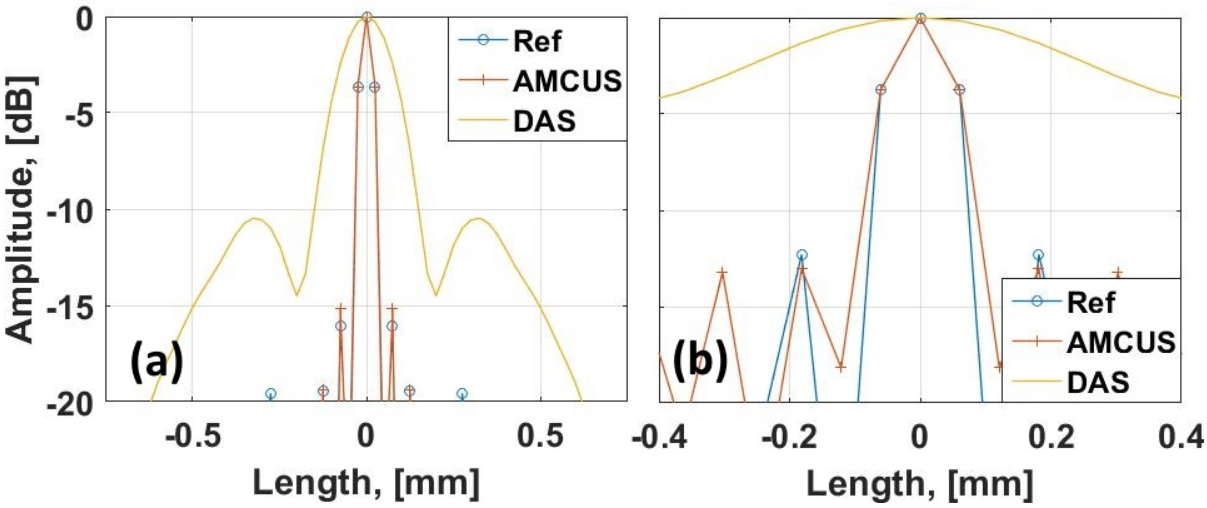

Figure 10.11: (a) - Longueur de l'autocorrelation axiale pour $\boldsymbol{\gamma}$ (AAC_{Ref}), $\hat{\boldsymbol{\gamma}}$ ($AAC_{Prop.}$) et $\hat{\boldsymbol{\gamma}}_{DAS}$ (AAC_{DAS}). Ces métriques sont mesurées sur la ligne qui passe par $x = 5\ mm$; (b) - Longueur de l'autocorrelation latérale pour $\boldsymbol{\gamma}$ (AAC_{Ref}), $\hat{\boldsymbol{\gamma}}$ ($AAC_{Prop.}$) et $\hat{\boldsymbol{\gamma}}_{DAS}$ (AAC_{DAS}). Ces métriques sont mesurées sur la ligne qui passe par $z = 35\ mm$.

(SC) (Fig. 10.12). Comme on peut le voir, le lobe principal de la SC est plus mince (axialement et latéralement) pour l'image B-mode $\hat{\boldsymbol{\gamma}}$ comparée à $\hat{\boldsymbol{\gamma}}_{DAS}$, ce qui signifie que le speckle dans $\hat{\boldsymbol{\gamma}}$ est plus proche de la référence que le speckle dans $\hat{\boldsymbol{\gamma}}_{DAS}$. Ces évaluations visuelles sont également confirmées par les mesures du WHM des lobes principaux de la SC. En effet, nous mesurons un WHM axial de $53.1\mu m$, $83.6\mu m$ et $213.7\mu m$ pour $\boldsymbol{\gamma}$, $\hat{\boldsymbol{\gamma}}$ et $\hat{\boldsymbol{\gamma}}_{DAS}$ respectivement. Les WHM latéraux correspondants sont $104.1\mu m$, $122.3\mu m$ et $364.4\mu m$.

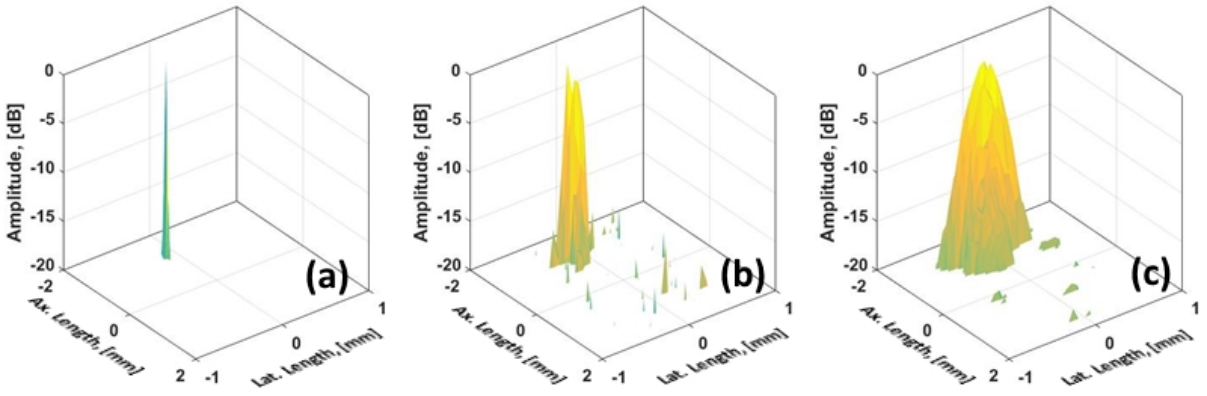

Figure 10.12: Résultat des mesures de la cohérence de la texture de l'image (SC) évaluée sur: (a) - $\boldsymbol{\gamma}$, (b) - $\hat{\boldsymbol{\gamma}}$ et (c) - $\hat{\boldsymbol{\gamma}}_{DAS}$.

10.10 Discussion

Dans les Sections précédentes, nous avons présenté un modèle direct général qui relie les données radiofréquence enregistrées aux signaux d'excitations, aux propriétés géométriques / acousto-électriques de la sonde ultrasonore et à la fonction de réflectivité du tissu. Le modèle général a été adapté au concept de composition cohérente des ondes planes, où les résultats obtenus ont montré une erreur relative sous 10% (pour chaque dispersion) par rapport aux données de référence (calculées à l'aide du programme Field II). Cependant, en raison de son origine, cette erreur a tendance à augmenter si la

densité du diffuseur augmente. Comme montré dans les Sections 10.4, 10.5 et 10.6, cette erreur peut être réduite grâce au partitionnement fin des éléments de la sonde ultrasonore et du support imagé.

Afin de réduire le temps d'acquisition des images, une émission codée simultanée d'ondes planes a été proposée et le modèle direct a été adapté en conséquence. Trois ondes planes ont été émises simultanément à l'intérieur du milieu afin d'obtenir un modèle direct bien déterminé. Les signaux d'excitation proposés a été un mélange de deux chirps linéaires (avec respectivement des fréquences instantanées croissantes et décroissantes) et une séquence binaire pseudo-aléatoire modulée en phase. Nous avons également décidé de compenser l'effet de la réponse impulsionnelle de la sonde ultrasonore afin de mieux préserver l'orthogonalité de ces signaux. Ainsi, la valeur maximale obtenue du rapport de corrélation croisée / d'autocorrélation (entre les signaux d'excitation) ne dépasse pas 17%. De plus, comme le modèle direct proposé tient compte du bruit "crosstalk" (son effet est donc compensé lors de l'inversion du modèle direct), l'estimation obtenue de la TRF n'a pas été influencée.

Les résultats de la simulation sur le fantôme parcimonieux ont montré que les résolutions axiale et latérale sont améliorées par un facteur de plus de six, par rapport à l'algorithme de reconstruction classique (DAS). Ces améliorations sont liées au fait que la modélisation proposée (AMCUS) ne repose pas sur les hypothèses DAS classiques (une impulsion de Dirac comme signal d'excitation, une sonde ultrasonore à largeur de bande infinie et une diffusion en champ lointain). Une étude exhaustive du pas de discrétisation a montré que la résolution spatiale fournie suit exactement la taille des cellules de la grille (du milieu discrétisé), ce qui permet d'affirmer qu'une discrétisation plus faible permettrait une meilleure résolution spatiale de l'image. Nous avons également observé que la qualité de la reconstruction des diffuseurs à l'intérieur de la TRF proposée sont quasi-constantes en fonction de la profondeur et de la position latérale (contrairement à DAS). Ce comportement était attendu car dans AMCUS, la discrétisation affinée des éléments émetteurs / récepteurs permet de modéliser la réponse impulsionnelle spatiale de la sonde. Enfin, la stabilité spatiale de la reconstruction et la résolution d'image fournie ont permis d'obtenir une image B-mode de la TRF très similaire à la référence. Les mesures sur les largeurs à mi-hauteur de $Ax.AC$ et de $Lat.AC$ ont également montré une amélioration apportée par AMCUS, par rapport au DAS (plus de 3 fois et 12 fois, respectivement). L'amélioration drastique de la largeur à mi-hauteur de $Lat.AC$ (qui dépasse fortement l'amplification de la résolution latérale) peut s'expliquer par le fait que pour une composition cohérente de seulement trois images d'ondes planes, la taille de speckle obtenue dans la direction latérale est beaucoup plus grande que sa taille en direction axiale.

Les résultats précédents ainsi que l'évaluation visuelle montrent une nette ressemblance entre la TRF estimée par AMCUS et la référence. Ces observations sont également prouvées par les mesures SC qui montrent un rétrécissement du pic d'inter-corrélation dans la direction axiale et latérale (d'un facteur de 1,5 et 1,9 respectivement), comparé aux valeurs obtenues sur l'image DAS.

11 Conclusion générale

Les travaux présentés dans ce manuscrit étendent le principe de l'imagerie ultrasonore ultra-rapide. Plus précisément, grâce à un mélange des concepts tels que imagerie par ondes planes, systèmes à entrées / sorties multiples et problèmes inverses, la méthode proposée permet de reconstruire des images avec une meilleure qualité que celles obtenues par les approches classiques d'imagerie. En plus, le résultats fournis sont obtenus que à partir des données acquises après une seule émission / réception ainsi présentant un gain en cadence d'acquisition.

Tout d'abord, un formalisme théorique général du phénomène de propagation des ondes acoustiques a été développé. Cela a permis de relier le signal électrique reçu par un transducteur piézoélectrique au signal d'excitation de la source acoustique. Les concepts théoriques ainsi développés ont été utilisés pour revoir les schémas d'acquisition existants. Il a été démontré que les méthodes d'imagerie qui nécessitent moins d'événements d'émission / réception (pour la même région imagée à l'intérieur du milieu) fournissent une qualité d'image inférieure à celles qui nécessitent plus d'événements d'émission / réception. Ainsi l'objectif de ce travail été présenté. Différentes méthodes de codage temporel des signaux d'excitation ont été présentées comme un moyen d'améliorer la qualité de l'image. Une technique appelée imagerie par synthèse d'ouverture codée, qui mélange les concepts des systèmes de télécommunication et de l'imagerie ultrasonore pour augmenter la cadence d'acquisition des images, a été présentée. Il a été démontré qu'une étude plus approfondie de cette méthode est nécessaire afin d'en comprendre pleinement les limites. Ainsi, l'objectif de la première contribution de ce travail est avancé.

Dans la première contribution de ce travail, une technique qui repose sur l'émission simultanée d'ondes planes codées a été développée. Tout d'abord, en s'appuyant sur le contexte théorique précédemment établi, un modèle mathématique direct des phénomènes de propagation / interaction tissulaire d'ondes planes ultrasonores, a été construit. Les propriétés du modèle direct résultant ont été étudiées et les exigences nécessaires sur le type / taille des signaux d'excitation, sur la taille du support d'image et sur la taille des données RF enregistrées ont été déduites. Il a été démontré que si ces exigences sont satisfaites, la qualité d'image obtenue est exactement la même que celle fournie par la technique d'imagerie conventionnelle. En outre, il a été démontré que ces exigences impliquent que, malgré l'émission simultanée, le gain de temps fourni par la méthode proposée est nul par rapport à l'imagerie par ondes planes classique. De plus, il a été observé que si les conditions nécessaires ne sont pas respectées, la qualité de l'image diminue considérablement lorsque la cadence d'acquisition fournie augmente. Les résultats expérimentaux ont prouvé la faisabilité de la méthode proposée et ont confirmé une fois de plus les considérations théoriques démontrées par les simulations. À la fin de cette grande partie de ce travail, un certain nombre de questions telles que : "est-il possible d'exprimer les échos générés par chaque onde plane en fonction d'une entité invariante ?" restaient sans réponses. Ces questions on tété les objectifs fondamentaux de la deuxième contribution de ma thèse.

L'apport le plus important de ces travaux peut-être considéré le développement théorique et la validation en simulation d'une méthode d'imagerie qui a le potentiel non seulement d'augmenter la cadence d'acquisition d'images par ondes planes classiques, mais aussi d'améliorer la qualité de l'image fournie. En s'appuyant sur les inconvénients des méthodes d'imagerie par synthèse d'ouverture codée et par ondes planes codées, la nécessité d'un noyau direct plus complexe permettant de modéliser la propagation des ondes ultrasonores / leur interaction avec le tissu a été démontrée. Ainsi, un modèle avancé reliant les échos rétro-diffusés reçus à la fonction de réflectivité du tissu (TRF) a été déduit. Il a été montré que le problème inverse basé sur le noyau construit pour une émission d'une seule onde plane est très mal posé. Le modèle avancé pour l'imagerie ultrasonore codée (AMCUS) a été conçu, qui repose sur le principe de base de la première contribution et consiste dans la combinaison des concepts tels que l'émission simultanée d'ondes planes codées et le modèle direct avancé. Les exigences générales que les signaux d'excitation / filtres de compression associés à chaque onde plane émise simultanément doivent satisfaire ont été énoncées. Pour l'estimation de la TRF, un problème inverse régularisé a été proposé, où l'information à priori sur la TRF a été la parcimonie de sa distribution des diffuseurs. De plus, les performances d'AMCUS ont été testées en simulation.Fantômes avec des distributions denses et moins denses de diffuseurs ont été testés et il a été observé qu'en raison de la limitation de la taille de la partition temporelle / spatiale, AMCUS fournit des données RF synthétiques avec une erreur de modélisation qui dépend de la densité de diffuseurs. Néanmoins, la qualité de l'estimation de la TRF, obtenue en inversant AMCUS, a été meilleure que celle fournie par les algorithmes classiques de reconstruction pour une cadence d'acquisition multipliée par trois (pour le cas simulé étudié ici).

12 Discussion: difficultés actuelles et perspectives

12.1 Sur le temps de calcul et les ressources utilisées

Il ne fait aucun doute que l'une des questions qui viendra à l'esprit de chacun au cours de la lecture de ce travail, est liée d'une certaine manière au temps de calcul nécessaire d'abord pour construire le noyau direct et après pour résoudre le problème inverse, lors de la reconstruction de la TRF basée sur AMCUS. Ces questions ont tous les droits d'exister, car dans un monde où les méthodes d'échographie sont largement connues surtout grâce à leur vertu "temps réel", une méthode qui fournit des images B-mode en "hors-ligne" peut être moins intéressante. Pour être juste, l'estimation de la TRF basée sur AMCUS est beaucoup plus lourde en calcul que les algorithmes de reconstruction classiques (tel que DAS) et encore plus que les algorithmes basés sur la reconstruction dans l'espace fréquentiel. En fait, malgré l'utilisation des avantages des matrices parcimonieuses et du calcul vectorisé (dans l'environnement MATLAB), la construction du noyau direct AMCUS est une opération qui peut prendre jusqu'à quelques dizaines d'heures (avec les paramètres indiqués dans la Section 4.10), sur un ordinateur doté d'un processeur Intel® Xeon® E5-2650L. Comme le montre la Sous-section 4.4.2, les matrices impliquées dans le calcul du modèle direct AMCUS peuvent atteindre plusieurs centaines de gigaoctets (l'ordinateur sur lequel la simulation AMCUS a été exécutée avait 380 Go et un disque dur avec une vitesse de rotation de 7200 tours par minute) ce qui implique que même charger le noyau dans la mémoire opérationnelle, peut prendre aux alentours d'une heure. Enfin, la dernière partie de la reconstruction de la TRF avec AMCUS, qui est la couche d'estimation (utilisant FISTA), s'arrête (erreur relative de 10^{-3} qui est généralement obtenue après plusieurs centaines d'itérations) en quatre heures environ. Dans la défense de notre méthode, nous pouvons affirmer qu'à ce stade, la partie la plus lourde de notre méthode en termes du temps de calcul, qui est la génération du modèle directe, pour une sonde donnée et une région d'intérêt à l'intérieur du milieu, ne doit être construite qu'une seule fois et peut ensuite être appliquée à tous les donnée RF acquises avec cette sonde particulière sur cette région d'intérêt donnée. Cela réduit considérablement le temps de calcul, mais il reste néanmoins dans la fourchette des quelques heures. Bien que ce temps de calcul soit encore loin du concept de "temps réel", la qualité de l'estimation de la TRF fournie devrait, pour commencer, au moins nous motiver en tant que chercheurs à optimiser le temps de calcul. Ainsi, si je continuais à travailler sur ce sujet, ma prochaine étape serait de combiner AMCUS avec le concept "sans matrice", développé par le groupe dirigé par Jean-Philippe Thiran à l'EPFL. À la base du concept "sans matrice" est la génération du modèle direct / inverse "à la volée" qui s'appuie sur des calculs parallélisés (sur GPU) pour obtenir des temps de calcul très faibles. Une telle amélioration permettra non seulement de travailler plus librement avec AMCUS (permettant de changer les paramètres de la sonde / milieu sans avoir à attendre longtemps la génération du modèle direct) mais aussi d'approcher (en termes du temps de calcul) l'estimation de la TRF basée sur AMCUS aux algorithmes de reconstruction comme

DAS.

12.2 Sur la performance d'AMCUS

En revenant à la Sous-section 4.4.2, où l'on a choisi la taille des pas de discrétisation pour le milieu imagé et pour les éléments de la sonde, on peut affirmer que la performance d'AMCUS augmenterait si ces pas étaient raffinés. Cependant, des plus petits pas de partition impliquent des plus grandes matrices dans le calcul du noyau direct AMCUS, ce qui fait que les performances d'AMCUS (à travers la taille des pas de discrétisation) sont liées au temps de calcul. Ainsi, dans le contexte d'une forte amélioration du temps de calcul avec la méthode "sans matrice", une augmentation de la performance d'AMCUS sera possible en raffinant les pas de discrétisation.

Ici, on peut aussi discuter du choix des paramètres de régularisation utilisés pour l'inversion d'AMCUS. En fait, dans ce manuscrit, nous avons présenté les résultats obtenus en utilisant seulement un terme de régularisation du type l_1 avec un poids déduit empiriquement pour chaque type de milieu imagé (poids plus petit pour une densité de diffuseur plus élevée et poids plus grand pour une densité de diffuseur inférieure) car c'est le terme l_p qui fourni les meilleurs résultats. Cependant, ce choix n'est pas rare pour la communauté ultrasonore, un grand nombre de méthodes de reconstruction basées sur des problèmes inverses utilisant le même terme pour obtenir les résultats finaux. En effet, une hypothèse aussi importante (que le milieu aie une distribution parcimonieuse de diffuseurs) n'est pas toujours adaptée au milieu imagé (d'où la diminution de la qualité de l'estimation de la TRF sur les kystes), cependant, tant qu'un modèle plus précis pour la distribution de diffuseurs dans le milieu n'est pas disponible, la norme l_1 fournit les meilleurs résultats. Une façon possible de déduire de tels modèles serait d'abord de reconstruire l'image à l'aide d'algorithmes classiques, puis, à partir de ces estimations de la TRF, de déduire la distribution de diffuseurs, puis de l'injecter dans l'inversion AMCUS. Bien qu'une telle méthode de calcul de la distribution de diffuseurs serait grandement affectée par les artefacts de reconstruction (causées par les performances des méthodes classiques), cette méthode pourrait tout de même fournir une bonne estimation préalable de l'amplitude et de la densité de diffuseur, ainsi améliorant la performance de l'estimation de la TRF basée sur AMCUS. En effet, une information à priori plus adaptée augmenterait aussi les performances des autres méthodes de reconstruction basées sur les problèmes inverses, cependant, l'avantage d'AMCUS est que d'une part il représente fidèlement l'émission / propagation / réception des ondes ultrasonores et d'autre part il fournit beaucoup plus de données grâce à l'émission simultanée des ondes encodées.

12.3 Sur la généralité de la reconstruction basée sur AMCUS

Un autre point que nous avons soulevé dans la Section 4.5 est que l'AMCUS et par conséquent l'estimation de la TRF basée sur AMCUS, peuvent s'adapter à tout schéma d'émission / réception. Bien que les résultats présentés dans ce manuscrit ne montrent que la performance d'AMCUS sur l'acquisition par ondes planes et l'acquisition simultanée par ondes planes (et les inversions correspondantes), les travaux réalisés en parallèle ont montré que AMCUS et capable de s'adapter à l'acquisition par synthèse d'ouverture classique et simultanée codée. De plus, la reconstruction basée sur AMCUS a montré des résultats prometteurs en obtenant des qualités d'image bien meilleures que celles fournies par les algorithmes de reconstruction classiques. Il s'agit d'un premier pas vers l'affirmation de la généralité d'AMCUS, la prochaine étape étant de l'adapter aux schémas d'acquisition basés sur des faisceaux étroits comme l'imagerie focalisée, l'acquisition multi-ligne et la transmission multi-ligne. À mon avis, de tels schémas d'imagerie s'adapteraient mieux à la reconstruction basée sur AMCUS puisque, grâce aux émissions focalisées, non seulement les signaux reçus contiendraient un niveau de bruit beaucoup plus bas (que les signaux reçus d'une insonification non focalisée) mais on pourrait également réduire la taille de la région d'intérêt du milieu (en réduisant ainsi le nombre d'inconnues dans le problème inverse associé à AMCUS). Une autre piste intéressante à explorer serait d'évaluer

la performance d'AMCUS lorsque tous les éléments de la sonde émettent avec des retards aléatoires des formes d'onde arbitraires (pas nécessairement similaires entre les éléments) générant ainsi des fronts d'onde sans une forme particulière (focalisé, divergent ou plan). Une telle méthode serait non seulement la preuve ultime de la généralité d'AMCUS, mais elle ouvrirait aussi la voie à de nouvelles méthodes d'imagerie.

12.4 Sur la mise en œuvre pratique de la reconstruction basée sur AMCUS

Ce qui manque dans l'état actuel de notre travail sur la reconstruction avec AMCUS, ce sont les résultats expérimentaux. Bien que l'on puisse discuter encore que le bruit de modélisation (qui peut atteindre des niveaux élevés d'énergie à l'intérieur des signaux AMCUS) peut être considéré comme un bruit d'acquisition, cela imite mal les signaux radiofréquence obtenus à partir d'expériences sur des fantômes réels. Toutefois, la récente mise en œuvre expérimentale de la reconstruction basée sur AMCUS sur un schéma d'acquisition à synthèse d'ouverture a donné des résultats prometteurs. Pour l'implémentation expérimentale, la méthode présentée dans le Chapitre 4 peut être utilisée, en commençant avec la génération des signaux d'excitation jusqu'à l'enregistrement des données radiofréquence (en fonction de la région d'intérêt à l'intérieur du milieu). Bien entendu, puisque les données radiofréquence sont nécessaires pour la reconstruction basée sur AMCUS, l'échographe utilisé devrait permettre de récupérer ce type particulier de données qui réduit le choix des échographes aux appareils de recherche. Une autre exigence importante pour la mise en œuvre expérimentale d'AMCUS est que les propriétés géométriques / acousto-électriques de la sonde ultrasonore doivent être connues afin de construire le noyau direct. Puisque les ressources du système (telles que décrites dans la Section 12.1), requises pour la reconstruction basée sur AMCUS, sont sans aucun doute bien au-dessus de ce que l'on possède sur un échographe de recherche, un calcul "hors-ligne" de la génération / inversion d'AMCUS devrait être fait. Un autre aspect à analyser lors de l'implémentation des signaux d'excitation encodés temporellement est la capacité de l'échographe à générer des formes d'ondes arbitraires. Alors que sur un système type Ula-Op (qui utilise des amplificateurs linéaires pour piloter la sonde ultrasonore) cette opération est simple, les signaux d'excitation utilisés dans la simulation étant aussi adaptés pour l'émission Ula-Op, sur un scanner qui utilise des sources de tension à trois états (polarité positive, négative ou nulle) pour alimenter la sonde, l'implantation d'AMCUS peut être plus difficile. Le problème de ces scanners est que, selon la complexité des signaux d'excitation (pour AMCUS, à cause de l'émission simultanée d'ondes planes encodées temporellement, ces signaux sont très complexes), la source à trois états génère une version plus ou moins fidèle à la forme d'onde souhaitée. Un moyen de surmonter cet inconvénient serait d'utiliser dans AMCUS non pas les signaux qui ont été théoriquement déduits (et utilisés dans la simulation) mais leur version à trois états (qui n'est pas une copie exacte du signal théorique, mais conserve néanmoins ses propriétés d'orthogonalité).

Un autre aspect des expériences sur des fantômes réels qui pourrait entraîner une diminution de la performance de la reconstruction basée sur AMCUS sont les phénomènes de propagation non linéaire des ondes acoustiques et de l'atténuation tissulaire. Alors que pour le premier phénomène je ne vois pas de solution pour le moment, pour le second, dans le contexte de nos travaux récents où nous avons montré la capacité d'une technique de compression d'impulsions à surmonter l'effet de l'atténuation, on peut penser à un moyen de modéliser ce phénomène dans AMCUS. En fait, l'atténuation tissulaire peut être modélisée par sa réponse impulsionnelle, donc pour une onde se propageant à une certaine distance, l'effet d'atténuation sur une impulsion de Dirac peut être déterminé à priori. En plus, comme nous l'avons montré dans le Chapitre 4, AMCUS est fortement basé sur les réponses impulsionnelles de tous les points à l'intérieur du milieu, ajoutant ainsi la réponse impulsionnelle de l'atténuation d'un point particulier à l'intérieur du milieu ne devrait pas être une tâche difficile.

12.5 Sur l'évolution vers l'imagerie 3D par ultrasons

Avec la compréhension de l'interaction entre l'onde ultrasonore et les tissus mous à l'intérieur du corps humain et avec la nécessité d'améliorer la qualité du diagnostic fourni, un domaine en plein essor dans la recherche sur les ultrasons est le développement de méthodes d'imagerie 3D rapides. Alors que dans ce manuscrit nous avons décrit le noyau direct AMCUS uniquement pour les sondes linéaires qui n'acquièrent des données qu'à partir d'un plan à l'intérieur du milieu, ce cadre peut être facilement étendu à une distribution d'éléments transducteurs sur une grille 2D qui reçoivent les échos d'une région d'intérêt 3D à l'intérieur du milieu. Le problème qui se pose ici, est étroitement lié à celui discuté dans la Section 12.1, et consiste en une augmentation importante du temps de calcul et des ressources (de calcul) nécessaires. Une telle extension de ces travaux est donc à prévoir sur long terme.

Appendix Part III

A On the principles of ultrasound wave propagation

Here the principle of ultrasound wave propagation is mathematically modeled.

Suppose that the small perturbation generated by the acoustic wave, generates slight ripples $p_1(\vec{r},t)$ and $\rho_1(\vec{r},t)$ inside the pressure P_0 and density $\rho_0(\vec{r})$ fields respectively (where $\vec{r}=(x_r,y_r,z_r)$ is the position vector of the point r). Thus, for a point $\vec{r}$, the new pressure and density can be written as [Jensen, 1991, Morse et al., 1969]:

$$\begin{aligned} P(\vec{r},t) &= P_0 + p_1(\vec{r},t) \\ \rho(\vec{r},t) &= \rho_0(\vec{r}) + \rho_1(\vec{r},t) \end{aligned} \text{ with } \begin{cases} p_1(\vec{r},t) << P_0 \\ \rho_1(\vec{r},t) << \rho_0(\vec{r}) \end{cases} \tag{A.1}$$

With the condition that the process of ultrasound wave propagation is adiabatic and no acoustic energy is converted into heat, the following relation between the pressure and density holds [Jensen, 1991, Chernov, 2017]:

$$\frac{\mathrm{d}P(\vec{r},t)}{\mathrm{d}t} = c^2(\vec{r})\frac{\mathrm{d}\rho(\vec{r},t)}{\mathrm{d}t} \tag{A.2}$$

with $c(\vec{r})$ – the propagation speed of sound inside soft tissues. Equation (A.2) concerns any particle, and represents the Lagrangian description of a medium particle in motion. However, since during the process of ultrasound imaging the acoustic sources / receivers are stationary, it is more appropriate to redefine (A.2) as a Euler description, which is linked specifically to one point in space and time:

$$\frac{1}{c^2(\vec{r})}\frac{\partial p_1(\vec{r},t)}{\partial t} = \frac{\partial \rho_1(\vec{r},t)}{\partial t} + \vec{u}\cdot\nabla\rho_0(\vec{r}) \tag{A.3}$$

where $\vec{u} = \mathrm{d}\vec{r}/\mathrm{d}t$ is the particle velocity, $\nabla = (\partial/\partial x\,,\,\partial/\partial y\,,\,\partial/\partial z)$ is the gradient operator and $\cdot$ is the scalar product.

At this point one can also define two more equations that link the medium density $\rho(\vec{r},t)$ and pressure $P(\vec{r},t)$ in a medium point $\vec{r}$ at a given time t:

- Conservation of mass – implies that for a small medium volume V around the point $\vec{r}$, the fluid mass variation inside V is proportional to the fluid flow through the closed surface $\mathscr{S}$ (that contains V). In other words no fluid mass is created nor lost inside the volume V. Its differential form is:

$$\frac{\partial\rho(\vec{r},t)}{\partial t} + \nabla\cdot(\rho(\vec{r},t)\,\vec{u}) = 0 \tag{A.4}$$

  where $\nabla\cdot$ represents the divergence operator.

- Conservation of momentum – implies that momentum inside the volume V at any time is given by the sum of the fluid momentum that passes through $\mathscr{S}$, the action of the pressure forces on the surface $\mathscr{S}$ and the action of the exterior forces $\mathbb{F}$. Its differential form is:

$$\frac{\mathrm{d}\vec{u}}{\mathrm{d}t} + \frac{\nabla P(\vec{r},t)}{\rho(\vec{r},t)} = \mathbb{F} \tag{A.5}$$

Now, adapting (A.4) to the approximation made in (A.1), yields:

$$\frac{\partial \rho_1(\vec{r},t)}{\partial t} + \nabla\big(\rho_0(\vec{r})\,\vec{u}\big) = 0 \tag{A.6}$$

Concerning the momentum conservation law, it will be supposed in this work that $\mathbb{F} = 0$, thus by applying (A.1) to (A.5) one can obtain:

$$\rho_0(\vec{r})\frac{\partial \vec{u}}{\partial t} + \nabla p_1(\vec{r},t) = 0 \tag{A.7}$$

A.1 Linear wave equation

Here, the equations (A.1), (A.3), (A.6) and (A.7) will be used in order to obtain the linear propagation equation of an acoustic wave inside soft tissues.

Consider the derivative with respect to time of (A.6) given by:

$$\frac{\partial}{\partial t}\Big(\frac{\partial \rho_1(\vec{r},t)}{\partial t} = -\nabla\big(\rho_0(\vec{r})\,\vec{u}\big)\Big) \Longleftrightarrow \frac{\partial^2 \rho_1(\vec{r},t)}{\partial t^2} = -\nabla\Big(\rho_0(\vec{r})\frac{\partial \vec{u}}{\partial t}\Big) \tag{A.8}$$

Combining (A.8) with (A.7) one can obtain:

$$\frac{\partial^2 \rho_1(\vec{r},t)}{\partial t^2} = -\nabla\big(-\nabla p_1(\vec{r},t)\big) \Longleftrightarrow \frac{\partial^2 \rho_1(\vec{r},t)}{\partial t^2} = \nabla^2 p_1(\vec{r},t) \tag{A.9}$$

Now, consider the derivative of (A.3) with respect to time obtained as follows:

$$\frac{\partial}{\partial t}\Big(\frac{1}{c^2(\vec{r})}\frac{\partial p_1(\vec{r},t)}{\partial t} = \frac{\partial \rho_1(\vec{r},t)}{\partial t} + \vec{u}\cdot\nabla\rho_0(\vec{r})\Big) \Longleftrightarrow \frac{1}{c^2(\vec{r})}\frac{\partial^2 p_1(\vec{r},t)}{\partial t^2} = \frac{\partial^2 \rho_1(\vec{r},t)}{\partial t^2} + \frac{\partial \vec{u}}{\partial t}\nabla\rho_0(\vec{r}) \tag{A.10}$$

At this point, one can combine the results of (A.9) and (A.10) with (A.7), to obtain the following relation:

$$\frac{1}{c^2(\vec{r})}\frac{\partial^2 p_1(\vec{r},t)}{\partial t^2} = \nabla^2 p_1(\vec{r},t) - \frac{1}{\rho_0(\vec{r})}\nabla\rho_0(\vec{r})\nabla p_1(\vec{r},t) \tag{A.11}$$

In (A.11) it can be seen that the pressure evolution in the medium point $\vec{r}$, depends on the medium density at rest $\rho_0(\vec{r})$ in this very point. As density inhomogeneities in any medium point $\vec{r}$ can be seen as deviations $\Delta\rho_0(\vec{r})$ that are superposed to a mean value ρ_m, the medium density at rest can be expressed as follows:

$$\rho_0(\vec{r}) = \rho_m + \Delta\rho_0(\vec{r}) \tag{A.12}$$

Fluctuations in the fluid density, imply variations in the propagation speed of sound at the medium point $\vec{r}$, defined as follows [Morse et al., 1969]:

$$c(\vec{r}) = \sqrt{\frac{\mathscr{K}(\vec{r})}{\rho_0(\vec{r})}} \underset{\text{Using A.12}}{\Longleftrightarrow} c(\vec{r}) = c_m + \Delta c_0(\vec{r}) \tag{A.13}$$

For the rest of this work, the hypothesis that the perturbations in both pressure and density fields are small in comparison to the mean values of these fields, is made. Thus, in (A.12) and (A.13) the following relations hold: $\rho_m >> \Delta\rho_0(\vec{r})$ and $c_m >> \Delta c_0(\vec{r})$. In such conditions, (A.11) can be rewritten as:

$$\frac{1}{\left(c_m + \Delta c_0(\vec{r})\right)^2}\frac{\partial^2 p_1(\vec{r},t)}{\partial t^2} = \nabla^2 p_1(\vec{r},t) - \frac{1}{\rho_m + \Delta\rho_0(\vec{r})}\nabla\left(\rho_m + \Delta\rho_0(\vec{r})\right)\nabla p_1(\vec{r},t) \tag{A.14}$$

Knowing that $\rho_m >> \Delta\rho_0(\vec{r})$ and $c_m >> \Delta c_0(\vec{r})$, one can use Taylor expansion in order to approximate the following two expressions:

$$\begin{aligned}
\frac{1}{c_m+\Delta c_0(\vec{r})} = \frac{1}{c_m}\cdot\frac{1}{1+\frac{\Delta c_0(\vec{r})}{c_m}} &\underset{\left(\frac{\Delta c_0(\vec{r})}{c_m}\to 0\right)}{\approx} \frac{1}{c_m}\left(1-\frac{\Delta c_0(\vec{r})}{c_m}\right)\\
\frac{1}{\rho_m+\Delta\rho_0(\vec{r})} = \frac{1}{\rho_m}\cdot\frac{1}{1+\frac{\Delta\rho_0(\vec{r})}{\rho_m}} &\underset{\left(\frac{\Delta\rho_0(\vec{r})}{\rho_m}\to 0\right)}{\approx} \frac{1}{\rho_m}\left(1-\frac{\Delta\rho_0(\vec{r})}{\rho_m}\right)
\end{aligned} \tag{A.15}$$

Replacing the results of (A.15) in (A.14), yields:

$$\begin{gathered}
\nabla^2 p_1(\vec{r},t) - \frac{1}{c_m^2}\frac{\partial^2 p_1(\vec{r},t)}{\partial t^2} = \\
-\frac{2\Delta c_0(\vec{r})}{c_m^3}\cdot\frac{\partial^2 p_1(\vec{r},t)}{\partial t^2} + \frac{(\Delta c_0(\vec{r}))^2}{c_m^4}\frac{\partial^2 p_1(\vec{r},t)}{\partial t^2} + \left(\frac{1}{\rho_m} - \frac{\Delta\rho_0(\vec{r})}{\rho_m^2}\right)\nabla\left[\Delta\rho_0(\vec{r})\right]\cdot\nabla p_1(\vec{r},t)
\end{gathered} \tag{A.16}$$

Since $\left(\Delta c_0(\vec{r})\right)^2/c_m^4 \to 0$ and $\Delta\rho_0(\vec{r})/\rho_m^2 \to 0$, (A.16) becomes:

$$\nabla^2 p_1(\vec{r},t) - \frac{1}{c_m^2}\frac{\partial^2 p_1(\vec{r},t)}{\partial t^2} = -\frac{2\Delta c_0(\vec{r})}{c_m^3}\cdot\frac{\partial^2 p_1(\vec{r},t)}{\partial t^2} + \frac{1}{\rho_m}\nabla\left[\Delta\rho_0(\vec{r})\right]\cdot\nabla p_1(\vec{r},t) \tag{A.17}$$

As one can see, in (A.17), the left side of the equation represents the pressure evolution as a function of time and space while the right side represents the wave behavior when it encounters tissue inhomogeneities that appear as speed and density variations $\Delta c_0(\vec{r})$ and $\Delta\rho_0(\vec{r})$ respectively. This very relation is called the equation of acoustic wave propagation inside inhomogeneous media. For a perfectly homogeneous medium, equation (A.17) becomes:

$$\nabla^2 p_1(\vec{r},t) - \frac{1}{c_m^2}\frac{\partial^2 p_1(\vec{r},t)}{\partial t^2} = 0 \tag{A.18}$$

B On the principle of the Fast Iterative Shrinkage Thresholding Algorithm (FISTA)

In this Section a brief explanation of the Fast Iterative Shrinkage Thresholding Algorithm (FISTA) is presented. For a more in-depth comprehension of the please check the paper [Beck and Teboulle, 2009].

In fact, in the work presented in this manuscript, we met twice the problem where we had the measurements $\boldsymbol{y}$, a direct kernel $\boldsymbol{\Gamma}$ that models the ultrasound wave propagation phenomenon and a vector $\boldsymbol{\chi}$ that was either the impulse response of the medium or its reflectivity function. The relation that linked these three vectors was what we called here the direct model (either the restrained model, showed developed in the first contribution, or the advanced model showed in the second contribution). This relation was written as follows:

$$\boldsymbol{y} = \boldsymbol{\Gamma} \cdot \boldsymbol{\chi} + \boldsymbol{b} \tag{B.1}$$

where $\boldsymbol{b}$ is a noise that can be either acquisition noise (added in simulation or present during the experimental implementation) or even modeling noise (present in the advanced direct model).

To find the vector $\boldsymbol{\chi}$ that fits (B.1), in this work we only focused on the inverse problem of the form:

$$\boldsymbol{\chi} = \underset{\boldsymbol{\chi}}{\operatorname{argmin}} \left\{ \|\boldsymbol{\Gamma} \cdot \boldsymbol{\chi} - \boldsymbol{y}\|_2^2 + \lambda \|\boldsymbol{\chi}\|_1 \right\} \tag{B.2}$$

where the first term represents the square error between the measurements and the synthetic measurements that one would obtain by passing though the direct kernel the obtained solution. In (B.2), the second term in the objective function represents the regularization term and is a prior information that helps follow among the solution that fit the data fidelity term, the ones that also fits the prior information. λ is a coefficient that allows giving more or less weight to the prior information, filtering though all the possible solutions of the data-fidelity term the ones that are more or less sparse (since the regularization term is a l_1 norm). Since, as shown in the previous Chapters, the kernel $\boldsymbol{\Gamma}$ can be very large (in terms of number of non null elements), an algorithm that would solve (B.2) in a computational efficient way is required. One of the most popular methods of solving (B.2) is the class of Iterative Shrinkage-Thresholding Algorithms (ISTA) [Beck and Teboulle, 2009]. At each iteration $k+1$, these methods estimate the new value of the solution through a relatively cheap matrix-vector multiplication involving $\boldsymbol{\Gamma}$ and $\boldsymbol{\Gamma}^T$ and a shrinkage / soft-thresholding step:

$$\boldsymbol{\chi}_{k+1} = \Upsilon_{\lambda t}\left(\boldsymbol{\chi}_k - 2t\boldsymbol{\Gamma}^T \cdot (\boldsymbol{\Gamma} \cdot \boldsymbol{\chi}_k - \boldsymbol{y})\right) \tag{B.3}$$

where t is the step size and $\Upsilon_\alpha(\boldsymbol{x})_i$ is the shrinkage operator and $\boldsymbol{\chi}_i$ is the i^{th} element of the $\boldsymbol{\chi}$ vector. $\Upsilon_\alpha(\boldsymbol{x})_i$ is defined as follows:

$$\Upsilon_\alpha(\boldsymbol{x})_i = \big(|\boldsymbol{x}_i| - \alpha\big)_+ \text{sign}(\boldsymbol{x}_i) \tag{B.4}$$

As it can be seen in (B.4), if the weight λ of the prior information is null, the shrinkage operator becomes the identity function $\Upsilon_0(\boldsymbol{\chi})_i = \boldsymbol{\chi}_i$. This implies that in (B.3) at each iteration k the solution will be updated as $\boldsymbol{\chi}_{k+1} = \boldsymbol{\chi}_k - 2t\boldsymbol{\Gamma}^T \cdot (\boldsymbol{\Gamma} \cdot \boldsymbol{\chi}_k - \boldsymbol{y})$, which is a simple gradient descent step that minimizes the data fidelity term in the objective function. For ISTA, the step t is set to be the inverse value of the Lipschitz constant $L = 2\gamma(\boldsymbol{\Gamma}^T \cdot \boldsymbol{\Gamma})$, where $\gamma(\boldsymbol{\Gamma}^T \cdot \boldsymbol{\Gamma})$ represent the $\boldsymbol{\Gamma}^T \cdot \boldsymbol{\Gamma}$ matrix eigenvalues. This makes the ISTA method to converge at a rate $1/k$ which is not sufficiently fast.

In order to accelerate the convergence rate in FISTA, the shrinkage operator $\Upsilon_\alpha(\boldsymbol{x})_i$ is applied not directly on the previous estimation of the solution $\boldsymbol{\chi}_{k+1}$ but on a combination of the two previous estimations $\boldsymbol{\chi}_k$ and $\boldsymbol{\chi}_{k-1}$. This linear combination $\beta(\boldsymbol{\chi})$ is obtained using adjusted values of the step $t_k + 1$ and is defined as:

$$\begin{gathered} \beta(\boldsymbol{\chi}) = \boldsymbol{\chi}_k + \left(\frac{t_k - 1}{t_{k+1}}\right)(\boldsymbol{\chi}_k - \boldsymbol{\chi}_{k-1}) \\ \text{with: } t_{k+1} = \frac{1+\sqrt{1+4t_k^2}}{2} \end{gathered} \tag{B.5}$$

Thus, the FISTA $k+1$ estimation becomes:

$$\boldsymbol{\chi}_{k+1} = \Upsilon_{\lambda t}\big(\beta(\boldsymbol{\chi})\big) \tag{B.6}$$

As one can see between (B.1) and $\big((B.5),(B.6)\big)$, the difference between the additional computation made in the a FISTA iteration when compared to ISTA, is a simple vector / constant multiplication and a vector / vector addition. However, as shown in [Beck and Teboulle, 2009], the convergence rate of the FISTA estimation is $1/k^2$ which is faster than ISTA. The optimization using FISTA can be stopped in two ways:

1. by choosing a certain number k_{max} of iterations that the algorithm needs to do before it stops. While this type of stopping criteria does not insure a good estimation, it can be very useful if one wants to limit the optimization running time.

2. by choosing a value ϵ_{min} of the mean square difference between two solution estimations $\boldsymbol{\chi}_{k-1}$ and $\boldsymbol{\chi}_k$ obtained from two consecutive algorithm iterations. Then, once the mean square difference between $\boldsymbol{\chi}_{k-1}$ and $\boldsymbol{\chi}_k$ drops bellow ϵ_{min} the algorithm stops.

C Regularized inversion of the direct model

As the name implies, in this Section the solution of the inverse problem related to (3.10) is computed by adding a mathematical regularization term. Indeed, as seen in the previous Subsection, pseudo-inverse based methods fail to provide good estimations of the pulse -echo impulse responses of the medium when the frame rate increases (compared to the conventional, successive method). This is a result of the fact that performance of these methods is directly related to the well-posedness (low condition number, unique solution) of the inverse problem. It turns out that, when one increases the frame rate of the method, the inverse problem becomes under determined thus, its solution becomes not unique (as seen in (3.23)) and the obtained estimations of the pulse echo impulse responses of the medium become not optimal. A way to reduce the solution space of a underdetermined inverse problem is by adding a mathematical regularization term [Beck and Teboulle, 2009]. Basically, this allows selecting between the total possible solutions (3.23) the one that follows the most the prior criterion included in the regularization term. This implies that in order to find the exact solution of the inverse problem one needs to have strong prior information on its behavior. Sorely, in most applications, this is not the case. In ultrasound, regularized type inversions are usually used in order to estimate the TRF [David et al., 2015, Besson et al., 2016, Besson et al., 2018]. However, since before imaging the medium, one can only guess what are the intrinsic properties of the medium's ROI, finding a general regularization term for ultrasound problems is still a hot topic. Thus, usually a sparsity prior on the ROI's TRF is made [David et al., 2015, Besson et al., 2016, Besson et al., 2018]. A typical formulation of a regularized inverse problem in ultrasound can be written as:

$$\hat{\boldsymbol{\gamma}}_{ROI} = \underset{\boldsymbol{\gamma}_{ROI}}{\operatorname{argmin}} \left\{ \|\boldsymbol{\Phi} \cdot \boldsymbol{\gamma}_{ROI} - \boldsymbol{o}\|_2^2 + \lambda \|\boldsymbol{\gamma}_{ROI}\|_1 \right\} \tag{C.1}$$

where $\boldsymbol{\gamma}_{ROI}$ represents the TRF of the medium's ROI, $\boldsymbol{o}$ represents this TRF's observation and $\boldsymbol{\Phi}$ is the kernel of the direct model that ties $\boldsymbol{o}$ to $\boldsymbol{\gamma}_{ROI}$. As it can be seen, the inverse problem in (C.1) contains two terms. The first one is the data attachment term and simply put, represents the non regularized inverse problem solved in the previous Subsection. As shown in (3.23)), an infinite number of solutions may minimize this term, thus the role of the second term (regularization term) is to find among these solutions the one that has the minimal l_1 norm (which implies that the solution is sparse). Finally, the weight λ allows forcing the solution to be more ($\lambda \longrightarrow 1$) or less ($\lambda \longrightarrow 0$) sparse.

At this point, one can find the equivalents for the terms $\boldsymbol{\Phi}$, $\boldsymbol{o}$ and $\boldsymbol{\gamma}_{ROI}$ (C.1) in the direct model (3.10), and solve the inverse problem in order to find the impulse responses of the medium. It can be observed that the following relations appear $\boldsymbol{\Phi} \Longleftrightarrow \boldsymbol{\Gamma}$, $\boldsymbol{o} \Longleftrightarrow {}_S\boldsymbol{y}_i$ and $\boldsymbol{\gamma}_{ROI} \Longleftrightarrow \boldsymbol{g}_i$. However, before drawing this parallels, consider the impulse response $\boldsymbol{g}_{64}^3$ showed in Fig.3.9. Zooming in on one of the echoes generated by the three scatterers inside the medium, the plot shown in Fig.C.1(a) is obtained. Here, as expected (it comes from (3.2)), it can be seen that the shape of the recorded echo follows

roughly the shape of the pulse-echo acousto-electrical impulse response ($h(t) *_t h(t)$) of the ultrasound probe. Now, if the convolution $h(t) *_t h(t)$ was a Dirac impulsion, the received echo would have been the one shown in Fig.C.1(b). The shape of this echo depends only on the spatial impulse response of the ultrasound probe at the given scatterer position and is addressed more in details in the next Chapter. Here, the idea is to observe that the convolution $h(t) *_t h(t)$ alters the shape of the echo, and more importantly that it changes the mathematical norm of the echo. Indeed the l_1 norm of the first echo is 6.46 and of the second 4.32. This leads to the conclusion, that if one wants to use a l_1 sparse

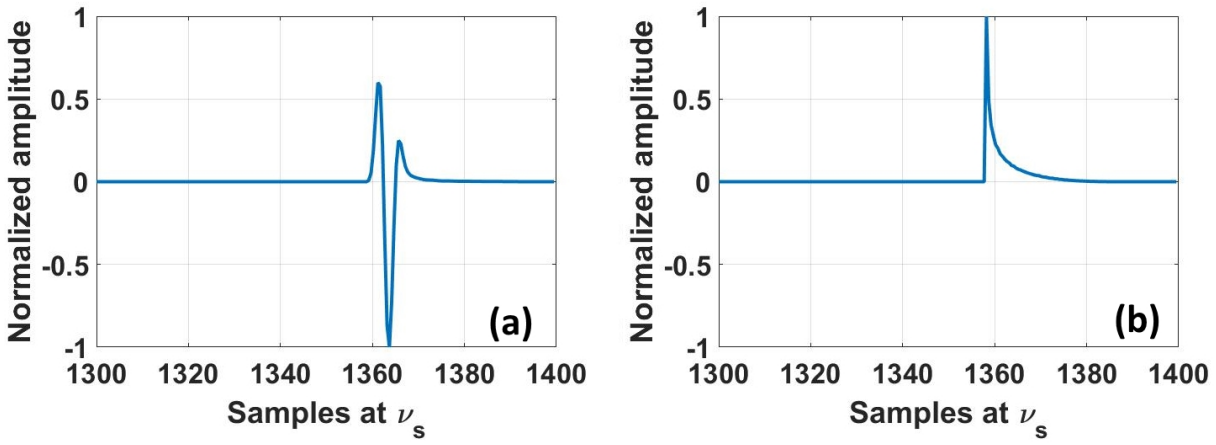

Figure C.1: Zoom on the signal $\boldsymbol{g}_{64}^3$ showed in Fig.3.9: (a) - If the pulse echo acousto-electrical ($h(t) *_t h(t)$) impulse response of the probe is band-limited (which is always the case in real world), (b) - If the pulse echo acousto-electrical ($h(t) *_t h(t)$) impulse response of the probe is a Dirac impulsion (purely hypothetical case).

based minimization in order to solve the inverse problem (C.1), it would be more accurate to search a solution of same type as the one showed in Fig.C.1(b).

In order to have a direct model that links echoes of waveform as the one shown in Fig.C.1(a) to the recorded RF data ${}_S\boldsymbol{y}_i$, one needs to consider the relations (3.2), (3.3) and (3.9). In (3.2), it can be seen that, by shifting the convolution product $h(t) *_t h(t)$ into the excitation waveform, the new relation for the received echoes (generated by the plane wave k) becomes:

$$
\begin{aligned}
y_i^k(t) &= e^k(t) *_t x_i^k(t) \\
\text{with: } x_i^k(t) &= w_i \sum_{j=1}^{N_{el}} \left[w_j \delta(t - t_j^k) *_t \int_V \gamma(\vec{r}) g_{ji}(\vec{r}, t)\, \mathrm{d}^2\vec{r} \right]
\end{aligned}
\tag{C.2}
$$

where $e^k(t) = a^k(t) *_t h(t) *_t h(t)$ is the new excitation of the plane wave k and $x_i^k(t)$ is the new pulse echo impulse response of the medium where each scatterer has a signature similar to the one shown in Fig. C.1(b). Following the same reasoning as the one presented in Subsection 3.1 it can be deuced that:

$$
\begin{aligned}
{}_S\boldsymbol{y}_i &= \boldsymbol{E} \cdot \boldsymbol{x}_i + \boldsymbol{b}_i \\
\text{with: } \boldsymbol{E} &= \begin{bmatrix} \boldsymbol{E}^1 & \boldsymbol{E}^2 & \cdots & \boldsymbol{E}^{N_{pwi}} \end{bmatrix} \text{ and } \boldsymbol{x}_i = \begin{bmatrix} \boldsymbol{x}_i^1 \\ \boldsymbol{x}_i^2 \\ \vdots \\ \boldsymbol{x}^{N_{pwi}} \end{bmatrix}
\end{aligned}
\tag{C.3}
$$

where each matrix $\boldsymbol{E}^k$ is computed as in (3.5) using the signals $\boldsymbol{e}^k$.

At this point, one can write the expression of the regularized inverse problem of the form (C.1) based

on (C.3):

$$\hat{\boldsymbol{x}}_i = \underset{\boldsymbol{x}_i}{\operatorname{argmin}}\{\|\boldsymbol{E}\cdot\boldsymbol{x}_i - {}_S\boldsymbol{y}_i\|_2^2 + \lambda\|\boldsymbol{x}_i\|_1\} \tag{C.4}$$

Since, as previously seen, the size of the matrix $\boldsymbol{E}$ depends on the length N_y of the recorded signals ${}_S\boldsymbol{y}_i$, on the number N_{pwi} and on the depth of the imaged medium (materialized in the length N_x of the signals $\boldsymbol{x}_i$), the number of entries that $\boldsymbol{E}$ contains is very high (couple of millions for $N_y = 1000$ and $N_{pwi} = 5$). This demands algorithms to solve (C.4) that does not require heavy computations on **E** (i.e:inverse, singular value decomposition, LU factorization). We decided to use the Fast Iterative Shrinkage Thresholding Algorithm (FISTA) [Beck and Teboulle, 2009] that uses cheap matrix-vector multiplications involving $\boldsymbol{E}$ and $\boldsymbol{E}^T$. Each step of FISTA adjusts the solution depending on the derivative of the data-discrepancy term ($\|\boldsymbol{E}_c\cdot\boldsymbol{x}_i - {}_S\boldsymbol{y}_i\|_2^2$) and its convergence rate was proven to be faster than classical iterative shrinkage algorithms [Beck and Teboulle, 2009]. A complete description of FISTA is presented in Section B. The stopping criterion for the algorithm was set to be a maximum number of optimization iterations of 100.

In order to assess the performance of the regularized inversion, simulation were made on two types of media: with a sparse (tens of scatterers in the medium's ROI) and a dense (several hundreds of thousands of scatterers in the medium's ROI) distribution of scatters. Two types of emissions of plane waves were tested: successive and simultaneous. The mixed echoes (with a $eSNR = 20dB$), received after the simultaneous emission of plane waves, were separated using two methods: non regularized inversion and regularized inversion.

In Fig.C.2 the results obtained when the condition $N_y = N_e + N_x - 1$ is no longer verified are

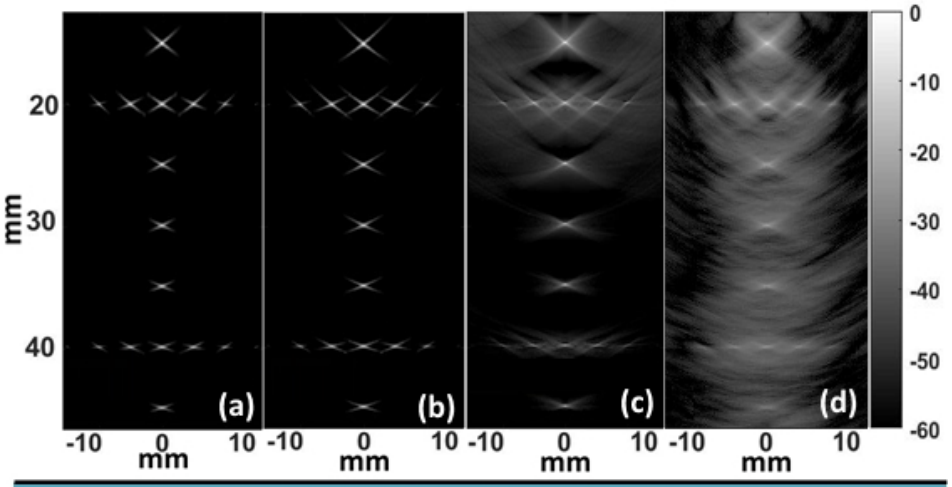

	5 CP-CPWC	4 CP-CPWC	SCE-CPWC FISTA	SCE-CPWC LSE
Axial res.	144 µm	141 µm	118 µm	118 µm
Lateral res.	379 µm	379 µm	352µm	352 µm

Figure C.2: Final images obtained on the wire phantom: (a) - Successive emission of $N_{pwi} = 5$ plane waves, (b) - Successive emission of $N_{pwi} = 4$ plane waves, (c) - Simultaneous emission of $N_{pwi} = 5$ plane waves with $\tau = 20\%$ reconstructed with FISTA and (d) - Simultaneous emission of $N_{pwi} = 5$ plane waves with $\tau = 20\%$ reconstructed with the non regularized method (pseudo-inverse).

presented . One can observe that the image resolution obtained using the simultaneous emission, regardless of the inversion method (regularized or not regularized) (Fig.2.3(c) and (d)), is better that the one obtained with the successive emission of plane waves (Fig. 2.3(a) and (b)): 22%/7% boost of respectively axial/lateral resolution (according to the table in Fig.C.2). This improvement results from the mathematical model of the geometrical impulse responses $x_i^k(t)$ (C.2) that does not include the

acousto-electrical impulse response of the probe elements at emission and reception $h(t)$. Thus, the new resolution of the image depends only on the spatial impulse response of the probe itself. Finally, the clear advantage of the reconstruction using the regularized inversion over the non regularized inversion can be seen in (Fig.C.2(a) and (d)). While the reason why the non regularized inversion fails to reconstruct the optimal solution when one increases the time gain was shown previously in Chapter 3, here the results are better since the regularized inversion gives the optimal solution (if it follows the prior properties set by the regularization term). The evolution of the CNR as a function of time gain τ

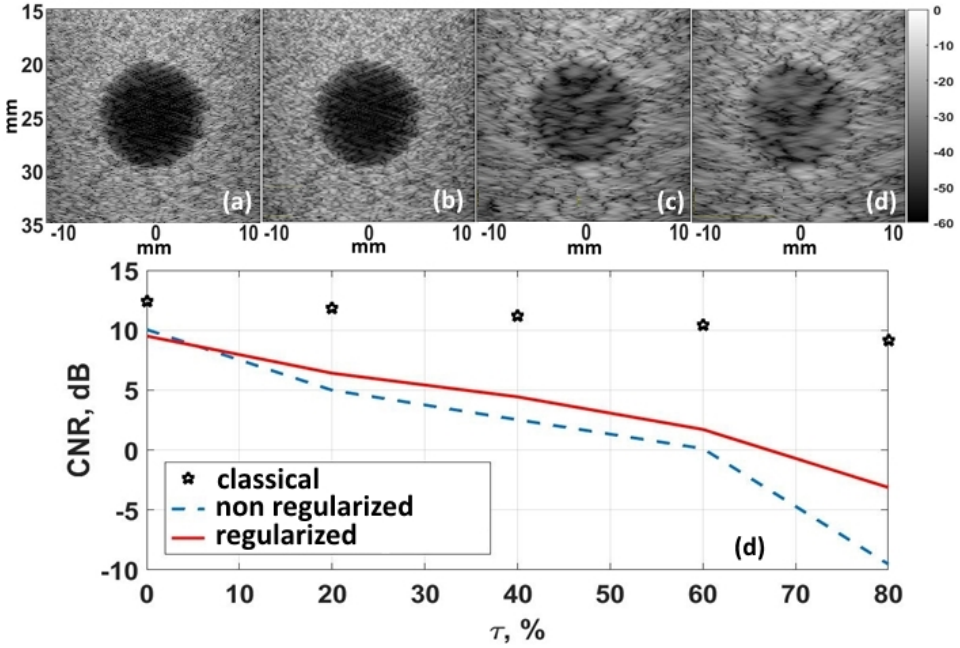

Figure C.3: Final images obtained on the cyst phantom: (a) - Successive emission of $N_{pwi} = 5$ plane waves, (b) - Successive emission of $N_{pwi} = 4$ plane waves, (c) - Simultaneous emission of $N_{pwi} = 5$ plane waves with $\tau = 20\%$ reconstructed with FISTA and (d) - Simultaneous emission of $N_{pwi} = 5$ plane waves with $\tau = 20\%$ reconstructed with the non regularized method (pseudo-inverse), (e) - Evolution of the CNR as a function of time gain. Note that for classical plane wave imaging the time gain is achieved by reducing the number of consecutive acquisitions.

(Fig.C.3(e)) shows again that the l_1-regularized reconstruction works better than a simple inversion using the pseudo-inverse. For instance, at $\tau = 20\%$ the regularized method provides a CNR of $6.41dB$ (Fig.C.3(c)) against $4.99dB$ obtained with the non-regularized inversion (Fig.C.3(d)). Nonetheless, both these results remain under the value of $CNR = 11.87dB$ obtained using the classical approach when only $N_{pwi} = 4$ plane waves are emitted successively(Fig.C.3(b)). Moreover, both regularized and non regularized methods fail to achieve similar CNR values as the conventional approach when the time gain increases, as it can bee seen in Fig.C.3(e). While for the non regularized approach this behavior is normal (ill-posed problem), the regularized inversion fails to perform better because in this case the l_1-norm is not accurate (dense distribution of scatterers) thus we are obliged to tune down the λ parameter in (C.4) as compared with the case from Fig.C.2(c). Finally, it can be observed in Fig.C.3(d) that the regularized inversion provides better image quality for any value of the time gain.

D Jointly optimized modulation / filtering technique for pseudo-orthogonal binary sequences

The first implementations [Miwa et al., 1981, Shen and Ebbini, 1996, Misaridis and Jensen, 1999] and [O'Donnell, 1992] of the temporal encoded excitation signals in ultrasound emission schemes had the only objective to increase the echo signal to noise ratio of the received signals. However, as the need for a better medical diagnostic grew, the requirement for a faster frame acquisition rate was raised. In [Gran and Jensen, 2008], a first try of achieving higher frame acquisition rates in synthetic transmit aperture using coding excitations, was successfully developed. The core principle on which this method relies is the simultaneous emission of temporal encoded waves. Later, the same principle was successfully applied to plane wave acquisition schemes [Bujoreanu et al., 2017b, Bujoreanu et al., 2017a, Bujoreanu et al., 2017c], where it was shown that the provided image quality depends closely on the excitation signals orthogonality. In fact, these techniques use inverse problem approaches in order to separate, from the received radio-frequency data, the echoes generated by each of the simultaneously emitted diverging / plane wave. However, the condition number of the direct model kernel, and thus the quality of the echo estimations are directly dependent on the auto / inter-correlation products of the excitation signals. In addition, in [Bujoreanu et al., 2017a] was shown that the best inversion results would be achievable with excitation signals that are perfectly orthogonal which implies that their auto-correlation is a very short impulsion and their inter-correlations is null for all time lags. In these works, the only excitation signals studied were phase modulated pseudo-random binary sequences. Therefore, here we study other types of binary sequence modulations with the objective to find the carrier that allows obtaining the best achievable orthogonality between the excitation signals. Moreover, in the context where the band-limited ultrasound probe can impair the correlation product of the emitted signals [Nowicki et al., 2007], to maintain the correlation properties of the excitation signals, we implement a pre-enhancement technique that overcomes the band-limited effect of the ultrasound probe. Furthermore, to account for the simultaneous reception of echoes generated by waves carrying different waveforms, we propose to use optimal Wiener Filters for compression.

D.1 On the choice of binary sequences

In ultrasound, a number of binary sequences has been already tested. Here one can mention the Hadamard codes [Tiran et al., 2015], the Golay codes [Chiao and Thomas, 2000], the Kasami codes [Álvarez et al., 2013] and the Gold codes [Schröder and Henning, 2014]. However, while being able to compress without generation of side-lobes, Hadamard and Golay codes are not able to provide a frame rate increase due to their complementarity property. The focus now remains on the Kasami and Gold codes, which are themselves obtained from pseudo-orthogonal m-sequences [Kettunen, 1997]. Since,

except for a slight variation in the auto-correlation / inter-correlation ratio, both Gold and Kasami codes can be seen as larger m-sequences sets, the choice between the sequence type depends on the number of simultaneously emitted excitation signals. Thus, given that for this case 2, 4, 6, 8, 10 and 12 simultaneous emissions are studied, the m-sequences set of length $n = 127$ bits is more than enough to generate 12 different binary sequences (for the set $m = 127$, there are 18 different m-sequences).

D.2 On the choice of the carrier signal

Perhaps the most common binary sequence modulation technique in the ultrasound domain is the phase shift keying (BPSK). This method consists in assigning to each arch of a sinusoid centered inside the ultrasound probe bandwidth a weight that correspond to a bit of the binary sequence. In recent works [Nowicki et al., 2007, Lashkari et al., 2012], it was shown that is also possible to modulate the binary sequences using a half cycle sinusoid, in other words each half-arch of a sinusoid is weighted with a bit of the binary sequence. In [Lashkari et al., 2016] was also shown that in order to increase even more the echo signal to noise ratio of the received echoes, it is possible to modulate a binary sequence using chirp signals.

In this study we covered the following seven types of modulation of the binary sequence $a^k = a_0^k, a_1^k, \cdots, a_{n-1}^k | a_i^k \in \{-1, 1\}$:

1. square wave modulation:

$$s_1^k(t) = \sum_{i=0}^{n-1} a_i^k \delta(t - iT_0) *_t \Big(\text{sgn}\big(\sin(2\pi \frac{t}{T_0})\big)\text{rect}\big(\frac{t}{T_0}\big)\Big) \tag{D.1}$$

   where $*_t$ represents the convolution in the time domain, $\delta(t)$ represents the Dirac delta function, $T_0 = 1/f_0$ is the period of a sinusoid centered at in the middle of the probe bandwidth B. In (D.1), $\text{sgn}(t)$ is the signum function, and $\text{rect}(t)$ is the rectangular function.

2. half arch of a sinusoidal signal:

$$s_2^k(t) = \sum_{i=0}^{n-1} a_i^k \delta(t - iT_0) *_t \Big(\sin(2\pi \frac{t}{T_0})\text{rect}\big(\frac{2t}{T_0}\big)\Big) \tag{D.2}$$

3. one arch of a sinusoidal signal:

$$s_3^k(t) = \sum_{i=0}^{n-1} a_i^k \delta(t - iT_0) *_t \Big(\sin(2\pi \frac{t}{T_0})\text{rect}\big(\frac{t}{T_0}\big)\Big) \tag{D.3}$$

4. three arches of a sinusoidal signal:

$$s_4^k(t) = \sum_{i=0}^{n-1} a_i^k \delta(t - iT_0) *_t \Big(\sin(2\pi \frac{t}{T_0})\text{rect}\big(\frac{t}{3T_0}\big)\Big) \tag{D.4}$$

5. chirp with a linear increase in frequency:

$$s_5^k(t) = \Big[\sum_{i=0}^{n-1} a_i^k \delta(t - iT_0)\Big] \cdot \Big(\cos\big(2\pi f_{lin}(t)\big)\text{rect}\big(\frac{t}{nT_0}\big)\Big) \tag{D.5}$$

   where $f_{lin}(t) = f_0 - \frac{B}{2} + \frac{B}{nT_0} t$ is the instantaneous frequency of the chirp. It is to be noted that this chirp modulation is different than the one proposed in [Lashkari et al., 2016], since for each binary sequence bit the instantaneous frequency is different, different bits of the sequence

being modulated with different frequencies. In [Lashkari et al., 2016] however, each sequence bit contains all the chirp frequencies, which makes the signal longer.

6. chirp with a logarithmic increase in frequency:

$$s_5^k(t) = \Big[\sum_{i=0}^{n-1} a_i^k \delta(t - iT_0)\Big] \cdot \Big(\cos\big(2\pi f_{log}(t)\big)\mathrm{rect}\big(\frac{t}{nT_0}\big)\Big) \tag{D.6}$$

with $f_{log}(t) = f_0\big(\frac{f_0+B}{f_0}\big)^{\frac{t}{nT_0}}$.

7. chirp with a quadratic increase in frequency:

$$s_5^k(t) = \Big[\sum_{i=0}^{n-1} a_i^k \delta(t - iT_0)\Big] \cdot \Big(\cos\big(2\pi f_{quad}(t)\big)\mathrm{rect}\big(\frac{t}{nT_0}\big)\Big) \tag{D.7}$$

with $f_{quad}(t) = f_0 + B\frac{t^2}{(nT_0)^2}$

It is to be noted that since the carrier of the signal $e_2^k(t)$ is a half arch of a sinusoid, for the same number of bits in the binary sequence, the signals $s_1^k(t)$, $s_3^k(t)$, $s_5^k(t)$, $s_6^k(t)$ and $s_7^k(t)$ would be twice as long as $s_2^k(t)$. Thus, in order to have all the signals of the same length we decided for the half arch sinusoid modulation to use sequences twice as long. The same principle was applied to $s_4^k(t)$.

D.3 On the excitation signal pre-enhancement

In [Nowicki et al., 2007, Oelze, 2007], it was shown that since the ultrasound probes are less efficient in some frequency bands than in others, the result of the pulse compression may be impaired in terms of temporal resolution and side-lobe level. Thus, in [Oelze, 2007, Benane et al., 2018] was proposed and successfully applied in experiments an emission technique that compensates the less efficient bands of ultrasound probe. This method consists in the deconvolution of the signal $e_j^k(t)$ by the pulse-echo acousto-electrical impulse response of the probe $h(t)$. The, pre-enhanced excitation signal becomes:

$${}_oS_j^k(f) = S_j^k(f)\frac{H^*(f)}{|H(f)|^2+\gamma} \tag{D.8}$$

where the upper case letters represent the Fourier Transforms of the temporal signals noted with the corresponding lower case letter. γ is a parameter that is manually set in order to avoid dividing by zero.

D.4 On the optimal pulse compression filtering

The emission / reception of the signals ${}_os_j^k(t)$ can be seen as the convolution between ${}_os_j^k(t)$ and the pulse-echo impulse response $h(t)$ of the probe. Since in (D.8) the deconvolution is not perfect (due to the presence of the term γ at the denominator) the received waveforms of the echoes are not $s_j^k(t)$ but approximate copies $\hat{s}_j^k(t)$. Indeed, as it was shown in Subsection 4.7.2, the received signals can be modeled as a superposition (over all the simultaneously emitted signals ${}_os_j^k(t)$) of the temporal convolutions between the signals $\hat{s}_j^k(t)$ and the impulse responses of the medium. However, in such case an optimization of the compression filters would be sophisticated. Instead, here we propose to model the received echoes as a linear superposition of the signals $\hat{s}_j^k(t)$. In such case, the optimal filters become:

$$\Psi_j^k(f) = \frac{\big(\hat{S}_j^k(f)\big)^*}{\sum_m |\hat{S}_j^m(f)|^2 + \beta} \tag{D.9}$$

where $()^*$ represents the complex conjugate, β is a hyper-parameter that depends on the acquisition noise, and as γ helps to avoid dividing by zero. As shown in [Oelze, 2007, Benane et al., 2018], by adding this term, it is possible to trade some of the temporal resolution in favor of the noise stability.

The complete pipeline of the proposed approach is summarized in Fig. D.1.

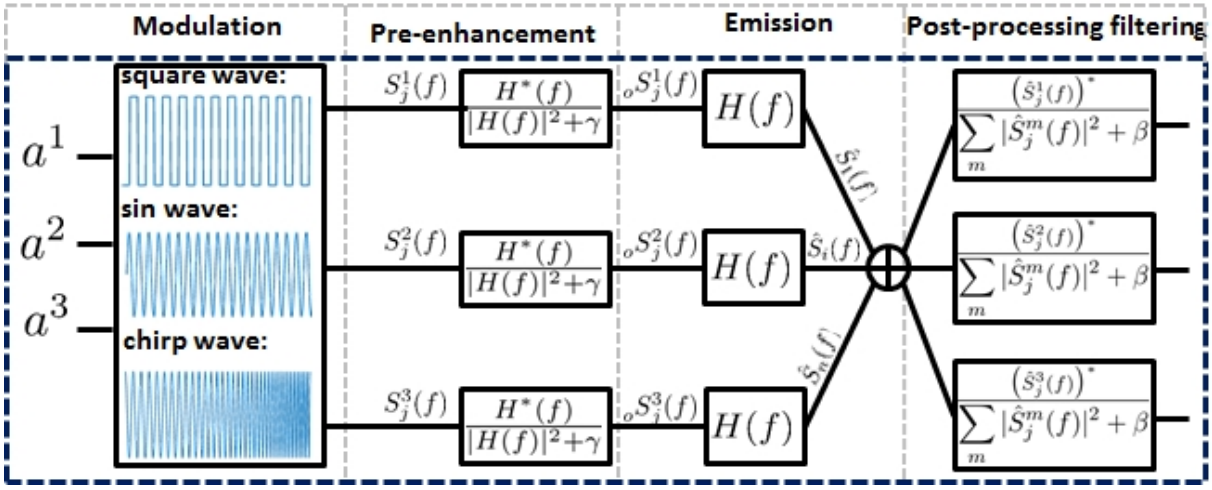

Figure D.1: The pipeline of the proposed approach illustrated for three simultaneously emitted excitation signals. After the binary sequence (a_i^k) modulation (Modulation), the signals $S_i^k(f)$ are deconvolved with the probe pulse-echo transfer function $H(f)$ (Pre-enhancement). The simultaneous emission / reception, simulated by the convolution with $H(f)$ and by the addition (Em. / Rec.), generates a mix of echoes $\hat{S}_i^k(f)$ (of waveform similar to $S_i^k(f)$). Thus, the influence of $H(f)$ is compensated. Optimal filtering is performed in reception (Post-processing filtering).

D.5 On the study results

For this study the st of m-sequences of length 127 bits was tested. The parameters of the employed ultrasound probe are summarized in Table 3.1. The modulation frequency f_0 was 8.5 MHz. These parameters resulted in a length of the $s_j^k(t)$ signals of $15\mu s$. In order to underline the advantages of the proposed jointly optimized modulation / filtering technique, two approaches were tested:

1. classical modulation / pulse compression approach. Here the sequences a^k are following almost the same pipeline shown in Fig.D.1, except that the "Pre-enhancement" block is not applied and in the "Post-processing filtering" the compression is done using the basic matched filter $\left(\hat{S}_j^k(f)\right)^*$.
2. jointly optimized modulation / filtering technique. Here the complete pipeline shown in Fig.D.1 is applied.

The provided performances are assessed in terms of Resolution (Res.) which represents the width at half height of the main compression lobe, side-lobe level (S. Lob.) which is the difference between the main lobe level and the maximum level of the side-lobes. Finally, the crosstalk (Crosstalk), which results of the interference between simultaneously emitted signals $sçk_j(t)$, was also measured. For the computation of the Crosstalk, the relation (4.50) was adapted to this study.

The obtained results are shown in Fig.D.2. As one can observe, without any optimization, the best resolution and crosstalk are obtained when the modulation is done with a half cycle sinusoid. In the same conditions, the modulation using a full sinusoidal cycle provides the best side-lobe level. Moreover, it can be observed that the proposed optimization provides improvements for all the studied

Mod. / S.emm	Square pulse	Square pulse-OPT	Sinosoid 0.5 cycles	Sinosoid 0.5 cycles-OPT	Sinosoid 1 cycles	Sinosoid 1 cycles-OPT	Sinusoid 3 cycles	Sinusoid 3 cycles-OPT	Metrics
2	235.3	**81.4**	108.6	**63.3**	190.1	**99.5**	253.4	**100.5**	Res [ns]
	-4.9	**-6.5**	-5.75	**-6.9**	-9.1	**-11.8**	-5.2	**-10.8**	S.Lob. [dB]
	9.2	**6.3**	6.8	**4.2**	8.9	**5.6**	12.1	**5.6**	Crosstalk
4	280.5	**153.8**	99.5	**81.8**	162.9	**99.5**	226.2	**101.4**	Res [ns]
	-4.7	**-3.4**	-6.1	**-5.8**	-8.4	**-10.8**	-5.1	**-9.1**	S.Lob. [dB]
	18.8	**13.7**	14.3	**8.7**	24.6	**9.5**	24.2	**9.2**	Crosstalk
6	352.9	**171.9**	135.7	**81.8**	217.2	**108.6**	320.1	**171.9**	Res [ns]
	-4.2	**-4.1**	-5.1	**-5.5**	-5.7	**-8.2**	-2.7	**-4.4**	S.Lob. [dB]
	28.1	**19.6**	20.2	**13.1**	30.5	**14.3**	27.8	**16.84**	Crosstalk
8	552	**226.2**	280.5	**126.7**	398.2	**135.7**	438.2	**153.8**	Res [ns]
	-1.7	**-3.9**	-3.2	**-5.1**	-5	**-5.2**	-2.4	**-3.6**	S.Lob. [dB]
	57.9	**31.1**	43.8	**22.9**	77.3	**22.1**	92.6	**22.6**	Crosstalk
10	597.3	**280.5**	2563.4	**162.9**	422.2	**144.8**	638	**176.7**	Res [ns]
	-1.7	**-3.1**	-2.6	**-4.8**	-2.8	**-4.9**	-0.5	**-5.1**	S.Lob. [dB]
	47.3	**24.7**	34.5	**19.2**	116.1	**20.9**	169.8	**23.3**	Crosstalk
12	733	**352.9**	316.7	**208.1**	1075.1	**181**	742.1	**362**	Res [ns]
	-0.5	**-3.3**	-1.8	**-4.8**	-0.5	**-4.9**	-0.6	**-3.2**	S.Lob. [dB]
	84.1	**42.4**	58.9	**32.1**	258.9	**34.4**	237.2	**41.8**	Crosstalk

Mod. / S.emm.	Linear chirp	Linear chirp-OPT	Logarithmic chirp	Logarithmic chirp-OPT	Quadratic chirp	Quadratic chirp-OPT	Metrics
2	171.9	**81.4**	171.9	**81.4**	190	**81.4**	Res [ns]
	-9.11	**-14.1**	-9.6	**-13.7**	-8.4	**-13**	S.Lob. [dB]
	9.9	**5.5**	9.3	**5.5**	10.6	**5.8**	Crosstalk
4	171.9	**90.5**	171.9	**81.4**	190	**81.4**	Res [ns]
	-6.8	**-11.6**	-5.7	**-9.1**	-6.6	**-10.5**	S.Lob. [dB]
	25.7	**11.9**	24.6	**12.6**	21.8	**13.6**	Crosstalk
6	306.8	**81.4**	217.2	**81.4**	298.6	**81.4**	Res [ns]
	-4.5	**-9.5**	-4.2	**-7.9**	-4.5	**-9.7**	S.Lob. [dB]
	43.3	**17.9**	44.5	**19.7**	38.5	**19.4**	Crosstalk
8	506.8	**81.4**	271.5	**81.4**	239.8	**99.5**	Res [ns]
	-2.8	**-6.7**	-2.4	**-7.3**	-3.1	**-5.7**	S.Lob. [dB]
	81.7	**30.1**	94.4	**33.6**	75.3	**37.1**	Crosstalk
10	850.7	**81.4**	244.3	**108.6**	411.8	**126.7**	Res [ns]
	-2.9	**-6.1**	-1.8	**-5.8**	-2.4	**-5.1**	S.Lob. [dB]
	76.6	**28.1**	98	**32.9**	84.8	**38.6**	Crosstalk
12	900.2	**271.5**	547.5	**108.6**	708.5	**468.7**	Res [ns]
	-0.1	**-4.5**	-1.3	**-5.1**	-1.1	**-1.1**	S.Lob. [dB]
	153.2	**54.1**	156.1	**63.6**	144.2	**81.7**	Crosstalk

Figure D.2: Tables summarizing the results of the presented study. The suffix "-OPT" stands for the OPTimization of the classical modulation / pulse compression technique achieved thanks to the jointly optimized modulation / filtering. Each column represents a modulation type (by groups of two: classical and OPTimized) and each row (S. emm.) represents a different number of simultaneously emitted excitation signals.

modulation (for the three metrics). Concerning the results obtained using the optimized modulation / compression technique, it can be seen that the chirp modulation provides a better overall resolution and side-lobe level, while the crosstalk being minimum for the sinusoidal modulation.

D.6 Conclusion

The result of this study summarize the performance of a number of methods for the binary sequence modulation applied to ultrasound imaging. A jointly optimized modulation / filtering technique was

proposed to ameliorate the obtained results. Further, studies could explore the performance of a mixed modulation technique based on a mix between the phase and frequency modulation.

Personal Publications Part IV

Journals

1. Benane, Y. M., **Bujoreanu, D.**, Lavarello, R. J., Varray, F., Escoffre, J. M., Novell, A., Cachard, C., Basset, O. (2018). Experimental Implementation of a Pulse Compression Technique Using Coherent Plane-Wave Compounding. IEEE transactions on ultrasonics, ferroelectrics, and frequency control, 65(6), pp. 1025-1036.

2. **Bujoreanu, D.**, Nicolas, B., Benane, Y. M., Liebgott, H., Friboulet, D. An Advanced Direct Model and its Inversion for Coded Ultrasound Imaging (in revision).

3. Benane, Y. M., **Bujoreanu, D.**, Badescu, E., Nicolas, B., Cachard, C., Liebgott, H., Basset, O. A robust chirp compression technique combined to ultrasound multi-line transmission to enhance spatial resolution and image contrast (ready for submission).

4. **Bujoreanu, D.**, Dorez, H., Boutegrabet, W., Moussata, D., Sablong, R., Rousseau, D. (2017). Robust graph representation of images with underlying structural networks. Application to the classification of vascular networks of mice's colon. Pattern Recognition Letters, 87, 29-37.

5. Parisse, N., Gourrier, A., Genthial, R., Debarre, D., **Bujoreanu, D.**, Rousseau, D. Graph encoding of multiscale structural networks from binary images Application to the lacuno-canalicular cellular network in bone (in revision).

International Conferences

1. **Bujoreanu, D.**, Benane, Y. M., Nicolas, B., Liebgott, H., Friboulet, D. Jointly optimized modulation/filtering technique for pseudo-orthogonal binary sequences. International Ultrasonics Symposium, 2018.

2. **Bujoreanu, D.**, Benane, Y. M., Liebgott, H., Nicolas, B., Basset, O., Friboulet, D. A resolution enhancement technique for ultrafast coded medical ultrasound. European Signal Processing Conference, 2018.

3. **Bujoreanu, D.**, Nicolas, B., Friboulet, D., Liebgott, H. Inverse problem approaches for coded high frame rate ultrasound imaging. Asilomar Conference on Signals, Systems, and Computers, 2017.

4. **Bujoreanu, D.**, Rasti, P., Rousseau, D. On the value of graph-based segmentation for the analysis of structural networks in life sciences. European Signal Processing Conference, 2017.

5. **Bujoreanu, D.**, Bernard, A., Nicolas, B., Liebgott, H., Friboulet, D. Simultaneous coded plane wave imaging: Implementation on a research echograph. International Ultrasonics Symposium, 2017.

6. **Bujoreanu, D.**, Liebgott, H., Nicolas, B. Simultaneous coded plane wave imaging in ultrasound: Problem formulation and constraints. International Conference on Acoustics, Speech and Signal Processing, 2017.

7. Benane, Y. M., **Bujoreanu, D.**, Lavarello, R., Bernard, A., Cachard, C., Basset, O. Enhaced second harmonic imaging using a pulse compression technique combined with ultrasound pulse inversion. International Ultrasonics Symposium, 2018.

8. Benane, Y. M., **Bujoreanu, D.**, Liebgott, H., Cachard, C., Basset, O. Ultrasound probe bandwidth enhancement combined with non-stationary compression filters to improve image quality. International Ultrasonics Symposium, 2018.

9. Benane, Y. M., **Bujoreanu, D.**, Badescu, E., R. Lavarello, Liebgott, H., Cachard, C., Basset, O. Experimental implementation of resolution enhancement compression for ultrasound diverging wave compounding using a tri-state voltage drive. International Ultrasonics Symposium, 2018.

10. Benane, Y. M., **Bujoreanu, D.**, Cachard, C., Nicolas, B., Basset, O. An enhanced chirp modulated Golay code for ultrasound diverging wave compounding. European Signal Processing Conference, 2018.

11. Benane, Y.M., **Bujoreanu, D.**, Lavarello, R., Cachard, C., Basset, O. An attenuation adapted pulse compression technique to enhance the bandwidth and the resolution using ultrafast ultrasound imaging. International Conference on Acoustics, Speech and Signal Processing, 2018 (**Prize for the best student paper**).

12. Badescu, E., **Bujoreanu, D.**, Petrusca, L., Friboulet, D., Liebgott, H. Multi-line transmission for 3D ultrasound imaging : An experimental study. International Ultrasonics Symposium, 2017.

13. Y. M. Benane, R. Lavarello, **Bujoreanu, D.**, Cachard, C., Varray, F., Escoffre, J-M., Novell, A., Basset, O. Ultrasound bandwidth enhancement through pulse compression using a CMUT probe. International Ultrasonics Symposium, 2017.

14. Y. M. Benane, R. Lavarello, **Bujoreanu, D.**, Cachard, C., Varray, F., Savoia, A., Franseschini, E., Basset, O. Ultrafast ultrasound imaging using a resolution and bandwidth enhancement technique. International Ultrasonics Symposium, 2017.

Bibliography

[Álvarez et al., 2013] Álvarez, F. J., Hernández, Á., Moreno, J. A., Pérez, M. C., Ureña, J., and De Marziani, C. (2013). Doppler-tolerant receiver for an ultrasonic lps based on kasami sequences. *Sensors and Actuators A: Physical*, 189:238–253.

[Badescu et al., 2017] Badescu, E., Bujoreanu, D., Petrusca, L., Friboulet, D., and Liebgott, H. (2017). Multi-line transmission for 3d ultrasound imaging: An experimental study. In *Ultrasonics Symposium (IUS), 2017 IEEE International*, pages 1–4. IEEE.

[Beck and Teboulle, 2009] Beck, A. and Teboulle, M. (2009). A fast iterative shrinkage-thresholding algorithm for linear inverse problems. *SIAM journal on imaging sciences*, 2(1):183–202.

[Benane et al., 2017] Benane, Y. M., Bujoreanu, D., Lavarello, R., Cachard, C., and Basset, O. (2017). An attenuation adapted pulse compression technique to enhance the bandwidth and the resolution using ultrafast ultrasound imaging. In *Internation Conference on Signal and Speech Processing (ICASSP), 2018*, pages 1–4. IEEE.

[Benane et al., 2018] Benane, Y. M., Bujoreanu, D., Lavarello, R. J., Varray, F., Escoffre, J.-M., Novell, A., Cachard, C., and Basset, O. (2018). Experimental implementation of a pulse compression technique using coherent plane-wave compounding. *IEEE transactions on ultrasonics, ferroelectrics, and frequency control*, 65(6):1025–1036.

[Besson et al., 2016] Besson, A., Carrillo, R. E., Bernard, O., Wiaux, Y., and Thiran, J.-P. (2016). Compressed delay-and-sum beamforming for ultrafast ultrasound imaging. In *Image Processing (ICIP), 2016 IEEE International Conference on*, pages 2509–2513. Ieee.

[Besson et al., 2018] Besson, A., Perdios, D., Martinez, F., Chen, Z., Carrillo, R. E., Arditi, M., Wiaux, Y., and Thiran, J.-P. (2018). Ultrafast ultrasound imaging as an inverse problem: Matrix-free sparse im-

age reconstruction. *IEEE transactions on ultrasonics, ferroelectrics, and frequency control*, 65(3):339–355.

[Black and Black, 1994] Black, U. D. and Black, U. D. (1994). *Emerging communications technologies*. PTR Prentice Hall.

[Briguet et al., 2014] Briguet, A., Fanet, H., Sappey-Marinier, D., and Vray, D. (2014). Imagerie médicale à base de champs magnétiques et d'ultrasons.

[Bujoreanu et al., 2017a] Bujoreanu, D., Bernard, A., Nicolas, B., Liebgott, H., and Friboulet, D. (2017a). Simultaneous coded plane wave imaging: Implementation on a research echograph. In *Ultrasonics Symposium (IUS), 2017 IEEE International*, pages 1–4. IEEE.

[Bujoreanu et al., 2017b] Bujoreanu, D., Liebgott, H., and Nicolas, B. (2017b). Simultaneous coded plane wave imaging in ultrasound: Problem formulation and constraints. In *Acoustics, Speech and Signal Processing (ICASSP), 2017 IEEE International Conference on*, pages 6254–6258. IEEE.

[Bujoreanu et al., 2017c] Bujoreanu, D., Nicolas, B., Friboulet, D., and Liebgott, H. (2017c). Inverse problem approaches for coded high frame rate ultrasound imaging. In *Signals, Systems, and Computers, 2017 51st Asilomar Conference on*, pages 1007–1011. IEEE.

[Capon, 1969] Capon, J. (1969). High-resolution frequency-wavenumber spectrum analysis. *Proceedings of the IEEE*, 57(8):1408–1418.

[Chernov, 2017] Chernov, L. A. (2017). *Wave propagation in a random medium*. Courier Dover Publications.

[Chiao and Thomas, 2000] Chiao, R. Y. and Thomas, L. J. (2000). Synthetic transmit aperture imaging using orthogonal golay coded excitation. In *Ultrasonics Symposium, 2000 IEEE*, volume 2, pages 1677–1680. IEEE.

[Chiao et al., 1997] Chiao, R. Y., Thomas, L. J., and Silverstein, S. D. (1997). Sparse array imaging with spatially-encoded transmits. In *Ultrasonics Symposium, 1997. Proceedings., 1997 IEEE*, volume 2, pages 1679–1682. IEEE.

[Coleri et al., 2002] Coleri, S., Ergen, M., Puri, A., and Bahai, A. (2002). Channel estimation techniques based on pilot arrangement in ofdm systems. *IEEE Transactions on broadcasting*, 48(3):223–229.

[Cook, 2012] Cook, C. (2012). *Radar signals: An introduction to theory and application*. Elsevier.

[David et al., 2015] David, G., Robert, J.-l., Zhang, B., and Laine, A. F. (2015). Time domain compressive beam forming of ultrasound signals. *The Journal of the Acoustical Society of America*, 137(5):2773–2784.

[Denarie et al., 2013] Denarie, B., Bjastad, T., and Torp, H. (2013). Multi-line transmission in 3-d with reduced crosstalk artifacts: A proof of concept study. *IEEE transactions on ultrasonics, ferroelectrics, and frequency control*, 60(8):1708–1718.

[Drukarev et al., 1993] Drukarev, A., Konstantinides, K., and Seroussi, G. (1993). Beam transformation techinques for ultrasonic medical imaging. *IEEE transactions on ultrasonics, ferroelectrics, and frequency control*, 40(6):717–726.

[Garcia et al., 2013] Garcia, D., Le Tarnec, L., Muth, S., Montagnon, E., Porée, J., and Cloutier, G. (2013). Stolt's fk migration for plane wave ultrasound imaging. *IEEE transactions on ultrasonics, ferroelectrics, and frequency control*, 60(9):1853–1867.

[Gran and Jensen, 2004] Gran, F. and Jensen, J. A. (2004). Identification of pulse echo impulse responses for multisource transmission. In *Signals, Systems and Computers, 2004. Conference Record of the Thirty-Eighth Asilomar Conference on*, volume 1, pages 168–172. IEEE.

[Gran and Jensen, 2008] Gran, F. and Jensen, J. A. (2008). Spatial encoding using a code division technique for fast ultrasound imaging. *ieee transactions on ultrasonics, ferroelectrics, and frequency control*, 55(1):12–23.

[Gran et al., 2004] Gran, F., Jensen, J. A., and Jakobsson, A. (2004). A code division technique for multiple element synthetic aperture transmission. In *Medical Imaging 2004: Ultrasonic Imaging and Signal Processing*, volume 5373, pages 300–307. International Society for Optics and Photonics.

[Haider et al., 1998] Haider, B., Lewin, P. A., and Thomenius, K. E. (1998). Pulse elongation and deconvolution filtering for medical ultrasonic imaging. *IEEE transactions on ultrasonics, ferroelectrics, and frequency control*, 45(1):98–113.

[Hamilton et al., 1998] Hamilton, M. F., Blackstock, D. T., et al. (1998). *Nonlinear acoustics*, volume 1. Academic press San Diego.

[Hansen et al., 2014] Hansen, H., Saris, A., Vaka, N., Nillesen, M., and De Korte, C. (2014). Ultrafast vascular strain compounding using plane wave transmission. *Journal of biomechanics*, 47(4):815–823.

[Hasegawa and Kanai, 2011] Hasegawa, H. and Kanai, H. (2011). High-frame-rate echocardiography using diverging transmit beams and parallel receive beamforming. *Journal of medical ultrasonics*, 38(3):129–140.

[Holfort et al., 2009] Holfort, I. K., Gran, F., and Jensen, J. A. (2009). Broadband minimum variance beamforming for ultrasound imaging. *IEEE transactions on ultrasonics, ferroelectrics, and frequency control*, 56(2):314–325.

[Jensen, 1991] Jensen, J. A. (1991). A model for the propagation and scattering of ultrasound in tissue. *The Journal of the Acoustical Society of America*, 89(1):182–190.

[Jensen, 1996] Jensen, J. A. (1996). Field: A program for simulating ultrasound systems. In *10TH NORDICBALTIC CONFERENCE ON BIOMEDICAL IMAGING, VOL. 4, SUPPLEMENT 1, PART 1: 351–353*. Citeseer.

[Jensen, 1999] Jensen, J. A. (1999). Linear description of ultrasound imaging systems: Notes for the international summer school on advanced ultrasound imaging at the technical university of denmark.

[Jensen et al., 2006] Jensen, J. A., Nikolov, S. I., Gammelmark, K. L., and Pedersen, M. H. (2006). Synthetic aperture ultrasound imaging. *Ultrasonics*, 44:e5–e15.

[Jensen and Svendsen, 1992] Jensen, J. A. and Svendsen, N. B. (1992). Calculation of pressure fields from arbitrarily shaped, apodized, and excited ultrasound transducers. *IEEE transactions on ultrasonics, ferroelectrics, and frequency control*, 39(2):262–267.

[Jespersen et al., 1998] Jespersen, S. K., Wilhjelm, J. E., and Sillesen, H. (1998). Multi-angle compound imaging. *Ultrasonic imaging*, 20(2):81–102.

[Jonassen et al., 2008] Jonassen, D., Spector, M. J., Driscoll, M., Merrill, M. D., van Merrienboer, J., and Driscoll, M. P. (2008). *Handbook of research on educational communications and technology: a project of the association for educational communications and technology*. Routledge.

[Kang et al., 2003] Kang, G., Costa, E., Weckerle, M., and Schulz, E. (2003). Optimum channel estimation over frequency-selective fading channel in multiple antenna systems. In *Communication Technology Proceedings, 2003. ICCT 2003. International Conference on*, volume 2, pages 1799–1803. IEEE.

[Karaman et al., 1998] Karaman, M., Bilge, H. S., and O'Donnell, M. (1998). Adaptive multi-element synthetic aperture imaging with motion and phase aberration correction. *IEEE transactions on ultrasonics, ferroelectrics, and frequency control*, 45(4):1077–1087.

[Kettunen, 1997] Kettunen, K. (1997). Code selection for cdma systems. *Department of Information Studies, University of Tampere, Finland*.

[Kotowick et al., 2013] Kotowick, K., Rohling, R., and Lampe, L. (2013). Adaptive compounding of synthetic aperture and compounded plane-wave imaging for fast ultrasonography. In *Biomedical Imaging (ISBI), 2013 IEEE 10th International Symposium on*, pages 784–787. IEEE.

[Lagarias et al., 1998] Lagarias, J. C., Reeds, J. A., Wright, M. H., and Wright, P. E. (1998). Convergence properties of the nelder–mead simplex method in low dimensions. *SIAM Journal on optimization*, 9(1):112–147.

[Lashkari et al., 2012] Lashkari, B., Manbachi, A., Mandelis, A., and Cobbold, R. S. (2012). Slow and fast ultrasonic wave detection improvement in human trabecular bones using golay code modulation. *The Journal of the Acoustical Society of America*, 132(3):EL222–EL228.

[Lashkari et al., 2016] Lashkari, B., Zhang, K., and Mandelis, A. (2016). High-frame-rate synthetic aperture ultrasound imaging using mismatched coded excitation waveform engineering: A feasibility study. *IEEE transactions on ultrasonics, ferroelectrics, and frequency control*, 63(6):828–841.

[Liu and Insana, 2005] Liu, J. and Insana, M. F. (2005). Coded pulse excitation for ultrasonic strain imaging. *IEEE transactions on ultrasonics, ferroelectrics, and frequency control*, 52(2):231–240.

[Lockwood et al., 1998] Lockwood, G. R., Talman, J. R., and Brunke, S. S. (1998). Real-time 3-d ultrasound imaging using sparse synthetic aperture beamforming. *IEEE transactions on ultrasonics, ferroelectrics, and frequency control*, 45(4):980–988.

[Lu, 1997] Lu, J.-y. (1997). 2d and 3d high frame rate imaging with limited diffraction beams. *IEEE transactions on ultrasonics, ferroelectrics, and frequency control*, 44(4):839–856.

[Mallart and Fink, 1992] Mallart, R. and Fink, M. (1992). Improved imaging rate through simultaneous transmission of several ultrasound beams. In *New Developments in Ultrasonic Transducers and Transducer Systems*, volume 1733, pages 120–131. International Society for Optics and Photonics.

[Mayer et al., 1990] Mayer, K., Marklein, R., Langenberg, K., and Kreutter, T. (1990). Three-dimensional imaging system based on fourier transform synthetic aperture focusing technique. *Ultrasonics*, 28(4):241–255.

[Misaridis and Jensen, 1999] Misaridis, T. X. and Jensen, J. A. (1999). An effective coded excitation scheme based on a predistorted fm signal and an optimized digital filter. In *Ultrasonics Symposium, 1999. Proceedings. 1999 IEEE*, volume 2, pages 1589–1593. IEEE.

[Miwa et al., 1981] Miwa, H., Hayashi, H., Shimura, T., and Murakami, K. (1981). Simultaneous multi-frequency ultrasonography the principle and technology. In *1981 Ultrasonics Symposium*, pages 655–659. IEEE.

[Montaldo et al., 2009] Montaldo, G., Tanter, M., Bercoff, J., Benech, N., and Fink, M. (2009). Coherent plane-wave compounding for very high frame rate ultrasonography and transient elastography. *IEEE transactions on ultrasonics, ferroelectrics, and frequency control*, 56(3):489–506.

[Morse et al., 1969] Morse, P. M., Ingard, K. U., and Beyer, R. (1969). Theoretical acoustics. *Journal of Applied Mechanics*, 36:382.

[Mosca et al., 2008] Mosca, F., Nicolas, J.-M., Kopp, L., and Couade, M. (2008). Temporal approach of the synthetic aperture imaging using hadamard matrix. *Journal of the Acoustical Society of America*, 123(5):3083.

[Nagai, 1985] Nagai, K. (1985). A new synthetic-aperture focusing method for ultrasonic b-scan imaging by the fourier transform. *IEEE transactions on sonics and ultrasonics*, 32(4):531–536.

[Nathanson et al., 1991] Nathanson, F. E., Reilly, J. P., and Cohen, M. N. (1991). Radar design principles-signal processing and the environment. *NASA STI/Recon Technical Report A*, 91.

[Nowicki et al., 2007] Nowicki, A., Trots, I., Lewin, P., Secomski, W., and Tymkiewicz, R. (2007). Influence of the ultrasound transducer bandwidth on selection of the complementary golay bit code length. *Ultrasonics*, 47(1-4):64–73.

[O'Donnell, 1992] O'Donnell, M. (1992). Coded excitation system for improving the penetration of real-time phased-array imaging systems. *IEEE transactions on ultrasonics, ferroelectrics, and frequency control*, 39(3):341–351.

[Oelze, 2007] Oelze, M. L. (2007). Bandwidth and resolution enhancement through pulse compression. *IEEE transactions on ultrasonics, ferroelectrics, and frequency control*, 54(4).

[Pages et al., 2015] Pages, N., Liebgott, H., and Nicolas, B. (2015). Emissions codées par ondes planes en imagerie ultrasonore ultra-rapide. In *Colloque GRETSI*.

[Papadacci et al., 2014] Papadacci, C., Pernot, M., Couade, M., Fink, M., and Tanter, M. (2014). High-contrast ultrafast imaging of the heart. *IEEE transactions on ultrasonics, ferroelectrics, and frequency control*, 61(2):288–301.

[Porée et al., 2016] Porée, J., Posada, D., Hodzic, A., Tournoux, F., Cloutier, G., and Garcia, D. (2016). High-frame-rate echocardiography using coherent compounding with doppler-based motion-compensation. *IEEE transactions on medical imaging*, 35(7):1647–1657.

[Prasad and Ojanpera, 1998] Prasad, R. and Ojanpera, T. (1998). An overview of cdma evolution toward wideband cdma. *IEEE communications Surveys*, 1(1):2–29.

[Quarteroni et al., 2008] Quarteroni, A. M., Sacco, R., and Saleri, F. (2008). *Méthodes Numériques: Algorithmes, analyse et applications*. Springer Science & Business Media.

[Rouyer et al., 2015] Rouyer, J., Varray, F., Pozo, E., Basset, O., Cachard, C., and Lavarello, R. (2015). Evaluation of a frequency-domain ultrasonic imaging attenuation compensation technique. In *Engineering in Medicine and Biology Society (EMBC), 2015 37th Annual International Conference of the IEEE*, pages 1560–1563. IEEE.

[Sandrin et al., 1999] Sandrin, L., Catheline, S., Tanter, M., Hennequin, X., and Fink, M. (1999). Time-resolved pulsed elastography with ultrafast ultrasonic imaging. *Ultrasonic imaging*, 21(4):259–272.

[Sandrin et al., 2002] Sandrin, L., Tanter, M., Catheline, S., and Fink, M. (2002). Shear modulus imaging with 2-d transient elastography. *IEEE transactions on ultrasonics, ferroelectrics, and frequency control*, 49(4):426–435.

[Schmerr Jr, 2014] Schmerr Jr, L. W. (2014). *Fundamentals of ultrasonic phased arrays*, volume 215. Springer.

[Schröder and Henning, 2014] Schröder, A. and Henning, B. (2014). Signal optimization of psk modulated gold-sequences for narrow band transducers. In *Ultrasonics Symposium (IUS), 2014 IEEE International*, pages 552–555. IEEE.

[Shen and Ebbini, 1996] Shen, J. and Ebbini, E. S. (1996). A new coded-excitation ultrasound imaging system. i. basic principles. *IEEE transactions on ultrasonics, ferroelectrics, and frequency control*, 43(1):131–140.

[Shoup and Hart, 1988] Shoup, T. and Hart, J. (1988). Ultrasonic imaging systems. In *Ultrasonics Symposium, 1988. Proceedings., IEEE 1988*, pages 863–871. IEEE.

[Siebert, 1988] Siebert, W. (1988). The early history of pulse compression radar-the development of an/fps-17 coded-pulse radar at lincoln laboratory. *IEEE Transactions on Aerospace and Electronic Systems*, 24(6):833–837.

[Skolnik, 1962] Skolnik, M. I. (1962). Introduction to radar systems mcgraw-hill. *NY USA*.

[Stepanishen, 1971] Stepanishen, P. R. (1971). The time-dependent force and radiation impedance on a piston in a rigid infinite planar baffle. *The Journal of the Acoustical Society of America*, 49(3B):841–849.

[Stetson et al., 1997] Stetson, P. F., Sommer, F. G., and Macovski, A. (1997). Lesion contrast enhancement in medical ultrasound imaging. *IEEE transactions on medical imaging*, 16(4):416–425.

[Tanter et al., 2002] Tanter, M., Bercoff, J., Sandrin, L., and Fink, M. (2002). Ultrafast compound imaging for 2-d motion vector estimation: Application to transient elastography. *IEEE transactions on ultrasonics, ferroelectrics, and frequency control*, 49(10):1363–1374.

[Tanter and Fink, 2014] Tanter, M. and Fink, M. (2014). Ultrafast imaging in biomedical ultrasound. *IEEE Transactions on Ultrasonics, Ferroelectrics, and Frequency Control*, 61(1):102–119.

[Tasinkevych et al., 2013] Tasinkevych, Y., Klimonda, Z., Lewandowski, M., Nowicki, A., and Lewin, P. (2013). Modified multi-element synthetic transmit aperture method for ultrasound imaging: A tissue phantom study. *Ultrasonics*, 53(2):570–579.

[Tasinkevych et al., 2012] Tasinkevych, Y., Trots, I., Nowicki, A., and Lewin, P. (2012). Modified synthetic transmit aperture algorithm for ultrasound imaging. *Ultrasonics*, 52(2):333–342.

[Thijssen, 2003] Thijssen, J. M. (2003). Ultrasonic speckle formation, analysis and processing applied to tissue characterization. *Pattern Recognition Letters*, 24(4-5):659–675.

[Thomenius, 1996] Thomenius, K. E. (1996). Evolution of ultrasound beamformers. In *Ultrasonics Symposium, 1996. Proceedings., 1996 IEEE*, volume 2, pages 1615–1622. IEEE.

[Tiran et al., 2015] Tiran, E., Deffieux, T., Correia, M., Maresca, D., Osmanski, B.-F., Sieu, L.-A., Bergel, A., Cohen, I., Pernot, M., and Tanter, M. (2015). Multiplane wave imaging increases signal-to-noise ratio in ultrafast ultrasound imaging. *Physics in Medicine & Biology*, 60(21):8549.

[Tong et al., 2014] Tong, L., Ramalli, A., Jasaityte, R., Tortoli, P., and D'hooge, J. (2014). Multi-transmit beam forming for fast cardiac imaging—experimental validation and in vivo application. *IEEE transactions on medical imaging*, 33(6):1205–1219.

[Torlak and Xu, 1997] Torlak, M. and Xu, G. (1997). Blind multiuser channel estimation in asynchronous cdma systems. *IEEE Transactions on Signal Processing*, 45(1):137–147.

[Toulemonde et al., 2015] Toulemonde, M., Basset, O., Tortoli, P., and Cachard, C. (2015). Thomson's multitaper approach combined with coherent plane-wave compounding to reduce speckle in ultrasound imaging. *Ultrasonics*, 56:390–398.

[Trots, 2015] Trots, I. (2015). Mutually orthogonal golay complementary sequences in synthetic aperture imaging systems. *Archives of Acoustics*, 40(2):283–289.

[Trots et al., 2004] Trots, I., Nowicki, A., Secomski, W., and Litniewski, J. (2004). Golay sequences-side-lobe-canceling codes for ultrasonography. *Archives of Acoustics*, 29(1).

[Tseng and Liu, 1972] Tseng, C.-C. and Liu, C. (1972). Complementary sets of sequences. *IEEE Transactions on Information theory*, 18(5):644–652.

[Tupholme, 1969] Tupholme, G. E. (1969). Generation of acoustic pulses by baffled plane pistons. *Mathematika*, 16(2):209–224.

[Van Wijk and Thijssen, 2002] Van Wijk, M. and Thijssen, J. (2002). Performance testing of medical ultrasound equipment: fundamental vs. harmonic mode. *Ultrasonics*, 40(1-8):585–591.

[Wagner, 1983] Wagner, R. F. (1983). Statistics of speckle in ultrasound b-scans. *IEEE Trans. Sonics & Ultrason.*, 30(3):156–163.

[Wiener et al., 1949] Wiener, N., Wiener, N., Mathematician, C., Wiener, N., Wiener, N., and Mathématicien, C. (1949). Extrapolation, interpolation, and smoothing of stationary time series: with engineering applications.

[Wright, 1985] Wright, J. N. (1985). Resolution issues in medical ultrasound. In *IEEE 1985 Ultrasonics Symposium*, pages 793–799. IEEE.

[Zachary et al., 2001] Zachary, J. F., Sempsrott, J. M., Frizzell, L. A., Simpson, D. G., and O'Brien, W. D. (2001). Superthreshold behavior and threshold estimation of ultrasound-induced lung hemorrhage

in adult mice and rats. *ieee transactions on ultrasonics, ferroelectrics, and frequency control*, 48(2):581–592.

[Zhang et al., 2016] Zhang, M., Varray, F., Besson, A., Carrillo, R. E., Viallon, M., Garcia, D., Thiran, J.-P., Friboulet, D., Liebgott, H., and Bernard, O. (2016). Extension of fourier-based techniques for ultrafast imaging in ultrasound with diverging waves. *IEEE transactions on ultrasonics, ferroelectrics, and frequency control*, 63(12):2125–2137.

[Zhao and Huang, 1997] Zhao, Y. and Huang, A. (1997). A novel channel estimation method for ofdm mobile communication systems based on pilot signals and transform-domain processing. In *Vehicular Technology Conference, 1997, IEEE 47th*, volume 3, pages 2089–2093. IEEE.

FOLIO ADMINISTRATIF

THESE DE L'UNIVERSITE DE LYON OPEREE AU SEIN DE L'INSA LYON

NOM : Bujoreanu
(avec précision du nom de jeune fille, le cas échéant)

DATE de SOUTENANCE : 26/11/2018

Prénoms : Denis

TITRE : Echographie compressée: une nouvelle stratégie d'acquisition et de formation pour une imagerie ultra rapide

NATURE : Doctorat

Numéro d'ordre : AAAALYSEIXXXX

Ecole doctorale : Électronique, Électrotechnique et Automatique (EDA160)

Spécialité : Département Sciences pour l'ingénieur

RESUME : Le manuscrit de cette thèse est divisé dans quatre chapitres. Dans le premier chapitre, un bref résumé des applications de l'imagerie échographique est donné de même que ses avantages. Le problème que ce travail adresse est indiqué et les objectifs de la thèse sont formulés. Un résumé succinct du manuscrit est également fourni. Dans le deuxième chapitre, le contexte théorique de la propagation des ondes acoustiques est fixé. De plus, sur la base de cette formulation, les schémas d'acquisition ultrasonore conventionnels sont revus et les métriques habituelles qui quantifient la qualité de l'image sont introduites. Ici, sont également résumées les approches déjà existantes visant à surmonter le compromis entre qualité d'image et cadence d'acquisition d'images. Dans les chapitres trois, quatre et cinq sont présentées les contributions les plus marquantes de cette thèse. Le chapitre trois détaille la première contribution de ce travail. Tout d'abord, il présente le contexte théorique d'une approche d'imagerie par ultrasons basée sur un modèle réduit de propagation des ondes ultrasonores codées temporellement dans les tissus mous. Ensuite, la simulation et les résultats in vitro sont présentés et discutés, les avantages / limites de la méthode étant soulignés. Dans le chapitre quatre les performances d'une approche d'imagerie basée sur un modèle avancé de propagation des ondes ultrasonores sont présentées. Tout d'abord, le modèle direct général est construit. Ensuite, le modèle avancé est associé au concept de codage temporel des ondes ultrasonores et son adaptation à un schéma d'acquisition ultra-rapide spécifique est illustrée. En outre, une approche par problème inverse est proposée afin de reconstruire l'image du milieu insonifié. Les performances du modèle direct et de la méthode de reconstruction sont évaluées au moyen de simulations numériques..

MOTS-CLÉS :

Laboratoire (s) de recherche : Centre de Recherche en Acquisition et Traitement de l'Image pour la Santé (CREATIS)

Directeur de thèse: Denis Friboulet

Président de jury :

Composition du jury : Adrian Basarab (rapporteur), Jianwen Luo (rapporteur), Jean-Philippe Thiran (rapporteur), Lori Bridal (examinatrice), Hervé Liebgott (co-encadrant), Barbara Nicolas (co-directrice de thèse), Denis Friboulet (Directeur de thèse)